ELECTROMAGNETIC TRANSITION STRENGTHS STUDIED WITH DOPPLER-SHIFT TECHNIQUES ACROSS THE CONTOURS OF THE VALLEY OF STABILITY

By

Charles Robert Loelius

A DISSERTATION

Submitted
to Michigan State University
in partial fulfillment of the requirements
for the degree of

Physics – Doctor of Philosophy

2017

ABSTRACT

ELECTROMAGNETIC TRANSITION STRENGTHS STUDIED WITH DOPPLER-SHIFT TECHNIQUES ACROSS THE CONTOURS OF THE VALLEY OF STABILITY

By

Charles Robert Loelius

The electromagnetic transition strengths between bound states in nuclei provide insight into nuclear structure. On one hand, from a single particle perspective the electromagnetic excitation and de-excitation of nuclei quantify the overlaps of nuclear wavefunctions, probing the internal configuration. On the other hand, in a collective model, the shape and dynamics of the nucleus are reflected in the electromagnetic transition strengths. For example, electric quadrupole transitions are sensitive to the deformation of a nucleus and distinguish between various pictures of collectivity, such as rotors and vibrators. In this work, electromagnetic transition strengths are studied through lifetime and Coulomb-excitation measurements. Nuclei across the contours of the valley of stability are studied to investigate features of nuclear structure and how they change near and far from stability.

The first experiment discussed in this work investigates the effect of the $N = Z = 28$ shell closure on collectivity in ^{58}Ni. ^{58}Ni has 28 protons and 30 neutrons, and therefore is not expected to exhibit enhanced collectivity compared to its neutron rich neighbors. However, a previous measurement of the lifetime of the 4_1^+ state indicates an enhanced $B(E2;4_1^+ \rightarrow 2_1^+)$ transition strength, suggesting unexpectedly large collectivity. The present work revisits the lifetime of the 4_1^+ state with a more sensitive technique, namely a Recoil Distance Method measurement at the National Superconducting Cyclotron Laboratory. The GRETINA detector array was employed with the S800 Spectrograph to measure the 4_1^+ state lifetime. The model independent $B(E2;4_1^+ \rightarrow 2_1^+)$ from the present work supports an unenhanced transition strength, as expected near the shell closure.

The second experiment discussed in this work is a study of the electromagnetic transition states in ^{27}Ne. ^{27}Ne is a loosely-bound neutron rich nucleus although it does not exhibit a halo structure

in its ground state. This work investigates the excited states of ^{27}Ne that lie closer to the particle threshold for features associated with a halo structure. The lifetimes of the $1/2^+$ and $3/2^-$ states in ^{27}Ne and the branching ratio of the $1/2^+$ state decaying into the $3/2^-$ excited state and $3/2^+_{gs}$ ground state are measured. These values are used to determine the $B(E1; 3/2^- \rightarrow 3/2^+_{gs})$ and $B(E1; 1/2^+ \rightarrow 3/2^-)$ values. It was found that the $B(E1)$ connecting the $1/2^+$ state to the $3/2^-$ state is at least 50 times larger than that between the $3/2^-$ and $3/2^+_{gs}$ states, indicating an extended radial component in the $1/2^+$ state wavefunction. Lifetime measurements of excited states in ^{28}Ne are also presented.

A new setup for performing Coulomb-excitation measurements based on heavy ion inelastic scattering with two targets is presented and employed to measure the $B(E2; 3/2^+_{gs} \rightarrow 1/2^+)$ strength in ^{27}Ne. The method is demonstrated through a reference measurement of the $B(E2; 0^+_{gs} \rightarrow 2^+_1)$ of ^{30}Mg. Combined with the lifetime measurement, the $B(M1; 1/2^+ \rightarrow 3/2^+_{gs})$ transition strength is extracted. The measured value is unhindered, indicating that the $1/2^+$ excited state of ^{27}Ne is not dominated by an s-wave component. The electromagnetic transition strengths in ^{27}Ne therefore indicate that the $1/2^+$ excited state may exhibit behaviors characteristic of deformed halos.

In summary, this study of electromagnetic strengths demonstrates the features of nuclei in the valley of stability, and explores new aspects of nuclear structure that arise toward the edges of stability. Concurrently, Doppler-shift methods are shown to be powerful tools for investigating the structure of nuclei across the nuclear landscape.

ACKNOWLEDGMENTS

This work, which I hope to be a small contribution to the ever growing library of human knowledge, is the product of numerous people's visions, support, and effort. I am especially grateful to my advisor, Dr. Hironori Iwasaki, who has guided me throughout the work enclosed here from experiment to analysis to written document. I have also been fortunate to have the constant support of my guidance committee, Dr. Remco Zegers, Dr. Morten Hjorth-Jensen, Dr. Lisa Lapidus, and Dr. Norman Birge. Their contributions to this work have been invaluable. This work would have been impossible without the tremendous effort from all the members of the National Superconducting Cyclotron Laboratory who kept the status bar green during the running of the experiments, and provided advice and help throughout.

I must also thank my professors at Rutgers University who brought me into this field. In particular, I must thank Dr. Yitzhak Sharon and Dr. Larry Zamick, who introduced me to electromagnetic transition strengths and hooked me in. I am also thankful to my undergraduate thesis advisor Dr. Ronald Gllman, Dr. Noemie Benczer Koller, and Dr. Gulhan Gurdal for their support in my undergraduate research. I would be remiss in not also thanking my undergraduate philosophy advisors Dr. Larry Temkin and the late Dr. Derek Parfit who helped me tremendously in clarifying both my future and my thoughts.

I am deeply indebted to my friends and fellow students at Michigan State University. This work is especially enriched by my fellow graduate students at the National Superconducting Cyclotron Laboratory, with whom I have often had numerous productive and entertaining conversations. In particular, I must thank my fellow lifetime group members for their advice and support, especially Dr. Chris Morse and Dr. Kenneth Whitmore. However, all my friends whether discussing ROOT or adventuring in Haumark have helped to make this work possible and meaningful.

I am also especially thankful for my many friends with whom I have worked with the Graduate Employees Union, including those I roped into organizing and revitalizing our union and building solidarity across campus. Likewise, I continue to respect my friends from the Council of Graduate

Students who have sought to make our university a more welcome and inclusive place. I hope to have helped you make Michigan State University at least a little bit more of a truly supportive community for all students, faculty and workers. I cannot express my gratitude to the many amazing people with whom I have had a chance to improve our community.

Everything in this work is due to the constant encouragement and support of my family. I am unendingly thankful for my parents, who have helped all along the way in my each and every endeavor. I am deeply grateful to Alexandra Genia for her support throughout this process and her constant faith in me. Finally, I am always thankful for my sisters, who are the most incredible people I know, and who always have my back.

Finally, I would like to thank my 7th grade English teacher Ms. Drukten, who introduced me to science-fiction books and got me into this whole mess to begin with.

TABLE OF CONTENTS

LIST OF TABLES

LIST OF FIGURES

CHAPTER 1

NUCLEAR STRUCTURE

1.1 Atomic Nuclei

Nearly all matter in everyday life is made up of atoms. As discovered by Rutherford, the atom consists of a positively charged nucleus that is surrounded by one or more electrons [1]. While the electrons are thought to be point particles with no internal structure, atomic nuclei are known to consist of positively charged protons and electrically neutral neutrons.

This work seeks to add to our knowledge of the structure of atomic nuclei near and far from stability through the study of the electromagnetic properties of nuclei. Therefore, it is necessary to outline current knowledge of nuclei, including observed trends in stable and unstable nuclei. Near stability, a number of models based on an independent-particle or collective picture of nuclei have been employed to understand nuclear structure. However, these models do not necessarily reproduce features of nuclei far from stability. In this section systematics of atomic nuclei and ways to interpret them will be discussed.

The protons and neutrons, or nucleons, interact not only through the electromagnetic force, but through the strong and weak nuclear forces. While the weak force is involved in nuclear decays, the strong nuclear force is involved in binding nuclei. In particular, the nuclear strong force is a short range interaction (with a range of 1-2 fm) that is generally attractive, with a repulsive contribution at very short distances [2][3]. The strong nuclear force in combination with the Pauli-exclusion principle leads to a rich structure in atomic nuclei [4].

Protons and neutrons are spin $1/2$ fermions, and thus obey the Pauli exclusion principle. The Pauli exclusion principle is a fundamental restriction on particles with non-integer spin, which requires that the total wavefunction be antisymmetrized. This can be stated as the requirement that [5]:

$$\psi(x_1,\ldots,x_i,x_j,\ldots,x_N) = -\psi(x_1,\ldots,x_j,x_i,\ldots,x_N) \tag{1.1}$$

where the x_i's represent the position and quantum numbers of the i-th fermion. One key result of this is that two fermions cannot occupy the same state with the same quantum numbers.

If one neglects the Coulomb term, neutrons and protons can be thought of as two states of a nucleon particle, differing in a new quantum number called isospin. The isospin of the nucleon is $\tau = 1/2$, with the proton having $\tau_z = -1/2$ and the neutron having $\tau_z = +1/2$ [6][7].

Figure 1.1 shows the Chart of the Nuclides. The nuclei are listed with proton number on the vertical axis, and neutron number on the horizontal axis. Those nuclei with the same number of protons are known as isotopes, and those with the same number of neutrons are isotones. In Figure 1.1, the color represents the decay mode. Unstable nuclei can decay through β decay, emitting an electron or positron, or by capturing an electron. β decay proceeds through the weak interaction and changes a neutron to a proton or vice-versa. Nuclei can also decay via the emission of one or more protons, neutrons, or bound α particles consisting of two neutrons and two protons.

It is critical to note, however, that there is a line of stable nuclei known as the valley of stability. These nuclei do not decay and thus make up the nuclei in the majority of ordinary atoms. Stable nuclei have been well described by both single-particle and collective models. However, it can be seen that in fact most nuclei are unstable.

One early view of atomic nuclei useful for qualitatively understanding their properties is the liquid drop model. In this model, nuclei are considered to consist of an incompressible fluid in a spherical droplet, because the short range repulsive interaction of the strong force and the Pauli-exclusion principle effectively prevent the compression of the nucleus. This means that, in reasonable agreement with experiment, the radius of the nucleus can be determined as $r_0 A^{1/3}$, where r_0 is generally 1.2 fm and A is the total number of nucleons [4]. From the liquid drop model, one can derive the Bethe-Weizsäcker semi empirical mass formula [9][10]:

$$M(A,Z) = (A-Z)m_n + Zm_p - a_1 A + a_2 A^{2/3} + a_3 \frac{Z^2}{A^{1/3}} + a_4 \frac{(A-2Z)^2}{A} \pm a_5 \frac{1}{A^{3/4}} \qquad (1.2)$$

In this equation m_n is the neutron mass, m_p is the proton mass, and the quantities a_i are various constants chosen to fit the data. Each of the terms with coefficients a_i are used to reproduce the

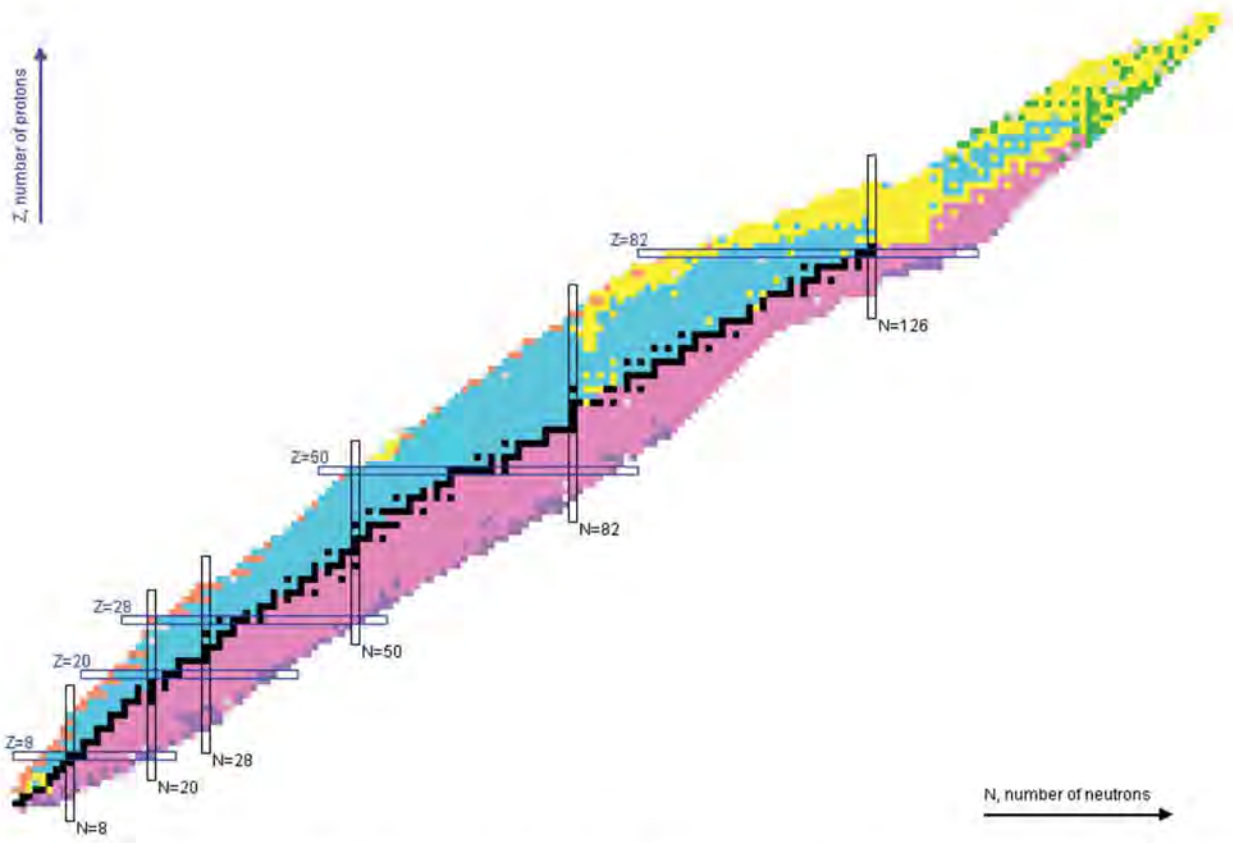

Figure 1.1 The Chart of Nuclides is displayed, with proton number Z increasing along the y-axis, and neutron number N increasing along the x-axis. The nuclei are color coded by decay type. Black represents stable nuclei. Pink decays vis β^-, blue through either electron capture or β^+, yellow through alpha emission, orange through proton emission, purple through neutron emission, and green through fission. The standard magic numbers are plotted for protons and neutrons. Figure is from [8].

binding energy of the nuclei, without which the mass would simply be the sum of the proton and neutron masses. As such, each of the terms can be related to the nuclear Hamiltonian.

The $-a_1 A$ term simply relates to the attractive feature of the strong force, while the $+a_2 A^{2/3}$ accounts for the missing binding energy at the surface of the nucleus. The $+a_3 \frac{Z^2}{A^{1/3}}$ term represents the repulsive Coulomb force acting on the protons. While these terms are clear from the liquid drop model alone, the remaining two terms are needed to match the experimental data and must be added. The $+a_4 \frac{(A-2Z)^2}{A}$ term accounts for the fact that stable nuclei tend to have similar numbers of protons and neutrons, especially at low masses. The $\pm a_5 \frac{1}{A^{3/4}}$ term is somewhat more

complicated, and represents a pairing force. This force is understood to lower the energy of states where nucleons pair off into total angular momentum and parity $J^\pi = 0^+$ states [4]. a_5 is taken to be positive for odd-odd nuclei, which are consequently less stable, and negative for even-even nuclei which are consequently more stable [9]. While the liquid drop model is a simple model of nuclear interactions, it can be of use for a conceptual understanding of stability in nuclei.

Each atomic nucleus has a ground state and may have one or more bound excited states. Each nuclear state can be described by its total angular momentum J, its parity, its energy, and its width. The total angular momentum J is the sum of the orbital angular momentum $\vec{l}$ and spin $\vec{s}$ of each of the nucleons.

In even-even nuclei, the ground state nearly always has total angular momentum and parity of $J^\pi = 0^+$. This can be understood as arising from the pairing contribution to the Hamiltonian, that lowers the energy of two identical particles coupled together to form a $J^\pi = 0^+$ state. The first excited state of even-even nucleus is normally a 2^+ state [4].

Among the most important features observed in nuclear trends are the behavior of nuclei with certain magic numbers of protons or neutrons [11][12][13]. Figure 1.2 shows the energy of the first excited 2^+ state for even-even nuclei across the chart of nuclides. One feature that is highlighted on the chart is the large 2_1^+ state energy for most isotopes with proton or neutron number $2, 8, 20, 28, 50, 82$, and 126. The features of these magic numbers show up in the systematics of other quantities as well, including natural nuclear abundances, the large number of stable isotopes within an isotopic (isotonic) chain, and electromagnetic transition strengths [4][11]. The quadrupole electromagnetic transition strengths are known to be correlated with excitation energies, and are found to be reduced at magic nuclei [11][14].

The magic numbers were independently identified as arising from closed shells by analogy to atomic structure by Mayer and Jensen [12][13]. This identification has led to the nuclear shell model, which treats nuclei as free particles in a central potential, leading to distinct energy levels and explaining the shell structure.

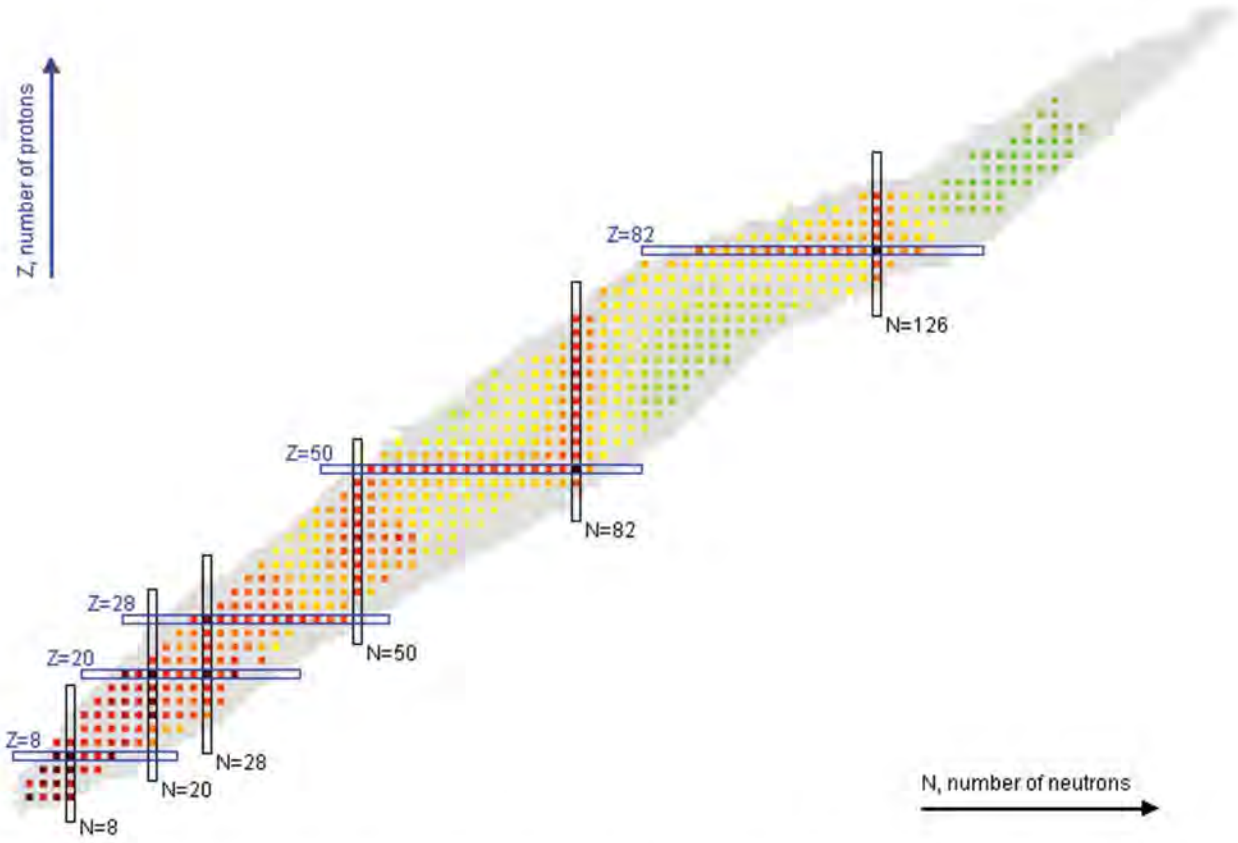

Figure 1.2 The chart of nuclei is shown for even-even nuclei. The nuclei are color coded by the energy of the first 2^+ excited state. Nuclei with energies up to 200 keV are colored in green. Those with energies up to 1 MeV are colored yellow. Those with higher energy are colored from orange to red. The magic numbers are highlighted, and demonstrate bands of large 2_1^+ energy. Figure and data are from [8].

1.2 Shell Model

The nuclear shell model arises from an independent-particle model in which the individual nucleons freely move through a central potential $V(r)$ [4]. That this model is appropriate for nuclei is not immediately apparent. Unlike the Coulomb potential in atoms, the nuclear binding potential is not generated from a central particle. The nuclear binding potential is instead generated by the individual nucleon-nucleon interactions. At the same time, the nucleons are packed to saturation, so that it may seem that they should be incapable of traveling freely in the volume of the nucleus. However, the Pauli exclusion principle means that in order for a given nucleon to be interacted with, it

must be able to somehow reach the next highest energy unoccupied state. For most nucleons in a nucleus the energy gap is large compared to the scattering interactions, so that the nucleons cannot be excited by collisions. Therefore, the effects of the dense packing do not result in an impediment to the free movement assumption. At the same time, the dense packing means that a given nucleon will experience only the average interaction of all of the nearby nucleons. This interaction can therefore be modeled as a central potential acting on each nucleon independently [4].

The central potential $V(r)$ used in the independent-particle model can be chosen from a number of options, including the Woods-Saxon and harmonic oscillator potentials. Figure 1.3 illustrates how the harmonic oscillator potential can be used to understand the magic numbers. The harmonic oscillator potential has exact solutions that result in degenerate energies for states with the same principle quantum number. These result in shell closures at $2, 8, 20, 40, 70$ and 112. However, only the first three shell closures agree well with the observed nuclear magic numbers.

It was the insight of Mayer and Jensen that it was possible to identify the magic numbers with energy gaps in the harmonic oscillator if the degeneracy of the orbital angular momentum and total angular momentum states was broken [12][13]. To accomplish this, an attractive l^2 term can be added to the Hamiltonian. This term lifts the degeneracy of the orbital angular momentum states. This term also makes the central potential more constant across all angular momenta by counteracting the increased harmonic oscillator potential experienced by states with higher l [4]. This is consistent with a constant nuclear density. The addition of a spin-orbit coupling term to the Hamiltonian of the form $V_{s.o.} = -V_{ls}V'(r)(\vec{l}\cdot\vec{s})$ lifts the degeneracy of the total angular momenta states, resulting in two total j states for each nl state [4]. If the magnitude of the spin-orbit term is comparable to the harmonic oscillator strength, the magic numbers can be reproduced.

The independent-particle model already accounts for a number of features that can be observed in nuclei. For example, the large 2_1^+ energy at the magic numbers can be understood as the increased energy needed to excite nucleons across the shell gap. The spin and parities of nuclei with one nucleon above or below a shell closure can be described as deriving solely from the single particle level structure. For example, ^{40}Ca has a magic number of neutrons and protons filling

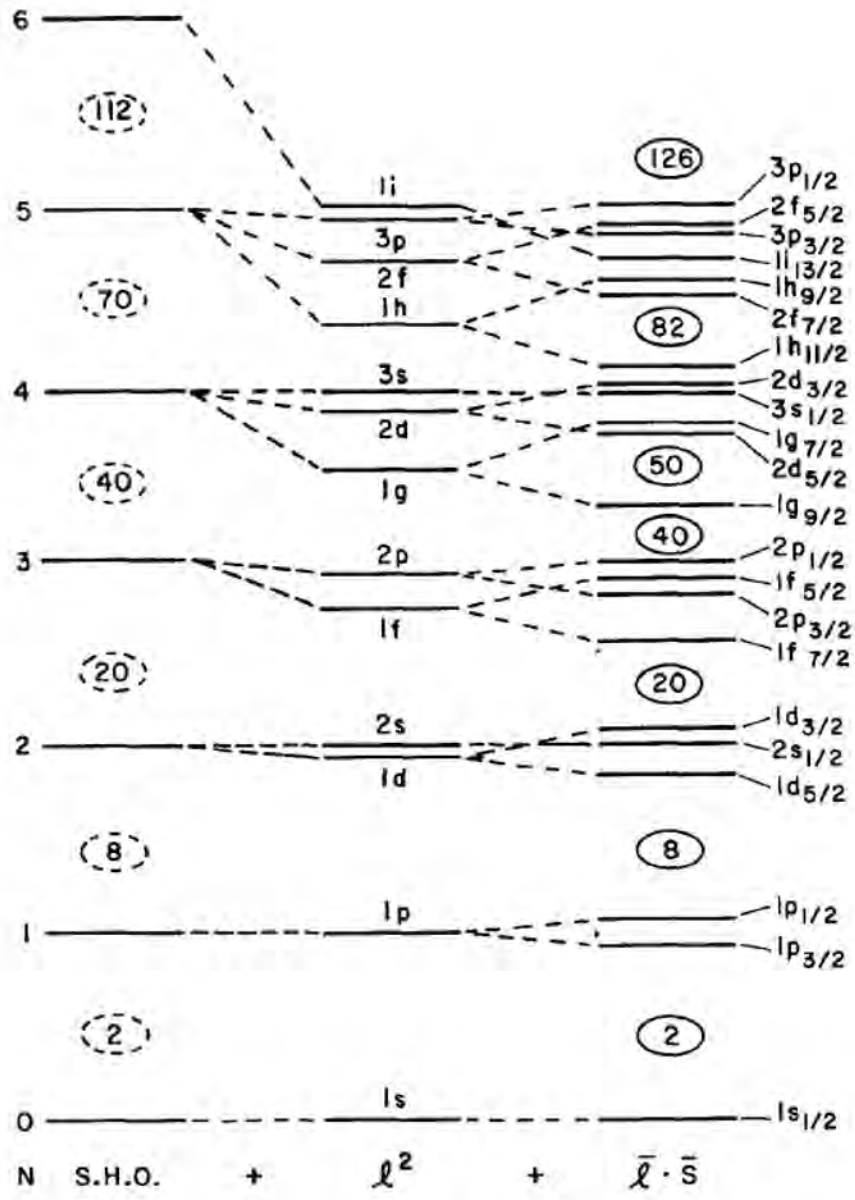

Figure 1.3 The energy levels for the harmonic oscillator (left) are shown and compared with those where an l^2 attractive term is added (center) and where that and a spin-orbit term are added (right). The shell gaps in the harmonic oscillator is compared to that of the magic numbers predicted with the inclusion of the l^2 and spin orbit terms. Figure is from [4].

through the $d_{3/2}$ orbital. The next highest level is the $f_{7/2}$, and it can be seen that the ground state spin and parity of ^{41}Ca is $7/2^-$, consistent with the expected total angular momentum and the negative parity arising from the $l = 3$ orbital angular momentum [15].

It is worth remembering that because protons and neutrons are distinguishable, they occupy separate energy levels. This also means that the energy levels for protons will be increased compared to neutrons to account for the Coulomb contribution.

At the same time, the single particle model must account for the impact of nucleon-nucleon interactions, which of course do contribute to nuclear structure and are especially important away from the shell closures. Therefore, in the shell model, a non-diagonal Hamiltonian is constructed of the form

$$H = \sum_k (T_k + U_k) + \sum_{k<l} V_{kl} \tag{1.3}$$

where the left hand sum is over single particle kinetic energies and a mean central potential, and the right hand side is the sum over various interaction terms.

The problem can be solved then in terms of solutions to the Hamiltonian $H^{(0)} = \sum_k T_k + U_k$. This leads to a Hamiltonian matrix with diagonal single particle energies and off diagonal interaction terms. However, the calculations are limited by the need for finite matrix size. This is accounted for in both the inclusion of only two body terms and by limiting the model space to be considered [5]. This allows for approximate solutions for the energies and wavefunctions of nuclear states through the diagonalization of the Hamiltonian matrices. Various Hamiltonians which can make reasonable predictions in specific mass regions have been developed using single particle energies and the interaction terms between orbitals.

1.3 Nuclei Far From Stability

Nuclei far from the valley of stability can exhibit behavior different from stable nuclei. Two features of interest in this work are the evolution of shell structure away from stability and the formation of halo nuclei near the driplines. Studies of these features of nuclear structure away from

stability have been facilitated by the advent of rare-isotope (RI) beams [16]. In this section the evolution of shell structure and halo nuclei will be discussed.

1.3.1 Evolution of Shell Structure

At stable nuclei, the well established magic numbers of nucleons are $2, 8, 20, 28, 50, 82$ and 126. However, for nuclei far from stability, the magic numbers can change due to the particular interaction of protons and neutrons narrowing or widening the shell gaps. One example of this is the island of inversion around ^{32}Mg [17][18][19][20]. Energy levels for excited states for odd A isotones with N=17 in this region are shown in Figure 1.4. In this neutron rich region, the gap between the *sd* and fp shells at $N = 20$ is reduced. This leads to the lowering of the energies of negative parity intruder states from the $f_{7/2}$ and $p_{3/2}$ orbitals [21].

At the same time that the magic number $N = 20$ disappears in the island of inversion, the magic number $N = 16$ manifests in neutron rich ^{24}O. In particular, ^{24}O has no measured bound excited states. Since it has a neutron separation energy of 3.6(3) MeV, the lack of excited states indicates that the shell gap here is at least of that order [22]. The large energy of the first excited state is an indicator of a magic number at $N = 24$ not seen in stable nuclei [22].

The evolution of shell structure is not restricted to the island of inversion around ^{32}Mg, nor to the shell closure at $N = 20$. In general, the shell gaps established for stable nuclei could change for proton or neutron rich nuclei. However, such changes can be more modest than at the islands of inversion.

The change in the shell gaps can be understood from a number of theoretical points of view. In particular, the nucleon-nucleon interaction contains a tensor contribution of the form [23]:

$$V_T = (\vec{\tau}_1 \cdot \vec{\tau}_2) \left([\vec{s}_1 \vec{s}_2]^{(2)} \cdot Y^{(2)} \right) f(r) \tag{1.4}$$

where $\vec{\tau}_i$ is the isospin of the i-th nucleon, $\vec{s}_i$ is the spin of the $i-$th nucleus, $[\ ]^{(K)}$ is the coupling of the operators in the brackets to the angular momentum K, Y is a spherical harmonic, and $f(r)$ is a function of the distance between the nucleons. For a nucleon with orbital angular momentum

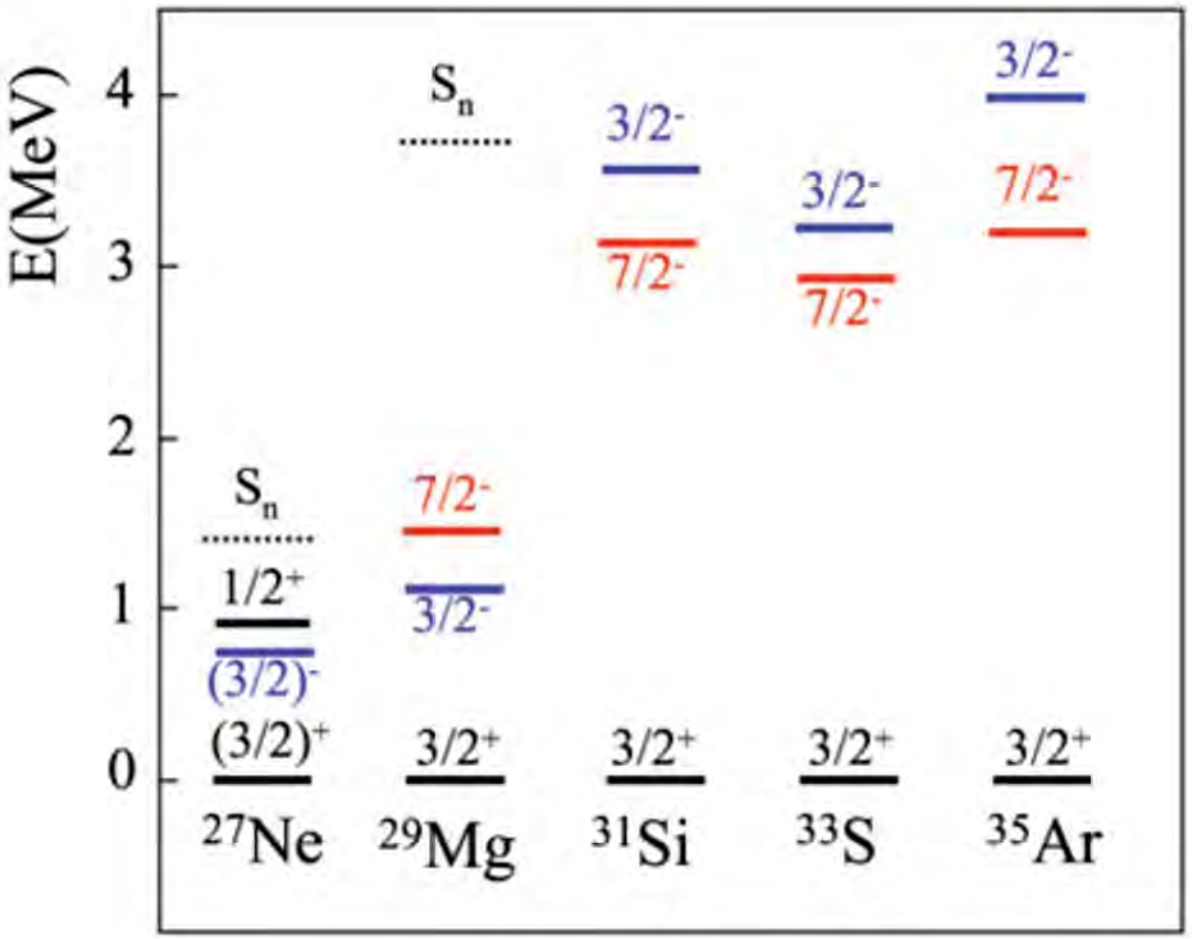

Figure 1.4 Level energies and spin parity in odd-A isotones with $N = 17$ near the island of inversion are shown. The $7/2^-$ and $3/2^-$ states arising from excitations over the $N = 20$ gap into the $f_{7/2}$ and $p_{3/2}$ orbitals are shown. As the N/A ratio increases, the energy levels of the $7/2^-$ and $3/2^-$ states lower from 3 MeV in ^{35}Ar to less than 1 MeV in ^{27}Ne. Figure is from [21].

l and spin $s = 1/2$, the total angular momentum can be either $j_< = l - 1/2$ or $j_> = l + 1/2$. The tensor force between two nucleons with total angular momenta j and j' is based on the relative orientations of the orbital and spin angular momenta. The tensor contribution to the potential is attractive between nucleons with oppositely coupled angular momenta, i.e. $j_<$ and $j'_>$. On the other hand, the tensor force is repulsive between nucleons with the same configuration $j_<$ and $j'_<$ or $j_>$ and $j'_>$ [23]. Therefore, changes in the proton configuration in nuclei can affect neutron shell closures through the tensor interaction, and vice-versa. In particular, if the single particle state for the valence protons is $j_<$, this will serve to lower the neutron single particle states with $j'_>$ and raise those with $j'_<$. This can manifest in sudden changes where the valence protons switch configuration [23].

Of particular interest in this work are the shell closures at $N, Z = 28$. The magic number at 28 is the first arising from the spin-orbit interaction [12][13]. The proton shell gap at $Z = 28$ varies between $N = 28$ and $N = 40$. However, in this case the shell gap increases with increasing neutron number, ranging between 5 MeV to 6 MeV. This can be understood as arising from an attractive interaction between the protons filling the $f_{7/2}$ orbital and the neutrons in the $f_{5/2}$ orbital [21]. On the other hand, along the $N = 28$ isotones the repulsive interaction between the proton in the $d_{3/2}$ orbital and the neutron in the $f_{7/2}$ orbital modifies the gap at $N = 28$. Therefore, the $N = 28$ shell closure, which is robust for ^{48}Ca, vanishes in ^{36}S and ^{34}Si [21].

In addition to providing insight into the nature of the nuclear force, the evolution of shell properties away from stability can give rise to other phenomena. For example, the disappearance of the $N = 8$ shell gap was evidenced by the $1/2^+$ ground state of ^{11}Be and was confirmed in observations of ^{12}Be [24]. The ground state occupation of the $2s_{1/2}$ orbital in ^{11}Be with $l = 0$ means that the valence neutron is not affected by a centrifugal barrier. This in combination with the low neutron separation energy causes the valence neutron to have a large radial extent, called a halo [25].

1.3.2 Halo Nuclei

Halo nuclei are a feature of nuclei far from stability, where there is a long tail in the radial density distribution of the nucleus [26]. The extended nuclear distribution is ascribed to one or more valence nucleons with a large radial extent decoupled from the remaining core of the nucleus [26]. The halo formation can then be understood from the perspective of a valence nucleon in a potential well generated by the core. If we assume that the valence nucleon is an s-wave neutron and approximate the potential as a finite square well, it is easy to conceptualize the halo formation. The wavefunction for the neutron outside of the square well potential can be described as [26]:

$$\psi(r) = \left(\frac{2\pi}{k}\right)\left(\frac{e^{-kr}}{r}\right)\left(\frac{e^{kR}}{1+kR}\right) \tag{1.5}$$

where R is the potential width and k is related to the neutron separation energy (S_n) as [26]:

$$k = \frac{\sqrt{2\mu S_n}}{\hbar} \tag{1.6}$$

where μ is the reduced mass of the system.

This means that the nuclear density, which is just $|\psi|^2$ is [26]:

$$\rho(r) \propto \frac{e^{-2kr}}{r^2} \tag{1.7}$$

The factor k then determines the overall slope of the decay in the distribution function. In stable nuclei, S_n is on the order of 6-8 MeV, and the k factor is relatively constant [26]. However, far from stability the S_n can be reduced by orders of magnitude. For example, the neutron rich nucleus ^{27}Ne has a neutron separation energy of approximately 1.4 MeV, while the two neutron separation energy in ^{11}Li is only 360 keV [26][27]. Therefore in these nuclei far from stability, the factor k can be reduced rapidly as a function of excess neutrons. This results in the distribution function having a larger radial extent [26].

Halo nuclei formation is also dependent on the angular momentum of the valence nucleon, as shown in Figure 1.5. This is because higher angular momentum states have a centrifugal barrier in their Hamiltonians, which serves to confine the wavefunction [28]. As is demonstrated in Figure

1.5 as the binding energy approaches 0, the nuclear density s-wave and p-wave states with $l = 0$ and 1 respectively diverge towards large radii. States with higher angular momentum on the other hand converge to a finite radius. As such, in addition to a low binding energy, halo nuclei require $l = 0$ or 1 to form [26].

A survey of observed and candidate ground state halo nuclei is presented in Figure 1.6. Consistent with the discussion above, these nuclei can be found far from stability, near the proton and neutron driplines, where the separation energies are reduced [26]. Experiments on these nuclei have determined certain characteristic behaviors of halo structure.

The first halo nucleus discovered was ^{11}Li, which was identified as having a large total interaction cross section for reactions on carbon at 790 MeV/u compared to nearby nuclei [29]. The large interaction cross section can be related to the radial extent of the nuclear matter distribution and thus serves as an indicator of halo properties.

Another technique first employed on ^{11}Li is to measure the momentum distribution of fragments from reactions where the halo neutrons are removed. Figure 1.7 shows the transverse momenta distributions of ^{6}He produced via reactions of ^{8}He on carbon and ^{9}Li produced from reactions of ^{11}Li on carbon [30]. The Heisenberg uncertainty relationship between position and momentum is:

$$\Delta x \Delta p \geq \frac{\hbar}{2} \tag{1.8}$$

The increased radial extension of the halo nuclei increases the uncertainty in position, resulting in a reduction of the uncertainty of the momentum distribution. This is observed in Figure 1.7, where the momentum distribution of ^{9}Li fragments produced from ^{11}Li has a component with a σ of 23 ± 5 MeV/c, as opposed to that of the ^{6}He, which is 71 ± 15 MeV/c [30]. Thus, the reduced width in momentum distributions also serves as a measurement of the radial extension in the nuclear distribution for halo nuclei [26].

In addition to the above, electromagnetic transition strengths have been used to study halo nuclei. Large dipole electromagnetic transition strengths have been measured in halo nuclei through the use of Coulomb-excitation and Coulomb dissociation measurements [31][32]. This is because

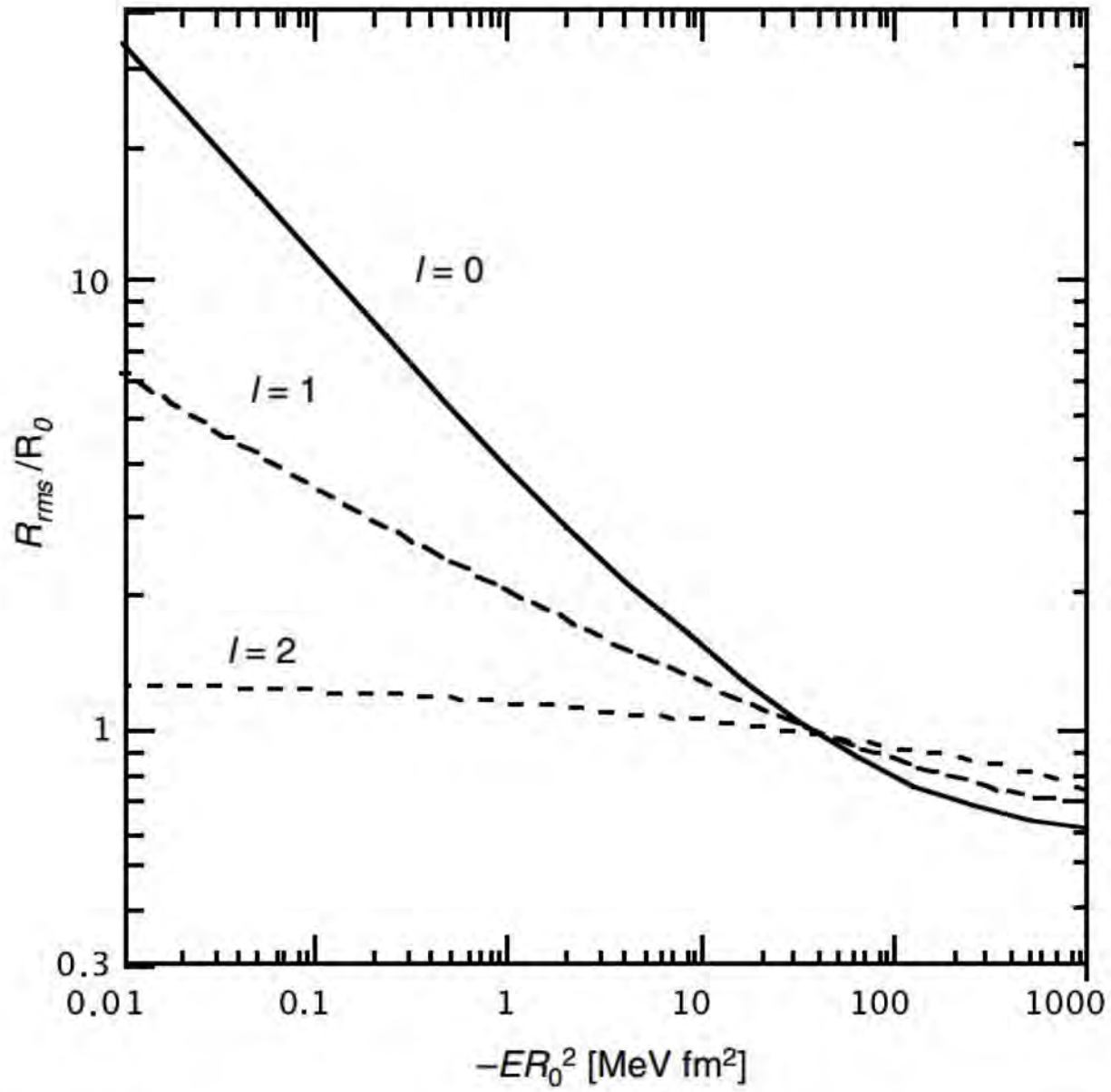

Figure 1.5 The root mean square radii of a nucleon in a square well potential are presented. The binding energy normalized by the size of the square well (R_0) is presented on the x-axis. The root mean square radius for each energy is displayed on the y-axis, scaled by the radius of the square well potential. Radii as a function of binding energy are shown for angular momenta $l = 0, 1$, and 2. The radii diverge as the binding energy approaches zero for $l = 0$ and 1 but converge for $l = 2$. Figure is from [26].

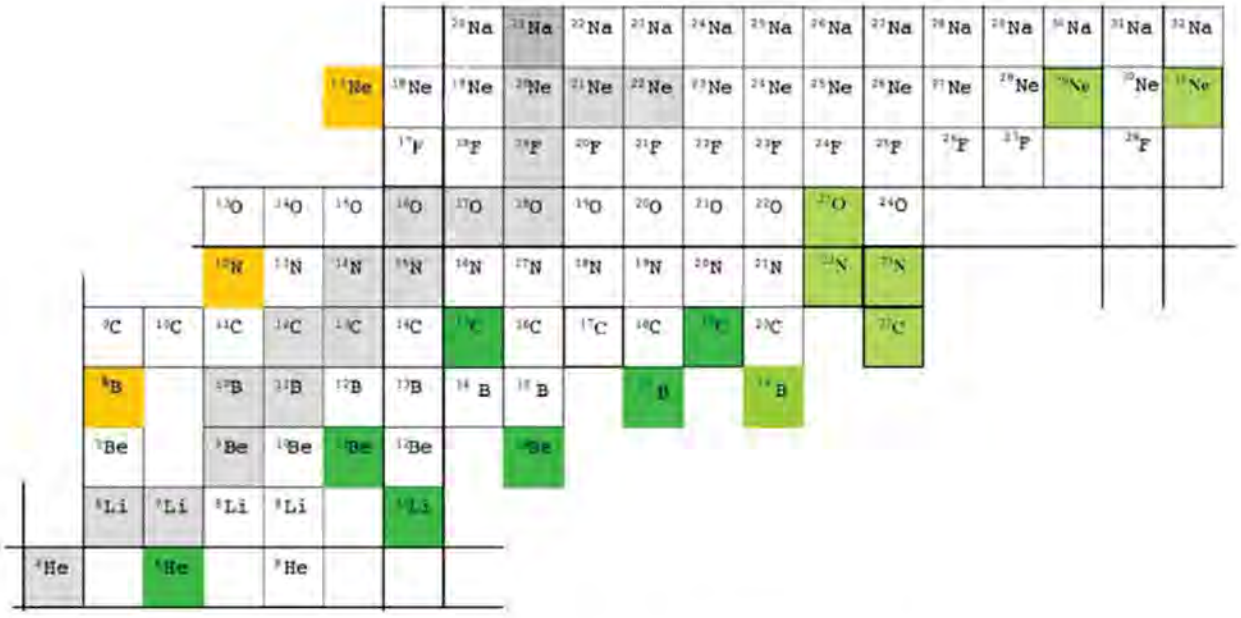

Figure 1.6 A focused view of the chart of nuclides is presented. Halo nuclei and potential halo nuclei are colored in. The valence nucleons in the orange colored nuclei are protons. The valence nucleons in the green colored nuclei are neutrons. The lighter shades of green are nuclei for which enhanced interaction cross sections have been measured. Darker shades of green are those nuclei for which both enhanced cross sections and narrow momenta distributions have been measured. Figure and discussion are from [26].

the electromagnetic transition strengths of interactions with nuclei is in part determined by their spatial extent.

1.4 Electromagnetic Transition Strengths

Electromagnetic transition strengths are a useful tool for understanding nuclear structure. The electromagnetic interaction is particularly involved in γ-ray decays of nuclear excited states and in scattering with Coulomb fields. The interaction of the electromagnetic field with a nucleon can be expressed in terms of electric and magnetic components decomposed by angular momenta. Therefore, the total electromagnetic interaction with nuclei can be expressed as [5]:

$$\hat{O} = \sum_{\lambda,\mu} \left(\hat{O}(E\lambda)_\mu + \hat{O}(M\lambda)_\mu \right) \tag{1.9}$$

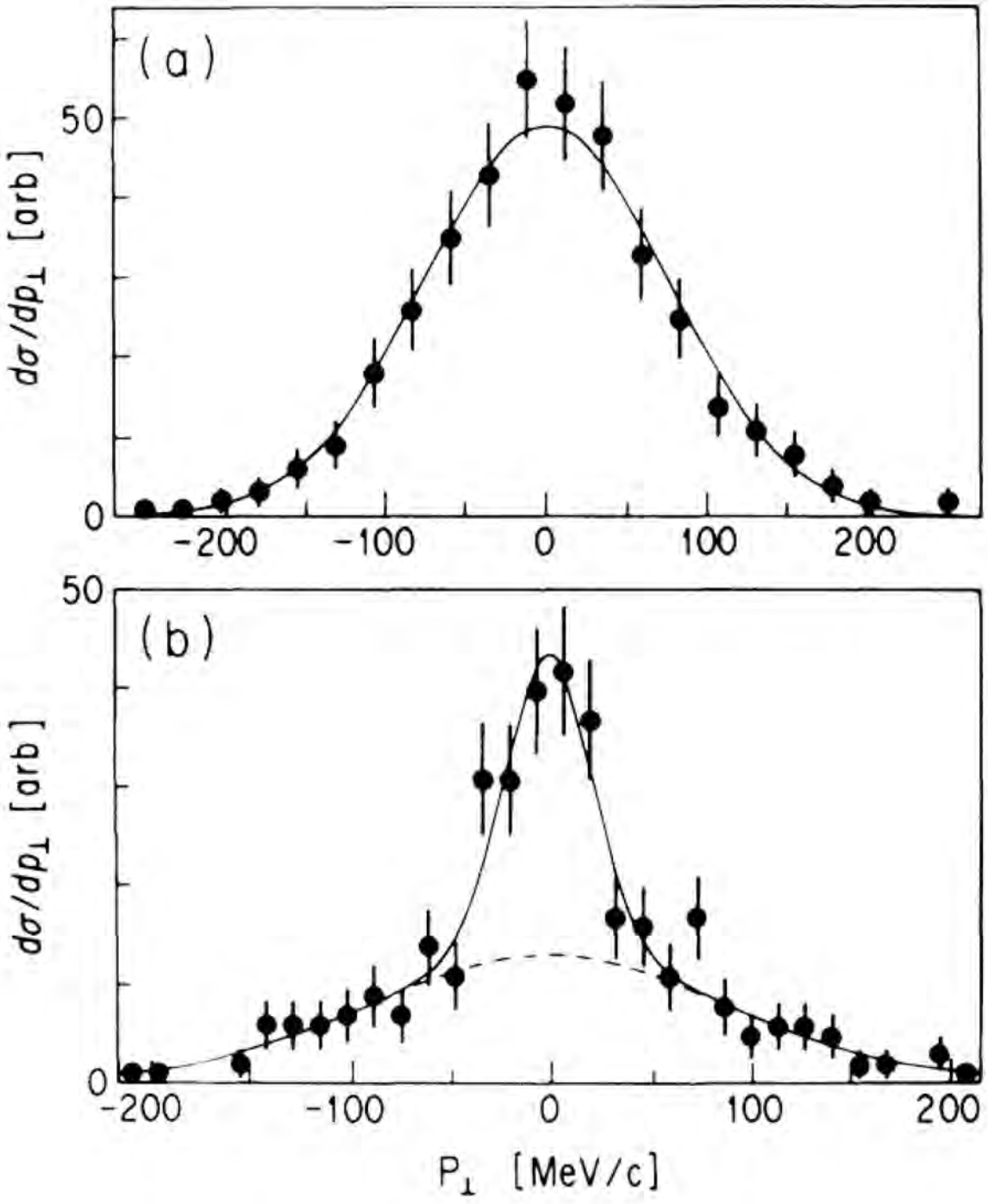

Figure 1.7 The transverse momenta distributions for (top) ^{6}He produced from reactions of ^{8}He+C and (bottom) ^{9}Li produced from reactions of ^{11}Li+C are presented. The incoming beam energy of the ^{8}He and ^{11}Li was 790 (20) MeV/u. The solid lines are fitted Gaussian distributions, while (bottom) the dotted line is a wide-momentum contribution to the distribution in ^{11}Li [30]. Figure is from [30].

The electric transition operator for a nucleon is given simply as [5]:

$$\hat{O}(E\lambda)_\mu = r^\lambda Y^\lambda_\mu(\hat{r}_i)e_i \tag{1.10}$$

In this equation Y^λ_μ is the spherical harmonic for angular momentum λ and projection μ. The e_i term is the effective charge of the nucleon under consideration. While for a bare proton, e_i would just be the proton charge e and for a bare neutron e_i would be 0, effective charges that vary from the bare charges are used in shell-model calculations with a non-interacting core in order to account for effects from center of mass corrections and core polarization induced by wavefunctions outside the model space [5]. Other no-core shell models exist that use the bare charges directly for certain mass regions [33][34].

The magnetic transition operator is given by the sum of the spin coupling and orbital angular momentum coupling terms as [5]:

$$\hat{O}(M\lambda)_\mu = \left(\vec{l}_i \frac{2g^l_i}{\lambda+1} + \vec{s}_i g^s_i\right)\vec{\nabla}\left(r^\lambda Y^\lambda_\mu(\hat{r}_i)\right)\mu_N \tag{1.11}$$

In this equation, $\mu_N = \frac{e\hbar}{2m_p c}$ is the nuclear magneton. The g^l_i and g^s_i are the orbital and spin g-factors for the i-th nucleon. These too may vary in shell-model calculations from the free nucleon g-factors for protons ($g^l_p = 1$, $g^s_p = 5.586$) and neutrons ($g^l_n = 0$, $g^s_n = -3.826$) to account for wavefunctions outside the model space [5].

The total electromagnetic interaction strength is just the sum of these matrix elements over all of the nucleons for each electromagnetic transition type $\pi = E, M$ and each angular momentum λ. The transition rate between two states with initial and final angular momenta J_i, J_f and transition energy E_γ connected by an electromagnetic transition element $\hat{O}(\pi\lambda)$ is [5] :

$$T_{i,f,\pi,\lambda} = \left(\frac{8\pi(\lambda+1)}{\lambda\left[(2\lambda+1)!!\right]^2}\right)\left(\frac{E^{2\lambda+1}_\gamma}{\hbar^{2\lambda+2}c^{2\lambda+1}}\right)\frac{\left|\langle J_f||\hat{O}(\pi\lambda)||J_i\rangle\right|^2}{2J_i+1} \tag{1.12}$$

The term on the right hand side of the equation is defined as the reduced transition strength for the interaction as:

$$B(\pi\lambda) = \frac{\left|\langle J_f||\hat{O}(\pi\lambda)||J_i\rangle\right|^2}{2J_i+1} \tag{1.13}$$

The reduced matrix element is independent of the angular momentum projection of the states, with the factor of $2J_i+1$ serving to average over those states. This means that the $B(\pi\lambda; J_i \rightarrow J_f)$ must be multiplied by a factor of $\frac{2J_i+1}{2J_f+1}$ to find the $B(\pi\lambda; J_f \rightarrow J_i)$ [5].

Electromagnetic transition strengths are often compared with the strength expected if the transition was solely due to a single independent nucleon changing state within the nucleus [35]. These are called Weisskopf units (W.u.) and are defined as [5]:

$$B_W(E\lambda) = \left(\frac{1}{4\pi}\right)\left(\frac{3}{(3+\lambda)}\right)^2\left(1.2A^{1/3}\right)^{2\lambda} e^2\mathrm{fm}^{2\lambda} \tag{1.14}$$

$$B_W(M\lambda) = \left(\frac{10}{\pi}\right)\left(\frac{3}{3+\lambda}\right)^2 (1.2A^{1/3})^{2\lambda-2}\mu_N^2\mathrm{fm}^{2\lambda-2} \tag{1.15}$$

The electromagnetic transitions between nuclear states are determined by parity and angular momentum selection rules. The operator $E\lambda$ is proportional to $r^\lambda Y_{\lambda\mu}$ and the $M\lambda$ operator is proportional to $\nabla(r^\lambda Y_{\lambda\mu})$. The parity of the spherical harmonics are determined by the angular component as $(-1)^\lambda$. The parity of the radial term is positive. In addition, the operator ∇ has a parity of -1. Therefore, the total parity of any $E\lambda$ operator is $(-1)^\lambda$ and for any $M\lambda$ operator is $(-1)^{\lambda-1}$ [7]. Parity conservation therefore requires that electric transitions between states with the same parity must occur via $E\lambda$ transitions with even λ, and transitions between states with opposite parity must proceed via $E\lambda$ transitions with odd λ. Parity conservation requires that magnetic transitions between states with the same parity must proceed via $M\lambda$ transitions with odd λ, while transitions between states with opposite parities must proceed via $M\lambda$ transitions with even λ [7].

The angular momentum selection rules further determine the electromagnetic transitions between nuclear states. The angular momentum conservation requires that

$$\vec{\lambda} + \vec{J}_f = \vec{J}_i \tag{1.16}$$

In quantum mechanics, this conservation results in the triangle rule, namely that [36]:

$$\left|J_f - J_i\right| \leq \lambda \tag{1.17}$$

This rule means that only transitions with angular momentum λ greater than the magnitude of the difference between the angular momentum of the initial and final state can occur. In addition, the fact that the photon is a massless spin-1 particle means that it must have a spin projection of ± 1 [7]. Angular momentum conservation then means that γ-ray transitions between states cannot occur via the $E0$ or $M0$ operators. In addition, the $\pi\lambda$ transition strength decreases rapidly with increasing λ. Therefore the overall transition strength tends to be dominated by the lowest λ transition strength. One exception to this is the competition between $E2$ and $M1$ strengths in transitions between states with the same parity and where $|J_f - J_i| \leq 1$ [7].

The electromagnetic transition strengths between states can be useful for understanding nuclear properties. The wavefunction of the nucleus is directly involved in the determination of the transition strength, meaning that changes in structure can manifest in changes to these quantities. For example, the $B(E2; 2_1^+ \rightarrow 0_{gs}^+)$ values are of interest in even-even nuclei, since in almost all cases the ground state is 0^+ and the first excited state is 2_1^+. The $B(E2; 0_{gs}^+ \rightarrow 2_1^+)$ value can be related to the deformation parameter β of the nucleus by the equation [37];

$$|\beta| = \left(\frac{4\pi}{3ZeR_0^2}\right)\sqrt{B(E2; 0_{gs}^+ \rightarrow 2_1^+)} \tag{1.18}$$

While the electromagnetic transition strengths are the more fundamental quantity, they can also be understood as a function of the geometry of the nucleus. In a simple liquid drop picture, the deformation parameter β represents the quadrupole deformation of the droplet compared to a spherical shape. Mathematically, this is represented where the quadrupole moment is Q_0 as [4]:

$$Q_0 = \frac{3}{\sqrt{5\pi}} ZR_0^2 \beta \left(1 + 0.16\beta\right) \tag{1.19}$$

Far from stability, electromagnetic transitions strengths are also useful for examining novel features in nuclei. $B(E1)$ transition strengths are related to the expectation value of the nuclear radius, and therefore are enhanced in halo nuclei [26]. For example halo nucleus ^{11}Be has the largest $B(E1)$ transition strength observed between bound states in nuclei, with a value of 0.36(3) W.u. [38]. On the other hand, nuclei at shell closures are spherical and the $B(E2; 2_1^+ \rightarrow 0_1^+)$ values

are small [21]. Therefore, the experimental $B(E2;2_1^+ \rightarrow 0_{gs}^+)$ values are indicators of changes in magic numbers. For example, the relatively large $B(E2)$ in ^{44}S with 28 neutrons is an indicator that the $N = 28$ shell closure disappears for neutron rich nuclei [21][39].

The transition strength in nuclei can be measured through the probability of exciting a state through the electromagnetic force or the probability of an excited state decaying via an electromagnetic transition. The transition rate for a particular mode $T_{\pi,\lambda,i,f}$ is the inverse of the partial lifetime for decays $f \rightarrow i$. In cases where the dominant transition is the $T_{\pi,\lambda,i,f}$, then the mean lifetime of the excited state is simply $\tau = \frac{1}{T}$ [5]. The transition strength can also be determined from the cross section of electromagnetic interactions with the nucleus. Methods of measuring these quantities are discussed in the following chapter.

CHAPTER 2

METHODS FOR MEASURING ELECTROMAGNETIC TRANSITION STRENGTHS

The electromagnetic transition strengths between bound states of nuclei can be determined through a number of experimental techniques. The measurement of the lifetimes of excited states can be used to determine the dominant transition strengths allowed by selection rules. In general, for a given state primarily decaying to one lower level, the electromagnetic transition strength would be dominated by the lowest angular momentum transition allowed by ΔL and parity considerations. If states decay to different levels or through multiple electromagnetic moments with similar strengths, the partial lifetimes of the states must be extracted. The partial lifetime between decays to different states can be found from the measured state lifetime and the branching ratio of decays to each of the lower states. Other methods to determine the relative contributions of different $B(\pi\lambda)$ strengths include measurements of γ-ray distributions [40].

Another set of methods used to extract $B(\pi\lambda)$ values are those that relate inelastic cross sections to electromagnetic transition strengths. In particular, Coulomb-excitation is the inelastic scattering of a nucleus in the electric field generated by another nucleus. The cross section for a nucleus to undergo Coulomb-excitation is determined in part by the electric transition strengths ($B(E\lambda)$) between its ground and excited states. In general, measurements of the cross section of the nuclei can be compared to coupled channel calculations from reactions theory to extract the $B(E\lambda)$ of interest. A number of complications present themselves in the measurement of Coulomb-excitation cross sections in rare-isotopes, because the beam energies available at rare-isotope facilities tend to be above the Coulomb-barrier. Therefore, there may be a nuclear contribution to the cross section that must be accounted for. These considerations have been addressed by intermediate energy Coulomb-excitation techniques that account for potential nuclear scattering.

In this section, techniques used to measure lifetimes and Coulomb-excitation cross sections are described. Additional techniques not used in this work are also briefly discussed. These techniques not currently used are of interest for understanding choices made in the current experiments and

for future measurements of excited states ^{27}Ne.

2.1 Lifetime Measurements

The excited states of atomic nuclei can decay to a lower energy state through various channels, including electromagnetic transitions. It is worth noting that by the Heisenberg uncertainty principle, the intrinsic energy width (Γ) of the state can be related to the lifetime of the state by [41]:

$$\tau\Gamma = \hbar \tag{2.1}$$

The overall energy width, and hence lifetime, may be made up in part by different partial widths corresponding to different transition strengths. In this case $\Gamma = \sum\Gamma_i$, where each Γ_i is related to the transition strength of one decay channel. It is also worth noting that the lifetime τ is the mean lifetime of the state, i.e. the amount of time that it takes for the total number of excited states to be reduced by a factor of e. This should not be confused with the half-life, which is the amount of time needed to reduce the total number of excited states by a factor of 2.

For a given transition between initial and final states I_i and I_f, and for an operator $\hat{O}$, the decay probability is proportional to the overlap of the initial and final states as mediated by the operator. The transition strength amplitude is inversely related to the lifetime of the state, and thus can be related to the overlap mediated by the operator [41]. That is:

$$\Gamma_i \propto \left|\langle\psi_f|\hat{O}|\psi_i\rangle\right|^2 \tag{2.2}$$

In the cases of interest in this work, these decays occur via γ-ray transitions mediated by the electromagnetic force. Therefore the lifetimes can be related to the reduced transition strengths $B(\pi\lambda)$.

The lifetimes of excited states can be measured through a number of methods suited to different lifetime regions. Figure 2.1 shows the regions accessible to each technique [41]. In this work, lifetimes between 0 and 20 ps are probed. In this region the most appropriate techniques are the Recoil Distance Method (RDM) and the Doppler-shift Attenuation method (DSAM). Both

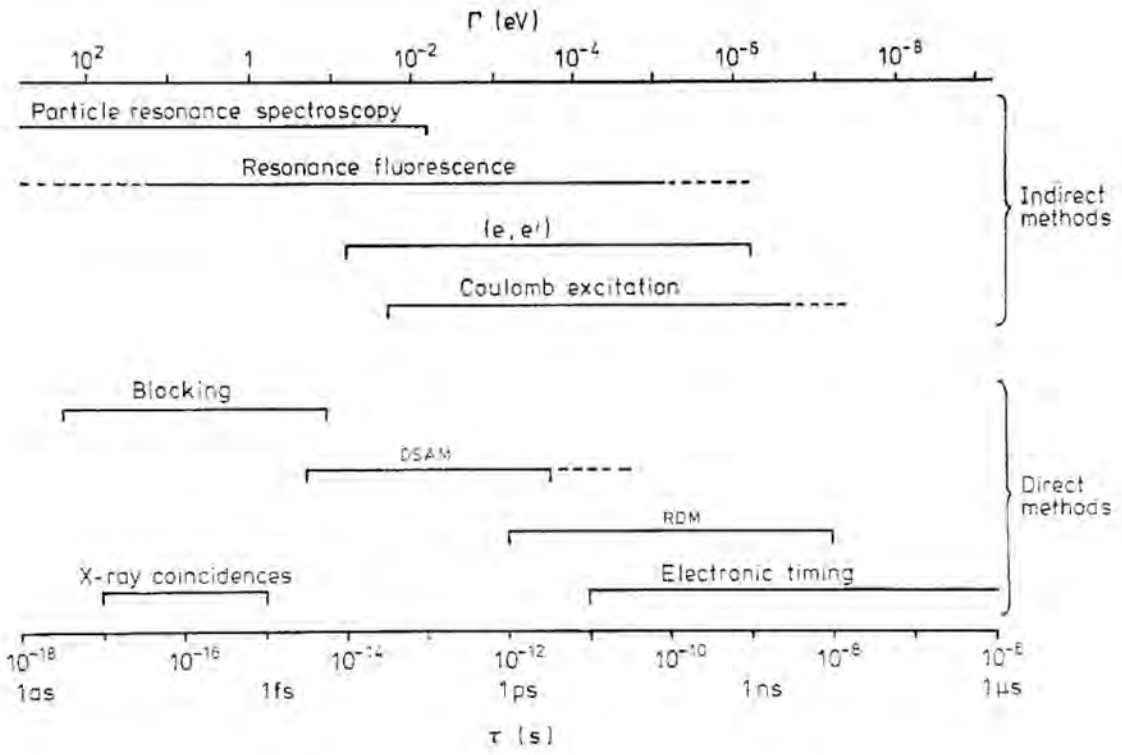

Figure 2.1 The lifetime regions accessible by direct and indirect measurement techniques are presented. The x-axis shows the lifetime region in lifetimes (bottom) and energy widths (top). Figure is from [41].

methods rely on the use of the Doppler-effect to determine lifetimes, which will be discussed briefly. In this work, the Recoil Distance Method was exclusively used to measure lifetimes, and will be the focus of the section. However, the Doppler-shift attenuation method may present future opportunities with rare isotope beams at low energies.

2.1.1 Doppler-shifting

The Doppler-effect is fundamental to the Recoil Distance and Doppler-shift Attenuation methods. The classical Doppler-effect is a simple phenomenon whereby the observed frequency of a wave is increased (decreased) for a source moving towards (away from) an observer. As photons propagate as waves, with energy $E = h\nu$, the observed energy of a photon is affected by the Doppler-effect. For in-beam nuclear physics experiments, the observed γ-ray energies are Doppler-shifted. This is

because the energy of the photon emitted from de-excitation of a nuclear excited state will have the energy of the difference between the levels in the projectile frame of the nucleus. But as in these experimental techniques the nuclei are moving relative to the detectors, the observed energy will be modified by the Doppler-effect. However, as the beams used in this work are at velocities near $30\% - 50\%$ of the speed of light, the relativistic Doppler-effect must be used. This is given as:

$$E_{Obs} = \frac{E_{cm}}{\gamma(1 - \beta \cos\theta_{lab})} \tag{2.3}$$

where E_{Obs} is the measured energy in the γ-ray detectors, E_{cm} is the transition energy of the nucleus in the projectile frame, β is the velocity of the nucleus in the lab frame relative to the speed of light, γ is the Lorentz factor $\frac{1}{\sqrt{1-\beta^2}}$, and θ_{lab} is the angle between the vector from the source to the position the γ ray is observed at and the velocity of the ion. The relativistic Doppler-effect is a simple consequence of the Lorentz transformation applied to the energy-momentum vector of the photon [42][43].

There are two key features of relativistic Doppler-shifting worth noting for lifetime measurement techniques. The first is that the Doppler-shifting is largest for small θ_{lab}, where the $\cos\theta_{lab}$ attains a maximum. The second is that for forward angles the larger the β is, the higher the observed energy is. These two facts determine much of what is required for successful Recoil Distance and Doppler-shift Attenuation Method experiments.

One final thing worth noting is the relativistic effect on γ-ray distributions. If the nucleus decays with an isotropic distribution of γ rays in the projectile frame, in the lab frame an observer will see an excess of γ rays along the direction of the motion of the nucleus, and a corresponding decrease in the direction opposite the motion. This can be understood as a Lorentz-focusing of γ rays emitted from nuclei moving at relativistic speeds. Therefore, the geometric efficiency increases for detectors located downstream from the nucleus, and decreases for upstream detectors. In the present experiments, the detectors are placed downstream at forward angles to benefit from the increased efficiency.

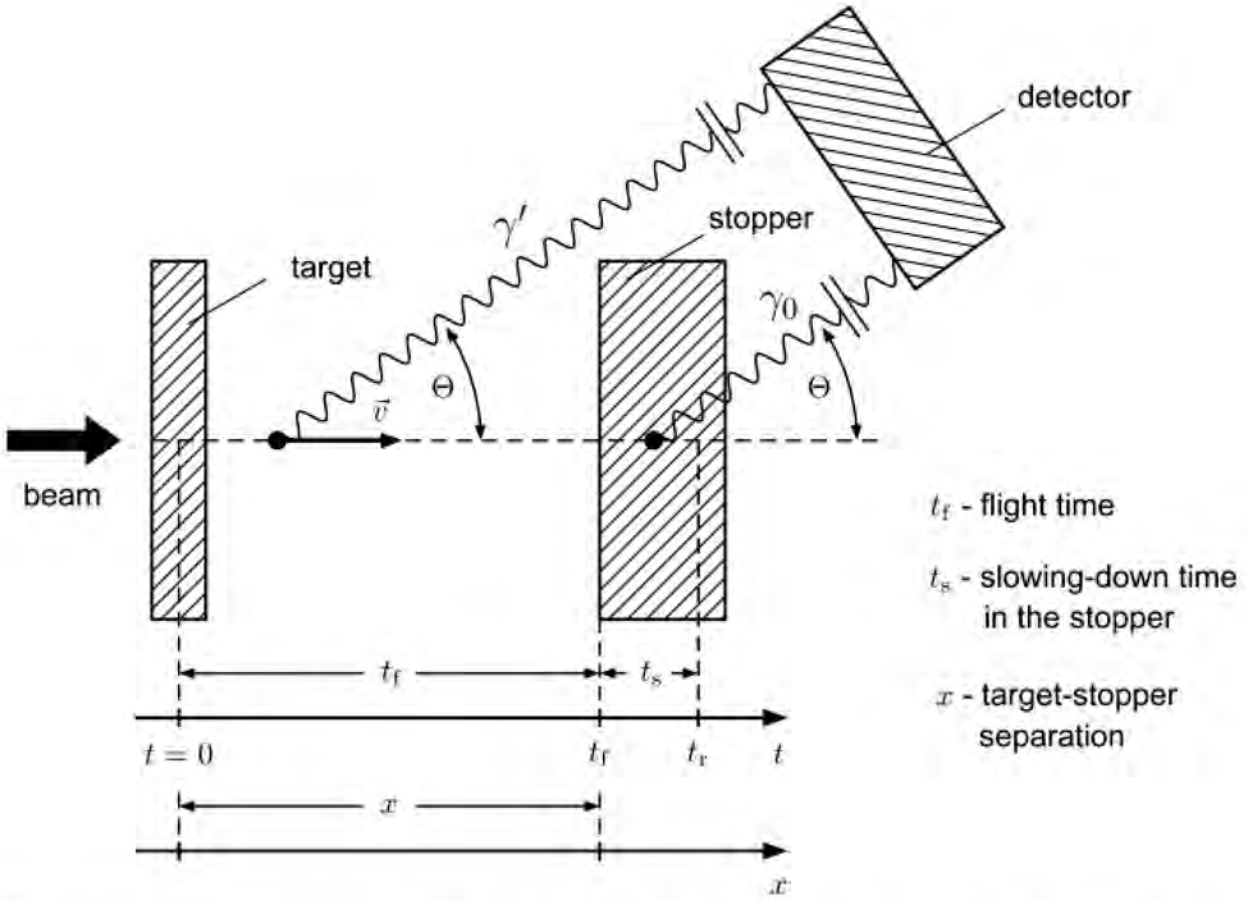

Figure 2.2 The prototypical Recoil Distance Method setup is displayed. An incoming beam produces excited states at a target. It then travels a distance x over the flight time t_f to a stopper foil. Decays occurring while the nucleus is between the target and stopper emit γ-rays with a Doppler-shifted energy. Decays occurring after the nucleus is slowed in the stopper emit with a lower energy. In the figure, the nucleus is stopped in the stopper, while in the present work nuclei are only slowed. For this reason, the foil used for stopping is instead called a degrader in the text. Figure is from [44].

2.1.2 Recoil Distance Method

The basic Recoil Distance Method setup is shown in Figure 2.2. The Recoil Distance Method was first described in [45] and more details including application to rare isotope beams can be found in [44]. The Recoil Distance Method is performed by producing a beam of excited nuclear states at a production target and sending that beam to a degrader that slows down the nuclei. The position between the production target and degrader is measured, along with the velocity, so that the total

travel time for nuclei from the target to the degrader is known. The nucleus will have its highest velocity β_{fast} when traveling between the target and degrader. After passing through the degrader, it will be slowed by interaction with the material and therefore will have a lower velocity β_{slow}. In the original technique, a thick metal stopper was used so that the β_{slow} was 0 [45]. However, in the present work with fast-moving rare-isotope beams, particle identification in a spectrograph is vital. A degrader foil is thus used which only slows but does not stop the beam. The γ-ray energy observed for decays taking place between the target and degrader will be

$$E_{fast} = \frac{E_{cm}}{\gamma_{fast}\left(1-\beta_{fast}\cos\theta_{fast}\right)} \tag{2.4}$$

The energy for γ rays emitted after the degrader will be

$$E_{slow} = \frac{E_{cm}}{\gamma_{slow}\left(1-\beta_{slow}\cos\theta_{slow}\right)} \tag{2.5}$$

It is worth noting that the θ_{fast} and θ_{slow} will be different because of the different locations of emission.

If one assumes an observer at 0°, the E_{slow} and E_{fast} will form two distinct peaks. In actual experiments, detectors are set at forward angles, so that the difference in $\cos\theta$ is minimized. In fast beam experiments, to identify the two peaks, the measured energy is Doppler-reconstructed to account for the in-flight emission. However, to preserve the separation between the two peaks, the β and θ_{lab} used in reconstruction are chosen to correspond to only one emission location, generally those corresponding to just after the degrader.

In an ideal scenario, the lifetime of the excited state can be found from the ratio of counts in each peak. This is because the total emissions from the state of interest (I_γ) over a given time range t_i to t_f can be modeled as [44]:

$$I_\gamma = \int_{t_i}^{t_f} \frac{N_0}{\tau}(1-e^{-t/\tau}) = N_0\left(e^{-t_i/\tau}-e^{tf/\tau}\right) \tag{2.6}$$

This equation can be applied to determine the total counts in each of the two peaks. The overall time of decays in the fast peak can be taken as $t_f = \frac{x}{v_{fast}}$ starting from t_i=0 at the production target.

Here, t_f is the flight time between the target and degrader, x is the distance between the target and degrader, and v_{fast} is the velocity of the ion between the target and degrader. The overall time for observation of decays in the slow peak can, in an ideal case, be taken as starting at t_f. The total observation time must be finite for the present work, as the traveling nucleus eventually passes out of range of the γ-ray detector. However, if the lifetime of the state is short enough compared to the total travel time, the time of observation of decays after the degrader can be approximated as infinite. This is similar to the original method in which the beam is stopped after the target, allowing observations to take place over an extended period [45]. In this case the total counts observed in the fast peak (I_{fast}) and slow peak (I_{slow}) will be

$$I_{fast} = N_0 \left(1 - e^{-\frac{t_f}{\tau}}\right) \tag{2.7}$$

$$I_{slow} = N_0 \left(e^{-\frac{t_f}{\tau}}\right) \tag{2.8}$$

Then it can be seen that the ratio of counts in the slow peak to overall counts is related to the lifetime by [44]:

$$R = \frac{I_{slow}}{I_{fast} + I_{slow}} = e^{-\frac{t_f}{\tau}} = e^{-\frac{x}{v\tau}} \tag{2.9}$$

Since the velocity (v) and the distance (x) between the target and degrader are known, the τ value can be extracted. In general it is required to take measurements with various distances between the target and degrader to account for feeding contributions, finite thickness effects, and decays occurring in the foils. The resulting curve is then fit to extract the lifetime τ. In the present work, due to experimental considerations, only two measurements are taken. A short distance measurement is taken to constrain the lifetime, while a long distance measurement is taken to constrain the direct population of states from reactions in the degraders.

The lifetimes accessible by this method are therefore related to the velocity of the ions and the distances between target and degrader, quantities which can be measured. As such, over the range of accessible distances and energies, lifetimes on the order of 1 ps to 10 ns are measurable [41].

While the basic principles of the recoil distances are straightforward to understand, there are a number of complications that must be accounted for. Primary among these considerations is

feeding, discussed below. Additionally, there are experimental limitations for the efficiency of detectors, the velocity distribution of the beam, finite size and thickness of the target and degrader, which must be accounted for. Additional considerations from γ-ray distributions, relativistic effects on γ-ray distributions, and more are discussed in [44]. In general these additional complications are accounted for by comparison of the measured spectral shapes with simulations incorporating the experimental setup [44][46].

2.1.2.1 Feeding

The decay of higher-lying states can populate the state of interest. This adds an additional component to the analysis, known as feeding. For example, consider a three state system with a ground state, a first excited state with lifetime 1 ps, and a second excited state with lifetime 10 ps, where each state decays into the decay below it. If in the experiment the second excited state is populated along-side the first, it will decay into the first excited state later than the initial population. This nucleus will then decay from the first excited state to the ground state in a time around 1 ps. However, as the first excited state was not populated until on average 10 ps after the initial reaction, the apparent lifetime of the first state will be lengthened to appear closer to 10 ps.

This can be modeled as a series of differential equations for each excited state populated in the reaction. The differential equations can be written as [44]:

$$\frac{d}{dt}n_i(t) = -\lambda_i n_i(t) + \sum_{k=i+1}^{N} \lambda_k n_k(t) b_{ki} \tag{2.10}$$

In this equation $n_i(t)$ is the number of nuclei in the excited state i at time t. The decay constants are denoted by λ_i, where $\lambda_i = \frac{1}{\tau_i}$. The sum on the right hand of the equation runs over all higher-lying states through the last state considered in the analysis, denoted N. The b_{ki} term represents the branching ratio from state k to state i, and is zero for any decays where the k-th state has energy below the i-th state.

This differential equation can be solved for the ratio of emitted γ rays before the degrader to

the total number of decays as [44]:

$$R_i(t) = P_i e^{-t\lambda_i} + \sum_{k=i+1}^{N} M_{ki} \left(\frac{\lambda_i}{\lambda_k} e^{-t\lambda_k} - e^{-t\lambda_i} \right) \tag{2.11}$$

where R_i is the ratio of of decays before the degrader to the total, λ_i is the decay constant for the ith state, P_i is the direct feeding intensity of the level i, and where [44]:

$$M_k i \left(\frac{\lambda_i}{\lambda_k} - 1 \right) = b_{ki} P_k - b_{ki} \sum_{m=k+}^{N} M_{mk} + \sum_{m=i+1}^{k-1} M_{km} b_{mi} \frac{\lambda_m}{\lambda_k} \tag{2.12}$$

This equation demonstrates the potential importance of feeding since each feeding state contributes to all of the states below it. Generally speaking, the observed feeding states along with branching ratios can be incorporated into the analysis, but require additional fitting for each τ_i and branching ratio b_{ik} for each state i for those values not previously measured.

2.1.2.2 Modifications to the Method

In the present work, the Recoil Distance Method was used to determine lifetimes. In the case of ^{58}Ni, a modified Recoil Distance Method using two degraders was performed. Modifications to the Recoil Distance Method are discussed below, to explain the interest in using two degraders in an experiment.

The standard Recoil Distance Method has been extended to include more than one degrader (stopper). In this case, three regions of velocity exist, denoted as β_{fast}, $\beta_{reduced}$ and β_{slow}. This setup enables the use of the Differential Recoil-Distance Method (DRDM), first proposed in [47]. In DRDM, the separation of the three peaks makes it possible to measure both the function $R(t_f)$ for a given time of flight t_f, but also the derivative of the function with respect to the time of flight. This allows for a direct measurement of the lifetime as [47]:

$$\tau_i = -\left(R_{ij} - b_{ij} \sum_h R_{hi}(t) \right) / \left(dR_{ij}(t)/dt \right) \tag{2.13}$$

where R_{ij} is the total number of transitions from state i to state j which occur after time t.

In addition, the DRDM provides a way to decouple the lifetime of the state of interest from short lived feeding times, as most feeding decays will occur in the β_{fast} region before the first

degrader. Then the ratio of decays in the regions after the first and after the second degrader will have a peak ratio determined primarily by the lifetime of the state of interest [47].

In addition to the Differential Recoil-Distance Method, the use of a target and two degraders makes it possible to use the Recoil Distance Method to simultaneously measure lifetimes in different regions of sensitivity [48]. An example spectrum using this technique is shown in Figure 2.3. If the first degrader is positioned a short distance from the target, and the second degrader a much larger distance, the ratio of peaks between the fast and reduced components can be used to determine a shorter lifetime. On the other hand the ratio of counts in the reduced and slow components can be used to determine the lifetime of a longer lived state. In the present work, the two degraders were kept at the same distance, which was sensitive to the lifetime of the excited state of interest.

2.1.3 Doppler-shift Attenuation Method

The Recoil Distance Method does not provide sensitivity to lifetimes below 1 ps [41]. For experiments with fast rare isotopes beams, this is because the minimum thickness for a degrader foil is around 100 μm to provide peak separation between β_{fast} and β_{slow}. In addition, thick target sizes are needed due to the small production cross sections of rare nuclei. However, the ion transit time over 100 μm is 1 ps, limiting the sensitivity. At the same time, the ion stopping time in matter for standard experiments tends to be on the order of 1 ps, which hinders the Recoil Distance Method.

Therefore, in order to measure lifetimes in this region additional techniques must be applied. Among these, the Doppler-shift Attenuation Method is of particular interest for the work presented here. The Doppler-shift Attenuation Method has been used previously to study ^{58}Ni, and may provide opportunities in the future for studying ^{27}Ne. As this technique is not used in the current work, however, it will only be briefly discussed.

The Doppler-shift Attenuation Method (DSAM) provides information on lifetimes on the order of 10 fs to 1 ps [41]. Figure 2.4 shows a typical DSAM setup. In this method, a target is made, often through implantation, with a backing material behind it. A beam of nuclei is impinged on the target, where it undergoes a reaction into an excited state of the nucleus of interest. The nucleus

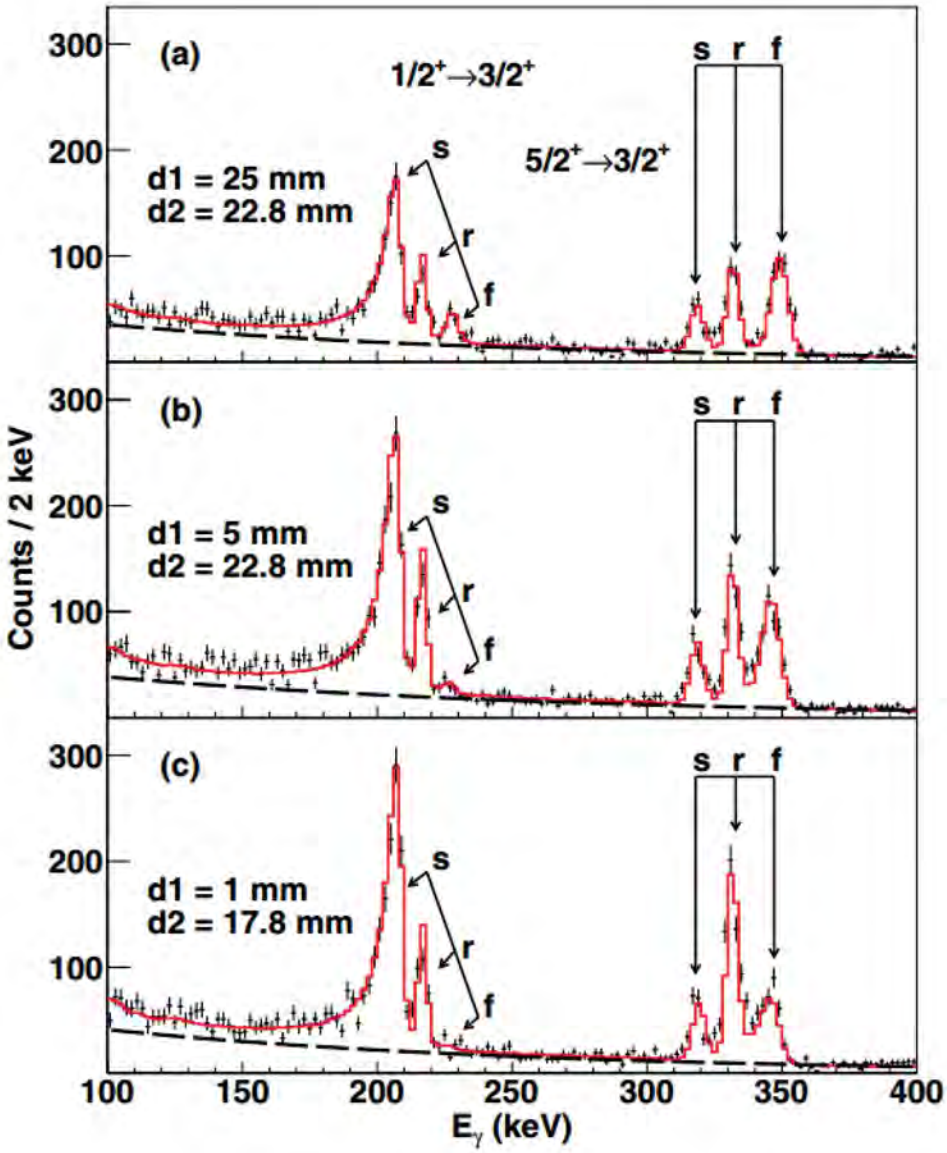

Figure 2.3 Gamma-ray spectra for ^{17}C using the Recoil Distance Method with two degrader foils. Three spectra are shown with different distances between the target and first degrader (d1) and first degrader and second degrader (d2). Simulated spectra are compared incorporating an exponential background. The peaks are identified as corresponding to β_{fast} (f), $\beta_{reduced}$ (r) and β_{slow} (s). The lifetime of the $1/2^+ \rightarrow 3/2^+$ state was measured to be 528^{+21}_{-14} ps, while that corresponding to the $5/2^+ \rightarrow 3/2^+$ was found to be $21.8^{+3.4}_{-3.3}$ ps. The different three peak structures demonstrate the ability to measure two different lifetime regions simultaneously. Figure and results are from [49].

then travels through the remainder of the target and the backing material, losing energy along the way, and eventually stopping. The excited state of the nucleus may decay while it is stopping or after it has stopped. If it decays before it has fully stopped, the γ-ray energy will be shifted by the Doppler-effect, but if it has stopped the energy will correspond to the transition energy.

The velocity of the nucleus after the mean lifetime ($\bar{v}$) can be determined from the Doppler-shift observed in the average energy of the observed γ ray ($\bar{E}_s$). DSAM measurements in general are performed using beams with non-relativistic velocities, and so the energy can be related by the equation [41]:

$$\bar{E}_s = \frac{E_0}{(1 - \frac{\bar{v}}{c}\cos\theta_\gamma)} \tag{2.14}$$

As such, the velocity can be determined and compared to the incoming velocity of the nucleus v_0. The Doppler shift attenuation factor is then defined as $F = \frac{\bar{v}}{v_0}$. The lifetime of the nucleus can then be extracted by comparison to a theoretical distribution of $F(\tau)$ as a function of the lifetime of the nucleus. The distribution $F(\tau)$ is a function of the stopping time of the recoiling nucleus in the stopping material (and the target). The stopping times of ions in matter in DSAM experiments tends to be on the order of 10^{-13} s, and therefore provides sensitivity to lifetimes in that range [41]. The stopping functions and corresponding Doppler-shifted spectra can be simulated using Monte-Carlo methods to determine the lifetimes [50].

More information on DSAM and other lifetime measurement techniques can be found in [41].

2.2 Coulomb-excitation Measurements

The reduced transition strengths $B(\pi\lambda)$ determined from lifetimes are related to the overlap of the excited state wavefunction (ψ_1) with the wavefunction of the state reached by the decay (ψ_0) as mediated by the relevant operator, $\langle\psi_1|\hat{O}|\psi_0\rangle$. Due to the Hermitian nature of observable operators, this must be equal to $\langle\psi_0|\hat{O}|\psi_1\rangle$, representing now the overlap for excitations from ψ_0 to ψ_1. Therefore the probability of excitation of the ground state of a nucleus into an excited state by the electromagnetic field can be related to the reduced matrix elements $B(\pi\lambda)$. The primary means of

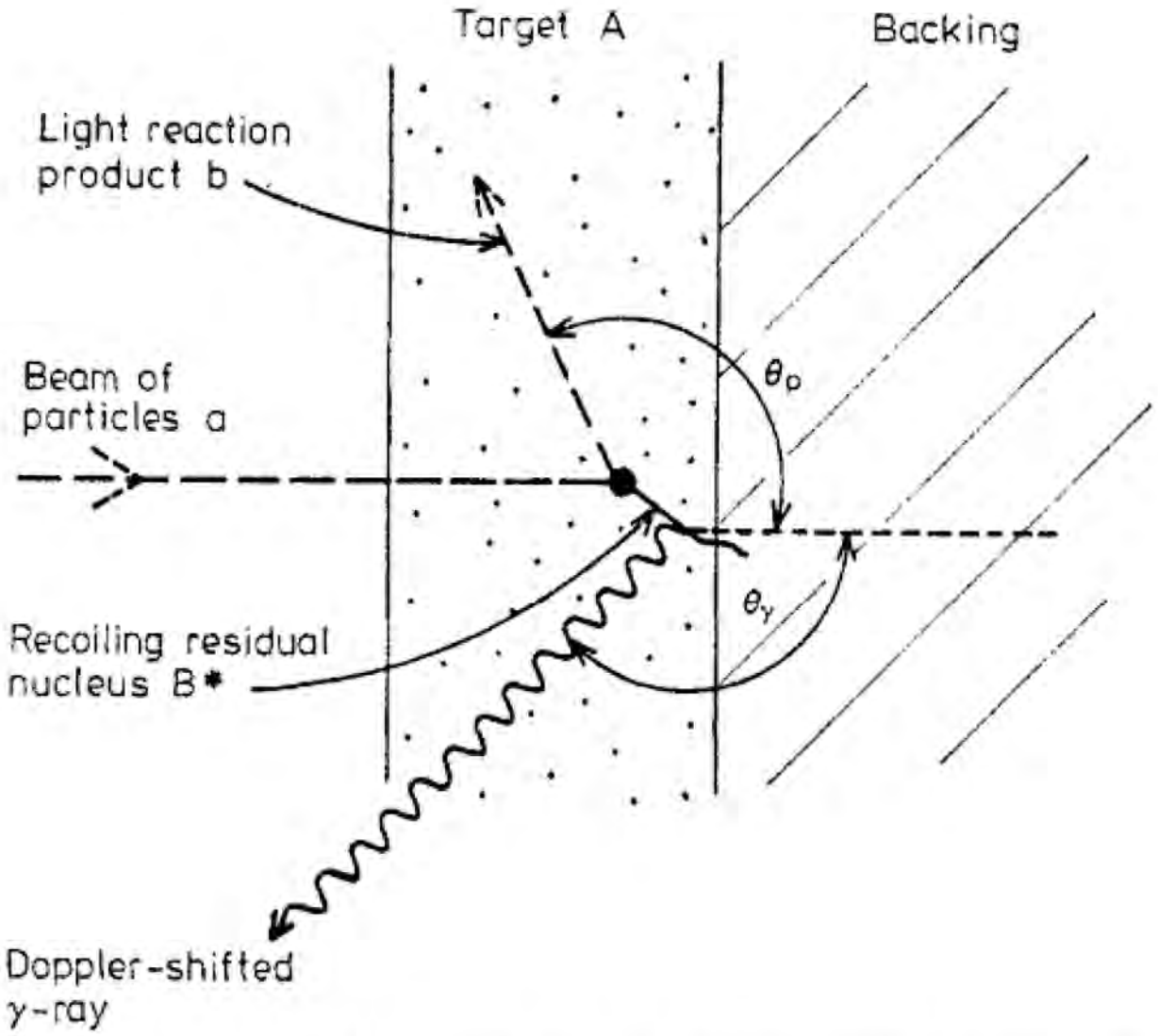

Figure 2.4 A prototypical DSAM setup is presented. The incoming particles A react in the target to induce excited states in the recoiling nucleus B. The γ-ray emitted in the excited state decays in the backing or target, with the location contingent on the lifetime of the state and the stopping time of the nucleus in the backing (target). The energy of the emitted γ ray will be shifted depending on the velocity of the nucleus B at the time of decay. The mean Doppler-shifted energy can be used to extract the mean velocity compared to the incoming velocity ($F = \bar{v}/v_0$). This is compared to the stopping time extracted from theory to determine the lifetime. Figure is from [41].

determining this interaction directly is through the inelastic scattering of nuclei in the electric field generated by other nuclei, known as Coulomb-excitation [41][51].

2.2.1 Safe Coulomb-excitation

The use of Coulomb-excitation to measure electromagnetic transition strengths was first performed using beam energies below the Coulomb-barrier. The Coulomb barrier is the energy needed for projectile nucleus to overcome the electric repulsion of the target nucleus and allow for direct nuclear-nuclear interactions. This energy is classically [51]:

$$E_B = \frac{Z_1 Z_2 e^2}{R} \tag{2.15}$$

where Z_1, Z_2 are the proton number of the projectile and the target nucleus respectively, e is the electron charge, and R is the effective radius of the interaction. R in general can be approximated as $R = 1.2(A_1^{1/3} + A_2^{1/3})$ fm, which is just the sum of the radii of the two nuclei. In standard kinematics, Coulomb-excitation is generally performed by using the projectile to excite the target nucleus, which is the formalism adopted here. However, in the present work experiments are performed in inverse kinematics, where the projectile is excited in the electromagnetic field of the target.

At safe energies, the only interaction affecting the target nuclei is the electromagnetic field generated by the projectile. In general, the electric component of the field is dominant, as the magnetic field generated by the moving charged particle is reduced in strength from the electric component by a factor of β^2 [51]. Thus the $B(E\lambda)$ transition elements can be extracted from the cross section of the interaction. Coulomb-excitation is in particular frequently used to measure $B(E2)$ values, due to the prominent transition from $0^+_{gs} \rightarrow 2^+_1$ in even-even isotopes.

In the non-relativistic approximation the cross section can be calculated as [51]:

$$\sigma_{E\lambda} = \left(\frac{Z_1 e}{\hbar v_i}\right)^2 \left(\frac{Z_1 Z_2 e^2}{m_0 v_i v_f}\right)^{-2\lambda+2} B(E\lambda) f_{E\lambda}(\eta_i, \xi) \tag{2.16}$$

where v_i is the velocity of the beam, v_f is the outgoing velocity of the projectile, m_0 is the reduced mass of the projectile and target ,and $f_{E\lambda}(\eta_i, \xi)$ is a function of the strength of the interaction and

change in velocity over the collision calculated in [51]. For a $B(E2)$ this can be simplified to [41]:

$$\sigma_{E2}(E) = C_{E2}(E - \Delta E')B(E2)f_{E2}(\eta_i, \xi) \tag{2.17}$$

where C_{E2} is a function of the charge and mass of the target, E is the energy of the beam and $\Delta E'$ is excitation energy of the level multiplied by $(1 + A_1/A_2)$.

As such, a measurement of the cross section of Coulomb-excitation gives direct access to the transition strength $B(E\lambda)$. Cross sections can be measured by γ-ray detection, where the overall count of measured γ rays corresponding to the energy of interest, scaled by the efficiency of the detector can be compared to the total number of projectiles and the number of nuclei in the target interacted with. In an experiment where the γ rays are measured in coincidence with ions of interest, this can be written as:

$$\sigma_{exp} = \frac{N_{coin}}{N_{inc}N_{target}\varepsilon(\gamma)\varepsilon(p)} \tag{2.18}$$

where N_{coin} is the number of coincident measurements between the projectile and γ ray, N_{inc} is the number of projectiles, N_{target} is the number of target atoms per unit area, and $\varepsilon(\gamma)$ is the efficiency of the γ-ray detectors, and $\varepsilon(p)$ is the efficiency of the ion detectors.

2.2.2 Intermediate Energy Coulomb Excitation

In safe Coulomb-excitation, there is no contribution from the nuclear-nuclear interaction which is hindered by the Coulomb-barrier. However, beam energies at rare-isotope facilities are generally above the Coulomb barrier, including those used in this work. To study such nuclei, intermediate energy Coulomb-excitation techniques have been developed. Intermediate energy Coulomb-excitation is relevant for nuclei with the relativistic energies of secondary beams produced at rare isotope facilities, meaning that there is no loss of yield from degrading beam energies to produce beams below the Coulomb barrier. The intermediate energy Coulomb excitation technique furthermore uses thick targets that offset the low intensity of rare isotope beams. Finally, the re-

action products can be identified in downstream detectors to tag coincident γ-ray signals, which is important for secondary beams with limited purity.

The first of two methods discussed here involves selection of the impact parameter to exclude nuclear contributions. The other involves determining the nuclear contribution to the reaction through measurement on a low Z target and then using this to constrain the nuclear contribution from a high-Z target in order to extract Coulomb-excitation cross sections.

2.2.2.1 Impact Parameter

In intermediate Coulomb energy measurements, the projectile nucleus is excited in the electromagnetic field of the target [52]. A selection for a minimum impact parameter (b_{min}) can be made by selecting events below a maximum scattering angle in the center of mass frame as [52]:

$$b_{min} = \frac{a_0}{\gamma} \cot(\theta^{cm}_{max}/2) \tag{2.19}$$

where

$$a_0 = \frac{Z_{pro} Z_{tar} e^2}{m_0 v^2} \tag{2.20}$$

This relationship allows for the selection of interactions between the projectile and target corresponding to an impact parameter larger than the nuclear interaction radius. This is done by finding the scattering angle θ_{lab} between the photon and the beam particle, which is related to the center of mass angle as [52]:

$$\tan\theta_{lab} = \frac{\sin\theta^{cm}}{\gamma(\cos\theta^{cm} + \beta^{cm}/\beta^{pro})} \tag{2.21}$$

where γ is the relativistic factor $\frac{1}{\sqrt{1-\beta^2}}$, β^{cm} is the center of mass velocity, and β^{pro} is the projectile velocity in the laboratory frame.

The restricted cross section for only impact parameters greater than the selected b_{min} can be related to the $B(\pi\lambda)$ by [52][53]:

$$\sigma_{\pi\lambda} \approx \left(\frac{Z_{pro} e^2}{\hbar c}\right)^2 \frac{\pi}{e^2 b_{min}^{2\lambda-2}} B(\pi\lambda) \times C(\lambda) \tag{2.22}$$

where $C(\lambda)$ is $1/(\lambda-1)$ for $\lambda \leq 2$ and is $2\ln(b_a/b_{min})$ for $\lambda = 1$. b_a is defined as $\gamma\hbar c\beta/E_\gamma$. As such, the electromagnetic transition strength can be directly calculated from the cross section [52].

2.2.2.2 Two Target Measurement

While the selection of impact parameters is well established for measuring electromagnetic transition strengths, it cannot be used in all cases. For example, yield or experimental constraints can prevent the use of the angular selection, which is the case in the present work where the maximum scattering angle is too small to constrain b_{min}.

In this case, it is possible to constrain or determine the nuclear contribution through the use of two targets, one with a large atomic number Z and one with a small Z. The low-Z material, for example carbon, can be used to determine the nuclear contribution. This is because the relative impact of the Coulomb interaction should be minimal and the cross section should be dominated by the nuclear contribution. The nuclear contribution measured from the low-Z target can provide a good estimate of the nuclear contribution for reactions in the high-Z target through reaction theory. The high-Z target, for example lead, should on the other hand have a substantial Coulomb contribution, and the cross section should be dominated by the Coulomb component. For example, this technique has been performed in [54][55].

In general, the relative contribution of nuclear and Coulomb interactions to the cross section is constrained by using a coupled-channel equation program [56][57]. These calculations are performed to determine the cross section of the Coulomb-excitation into one or more states of interest, and include couplings and excitations between the states of interest. Additionally, the interactions into channels not explicitly included in the calculations are approximated using an optical potential derived from measurements of other nuclei [58]. In these coupled-channel calculations, the structure of the nucleus of interest can be treated in a collective mode or by setting matrix elements directly. These allow for the calculation of the nuclear and Coulomb contributions independently.

The calculations can then be performed to vary the interaction strength of the nuclear component to match the observed cross section on the light Z target. With this transition strength fixed,

the calculations can then be performed varying the Coulomb contribution to the transition strength, the $B(E\lambda)$, to reproduce the cross section of the high Z material. This allows for the extraction of the $B(E\lambda)$ transition strength.

It is worth noting that this method, unlike lifetime measurements requires a theoretical treatment of the scattering process. The extracted $B(E\lambda)$ will depend on the choice of optical potential and the method of determining the relative nuclear contribution to the interaction. The uncertainty in theory can be found by comparing against various optical potentials, and trying various assumptions for the relationship between the Coulomb and nuclear interaction strengths [55]. More on these calculations can be found in [56][57].

CHAPTER 3

BEAM PRODUCTION AND MEASUREMENT DEVICES

In this work, electromagnetic transition strengths were determined by lifetime and intermediate energy Coulomb-excitation measurements. The Recoil Distance Method and Coulomb-excitation experiments employed in this work require the use of specialized equipment. In particular, these experiments involve the production of fast rare-isotope beams, the measurement of γ-ray energies and yields, the precise placement of target and degrader foils in the beamline, and the identification of the reaction products of interest. These experiments were performed at the National Superconducting Cyclotron Laboratory, which hosts equipment that make these measurements possible. In this chapter, the devices used at the National Superconducting Cyclotron Laboratory will be discussed.

The rare isotope beams were provided by the Coupled Cyclotron facility and the A1900 fragment separator, which are discussed first. The reaction products were identified using the S800 Spectrograph, so that γ rays emitted from those products could be identified in coincidence. Gamma rays were measured using the Gamma Ray Energy Tracking In-flight Nuclear Array (GRETINA) high purity germanium detector array. Finally, the target and degrader foils were mounted on the TRIPLEX plunger, which was used to mount and precisely separate the foils.

3.1 National Superconducting Cyclotron Laboratory

The experiments discussed in this text were performed at the National Superconducting Cyclotron Laboratory (NSCL) at Michigan State University (MSU). Figure 3.1 from [59] is provided to show the outline of the layout at the NSCL for accelerating a primary beam from an original ion source and producing a secondary rare isotope beam. The NSCL is a NSF sponsored user-facility that provides rare-isotope beams at energies around $60-120$ MeV/u. The NSCL has recently installed a reacceleration facility that produces rare isotope beams at energies of $3-5$ MeV/u [60]. The

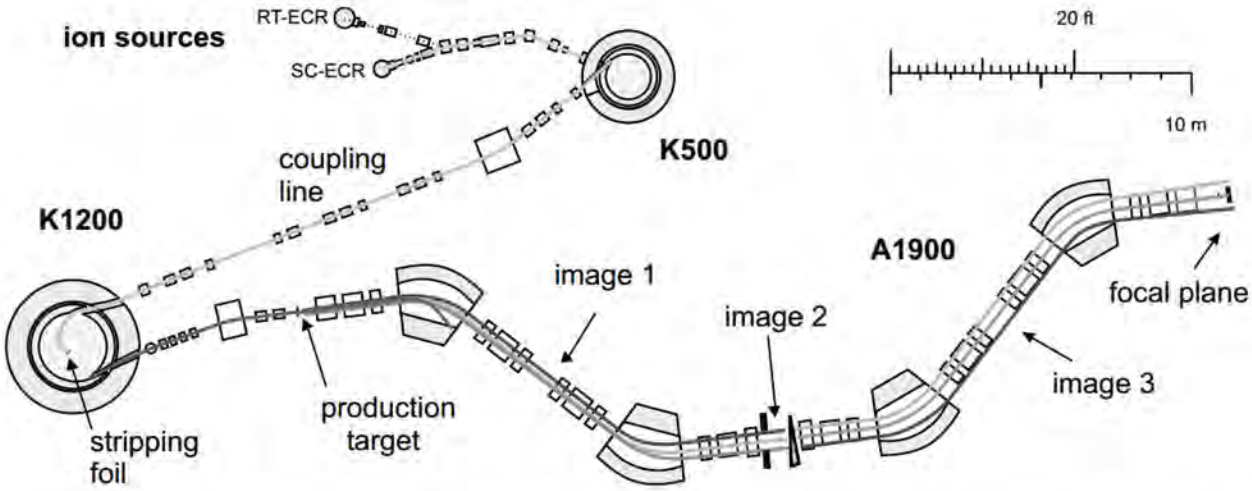

Figure 3.1 The layout of the NSCL showing the ion sources, K500 and K1200 cyclotrons, and the A1900 is shown. Figure is from [59].

facility also hosts experimental devices used in measurements presented here.

This section will describe the process by which rare isotope beams are produced at the NSCL [61]. The primary beam is produced from a stable or very long lived isotope. The stable isotope is ionized and sent to the coupled cyclotrons. There, it is accelerated to approximately 50% of the speed of light. The primary beam is then sent to a production target, where the beam is fragmented into various nuclei. The secondary rare isotope beam is produced by filtering the reaction products in the A1900 fragment separator [59]. This results in a rare isotope beam with energies corresponding to approximately 40% of the speed of light to be delivered to the experimental vault. The beam production process is discussed in greater detail in the sections below.

3.1.1 Ion Source

The production of the primary beam at the NSCL begins with the ionization of atoms, which is accomplished using one of the available ion sources, the Superconducting Source for Ions (SuSI) [62] and ARTEMIS [63]. SuSI and ARTEMIS are electron cyclotron resonance ion sources. These produce a charged plasma that can be accelerated in the cyclotron. The ion source used in this work was SuSI, which uses superconducting magnets to produce the magnetic fields needed for electron

cyclotron resonance [62].

In an electron cyclotron resonance (ECR) ion source, the method of ionization is to remove electrons one at a time from an atom until the desired charge state is reached through collisions with free electrons [64]. This is accomplished by creating a gas of the isotope to be ionized, generally at or below 10^{-6} torr [64] to avoid ion-atom collisions which serve to lower the overall ionization of the plasma. A magnetic field is generated across the gas, which serves both to confine the plasma and to enable the ECR heating. As the ions and electrons in the plasma are charged particles, they will be confined by the magnetic field as the Lorentz force, $\vec{F}_L = q\vec{v} \times \vec{B}$, will cause them to rotate in circles at the cyclotron frequency $\omega_c = \frac{qB}{m}$.

However, to trap the ion in both the transverse and parallel direction, a magnetic mirror configuration is used [65]. The magnetic field in a magnetic mirror varies in magnitude along the length of the trap, attaining a maximum at the edges and a minimum in the center. However, particles with directions of velocity below a critical angle from the magnetic field will not be trapped. The overall confinement time is finite due to ion-ion collisions which can change the velocity of the ion [65]. An electric field is then used to guide the ions that become unconfined to their destination, in this case the K500 cyclotron [64].

One additional consideration that motivates the use of ECR ion sources is that higher energy free electrons, with energy on the order of 1 keV, have larger cross sections for removal from an atom. At the same time, higher energy ions decrease overall beam quality by decreasing the confinement time and also can increase the energy spread of the resulting beam [64]. It is therefore necessary to add energy selectively to the system, preferentially energizing the electrons. This is possible by applying an RF field at the cyclotron frequency of the electrons in the plasma. The cyclotron frequency of the electrons is much larger than that of the ions due to the small mass of the electron (0.5 MeV) compared to ions ($>$ 1000 MeV). Hence, the energy is imparted selectively to the electrons. Therefore the RF field preferentially increases the temperature of the electrons in the plasma without exciting the ions [64]. This increases the free electron-ion collisions and thus the rate of ionization.

A final detail of the ion production at the NSCL worth noting is that the ECR method can be applied directly to a gas. However, for a metallic source, a plasma must be produced by another means [64]. At the SuSI source this is accomplished using an external oven, which heats the metal until it produces a gaseous form which can then be used in the ion source directly. The isotopes used in the experiments discussed here were gaseous ^{78}Kr and metallic ^{48}Ca. For these experiments, the ionization at SuSI was not complete, for example the ionization of the ^{48}Ca was only to 8^+. Instead, the ions were fully stripped at the coupled cyclotrons.

3.1.2 Coupled Cyclotrons

The K500 and K1200 coupled cyclotrons are used to accelerate the primary beam to energies corresponding to nearly 50% of the speed of light. As cyclotron accelerators, these operate on the principles first developed by Lawrence in [66]. The cyclotron accelerator has an advantage that particles can be accelerated in a compact area, with the voltage applied repeatedly to a single ion, thus allowing for a large energy transfer without the need for prohibitively high voltages [67]. A cyclotron consists of two fundamental devices, a magnetic field over the entirety of the device, and electrodes called dees which induce an rf electric field that can be used to accelerate the particles [67]. The magnetic field is applied perpendicular to the electric fields, so that the ions will experience a Lorentz force. As in the ion source, the particles will rotate in a circular orbit with radius ρ and frequency $\frac{qB}{m}$. The radius of the circle can be derived for non-relativistic particles as :

$$\vec{F} = q\vec{v} \times \vec{B} = \frac{mv^2}{\rho} \rightarrow \rho = \frac{mv}{qB} \tag{3.1}$$

where m is the mass of the ion, q is the charge of the ion, B is the applied magnetic field, $\vec{v}$ is the velocity, and F is the force.

The ions are accelerated by the electric field between the dees. The rf frequency for the applied electric field is set to the cyclotron frequency of the ion in the constant magnetic field. Therefore, as the ion travels between the dees, it will experience an electric field that is always constant relative

to its direction of motion. This means that once the ion is traveling in the correct direction, it will continuously experience an increase of energy, and thus velocity.

The dependence of the radius on the velocity relates the maximum energy of the beam to the radius of the cyclotron. As the ion is accelerated, the radius of the ion's path through the magnetic field will increase. At the maximum energy it reaches the outermost part of the cyclotron and is then guided into a beamline. As such, the energy of the beam is effectively determined by the ion's charge and mass, the magnetic field strength and radius of the cyclotron. The overall increase in energy from acceleration of the cyclotron can be calculated as [67]:

$$\Delta E = \frac{q^2 B^2 R^2}{mc^2} \tag{3.2}$$

The coupled cyclotron facility at the NSCL enables the production of higher energy and intensity beams than the use of the K1200 Cyclotron alone. The ion source can be used to select more abundant charge states and send those to the K500. The K500 Cyclotron is used to accelerate the partially stripped ions to velocities near 10% of the speed of light in approximately 230 turns. After reaching their final velocity in the K500, the ions are guided to the K1200 Cyclotron and injected through a stripper to fully strip the ions [61]. The fully stripped ions are then accelerated in the K1200 cyclotron to energies corresponding to velocities of 50% of the speed of light and sent to production target and A1900 fragment separator, where the radioactive secondary beam is produced [61].

It is worth noting that the beams produced by the Coupled Cyclotrons are necessarily not continuous, but are discrete in timing. This is due to the rf electric pulses needed to accelerate the ions, which creates discrete windows of acceleration and hence transfer of ions from the cyclotrons to the beamline.

3.1.3 Production and Separation of Fragments

The secondary beam of radioactive ions is produced by impinging the primary beam on a target to induce fragmentation reactions. In a fragmentation reaction at the NSCL, the fast beam interacts

with the target nucleus, causing the beam to split into multiple nuclei, including free nucleons. The fragments from this reaction continue at a significant portion of the energy of the incoming beam, allowing them to be used as a secondary beam of interest [61][68][69]. The target generally used at the NSCL is beryllium, which is chosen due to its high number density, which makes fragmentation reactions more likely.

The fragmentation reaction produces many of the possible nuclear products that can result with fewer neutrons or protons than the incoming particle [68]. This allows for the production of radioactive isotopes, as nuclei closer to the driplines can be produced in reactions that remove more protons than neutrons or vice-versa. This however leads to the outgoing product of the fragmentation containing a combination of numerous isotopes, only a very few of which may be of interest at any time. The A1900 fragment separator is therefore employed, which allows for the selection of the reaction products of interest.

3.1.3.1 A1900 Fragment Separator

The A1900 fragment separator consists of 28 superconducting iron-dominated magnets [59]. Twenty-four of these are focusing quadrupole magnets. The remaining four are dipole magnets [59]. The magnetic field in each magnet can be selected by changing the applied currents. In addition an aluminum wedge is placed between the first and second pairs of dipole magnets [59]. The first set of dipole and quadrupole magnets before the wedge are used to separate out the fragments by their momentum to charge ratio. This is because the bending radius is determined by $\rho = \frac{mv}{qB}$. Since only particles with a certain radius will make it through the dipoles and subsequent slits, particles of constant momentum to charge ratio can be selected by taking a particular magnetic field and applying it. The rigidity of the beam, or $B\rho$, is given by $\frac{mv}{q}$. Since the velocity tends to be similar for each reaction product from fragmentation, the rigidity is determined by the ratio of mass (A) to charge (Z) of the fragments.

The wedge is used to slow the particles down differentially by a factor proportional to the square of the atomic number (Z^2) of the ion. This second level of selection means that ions with

the same selected incoming $B\rho$ but with different atomic numbers will have different outgoing momenta. Therefore, the rigidity of the outgoing ions will be differentiated according to their atomic numbers. The second set of quadrupole and dipole magnets is then used to select a new rigidity determined by the energy loss in the fragments of interest. This allows for the purification of the rare isotope beams used in experiments [70].

After the production of the secondary beam, the ions are sent to a scintillator called the extended focal plane scintillator (xfp). The scintillator is used for timing measurements of the secondary beam at the A1900 focal plane. These timing measurements are combined with other timing measurements for the beam to determine a time of flight. The time of flight can be used to identify the incoming ions.

The selected ions are then sent to the rest of the facility through dedicated beamlines. In the following experiments, the secondary beam was sent to the S3 vault, where the S800 Spectrograph was used in conjunction with the GRETINA array and the TRIPLEX.

3.2 S800 Spectrograph

The S800 Spectrograph is a piece of equipment at the NSCL that enables the identification of reaction products. Figure 3.2 from [71] shows the layout of the S800 Spectrograph in the S3 vault. As a spectrograph, the S800 provides position and momentum information for particles at the target position reconstructed from the focal plane particle information using inverse transfer maps [71]. The S800 Spectrograph can also be set up in conjunction with other detectors, making correlated data sets. In the experiments that are discussed here, the secondary beams are impinged on another target, causing them to undergo various reactions to produce the isotope of interest. This has the secondary effect of creating other isotopes, which may contaminate the results of the experiment. In addition, the beam profile information can be used to improve Doppler-correction. Therefore the S800 was employed to identify particles, reconstruct their trajectory at the position where the reaction of the secondary beam on target occurs, and tag coincident γ-ray measurements.

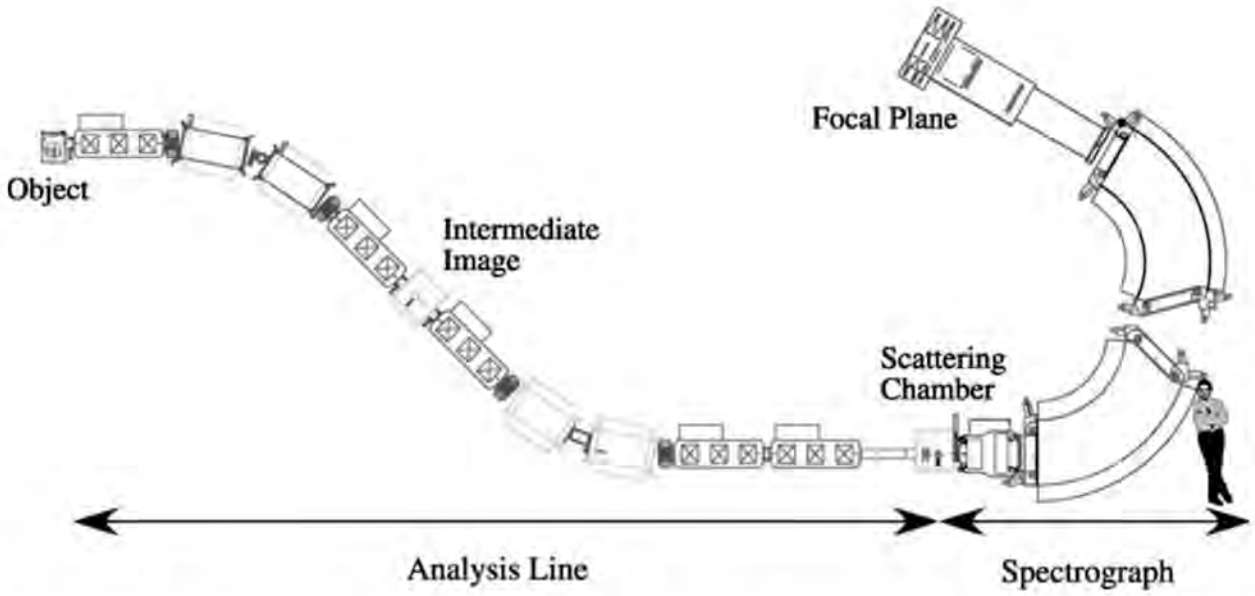

Figure 3.2 The layout of the S800 is presented, showing the analysis line and the spectrograph. The figure is from [71].

In this section, the features of the S800 Spectrograph are described along with calibrations common to the experiments discussed in this work.

3.2.1 Magnets and Optics

The S800 is made up of a series of superconducting magnets in the analysis line and in the spectrograph itself. The magnets are used to guide the beam through the S800. In the spectrograph, as in the A1900, a magnetic field is used to separate out ions by their magnetic rigidity. This creates a position dependence on momentum at the S800 focal plane. Furthermore, since the time of flight through the S800 is therefore determined by the cyclotron frequency $\omega = \frac{qB}{m}$, the time of flight can be used to separate particles out by their charge to mass ratio. The S800 is thus equipped with a number of detectors which allow for the extraction of time-of-flight, position, and other quantities.

The S800 can be operated in two modes: the focus mode, and the dispersion matching mode. In the focus mode, the S800 is achromatic in the analysis line. The magnets do not correct for intrinsic momentum distribution at the focal plane. This decreases the overall resolution of the S800, but provides for a momentum acceptance of $dp/p = 5\%$. This can be compared to the

dispersion matching mode, in which the S800 is achromatic in the focal plane. This reduces the impact of the initial momentum distribution of the incoming beams. However, this also leads to a more limited momentum acceptance of $dp/p = 1\%$. In this work, the focus mode is used because the yield is more important than the energy resolution [71].

In addition, although most information from the S800 comes from detectors installed in the spectrograph, which is downstream from the target location, it is possible to reconstruct position and energy information at the target position. The fringe effects of the magnets are modeled using a function $B(z) = \frac{1}{1+\Sigma a_i z^i}$ fit to the magnetic fields. This information is then used in the code COSY Infinity [72], which calculates a transfer map for particles through the S800. The transfer map is a 4×4 matrix that relates the quantities at the focal plane (x_f, a_f, y_f, b_f) to the quantities at the target position (d_t, a_t, y_t, b_t). Here x is the displacement of the ion in the dispersive plane, y is the displacement of the ion in the non-dispersive plane, a is the trajectory angle in the dispersive plane, b is the trajectory angle in the non-dispersive plane, and d is the energy of the ion. In all cases the f subscript denotes the quantity at the focal plane, and the t subscript denotes the quantity at the target position [71][72]. These quantities are also sometimes denoted as afp, xfp, ata, xta, etc. to represent quantities at the focal plane (fp) and target (ta) positions.

3.2.2 Timing Scintillators

The S800 Spectrograph incorporates plastic scintillators to provide time of flight measurements through the S800. When ions interact with the scintillator, they excite the molecules of an organic scintillator material dissolved into the plastic. The excited molecules de-excite by emission of fluorescent light. Photo-multiplier tubes are positioned on the scintillators [73]. The photo-multiplier tubes convert the fluorescent photons into electrons, and then amplify the current. The measured pulse time can then be taken as the timing of the interaction. As plastic scintillators have a short decay constant, generally on the order of 1 ns or less, they are suited for measuring time of flight measurements [74].

There are two locations where plastic scintillators are used in the S800, at the object position

in the analysis line (OBJ) and at the end of the spectrograph (E1) [71]. At the E1 position, a 1 cm thick plastic scintillator is placed. The time of flight between the OBJ and E1 scintillators can thus be calculated from the difference in the timing between the two scintillators. In addition, the E1 scintillator is used as the S800 trigger, from which a coincidence window is available to correlate events between secondary devices and the S800.

3.2.3 Cathode-Readout Drift Chambers

The S800 has two Cathode-Readout Drift Chambers (CRDC) within the spectrograph portion, CRDC 1 at the focal plane and CRDC 2 located 1 m downstream, which are used to provide position and trajectory information for the particles. The CRDCs are detectors filled with gas, a mixture containing 80% of CF_4 and 20% of C_4H_1O [73]. They have an active depth of 1.5 cm and an active area of 30 cm in the non-dispersive plane by 59 cm in the dispersive plane. When an ion traverses the CRDC, it ionizes the gas. The resulting free electrons are collected on an anode wire, which is located between cathode pads behind and in front. There are 224 pads, each of which is 2.54 mm wide. The induced charge on the cathodes is read out and fit to a Gaussian to provide position information in the dispersive direction [73]. The position information in the non-dispersive direction is determined from the drift time relative to the E1 scintillator timing. It takes longer to get to the wire from farther away, with drift times varying between 0 to 20 μs [75]. CRDC 1 is used for determining the x_f and y_f positions directly, due to its location, while CRDC 2 is used to determine the trajectory by comparing the x and y positions downstream 1 meter to the x and y positions at the S800 focal plane.

3.2.4 Ion Chamber

The S800 Spectrograph uses an Ionization Chamber to identify nuclei by their atomic number (Z), as the energy loss in the chamber is proportional to the square of the atomic number of the nucleus. The ionization chamber is located downstream of the CRDCs and upstream of the scintillators.

The ionization chamber is a Frish grid design and consists of sixteen parallel-plate ion chambers, which are filled with P10 gas of 90% argon and 10% methane [73][75]. The ions passing through the chamber will cause electrons to be ejected from the gas, ionizing it. As described by the Bethe formula, the total energy deposited is proportional to the square of the atomic number as [74]:

$$-\frac{dE}{dx} = \frac{4\pi e^4 Z^2}{m_0 v^2} NB(v) \tag{3.3}$$

In this equation, Z is the atomic number of the ion, e is the electron charge, m_0 is the electron mass, v is the velocity of the ion, N is the number density of the absorbing material, and B is a function of the velocity of the ion and the ionization properties of the absorbing material [74].

The electrons and ions are collected at anode-cathode pairs in the 16 chambers. As the amount of free-electrons and ions excited is proportional to the energy deposited by the incoming nuclei, this can be expressed as an energy loss of ions in the detector, and thus provide separation based on their atomic number.

3.2.5 IsoTagger

The S800 Spectrograph has been equipped with the IsoTagger configuration to identify long-lived isomeric states in nuclei [76]. The IsoTagger device consists of a stopper at the end of the S800 and detectors used to identify β particles and γ rays. The stopper is a 6.35 mm thick Aluminum plate [76]. The detectors are 32 closely packed CsI(Na) crystals coupled to photomultipliers. The CsI detectors can be used independently as a hodoscope to provide charge state identification [77]. The travel time for ions from the target position to the IsoTagger is 150 ns. Therefore, the IsoTagger can be used to identify states with lifetimes comparable to or longer than 150 ns. The IsoTagger is used with two different triggers. The first trigger is a coincidence trigger with a 20 μs window to record γ rays measured in the CsI coincident with ions measured at the E1 scintillator. The second trigger condition is for the individual CsI crystals, which are not tagged, but are instead timestamped to allow for offline correlation analysis [76]. The latter trigger is necessary to observe isomers with long lifetimes.

3.2.6 Calibrations

Each of the detectors used in the S800 Spectrograph must be calibrated for use in the experiments. The calibrations from the experiment e14045 investigating ^{27}Ne are demonstrated below to describe the calibration procedure used in both experiments.

3.2.6.1 Timing Scintillators

The time of flight between the scintillators at the object position of the S800 and the E1 scintillator at the end of the spectrograph are used for particle identification. However, the fragments identified in the S800 have a momentum distribution that means they do not all take the same path in traveling through the S800. If the fragment has a large trajectory angle, the flight time will be larger than for an ion with the same magnitude of momentum traveling a straight line. Therefore a lower (higher) magnitude of momentum will increase (decrease) the time of flight. This means that the x position and angle of trajectory a, which are reflective of the momentum distribution, are correlated with the time of flight.

In order to identify the nuclei unambiguously, the position and trajectory dependence of the time of flight must be factored out. Therefore, corrected times of flight are calculated using a linear function to relate the displacement and trajectory of the ions in the dispersive direction in the focal plane (xfp and afp respectively) to the various timing scintillators. These corrections are of the form:

$$T_{corr} = T_{uncorr} + C_1 \times \texttt{afp} + C_2 \times \texttt{xfp} \tag{3.4}$$

The coefficients C_i are chosen to make each corrected time-of-flight independent of the xfp and afp. These corrections are done for the time of flight from the E1 scintillator to the A1900 XFP scintillator and to the S800 OBJ scintillator. An example of the calibration for the time-of-flights is presented below in Figure 3.3.

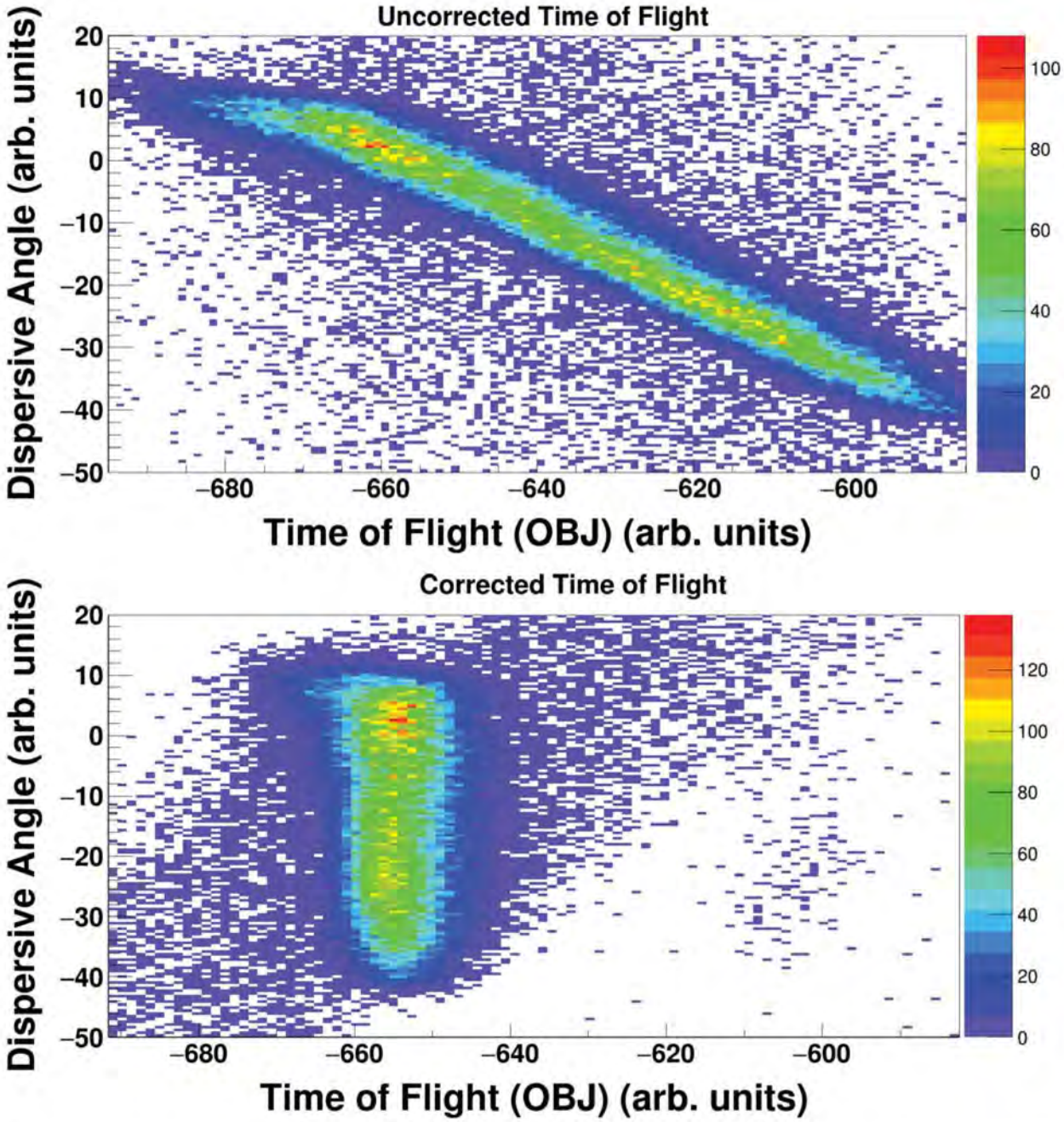

Figure 3.3 Uncorrected (top) and corrected (bottom) graphs are shown for dispersive angle in the focal plane compared with the time of flight from the S800 Object to E1 scintillators. The corrected graph shows no dependence of the time of flight on the angle, compared with the uncorrected graph which shows a substantial correlation. Similar corrections are performed for the A1900 XFP scintillator for both the dispersive angle and dispersive displacement.

3.2.6.2 Ion Chamber

The ion chamber, consisting of sixteen individual parallel plate chambers, needs to be gain matched to ensure that no one of the sixteen sub-components is over-represented in determining the energy loss in the chamber, which could lead to less accurate particle identification. To address this, the 16 ion chamber pads are calibrated to provide equal contributions to the energy measurement based on a sample from the incoming secondary beam. The charge deposited and collected in the ion chamber is position dependent, as the number of electrons and ions collected depends in part on the momentum of the incoming ion, which is correlated with the dispersive position. The ion chamber output must therefore be corrected for the position of the ions in the chamber to ensure sensitivity to the atomic number. These corrections are incorporated using a simple exponential to model the relationship between the energy deposited to the energy detected as

$$E_{corr} = E_{uncorr} \times e^{-C_1(x-x_0)} \tag{3.5}$$

The parameters C_1 and x_0 can then be fit to a correlation graph of energy detected vs position for a particular isotope to improve the particle identification.

3.2.6.3 CRDC

The CRDCs are used to measure the position and trajectory of fragments in the S800. However, the raw CRDC signals are sensitive to changes in the temperature and pressure of the gas, which must be corrected for.

The CRDCs are calibrated for position and trajectory by using two metal masks, each of which is placed in front of one of the CRDCs during a portion of the experiment. A comparison of the calibration data to the expected mask positions is shown in Figure 3.4. The masks have holes with known positions in them, which allow the beam through to interact with the CRDCs. These interactions can then be calibrated against the known positions of the holes in the masks. This calibration allows for a reconstruction of positions and trajectories in the dispersive and non-dispersive

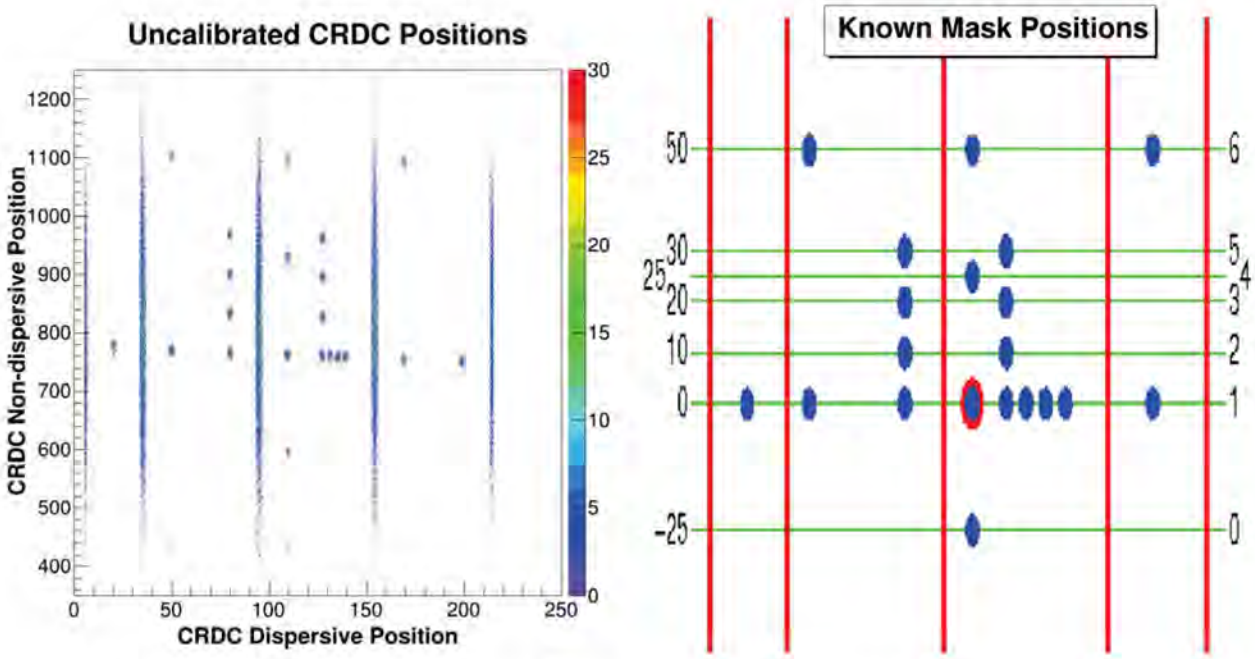

Figure 3.4 The uncalibrated data (left) and known mask positions (right) are shown. The regions of activity in the data correspond to the positions in the mask, and can be compared by the number of holes in each region to uniquely identify the locations. The arbitrary units for the data (left) are distinguished from the mm units for the mask (right). The mask image is from [78].

planes. This allows for a reconstruction of those positions at the target and a correlation between the energy of ions at the target and their position in the dispersive plane.

Because of changes to the pressure and temperature of the gas among other reasons, the positions in the CRDC may drift over the course of the measurement. This is accounted for on a run by run basis, where it is assumed that the beam spot is stable over the course of the experiment. The values for each of the calculated positions and angles at the target position are then centered at zero by adjusting the parameters relating the CRDC readouts to the positions.

In addition, as in the ion chamber, the 224 pads need to be gain matched to ensure that each pad is equally weighted. An example of the gain matching for the CRDC pads is shown in Figure 3.5 for the first CRDC at the focal plane. The uncalibrated and calibrated spectra are compared, and the clear improvement in consistency after gain matching is apparent particularly at the highest numbered pads.

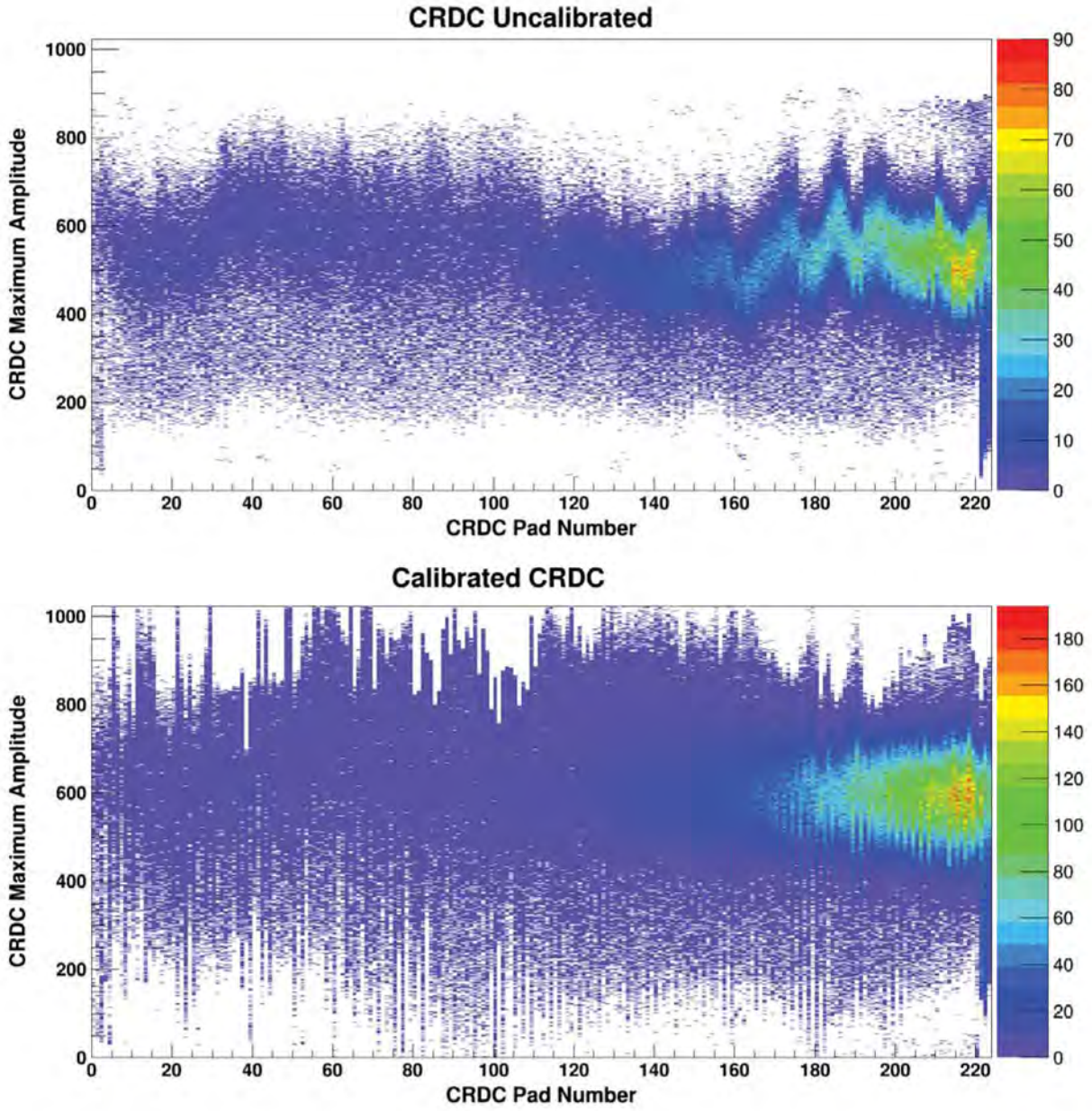

Figure 3.5 The maximum response amplitudes for each pad are histogramed for the uncalibrated (top) and gain matched (bottom) CRDCs. The calibration prevents any one pad from having too much influence over the resulting position measurement, and can be seen by the roughly straight line in the amplitudes plotted out by pad number in the bottom figure. This is performed for both CRDCs to ensure proper calculation of both positions and angles.

3.3 GRETINA

The precise measurement of γ-ray energies and interaction points is vital to the Recoil Distance Method and the Coulomb excitation experiments described in this work. These precise measurements are enabled by the Gamma Ray Energy Tracking In-Flight Nuclear Array (GRETINA). GRETINA is a high purity germanium detector array designed for in-beam measurements to provide high efficiency and excellent energy and position resolution [79]. In this section, the basics of γ-ray interactions with matter and the principles of high purity germanium detectors (HPGe) will be discussed. The GRETINA array will then be described in greater detail.

3.3.1 Gamma-ray Interactions With Matter

To comprehend the γ-ray spectra from Germanium detectors, it is important to understand the three primary types of interactions between γ rays and matter. Namely, these are photoabsorption, Compton scattering, and pair production. The energy regions where each mechanism has the largest cross section is shown in Figure 3.6. Each of these γ-ray interactions result in the production of high energy-electrons.

It is also worth noting that Rayleigh scattering is a form of elastic scattering between photons and atoms. However, Rayleigh scattering is unlikely at energies near 1 MeV and does not impart a significant amount of energy into the material. Therefore, Rayleigh scattering is not generally important for γ-ray detection [74].

3.3.1.1 Photoabsorption

Photoabsorption occurs when a γ-ray is completely absorbed by an atom. In this case, the energy of the γ ray is converted into the excitation of a bound atomic electron into the continuum. As such, the total kinetic energy of the electron released will be $E_e = E_\gamma - W$ where W is the work function of the electron needed to excite it into the continuum. Because of energy and momentum conservation, photoabsorption can only take place with bound electrons [74].

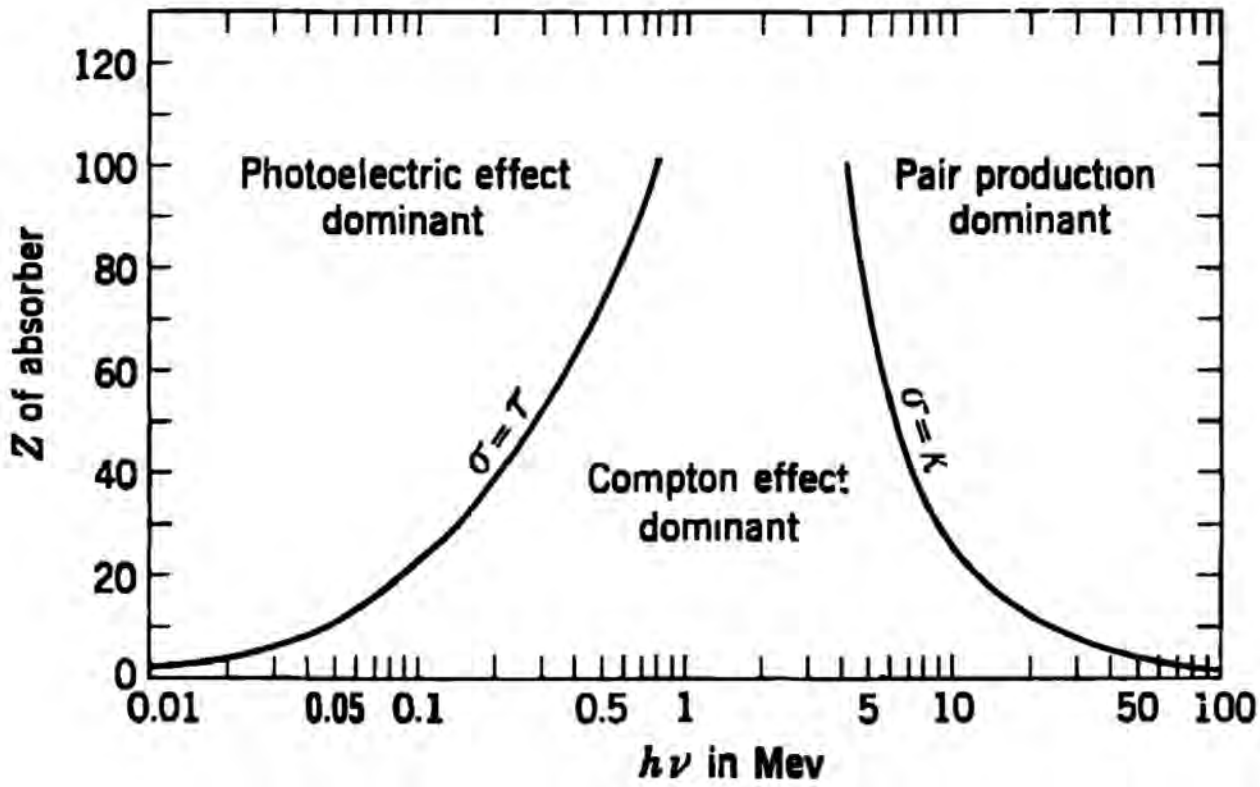

Figure 3.6 The regions where each of the photoelectric, Compton scattering and pair production cross sections are dominant are presented as a function of photon energy and the atomic number of the absorbing matter. The lines where cross sections are equal between the neighboring effects are shown to demarcate three regions. Figure is from [80].

Photoabsorption tends to have the largest cross section for the lowest energy γ rays, but its cross section is still significant for even higher energy γ rays [74]. Because photoabsorption converts all of the energy of a photon into measurable electron kinetic energy, it leads to a clear peak at the energy of the transition, representing the most important process in γ-ray spectroscopy. This is in contrast to the more complicated Compton-scattering and pair production, which may result in the emission of a lower-energy γ ray to undergo another reaction.

3.3.1.2 Compton Scattering

Compton scattering is an interaction of a photon with a free electron, where momentum and energy is transferred to the electron. While the electrons in germanium atoms are bound, the bind-

ing energy is small compared to the energy of the γ ray and the interaction is well described by Compton-scattering [74].

As this is effectively a form of inelastic scattering, it becomes significant at energies comparable that of the electron mass, at 511 keV. The reaction produces two outgoing particles, an energetic electron and a deflected γ-ray with reduced energy. The electron will be detected in the germanium detector. Meanwhile, the scattered γ ray is free to continue travelling through the detector, either interacting again with the material or escaping the detector volume. If the photon does escape, it leaves only a partial energy deposit in the detector [74].

The energy of the scattered γ ray is determined by the scattering angle as [74]:

$$E'_\gamma = \frac{E_\gamma}{1+\frac{E_\gamma}{m_e c^2}(1-\cos\theta)} \tag{3.6}$$

The remaining energy is imparted to the electron and measured in the detector. To the lowest order the scattering cross section of photons on electrons can be described by the Klein-Nishina formula [74]:

$$\frac{d\sigma}{d\theta} = Zr_0^2\left(\frac{1}{1+\alpha(1-\cos\theta)}\right)^2\left(\frac{1+\cos^2\theta}{2}\right)\left(1+\frac{\alpha^2(1-\cos\theta)^2}{\left(1+\cos^2\theta\right)\left(1+\alpha(1-\cos\theta)\right)}\right) \tag{3.7}$$

where α is the fine structure constant ($\approx \frac{1}{137}$).

The Compton-scattered photons, when measured, cause a step-like discontinuity in the spectrum, called a Compton-edge. The Compton-edge is located at the maximum energy imparted into the detector at $\theta = \pi$. Therefore, the Compton edge will occur at [74]:

$$E_{C.E.} = \frac{E_\gamma}{1+\frac{2E_\gamma}{m_e c^2}} \tag{3.8}$$

One advantage of the GRETINA system to be discussed in the later section on addback is that the position resolution afforded allows for the reconstruction of multiple interactions to sum up multiple Compton scatterings and recover the energy of the emitted γ ray.

3.3.1.3 Pair Production

In quantum electrodynamics, photons can be considered as eigenstates of an uncoupled photon field, while electrons and positrons are eigenstates of an uncoupled electron field. However, in reality these fields are coupled, and the eigenstate of an electromagnetic propagation is not a pure photon, but rather a superposition of photons and a virtual electron-positron pair, among other higher order Feynman-diagrams [81]. In free-space, it is impossible for the photon to become an electron-positron pair because there is no way to conserve both momentum and energy in the conversion. However, in the presence of a charged particle, generally atoms, photons can conserve energy and momentum by imparting a fraction of the energy into the atom [74]. Therefore, it is possible for photons with more than twice the energy of an electron mass to undergo pair-production in the detector. In this case, the positron will almost certainly annihilate on an electron and thus re-emit two γ rays around 511 keV, which will either escape or undergo Compton-scattering or photo-absorption. The electron will interact with the material and thus be measured directly. As with Compton-scattering, the multiple interactions of the photon can be summed together using GRETINA's position resolution.

3.3.2 γ-ray Detection

γ rays, being high energy photons, can be measured through interactions with matter. There are a number of detector types used to measure γ rays, including scintillating materials such as sodium iodide (NaI) detectors and semiconductor detectors. High purity Germanium detectors, including those used in GRETINA, are semi-conductor detectors, which are discussed briefly here.

3.3.2.1 Semi-conductor detectors

In solid state physics, electrons can be considered to form a band structure in many materials, as opposed to the individual molecular wavefunctions throughout the material. In a simple picture ignoring higher energy bands and deeply bound states, electrons can occupy one of two bands, a

valence band and a conduction band. The valence band consists of electrons at the outer shells in the molecules, and are bound to particular locations in the material [74]. The conduction band consists of electrons that are capable of traveling throughout the material [74]. There may be an energy gap between the valence and conduction bands, called the band gap [74]. Insulators have large band gaps, above 5 eV, while conductors effectively have no band gap, with the valence band serving as the conduction band. Semiconducting materials have a small but finite band gap, less than 5 eV. Semiconductors are useful as they can be doped with other materials or have electric fields applied to change the band gap and induce different electrical properties [74].

Semiconductors may be doped with electron donor or accepting materials to create an imbalance in the electron to hole ratio. Semiconductor materials with more of an electron donor impurity are designated as n-type, while those with more of an electron accepting impurity are p-type. Where a p-type and n-type semiconductor are joined, a junction is formed where electrons and holes recombine and there is a region with no excess electrons or holes. An electric field manifests across this zone, which is called the depletion region [74].

γ-rays are detected in semi-conductors through the measurement of free electrons and holes produced in the depletion region by the interaction. A reverse bias voltage is applied to the detector to make an extended depletion region in the semiconductor [74]. As discussed below, the primary interactions between γ rays and matter involve the production of high energy electrons. These high energy electrons, when interacting at the depletion region, excite electrons into the conduction band as they stop in the material. The electron-hole pairs then drift apart under the influence of the electric field, and the total voltage induced by the electrons (holes) is measured. This total voltage is directly related to the number of electron-hole pairs excited, and hence the total energy deposited by the electron.

3.3.2.2 High Purity Germanium Detectors

High purity Germanium (HPGe) detectors are well established devices for detecting γ-ray energies, and are especially useful for their resolution of approximately a few keV, which allows for the

separation of peaks close in energy. This is necessary for the experimental methods used here to measure lifetimes and Coulomb-excitation, as the differences in the Doppler-shifted energies used is on the order of 50 keV for a 1-MeV γ ray. HPGe detectors work by taking advantage of the semiconducting properties of germanium.

Germanium requires 2.9 eV on average to excite an electron-hole pair, meaning that interactions of γ-rays with energies on the order of 1 MeV will produce approximately 350,000 electron-hole pairs [74]. This is higher than the band gap of 0.7 eV due to momentum conservation and other modes of energy deposition that do not excite electron-hole pairs [82]. The statistical error from $\sqrt{n}$ is then approximately 0.15% [74]. Silicon has a similar energy to excite an electron-hole pair, 3.7 eV. However silicon has a smaller atomic number and cannot be made larger than a few mm in thickness due in part to the impractically large voltage that would need to be applied [83]. Therefore, γ rays cannot easily be completely absorbed in silicon detectors.

By contrast, the low impurity in the germanium detector allows for the creation of depletion zones of thickness on the order of centimeters. The thickness of the depletion region is [74]:

$$d = \left(\frac{2\varepsilon V}{eN}\right)^{1/2} \tag{3.9}$$

where ε is the dialectic constant of the Ge, V is the reverse bias voltage, and N is the concentration of impurities throughout the material. Hence, reducing N makes it possible to get a larger depletion region, useful for measuring γ-rays which at energies around 1 MeV have attenuation lengths on the order of 1 cm through germanium [84].

While high purity germanium is generally extremely pure, with approximately 10^{10} atoms/cm^3 of impurities in the material, the impurities still induce a slight bias in the material as with other semi-conductors [74]. These slight biases are called π-type for a slight advantage for electron absorbers and ν-type for a slight advantage to electron donors. As with other semi-conductor detectors, a reverse bias must then be applied across the germanium to enable its use as a detector. This is accomplished in germanium by implanting high concentrations of absorber or donor ions into the surface of the detector. These result in regions with large numbers of free electrons or

holes, and are called p^+ or n^+ contacts [74].

The need to apply a reverse bias to the detector leads to two natural configurations, a parallel plate-like planar setup, and a cylindrical coaxial setup. As crystal growth restricts the overall size of planar detectors, GRETINA consists of a coaxial design which is discussed here. In a coaxial setup, the germanium crystal is grown and shaped to be a cylinder in shape, and the center of the crystal is removed to create an inner cylinder. For an n-type detector, which GRETINA consists of, generally the outer portion of the cylinder is made to be a p^+ contact, and the inner core is made a n^+ contact. A positive voltage is applied to the n^+ contact and the outer contact is grounded, so that the detector is reverse biased to make a large depletion region [74].

One consequence of the small band gap in high purity germanium is that HPGe detectors must be kept cold to prevent thermal noise from swamping the detector. This is accomplished for GRETINA through the use of a dewar which stores liquid nitrogen attached to each of the detectors. These dewars are connected to the liquid nitrogen lines at the NSCL so that the detectors can be kept cold.

3.3.3 GRETINA Design

GRETINA is an array of individual coaxial HPGe detectors arranged to cover a large solid angle. Each detector consists of four HPGe crystals, each of which has a central contact [79]. The outer contact of the crystals is segmented into six angular strips and six depth strips for a total of 36 segments, as shown in Figure 3.7. Each crystal is approximately 90 mm in length and 80 mm in diameter, while each segment is on the order of 10 mm thick [79].

Figure 3.8 shows the GRETINA setup used in the ^{27}Ne experiment during March 2016. GRETINA was originally designed to have seven detectors but is now planned to have twelve total detectors. At the time of the measurement of ^{58}Ni during the first GRETINA campaign at the NSCL, seven of the detectors had been fabricated and were employed. During the second campaign in 2016 when ^{27}Ne was studied, two additional detectors had been made and a total of nine detectors were

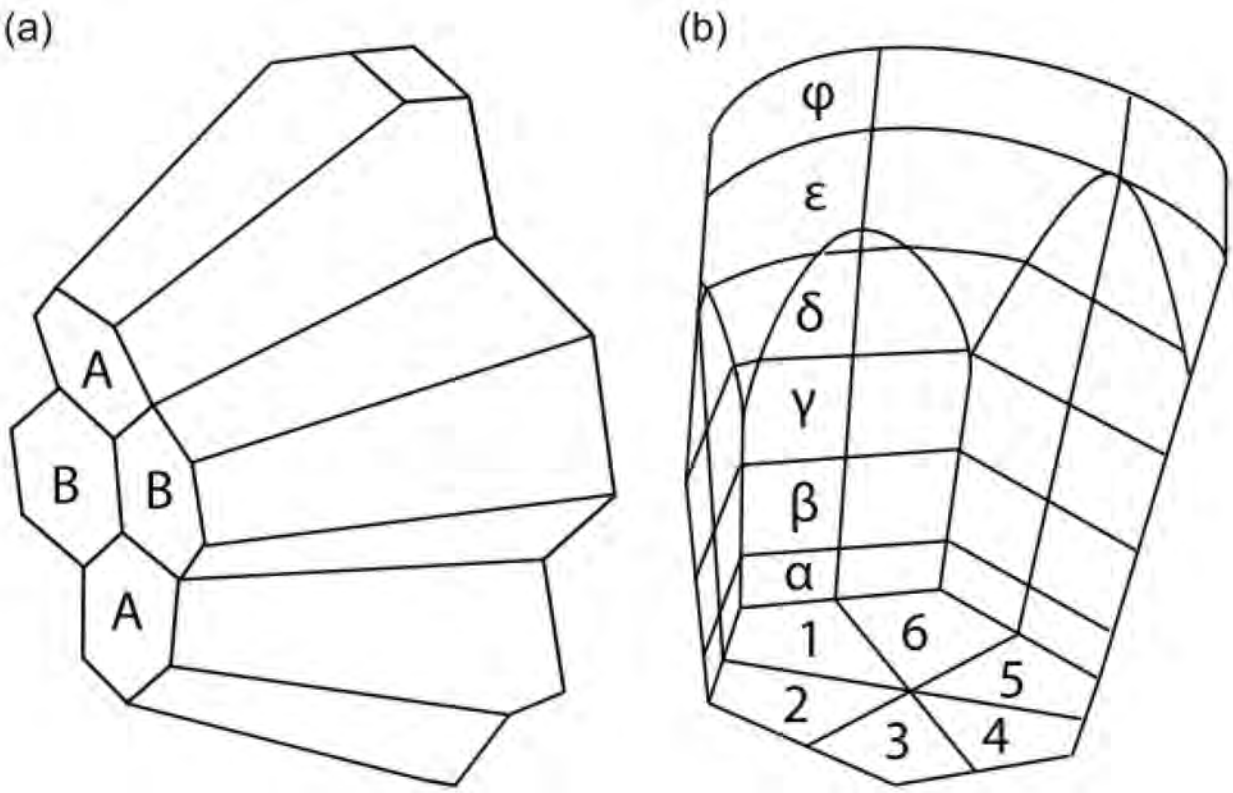

Figure 3.7 (left) The design of a detector in GRETINA is shown, with four crystals aligned into a cluster to increase detection area. (right) The segmentation of each crystal is shown for the six angular and six depth slices leading to 36 total segments. Figure is from [79].

employed. In the long run, GRETINA is planned to be converted into a 4π array, Gamma Ray Energy Tracking Array (GRETA), which will consist of 30 total detectors [85].

The segmented crystals used in GRETINA allow for a position resolution of 2 mm for the interactions. The segmentation provides position information up to the segment size on its own, but this is on the order of 10 mm or larger for each segment. The additional sub-segment resolution is enabled by signal decomposition.

3.3.4 Signal Decomposition

The use of signal decomposition to achieve sub-segment resolution is a defining feature of the GRETINA array. When a γ ray interacts with a GRETINA crystal, it will induce a voltage pulse not only in the segment the interaction occurs in, but also in the neighboring segments through the

Figure 3.8 The GRETINA setup used in the ^{27}Ne experiment in March 2016 is shown. Nine GRETINA detectors were used in the experiment, which are arrayed around the beampipe for the TRIPLEX plunger.

image charge of the electric field. The overall timing of the pulse, and consequently its shape, is dominated by the drift time of electrons and holes in the detectors, which in turn is sensitive to the position of the interaction. Therefore the pulse shape and amplitude in each of the segments can be used to determine the position to a sub-segment level [79].

An additional complication occurs because in most cases, except photoabsorption of the emitted γ ray, multiple interactions will occur within the timing window of GRETINA. Therefore, the total pulse signals will consist of the sum of pulses induced by each interaction. In order to decompose this superposition into individual interactions, a basis composed of simulated signals from point charge interactions on a non-uniform grid with average spacing of 1 mm has been developed.

GRETINA has an auxiliary computer system that processes each GRETINA signal, and performs a χ^2 best fit analysis on each of the signals to the simulated basis. This decomposes the signal into multiple interactions with a position resolution better than 2 mm [79].

3.3.5 Addback

The signal decomposition of GRETINA enables the use of addback to improve the measurements of γ rays. Addback is a means of recovering the energies of γ rays affected by Compton-scattering or pair-production. The energies of γ rays interacting in neighboring segments can be summed up, so that the total energy deposited in the region is reconstructed. To use the method, it is necessary to determine what type of region the summing should be performed over. A number of methods are possible, for example the region can be the four crystals of a detector, every GRETINA detector, or a region based on the expected kinematics of the photons, as is done in tracking algorithms [86]. However, in the results shown here, the addback is performed using a spherical addback technique, which is also shown in Figure 3.9.

Spherical addback is a recursive method, which works first by looking at all of the hits in GRETINA. The highest energy interaction is chosen as the first interaction point, which may have photo-absorbed, scattered, or been part of a pair-production. This highest energy interaction is also used to determine the angle of emission of the γ ray. Then, all points within a sphere of a chosen radius, which is a parameter of the method, are added together. The radius is chosen based on a comparison of yields and signal-to-noise ratio of the γ ray of interest. The interactions with that sphere are then considered as one event, and removed from the list of events. Then, recursively, the remaining hits are searched for the highest energy and a sphere is drawn around it, and so on until all of the points have been added together.

In a simple picture with only one γ ray involved, the effect of addback is to increase the yield in the peak, and to reduce the lower energy yields in the Compton-edge. A simulated example using the spherical addback is shown in Figure 3.10 and compared to the singles without addback.

However, in the data there are a number of compounding effects that complicate the spectrum

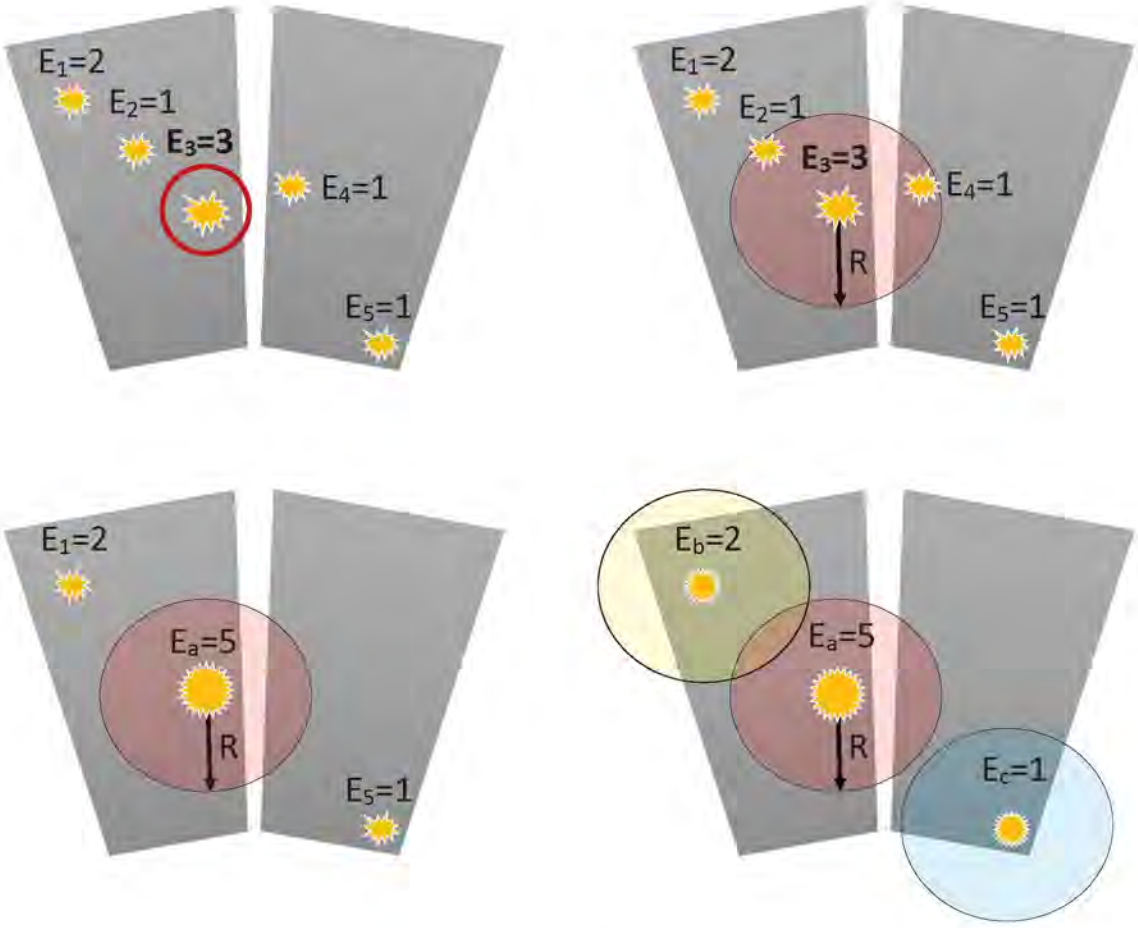

Figure 3.9 The spherical addback method is shown for a case of five interactions across two crystals. Interactions are labeled with energies in arbitrary units. Raw interactions are represented by a flash, while added back interactions are represented by a many-point star. The energies of the raw interactions are denoted with a number in the subscript ($E_1, E_2, ...$). Energies of the added back interactions are denoted with a subscript letter ($E_a, E_b, ...$). (Top-left) In the first step of the process, the highest energy interaction is identified. (Top-right) A spherical cut is made, including any interactions within radius R. (Bottom-left) The interactions within the spherical cut are summed to create a single addback interaction. The interactions in the addback are no longer used in the algorithm, and the process repeats again. (Bottom-right) The remaining two hits have only themselves within the radius of the highest energy hit and the addback interaction is the same as the original interaction. Note that in the first frame the E_1 interaction is within the radius R of E_2, but E_2 is removed from consideration in the third frame. In this work a radius of 7.5 cm is employed.

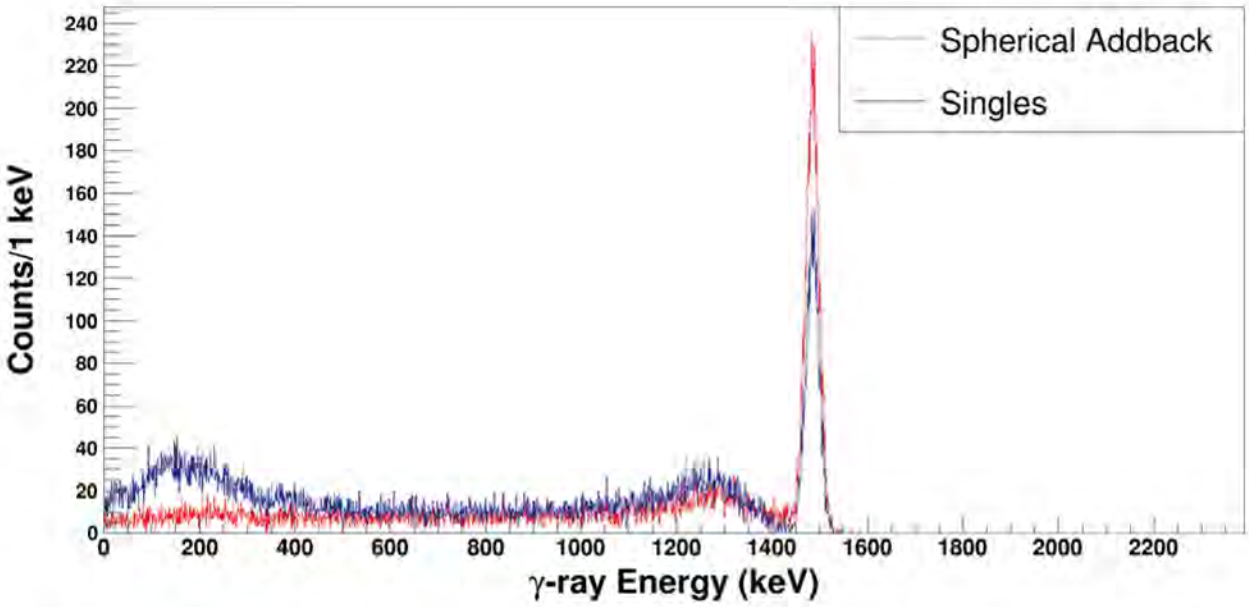

Figure 3.10 A GEANT4 simulation [87] of a single γ-ray transition measured by GRETINA is shown, with a comparison between singles and a spherical addback. The singles replicate the summing up of all energies within a single GRETINA crystal, while the spherical addback is as described in the text with a radius of 7.5 cm. The state energy is assumed to be 1480 keV, and the Compton-edge can be observed at around 1300 keV, with scattered events extending back towards 0 keV. A clear reduction in the Compton-events and an increase in the peak yield is apparent for the spherical addback compared to the singles.

compared to the simple picture in the simulation. This is partly because of possible accidental coincidences with background, which can lead to the unwanted summing of background events with the γ rays of interest and a loss of peak yield. In addition, γ rays of higher energy than the peaks of interest may Compton-scatter into the region. The γ ray of interest is denoted γ_0 and the higher energy γ ray is denoted γ_H. When the addback is applied, the Compton events from γ_H will be summed up into the peak. This consequently reduces the background in the γ_0 peak arising from the Compton scattering of γ_H. This may decrease the overall yield in the γ_0 peak, but increases the signal to background ratio.

In Figure 3.11, three different addback comparisons are shown, a spherical addback with radii of 4 cm, 7.5 cm, and 15 cm is applied to a ^{58}Ni spectrum. It is worth observing that at energies below 1-MeV, there is a significant amount of background from the Compton-scattering of high energy γ-rays. Thus, larger radii lower the total counts in the energy region. So, for the 7.5 cm

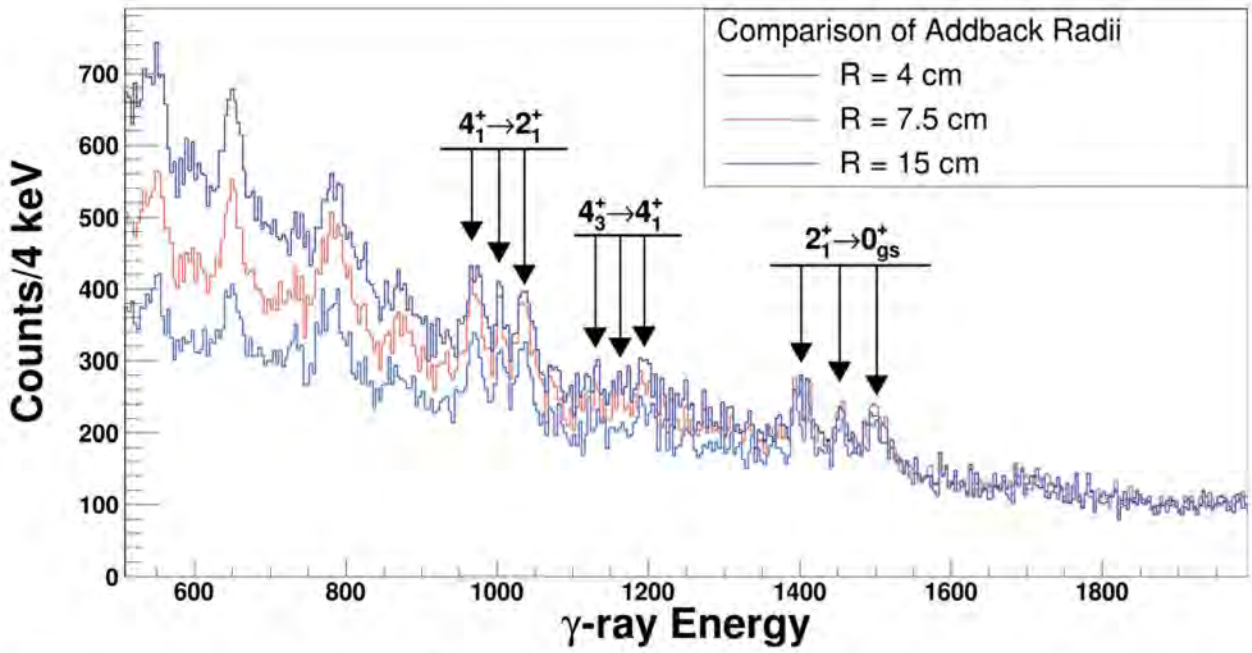

Figure 3.11 A γ-ray spectrum of ^{58}Ni is shown for a Recoil Distance Measurement with three foils each separated by 1 mm, as discussed in Chapter 4. Spherical addback radii of 4, 7.5 and 15 cm are compared, and discussed in the text.

case, the peak at around 650 keV has roughly the same yield as for the 4 cm case, but with less background. However, once the radii become too large, accidental coincidences can be summed in with the actual photopeaks, pair production, and Compton-scattered events. This leads to a reduction of the peaks, as can be seen in the 15 cm radius addback, where the background is lowered but so is the yield for the peaks between 500 and 1200 keV. In the experiments discussed here, the spherical addback radius determined is 7.5 cm. This is roughly twice the attenuation length of a 1 MeV γ ray in Germanium [84].

3.3.6 Doppler Reconstruction

All of the measurements in this work rely on the Doppler-effect to succeed, making the ability to reconstruct the projectile-frame energies of γ rays important. To reconstruct the γ-ray energy, the lab-frame energy must be corrected for the relativistic Doppler-effect as:

$$E_{Cor} = E_{Obs}\gamma(1 - \beta_{Cor}\cos\theta_{lab}) \tag{3.10}$$

In this equation, β_{Cor} is the ion velocity used for the correction, γ is the corresponding Lorentz factor for β_{Cor} and θ_{lab} is the laboratory frame angle between the γ-ray emission and the beam axis. To reconstruct the energy would require the velocity, ion position and trajectory, and γ-ray interaction position, which are not known exactly. However, through the coupled use of GRETINA and the S800, it is possible to extract Doppler-correction factors.

As discussed in Section 3.2.1, the S800 inverse map can be used to determine the non-dispersive displacement, the dispersive and non-dispersive angles of trajectory, and the energy of the ion at an upstream position. The inverse map is generally determined for the downstream degrader face. The S800 rigidity is used to determine a central β value for the ions of interest. The difference from the central value is incorporated by using the ion energy information from the S800 to determine the β_{Cor}. The interaction position information from GRETINA is used to calculate the angle relative to the position of the ion at the degrader face, which is taken as θ_{lab}.

3.3.7 Timing Between S800 and GRETINA

One complication when using fragmentation reactions is the creation of laboratory frame γ rays from neutron reactions on the beampipe and the GRETINA detectors themselves. These γ rays, when a Doppler-reconstruction is applied, can overlap with peaks of interest and complicate the resulting spectrum. However, as a number of these neutron induced γ rays come from states with lifetimes on the order of nanoseconds or longer, a timing cut between GRETINA and the S800 can be used to filter out the unwanted background.

Figure 3.12 shows a plot of γ-ray energy plotted against the difference in timing between GRETINA and the S800 E1 scintillator, with a sample timing cut drawn in red on top. The key features of this figure are that for energies above 500 keV most counts are located between channels -50 and -65, which corresponds to the time that the ion is at the target position. Above and below this band, at energies around 511 keV, 600 keV, 700 keV and 1460 keV, vertical lines can be observed in the plot. These are the γ-ray energies from the products of certain neutron reactions, the electron annihilation energy (511 keV), and natural background ^{40}K (1460 keV). The vertical

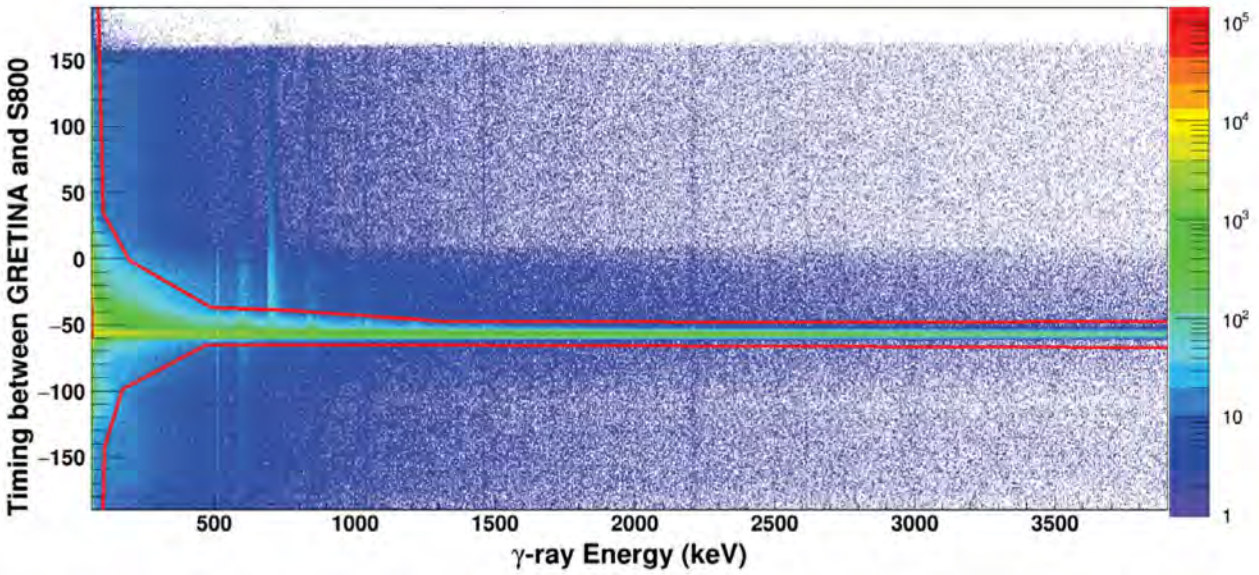

Figure 3.12 The difference in GRETINA and S800 timing is plotted as a function of the γ-ray energy. A sample timing cut to reduce the impact of neutron-induced backgrounds is shown in red. Neutron induced backgrounds can be seen at the vertical lines at 511 (electron annihilation energy), 590 (^{76}Ge), 700 (^{72}Ge), 850 (^{27}Al),1040 (^{70}Ge), 1460 (^{40}K), and 2614 (^{208}Tl) keV. The band along the cut between -50 and -70 represents γ rays coincident with ions near the target position.

lines are caused by the independence of these γ rays from the beam timing signal. A cut on the timing between the S800 and GRETINA can then selectively remove these backgrounds.

3.3.8 Calibration

The efficiency of GRETINA is incorporated into simulations used for both lifetime measurements and Coulomb-excitation measurements. In the lifetime measurements only the relative efficiency of higher and lower energy γ rays is critical. The energy difference between different Doppler-shifted peaks corresponding to the same transition in a lifetime measurement is on the order of 100 keV so that the differences in efficiency are well reproduced in the simulation. On the other hand, for Coulomb-excitation, the absolute efficiency of GRETINA is vital. The geometric efficiency of GRETINA is determined from simulations that incorporate the detector geometry as well as attenuation through the detectors, foils and other components. In the simulation, an isotropic distribution of γ rays is assumed in the projectile frame, and then the boosted frame angular dis-

tribution is calculated. As the projectiles are at energies between a third and half of the speed of light, the relativistic shift in geometry changes the expected efficiency by forward-focusing the γ rays.

However, the intrinsic efficiency of the GRETINA detectors and the attenuation of the γ rays through the target and degrader foils must be accounted for. This is done by using γ ray sources that are placed in various configurations with the plunger device.

For example, a ^{152}Eu source was used in the March 2016 experiment in two settings, and was used with only the target foil mounted, and with both the target and degrader foil mounted and separated by 25 mm. In the latter case, measurements were made with the source on the target and with the source on the degrader to account for different geometric efficiencies and attenuation lengths. The γ ray sources have known intensities and a known branching ratio for the emission of each γ ray with different energy per ^{152}Eu decay. Therefore, the efficiency could be calculated and compared to the simulated efficiency. In this case, the efficiency in the simulation was found to be 25% larger than in the data. This discrepancy may be due to the upstream position of the target which can lead to attenuation through the TRIPLEX and material surrounding the detectors not included in the simulations. In addition details in the structure of the GRETINA detectors may have an impact on efficiency not taken into account.

A comparison of the data and simulation for the ^{152}Eu source on the degrader face for selected γ-ray peaks is shown in Table 3.1. The total emissions expected are determined in the data from the activity of the source, the probability distribution for γ-ray emissions, and the length of time of the run. The total emissions for the simulation are determined from the number of simulated events and the branching ratio of the simulated ^{152}Eu. In the data the efficiency must take into account the deadtime of the system, which was approximately 72%.

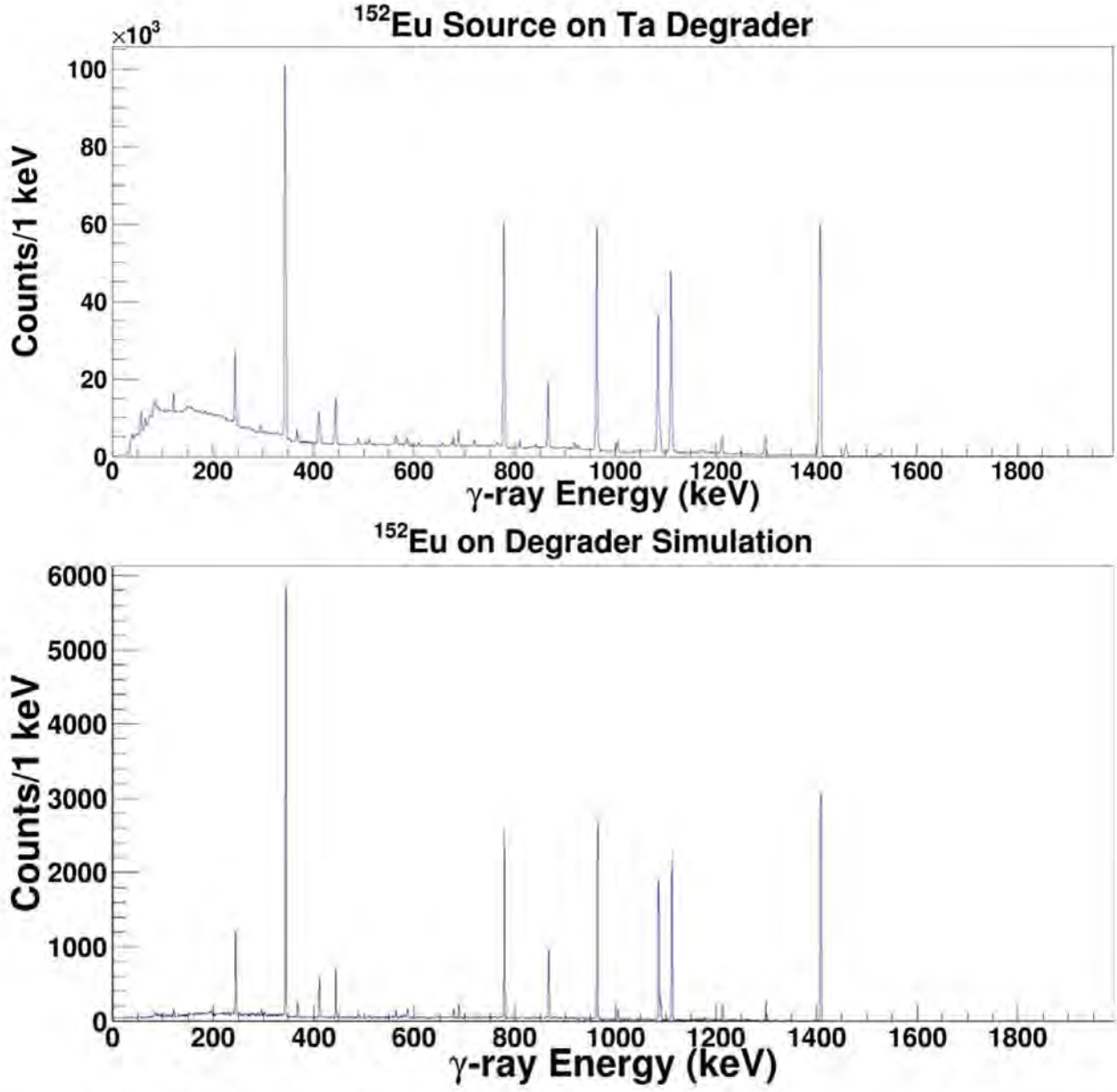

Figure 3.13 Spectra for a Eu-152 source placed on a 0.92 mm Ta Degrader 12 cm upstream of the GRETINA center for (top) data and (bottom) GEANT4 simulation are presented. The efficiencies can be compared to each other to determine the scaling need from the simulation.

γ-ray Energy (keV)	Efficiency in Data (%)	Efficiency in Simulation (%)	Scaling Factor
1086	5.6± 0.2	7.8 ± 0.1	0.71±0.04
1112	4.8 ± 0.2	6.6± 0.1	0.72 ±0.04
1408	4.4 ± 0.2	5.9 ± 0.1	0.75 ±0.04

Table 3.1 The efficiencies in data and simulation for a ^{152}Eu source are shown along with error and the ratio of the efficiency in data to the efficiency in simulation. Error is from uncertainties in the source activity and statistical error in the simulation and data. The efficiencies in data are generally $25\% - 30\%$ smaller than in simulation. This adjustment is taken into account in the cross section data.

3.4 TRIPLEX

The Recoil Distance Method and Coulomb-excitation techniques require the precise placement and control of target foils in the beamline. This precise movement is afforded by the Triple PLunger for Exotic Beams (TRIPLEX) [48]. The TRIPLEX is a plunger device that can hold up to three foils, two of which can be moved independently with respect to a middle foil placed at a fixed position.

The TRIPLEX layout is shown in Figure 3.14. The TRIPLEX consists of a bearing structure that enables the separation of the foils, a foil mounting structure that enables the mounting and aligning of foils, and a support apparatus to place the TRIPLEX into a beam-line and connect its electronics. The TRIPLEX makes use of two motors and measurement devices to ensure precise and accurate placements of foils.

3.4.1 Bearing Structure and Motors

The TRIPLEX is able to precisely position the three foils relative to one another through its bearing structure. The main structure consists of three concentric stainless steel tubes. The middle tube is connected to the support structure and is immobile. The outer and inner tubes are separated from the middle tube and held by four sliding bearings. The outer and inner tubes are each connected to the spindle of a piezoelectric motor (one on each side of the plunger). The connection is made using an elastic wire to connect the motors to rings clamped to the movable tubes to avoid any radial forces on the tubes, which ensures a smooth parallel motion of the foils [48].

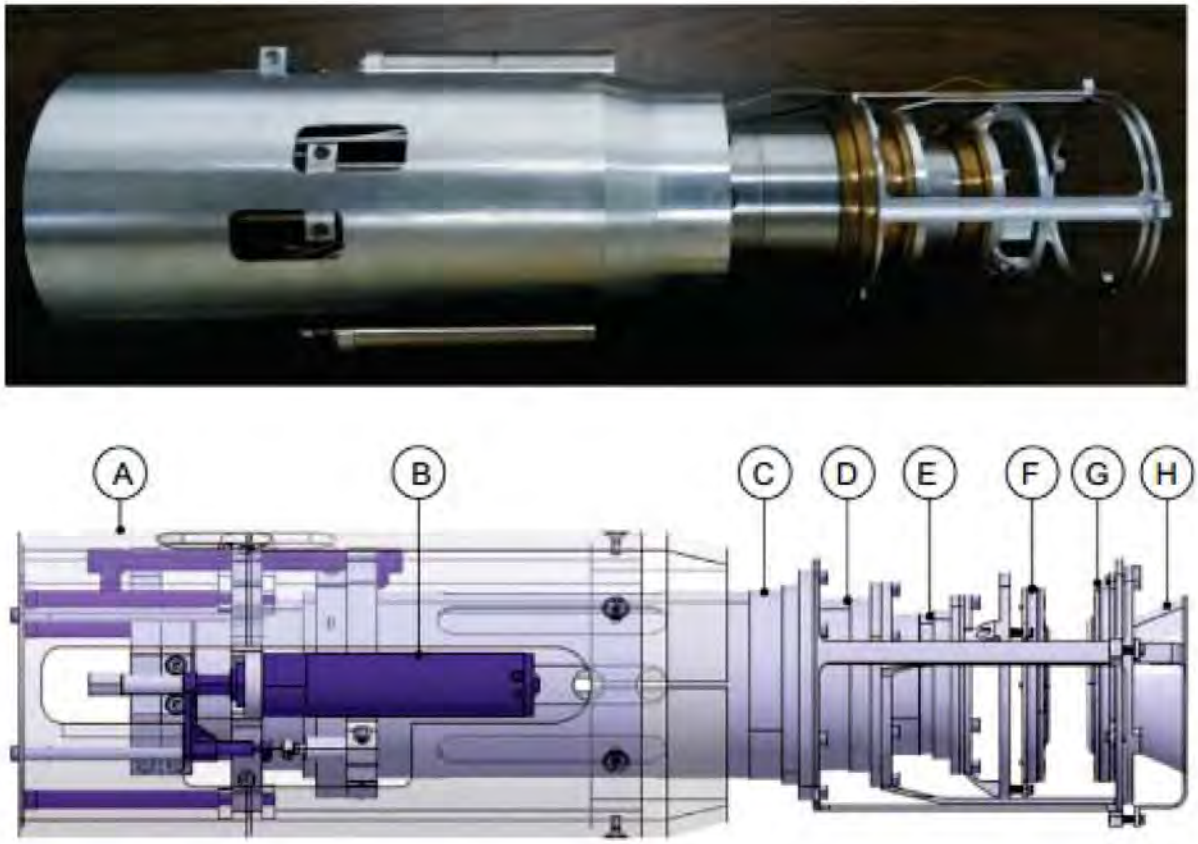

Figure 3.14 (top) A photograph of the TRIPLEX is shown compared to (bottom) a schematic of the TRIPLEX. In the schematic the labeling is as such: (A) The support frame, (B) Motor used to position the target foil, (C) the outermost tube, used to adjust the position of the second degrader, (D) The immobile central tube used to mount the degrader, (E) The inner tube, used to move the target, (F) The foil mounting structure for the target attached to the inner tube (E), (G) The foil mounting structure for the first degrader, which is immobile and connected to the central tube (D), (H) The foil mounting structure for the second degrader, attached to the outermost tube (C). Figure and identification are from [48].

The TRIPLEX is driven by two N-381 NEXACT linear actuators from Physik Instrumente, which is a piezoelectric motor. Piezoelectric motors work by application of electric fields to piezoelectric materials that expand in the direction of an applied electric field as illustrated in Figure 3.15. The piezoelectric material is set up as a number of actuator pairs attached to a guided runner. Each actuator consists of two blocks, a vertically aligned material attached to the moving rail and a horizontally aligned material that can be attached to a guiderail if a vertical electric field is applied to the vertical group. The electric field for the horizontal components in each pair are oppositely oriented, so that the applied electric field will cause one to expand to the left and the other to the right. The actuators can be made to step across the runner by applying a field to cause the first actuator to connect with the guide rail. Then the horizontal components are activated, causing an extension in the horizontal direction opposite that of the direction to be traveled. Then the actuators are switched vertically, so the second actuator is now connected to the guide rail, and the horizontal field is inverted, causing a net shift into the direction of motion.

The target and second degrader tubes can be moved over a range of approximately 25 mm. The target can be moved upstream 25 mm from the fixed first degrader position, while the second degrader can be moved up to 25 mm downstream.

3.4.2 Foil mounting structures

The target, first degrader, and second degrader foils are mounted onto aluminum frames attached to the three tubes by brass rings. The foils to be used with the TRIPLEX must be glued to specialized mounting cones, which can then be attached to the aluminum frames by three screws. These cones are insulated from the TRIPLEX and one another so that the capacitance between the two foils can be measured. The target cone and degrader cone face each other directly, while the second degrader cone is designed to fit within the first degrader, which requires that the second degrader foil be a circular shape [48]. The target and first degrader foils are generally square foils with a size dimension of 50×50 mm^2. The second degrader foil has a radius of around 47.5 mm.

To ensure that the separation is consistent across the foils, it is important to make sure that

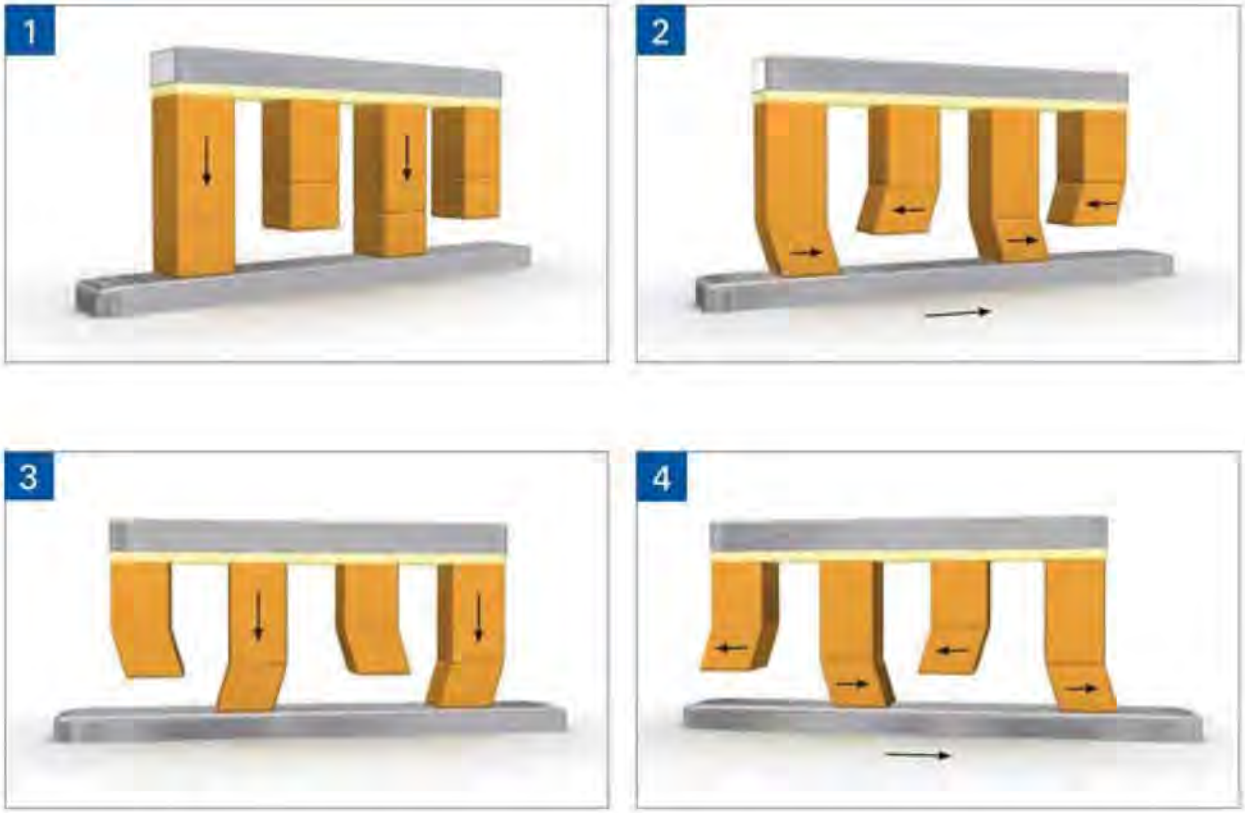

Figure 3.15 The stepping action of the N-381 NEXACT piezoelectric motor is shown in four figures. In (1) the first actuator is made to connect with the guiderail. In (2) the horizontal electric fields are applied, causing the first actuator to expand in the direction contrary to the motion of the motor, but the second actuator expands in the direction of the motion. In (3) the first actuator is removed from the guiderail and the second actuator connected. In (4) the horizontal electric field is reversed, causing the materials to expand against the direction of motion, leading to a net motion for the runner. Figure is from [88].

the foils are parallel to one another. This is accomplished by the use of springs attached to the mounting screws for the target and second degrader. The screws can be adjusted on each of the three mounting points for the cone. First the target and degrader are mounted and brought near contact. The capacitance is measured between the two foils, and the screws in the target cone are adjusted until the maximum capacitance is reached. When this is accomplished, the foils are parallel to each other. When three foils are used, the alignment must be done in three steps. First the target is aligned with the first degrader. Then the first degrader is unmounted, and the second degrader is mounted. The second degrader and target are brought near contact. The screws in the

second degrader are then adjusted until the second degrader is aligned with the target. Then the second degrader and target are separated and the first degrader is remounted. Then the alignment of the target with the first degrader is checked by measuring the capacitance. If the measured capacitance is consistent with the previous alignment of the target and first degrade, the three foils are considered aligned [48].

3.4.3 Support Structure

The unmoving parts of the TRIPLEX are attached to a support ring and an outer support frame. The outer frame connects to six screws that are used to align the TRIPLEX within the beam pipe. The motors used to drive the inner and outer tubes are directly connected to the support ring, as are two TESA inductive-working micrometers used to measure the distances driven by the motors [89]. Furthermore, wires are connected from the upstream side of the support frame which can be attached to the mounting screws for the target, first degrader and second degrader. The wire from the first degrader can be connected to a pulse generator, while the wires from the target or second degrader can be connected to either an oscilloscope or a multi-channel analyzer to determine the induced voltage. This allows for a measurement of the capacitance of the foils.

3.4.4 Beam Pipe

The TRIPLEX requires the use of a specialized beam pipe to align the TRIPLEX in the beamline and to allow for manipulation and readout of the electronic components. The TRIPLEX beam pipe is designed for use with HPGe detector arrays such as GRETINA, and is made from aluminum in order to minimally attenuate γ rays. The downstream section of the beam pipe has a flange designed to be attached to a downstream spectrometer, in these experiments the S800. The beampipe is also long enough to allow for the plunger to be placed upstream from the center of the array, as many measurements made in these experiments benefit from a larger detector efficiency for events emitted at small angles, which can be accomplished by moving the target upstream of the center

of the array. In these experiments, the target was placed approximately 13 cm upstream of the GRETINA center.

The upstream portion of the beam pipe has a diameter of six inches to accommodate the cabling of the TRIPLEX electronics. A number of electric feedthroughs are installed in the beampipe that can be connected to the TRIPLEX device, to allow for readout and control of the motors, readout of the TESA micrometers, connection of the pulse generator, and readout of the induced pulses. The upstream portion of the beam pipe also includes six alignment screws which can be adjusted to align the TRIPLEX with the beam axis.

3.4.5 Distance Measurements

The precise placement and adjustment of the three foils in the beamline is central to the methods used in this work. The measurement of the separation between the foils is afforded by three different tools that can be cross-checked for consistency.

3.4.5.1 Linear encoder

The first measurement available is directly from the driving motors. Each actuator is equipped with a linear encoder which provides information on the relative difference between the starting position of the motor and the final position of the motor after being driven. In principle, the linear encoder provides sub-μm resolution, but cross-checks are needed.

3.4.5.2 TESA micrometer

The second measurement is made via the an inductive-working micrometer, GTL21 from the TESA group [48]. The micrometer can measure compression over the range of $\pm$ 2 mm, and can be used for sub-μm distance measurements across that region. The TESA micrometer can be moved along the support frame to change the sensitive region. The TESA precision is considered to be better

than that of the linear encoder, but it also provides only a relative distance measurement. The TESA measurements can be compared to the linear encoder measurements to ensure consistency.

3.4.5.3 Capacitance

While the linear encoder and TESA micrometer provide precise measurements of the relative distances between foils, they do not on their own provide a measurement of the absolute distance between the foils. To obtain the absolute distance, the relative distance tools are calibrated using a capacitance measurement of the foils. As mentioned above, each foil can be connected to either a pulse generator or an oscilloscope/multi-channel analyzer after processing through a spectroscopic amplifier. In fact, in these experiments both the multi-channel analyzer and the oscilloscope were used to check consistency. Therefore, an exponential voltage from a pulse generator can be applied to one foil and the induced voltage read out.

The two foils can be treated as a parallel plate capacitor, for small distances between the foils. Therefore the capacitance can be modeled as:

$$C_{pp} = \frac{\varepsilon_0 A}{d} \tag{3.11}$$

where C_{pp} is the capacitance of two conductive parallel plates, ε_0 is the permittivity of free space, A is the area of the foil and d is the distance between the two foils.

The pulse generator in connection with the two foils and the readout can be modeled as an RC circuit between the internal resistance of the system and the capacitance of the two foils. For an RC circuit with an AC voltage with frequency ω, the voltage drop across the capacitor can be modeled as [90]:

$$\frac{V_C}{V_0} = \frac{1}{1 + i\omega RC} \tag{3.12}$$

where V_C is the voltage drop across the capacitor, V_0 is the voltage of the pulse generator, C is the capacitance of the two foils, and R is the internal resistance of the circuit. Therefore, the voltage

on the second foil relative to the ground is simply $V_{C_2} = V_0 - V_C$ which leads to:

$$\left|\frac{V_{C_2}}{V_0}\right| = \frac{\omega RC}{\sqrt{1+\omega^2 R^2 C^2}} \propto \frac{1}{\sqrt{d'^2+1}} \tag{3.13}$$

where $d' = 1/\omega RC$ is a dimensionless term proportional to the separation of the foils. While the applied voltage in this case is not AC, the exponential voltage can be Fourier decomposed into a sum of such terms so that the discussion is still generally valid.

For distances $d' << 1$, the capacitance reaches a saturation value and the induced voltage $V_{C_2} = V_0$. At distances $d' >> 1$ the equation is no longer valid, as the parallel plate model does not hold. In this case, the induced voltage becomes near zero and fluctuations cannot be distinguished from other electronic noise. In the region between these two extremes, where d is on the order of 10-100 μm in actual cases, the capacitance is inversely proportional to the distance between the foils.

The absolute distance between the two foils is calibrated by applying a voltage to one foil and measuring the induced voltage on the second foil over a range of distances. For example, for a target-degrader combination, the target is driven towards the degrader until the induced voltage saturates. This position is taken as the electrical contact position. From this position, the target is separated from the degrader in steps. At each position, the induced voltage is measured. The distance from the contact position is measured using the linear encoder and the TESA micrometer as well.

A calibration curve is then created by plotting the inverse of the voltage as a function of the distance from the electrical contact position measured by the TESA (linear encoder). An example of a voltage plot and a calibration curve employed in the ^{27}Ne experiment is shown in Figure 3.16. A linear fit is performed, and the x intercept, where the voltage would diverge, is determined. This would be expected contact position for the linear fit, and can be compared to the electrical contact position. The electrical contact position was found in the ^{27}Ne experiment to agree within 30 μm of the actual contact position.

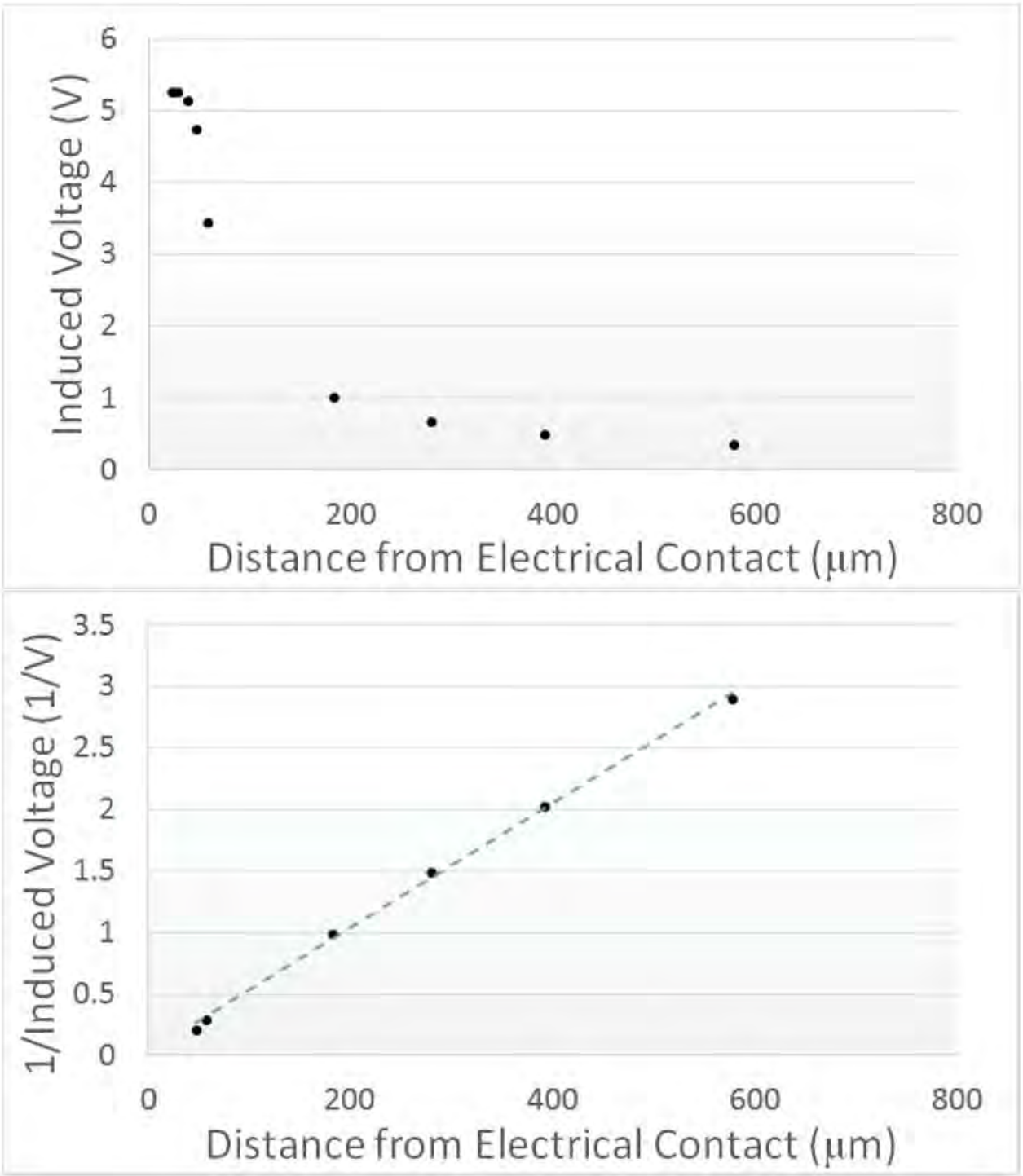

Figure 3.16 Plots showing the (top) induced voltage and the (bottom) reciprocal of the induced voltage between a beryllium and tantalum foil as a function of the separation between them. The distance was measured using the linear encoder of the TRIPLEX, and is based from the point of electrical contact. In the top figure, saturation near 0 μm can be seen, after which the $1/d$ behavior dominates. In the bottom figure, the points near saturation are removed. A linear fit to the data is also shown. For this case, the contact derived from the linear fit is within 10 μm of the measured electrical contact.

CHAPTER 4

INVESTIGATION I: ^{58}NI 4_1^+ LIFETIME MEASUREMENT

The first experiment discussed as part of this work is a measurement of the lifetime of the first 4^+ state of ^{58}Ni [91]. This measurement at stability probes collectivity in the vicinity of the shell gap at $N = Z = 28$. A previous measurement of the $B(E2;4_1^+ \rightarrow 2_1^+)$ has indicated enhanced collectivity in ^{58}Ni relative to expectations near a shell closure. A new measurement is described and the results are discussed. The present measurement is shown to resolve the discrepancy.

4.1 Shell Closure at N=Z=28

The Nickel isotopes are of significance for nuclear structure as Nickel has a magic number of protons with $Z = 28$ and spans over three doubly magic nuclei. These doubly magic nuclei include the most neutron deficient doubly magic nucleus ^{48}Ni [92], the N=Z nucleus ^{56}Ni [93], and the neutron rich ^{78}Ni [94][95]. Furthermore, ^{68}Ni is of interest as a semi-magic nucleus at the subshell closure at $N = 40$, a magic number for the harmonic oscillator [96]. This wide range of shell closures covered by the isotopic chain has led to much interest in the Nickel isotopes as benchmarks for shell-model calculations [91][97][98]. From a shell-model perspective, the closed-shell occurring at 28 nucleons is significant as the first closure arising from spin-orbit effects instead of from harmonic-oscillator levels. The $f_{7/2}$ orbit is lowered by the spin-orbit coupling, separating it from the remainder of the pf-shell. This results in an energy gap that manifests as a magic number.

The evidence of the (sub)shell closures for neutrons at $N = 28$ and 40 comes in part from the systematics of isotopic chains. For example, for the Nickel isotopic chain, the energies of the first 2^+ and 4^+ states attain a maximum at ^{56}Ni, where $N = Z = 28$, indicating that the energy of the gap between the $f_{7/2}$ and the remainder of the pf shell is significant. The energy of the 2_1^+ and 4_1^+ states in ^{68}Ni also significantly increase. Similarly, the $B(E2;2_1^+ \rightarrow 0_1^+)$ attains a minimum at ^{56,68}Ni, indicating a substantial decrease in collectivity arising from the same large energy gap.

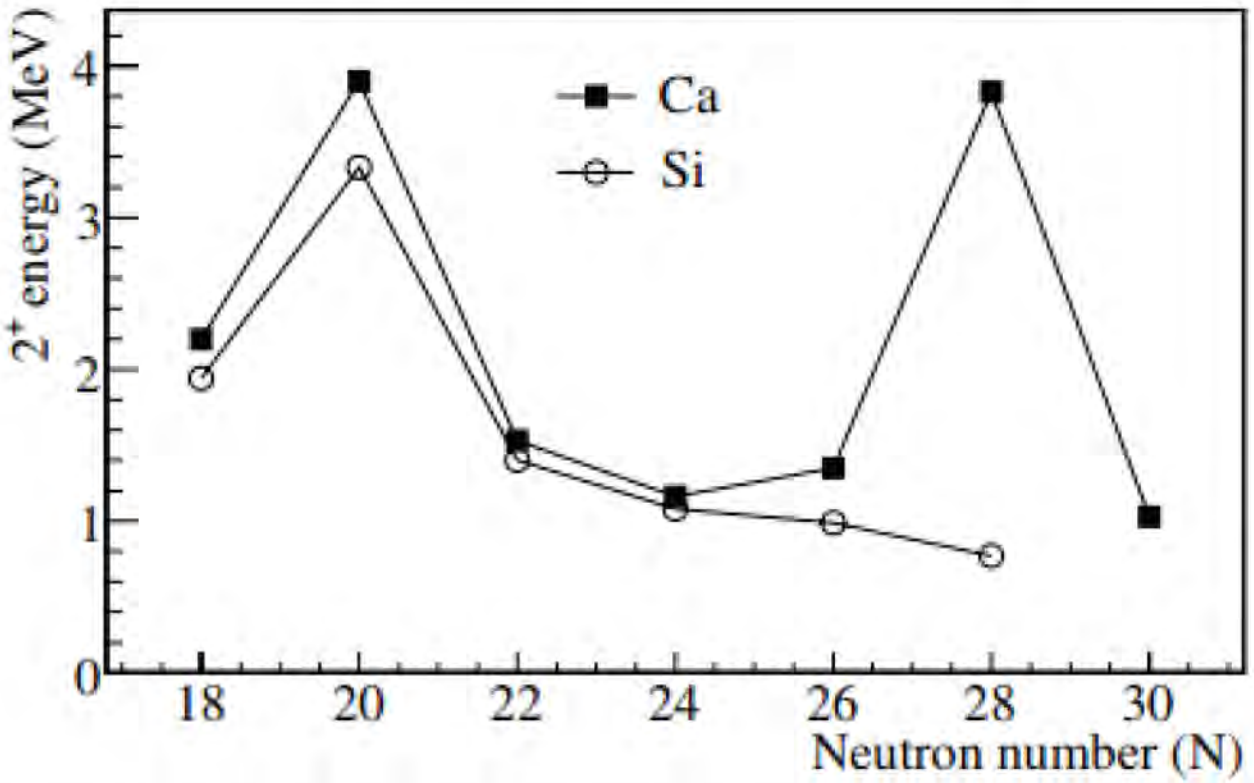

Figure 4.1 2_1^+ energies for Ca and Si isotopic chains near $N = 28$. The difference in systematics shows the decreasing energy gap for the N=28 magic number for nuclei far from stability. Figure is from [99].

The $N = 28$ shell closure disappears in neutron-rich nuclei [99]. The reduction of the $N = 28$ shell gap in neutron rich nuclei is also indicated in the systematics, as shown in Figure 4.1. The energy of the 2_1^+ state in ^{42}Si, with the neutron number $N = 28$ is lower than in nearby ^{40}Si with $N = 26$. This is contrary to the expectation of a maximum 2_1^+ energy at a shell closure, and is unlike the case of ^{48}Ca, where the $N = 28$ shell closure is still significant.

Even in nuclei near stability the $N = 28$ shell closure is known to be modest. For example, shell-model calculations of ^{56,68}Ni lead to ground state wavefunctions with substantial contributions from excitations across the $N = 28, 40$ and $Z = 28$ energy gaps [96][100][101]. Furthermore, the $B(E2; 2_1^+ \rightarrow 0_1^+)$ in the Nickel isotopic chain can not be reproduced using shell-model calculations without including proton and neutron excitations from the $f_{7/2}$ orbital into the remaining pf shell.

A comparison across the Nickel isotopes from A=56 to A=68 of the state energy levels and

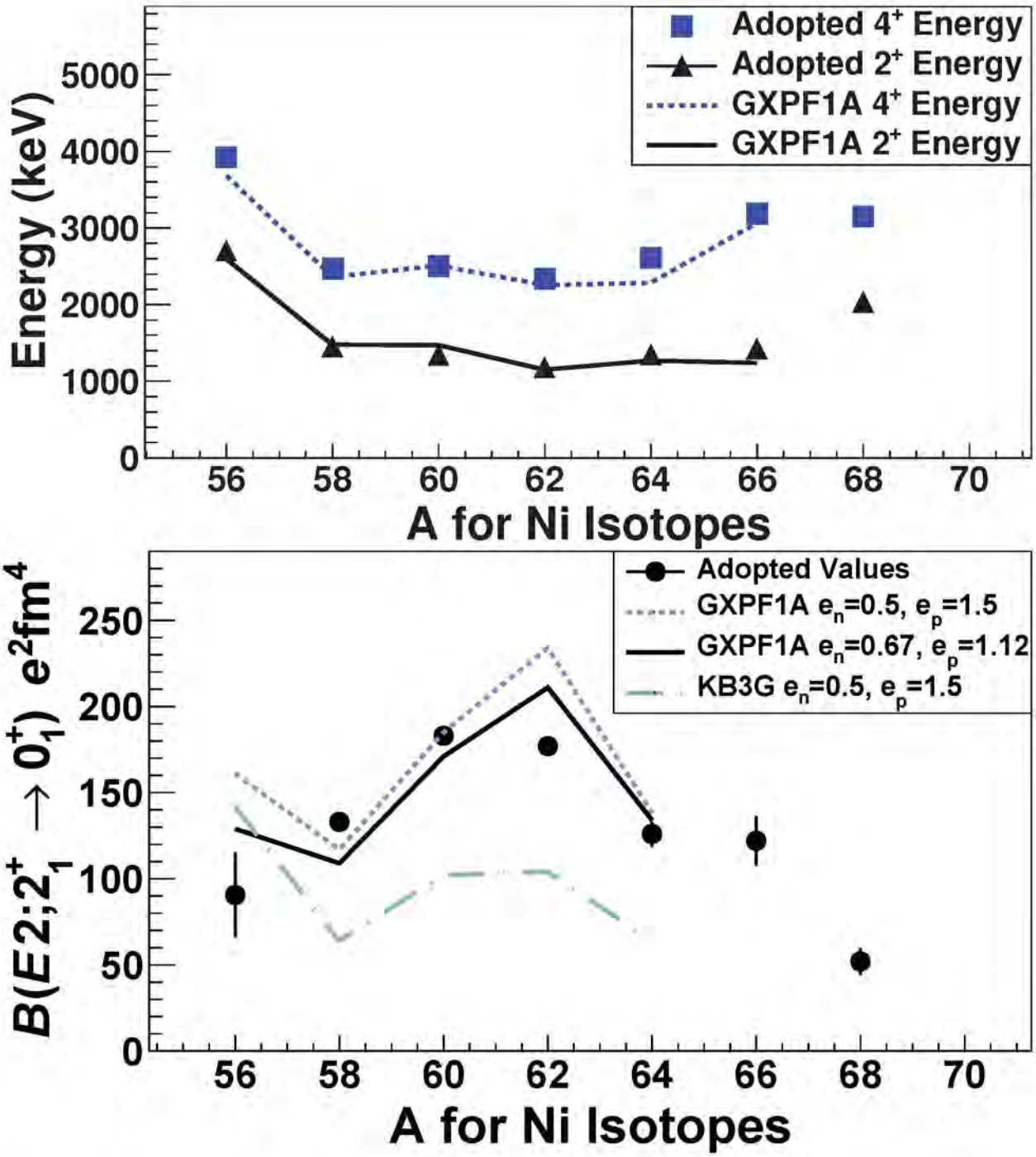

Figure 4.2 (top) The observed state energies for the 4_1^+ and 2_1^+ levels in the even-even Nickel isotopes between A=56 and A=68 are shown and compared to calculations from the GXPF1A shell model interaction. (bottom). The observed $B(E2;2_1^+ \rightarrow 0_1^+)$ transition strengths for the even-even Nickel isotopes between $A = 56$ and $A = 68$ compared against predictions from the KB3G interaction and the GXPF1A interaction with standard and modified effective charges. These figures are from [91].

$B(E2;2_1^+ \rightarrow 0_1^+)$ transition strengths from experimental values is presented in Figure 4.2 [102][103]. The systematics of the energies of the 2_1^+ and 4_1^+ states indicate an increase at ^{56}Ni. This is consistent with the expectation if the $N = 28$ shell closure is present. Furthermore, at a shell closure it is expected that the nucleus should be spherical and the $B(E2)$ transition strengths should be reduced. It can be seen in the systematics that the $B(E2;2_1^+ \rightarrow 0_1^+)$ values attain a maximum at midshell between ^{56}Ni and ^{68}Ni. The $B(E2;2_1^+ \rightarrow 0_{gs}^+)$ values smoothly decrease towards minima in the values is observed at ^{56}Ni and ^{68}Ni.

The data are also compared to shell-model calculations in the full pf-shell model space using the KB3G and GXPF1A interactions [102][103]. The KB3G interaction is a modification of the earlier KB3 interaction intended to reproduce the appropriate energy gap for the $N = Z = 28$ magic number [103]. The GXPF1A shell model interaction is a modified version of the GXPF1 interaction, which was fit to experimental values of the binding and state energies in 87 nuclei in the pf shell [104]. In GXPF1A five two-body matrix elements have been adjusted to match energies in neutron-rich Ca, Ti, and Fe [102]. As expected, the shell-model calculations also predict the increased state energies at ^{56}Ni. The $B(E2;2_1^+ \rightarrow 0_{gs}^+)$ predictions anticipate a maximum at midshell which gradually decreases towards the closed (sub)shells at ^{56,68}Ni.

4.2 ^{58}Ni 4_1^+ Lifetime

As ^{58}Ni has just two neutrons more than the doubly magic nucleus ^{56}Ni, it is expected to be sensitive to core excitations across the proton and neutron $f_{7/2}$ shells. As a stable nucleus, the energy levels of ^{58}Ni have been well established, and the $B(E2;2_1^+ \rightarrow 0_1^+)$ has been studied through Coulomb-excitation and lifetime measurements [105][106]. Indeed, shell-model calculations can only reproduce the values fo the $B(E2;2_1^+ \rightarrow 0_1^+)$ if excitations above the $N = Z = 28$ shell closure are permitted [105].

The $B(E2;4_1^+ \rightarrow 2_1^+)$ has also been measured once before in ^{58}Ni. A Doppler-shift attenuation method measurement resulted in a lifetime of 5.4 ± 0.6 ps [106]. The DSAM spectrum from

Kenn's measurement of ^{58}Ni is shown in Figure 4.3 [106]. This corresponds to a $B(E2;4_1^+ \rightarrow 2_1^+)$ value of $148^{+16}_{-15} e^2\mathrm{fm}^4$. This value is significantly larger than the $B(E2;4_1^+ \rightarrow 2_1^+)$ value for nearby ^{60}Ni which is 77(34) $e^2\mathrm{fm}^4$. This is somewhat surprising, as it might be anticipated that the $B(E2;4_1^+ \rightarrow 2_1^+)$ values should follow the behavior of the $B(E2;2_1^+ \rightarrow 0_1^+)$ values and attain a maximum at midshell with a smooth trend towards minima at the shell closures at ^{56,68}Ni. The apparently enhanced $B(E2;4_1^+ \rightarrow 2_1^+)$ value in ^{58}Ni may be a result of the scarcity of data for lifetime measurements of 4_1^+ states in the Nickel isotopes, or may be caused by additional contributions from higher-lying *sdg* orbitals or excitations over the $N = Z = 20$ shell closure.

The only previous measurement was performed using DSAM, which is primarily sensitive to lifetimes of 1 ps or less as shown in Figure 2.1 [41]. Assuming that the sensitivity of the Recoil Distance and Doppler Shift Attenuation methods overlap near 5 ps, the upper bound for the $B(E2;4_1^+ \rightarrow 2_1^+)$ from a lifetime measured with DSAM would then be near 150 $e^2\mathrm{fm}^4$. However, the systematics of the $B(E2;4_1^+ \rightarrow 2_1^+)$ would be restored with a lifetime longer than approximately 10 ps. Furthermore, the data cannot be reproduced by the previously mentioned shell-model calculations which predict a lifetime between 10 and 20 ps and a consequent reduction in collectivity consistent with the shell gap [91][102][103]. Therefore, in order to confirm or refute this potential enhancement in $B(E2;4_1^+ \rightarrow 2_1^+)$, a new measurement of the lifetime of the 4_1^+ excited state in ^{58}Ni was performed to distinguish between the literature value of 5.4 ps and the 10-20 ps value expected for an unenhanced $B(E2)$.

4.3 Recoil Distance Experiment on ^{58}Ni

The lifetime of the 4_1^+ excited state of ^{58}Ni was measured using the Recoil Distance Method. The Recoil Distance Method can be set up to be sensitive to lifetimes on the order of 10 ps. Therefore, it is able to distinguish between the previous experimental value of 5.4 ps and the 10-20 ps consistent with an unenhanced $B(E2)$. The experiment e11013 was performed at the National Superconducting Cyclotron Laboratory on campus at Michigan State University and employed the

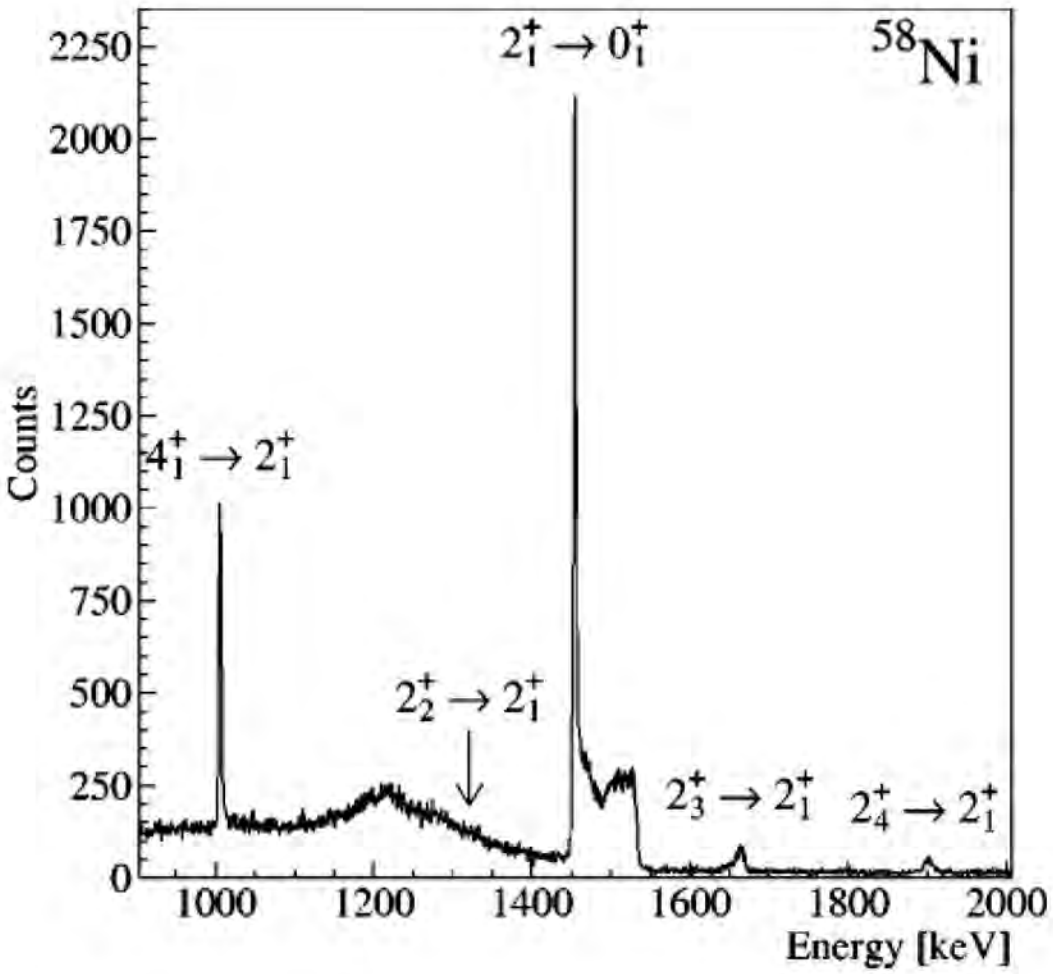

Figure 4.3 Doppler-shift attenuation method spectrum for ^{58}Ni from [106]. The lifetime is extracted from the relative yield in the Doppler-shifted and un-shifted parts of the peak and compared to the stopping time in the material. Lifetimes were extracted for each of the 2_1^+, 4_1^+, 2_3^+ and 2_4^+ excited states.

S800 Spectrograph in coincidence with the GRETINA detector array [61][71][79]. The experiment was run with the same setup as in [107].

The coupled-cyclotron facility at the NSCL was used to produce a primary beam of ^{78}Kr at 150 MeV per nucleon. This beam was impinged on a ^{9}Be target to produce a secondary cocktail beam, which included ^{74}Kr. The cocktail beam was sent to the A1900 fragment separator to produce a secondary beam of ^{74}Kr at 93 MeV per nucleon at a purity of 40% with a total intensity of approximately 10^5 particles per second [107]. The excited states of interest in ^{58}Ni were produced from multi-nucleon removal reactions on the target, and recoil particles were identified and tagged using the S800 [71].

The TRIPLEX Plunger device was employed to place the target and degrader foils into the beam-line and set the distances between them precisely [48]. The TRIPLEX was used with a three foil configuration. The target was a 750-μm ^{9}Be foil. The first degrader was a 125-μm Ta foil. The second degrader was a 90-μm Ta foil. This results in a three peak structure in the γ-ray spectrum where the relative peak yield is sensitive to the lifetime. To maximize the sensitivity of the measurement to lifetimes near 10 ps, a 1-mm distance between the target and the first degrader and a 1-mm distance between the distance between the first degrader and second degrader were chosen. This is because the flight time over 1 mm of the ^{74}Kr beam at 30% of the speed of light is approximately 10 ps.

However, as the excited states of ^{58}Ni could be produced by fragmentation of the secondary beam on the degraders, it is necessary to take measurements with the foils separated at a larger distance to constrain these reactions. This was done by setting the separation between the target and the first degrader to 10 mm, while maintaining the distance between the second degrader and first degrader at 1 mm. This means that any excited states that are produced on the target will decay back to the ground state before the beam is slowed in the degraders. Therefore the ratio of the counts in each of the three Doppler-shifted peaks provides a measurement of the relative amount of excited states produced by reactions in the target compared to those produced by reactions in the degraders.

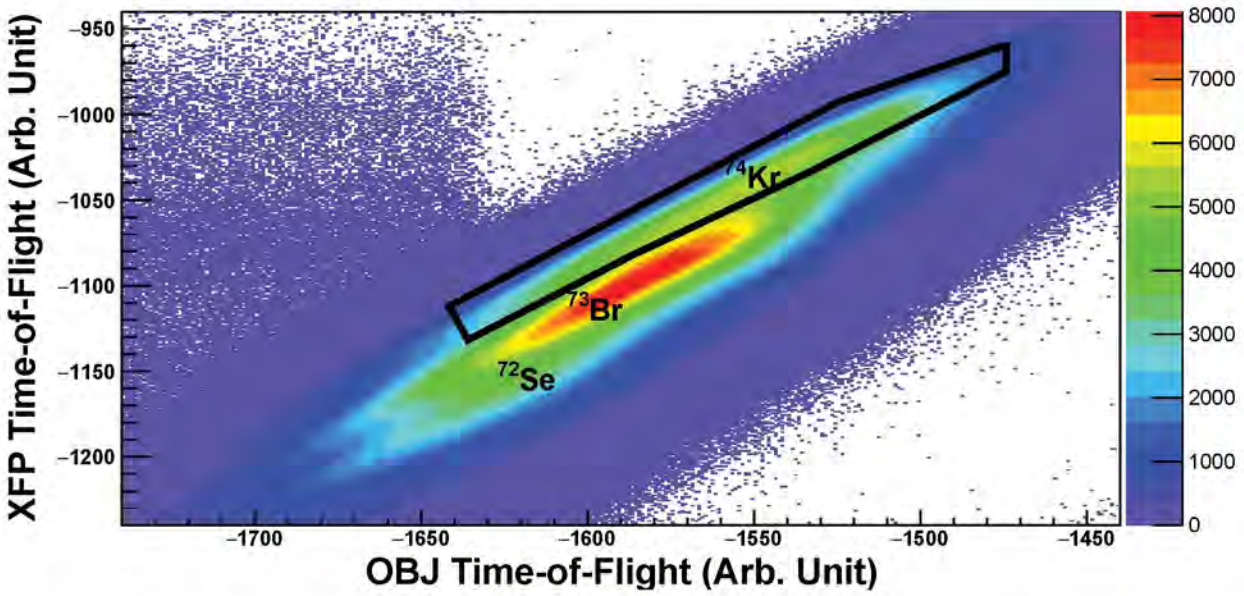

Figure 4.4 A timing signal correlation plot used as a particle identification for the incoming beam of interest is presented. The A1900 XFP scintillator timing signal is shown on the y-axis and S800 OBJ scintillator timing signal is shown on the x-axis. The components of the incoming cocktail beam are identified. ^{74}Kr is highlighted with a cut, while contaminants ^{73}Br and ^{72}Se are also labeled.

The γ rays emitted from the de-excitation of the ^{58}Ni nuclei were measured using the GRETINA array [79]. The GRETINA array was used with seven detector modules. In order to maximize the efficiency of GRETINA to γ-rays emitted at a small angle from the beam axis at the first degrader, the TRIPLEX target was positioned 13 cm upstream of the pivot point. As a result, four of the detector modules were placed at laboratory angles between 20° and 50°, which were used for the lifetime measurement. The remaining three detectors were arranged at between 70° and 90°, and were used to identify higher-lying states and coincidence relations.

4.3.1 Particle Identification

The incoming beam of ^{74}Kr was identified using a correlation plot between the timing signals from the XFP and OBJ scintillators. The resulting particle identification (PID) plot is shown in Figure 4.4.

The particle identification of the reaction residues was done using the energy deposited in the

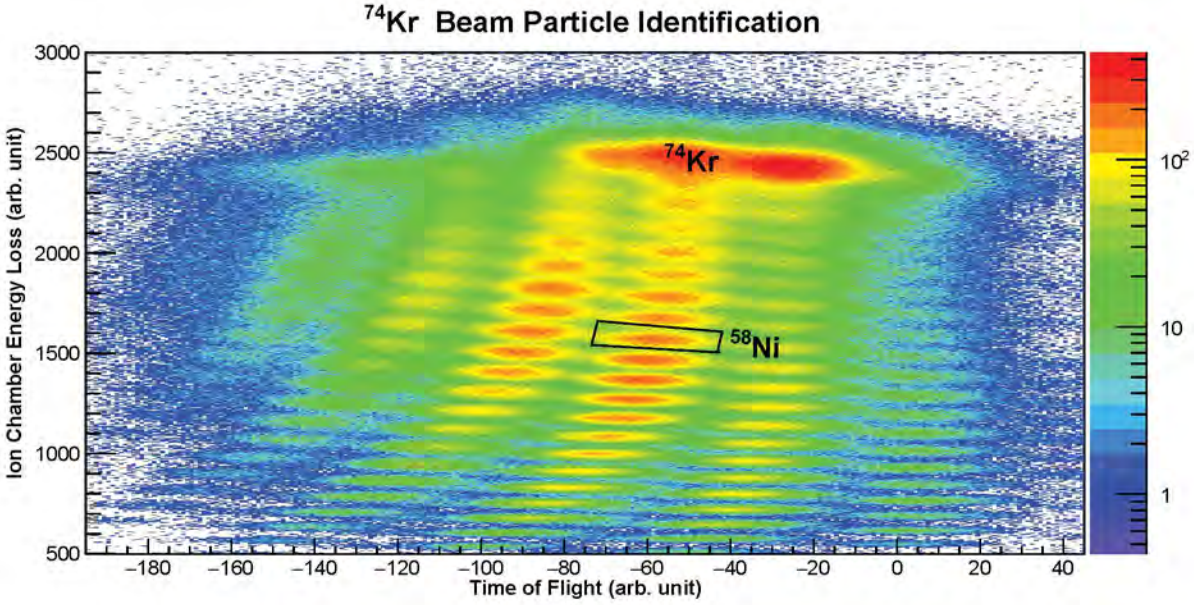

Figure 4.5 A particle identification plot for the reaction residues is presented. The y-axis shows the Ion Chamber ΔE while the x-axis shows the trajectory-corrected timing signal from the S800 OBJ scintillator. The particle identification plot is gated on the ^{74}Kr incoming beam. The ^{58}Ni residue is identified with a cut and labeled.

S800 ion chamber and the corrected time-of-flight for the OBJ scintillator. The resulting particle identification plot for this experiment is shown in Figure 4.5.

The PID shown in Figure 4.5 contains many nuclei in the upper pf shell. The ^{74}Kr secondary beam can be easily identified by the large yield near the top of the graph. Each nearly horizontal line below that identifies a different isotopic chain with constant Z. At the far right of the graph a vertical straight line identifies the $N = Z$ line of constant $A/Z = 2$. From this information, the other nuclei, including the labeled ^{58}Ni nucleus can be identified.

4.4 ^{58}Ni γ-ray Spectra

In order to constrain the lifetime of the 4_1^+ state of ^{58}Ni, the observed transitions and background in the γ-ray spectra tagged for ^{58}Ni need to be understood. In order to identify these states and backgrounds it is necessary to incorporate Doppler-correction to account for the Doppler-shifted energies from in-beam gamma-ray emission.

In this experiment, the Doppler-correction was optimized for decays that occur after the first degrader and before the second degrader. As the target foil in the TRIPLEX was located upstream of the GRETINA detector, the Doppler-correction angles were determined by assuming decays occurred at the downstream face of the first degrader. The β for Doppler-correction was set for the average velocity of ^{58}Ni particles between the two degrader foils. The β value was calculated based on the measured $B\rho$ value from the S800 rigidity and accounting for energy loss in the second degrader. The program LISE++ was used to calculate the expected energy loss through the foil to calculate the appropriate β, which was found to be 0.324 [108].

The Doppler-reconstruction will thus result in three peaks in the spectrum when a cut is applied for γ-ray emission angles below 40°. The highest energy peak is from decays between the target and first degrader and called the fast peak. The peak centered on the actual transition energy (shown in Figure 4.6) is from decays between the first and second degrader and called the reduced peak. Finally, the lowest energy peak is for decays occurring after the second degrader and is called the slow peak.

The Doppler-corrected and uncorrected γ-ray spectra for ^{58}Ni are presented in Figure 4.7 for the 1-mm setting. Forward-angle data was selected by introducing a cut on GRETINA angles less than 40°. In addition, a spherical addback was employed with a radius of 7.5 cm to increase the signal-to-background ratio. The 7.5-cm radius was chosen to balance the gain from summing Compton-scattered photons with the losses from accidental coincidence, which were not insignificant due to the large background from the multi-nucleon removal reaction employed in this study. In order to reduce background, only γ rays detected within a restricted timing window are included.

In the Doppler-corrected spectrum, the $4_1^+ \rightarrow 2_1^+$ transition at 1005 keV and the $2_1^+ \rightarrow 0_1^+$ transition at 1454 keV manifest a clear three peak structure, as expected. Hints of a three peak-structure for the $4_3^+ \rightarrow 4_1^+$ transition at 1161 keV are also apparent. A partial level scheme for ^{58}Ni presented in Figure 4.6 shows the transitions observed in the data. A small excess of yield at 870 keV is consistent with the fast component of the $7_2^+ \rightarrow 6_2^+$ transition in ^{58}Ni. A $\gamma-\gamma$ analysis was performed to investigate possible coincidences between the 870-keV γ rays and other known

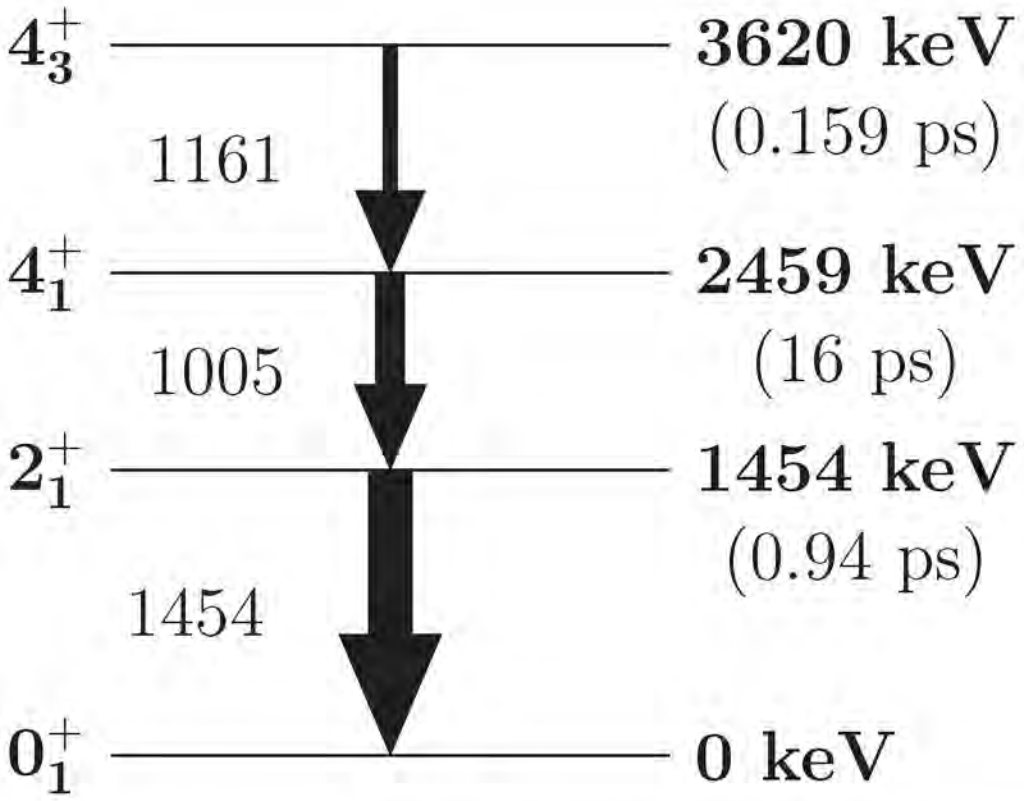

Figure 4.6 A partial level scheme of ^{58}Ni showing states observed in the Recoil Distance Method experiment. The lifetimes in parentheses are from the present measurement for the $4_1^+ \rightarrow 2_1^+$ state and for the remainder are from the NNDC evaluation [109]. The thicknesses of lines represent the relative yield from each transition. Figure is from [91].

transitions. However, the 870 keV γ ray was found not to be in coincidence with the other observed transitions and thus could not be identified as part of the decay scheme.

4.4.1 Laboratory Frame Background

In this work, a number of clear discrete peaks are identified which originate from the laboratory frame background γ rays, as shown in Figure 4.7. The laboratory frame background was primarily generated by neutron-induced reactions on Aluminum and Germanium in the beam pipe and detectors. The manifestation of a clear peak structure in the Doppler-corrected spectra is a consequence of the cut on the GRETINA angles.

The laboratory frame γ-rays are identified through comparison to well known background for

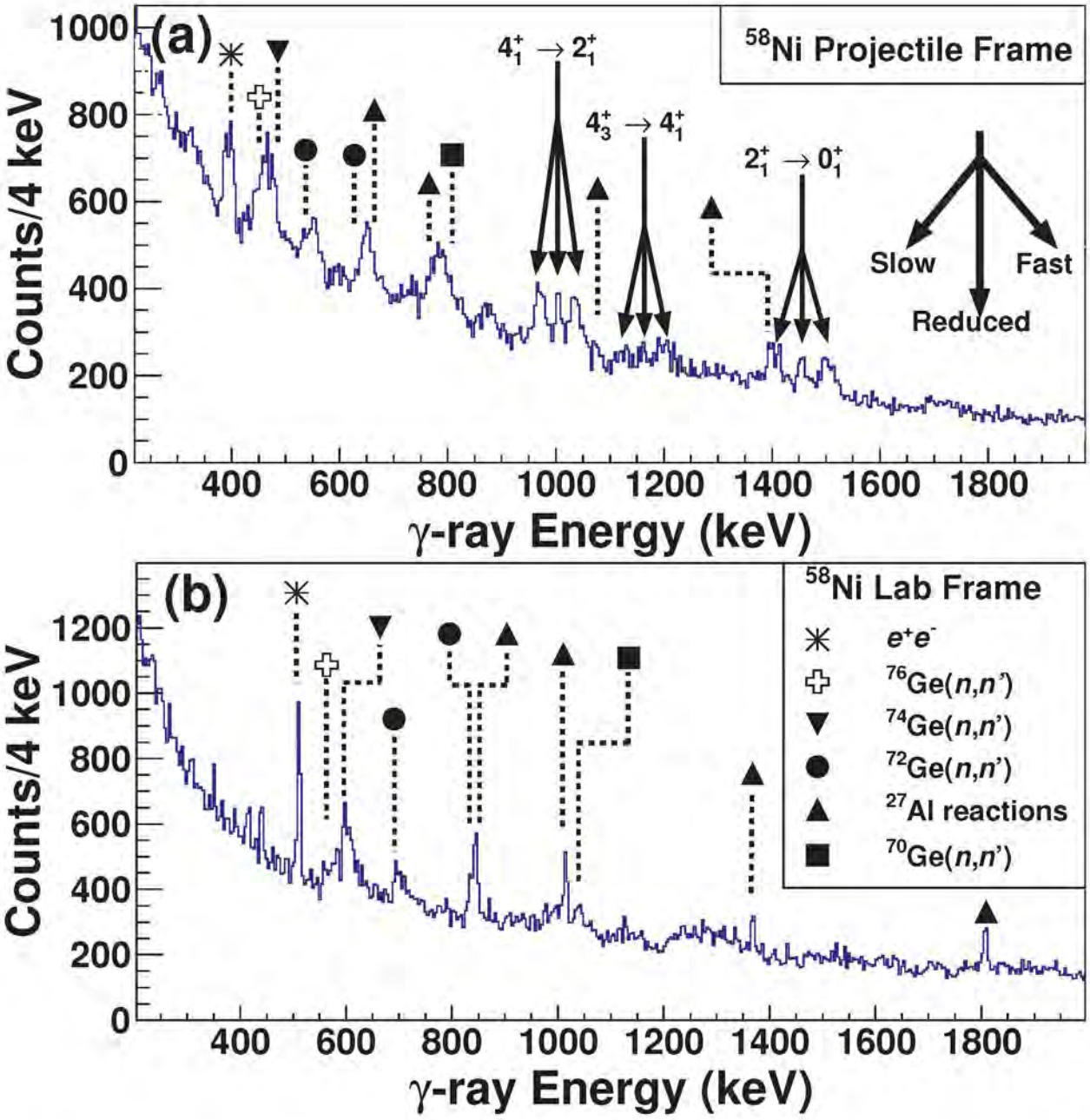

Figure 4.7 The Doppler-corrected (top) and lab-frame spectra for the 1-mm separation at forward angles are shown. The arrows in the Doppler-corrected spectrum identify the three-peak structure for observed ^{58}Ni transitions. In both the Doppler-corrected and lab-frame spectra γ-ray peaks from laboratory frame backgrounds are identified and labeled.

Target-Degrader Separation	Counts in 1369 keV Peak	Counts in 1808 keV Peak
1-mm	355	513
10-mm	248	319

Table 4.1 Observed γ-ray counts from neutron induced reactions on ^{27}Al for 1-mm and 10-mm separations.

in-beam experiments using Germanium detectors [74]. The identified reactions are labeled in the uncorrected γ-ray spectrum in Figure 4.7 and include e^+e^- interactions at 511 keV and inelastic neutron scattering on Germanium isotopes in GRETINA. The most important reactions for this experiment are the neutron induced reactions on ^{27}Al in the beam-pipe and GRETINA frame and detectors. In particular the $^{27}\mathrm{Al}(n,\alpha)$ reaction results in a γ ray at 1369 keV and the $^{27}\mathrm{Al}(n,d\gamma)$ results in a γ ray at 1808 keV. When Doppler-corrected in this experimental setup, these energies overlap with those of the three-peak structures coming from decays of the excited states of ^{58}Ni. In particular the 1369 keV transition results in a peak near 1070 keV that overlaps with the fast part of the $4_1^+ \rightarrow 2_1^+$ peak, while the 1808 background results in a peak around 1400 keV, near the slow component of the $2_1^+ \rightarrow 0_1^+$ transition.

The laboratory frame background γ rays that when Doppler-corrected overlap with the transition energies must be accounted for. Counts in the background peaks were estimated by taking an integral of the background energy region and subtracting off a constant background. A summary of the results is shown in Table 4.1.

A GEANT4 simulation package was employed to generate simulated spectra incorporating the beam properties, GRETINA geometry and efficiencies, and the lifetimes of excited states [46]. The simulations were then fit to the data to determine the lifetime. To account for the laboratory frame background, the 1369 keV and 1808 keV signals were simulated for the entire array. The resulting γ-ray spectrum was then scaled to reproduce the appropriate number of counts in each peak. This histogram was then added to simulations for the 10-mm and 1-mm spectra when fitting to data in order to account for the background.

4.5 ^{58}Ni Data Analysis

The GEANT4 based simulation package incorporates the S800, TRIPLEX and GRETINA to make simulated γ-ray spectra [46][87]. These simulated spectra were fit to data using a χ^2 minimization, where the amplitude of the simulated spectrum, an exponential background, and the lifetime of the 4_1^+ state are variable parameters. In addition, other parameters had to be constrained to extract a lifetime. These parameters were the contribution from reactions in the degraders and effects from feeding of higher-lying states. The GEANT4 simulation incorporates reaction kinematics, velocity changes in the foils, and γ-ray interactions with matter, including attenuation and detection in GRETINA. Best fit spectra incorporating an exponential background, and contributions from neutron-induced background are compared to the data for the 1-mm and 10-mm data sets in Figure 4.8.

The 10-mm data set was used to constrain both the relative population of states in ^{58}Ni and the ratio of population in the target to the degraders. The best fit proportion of populations was found to be $25 \pm 5\%$ for the 2_1^+, $50 \pm 5\%$ for the 4_1^+ state and $25 \pm 5\%$ for the 4_3^+ state. The ratio of populations in the target to the degraders was determined to be 13^{+4}_{-2}. The population ratio between the first and second degraders was estimated as being the ratio of their thicknesses, 1.389. The errors determined here are of statistical origin from a χ^2 minimization.

It is worth noting that the apparent ratio between the population in the target and the degraders is smaller than the best fit of 13^{+4}_{-2}. This is because the S800 rigidity is optimized for $N = Z$ nuclei, which means that only the lower momentum tail of the ^{58}Ni distribution can be accepted. This can be understood by examination of the spectrum in Figure 4.9, which shows the spread of energy at the exit of the second degrader (dta). It is apparent from the spectrum that the lower energy tail of the distribution is being selected for by the S800. As the ^{58}Ni fragments are made from a ^{74}Kr beam, and as energy loss in materials is proportional to the square of the atomic number, it follows that there will be more energy loss in the degrader for the ^{74}Kr beam than for a ^{58}Ni particle. Therefore, the low energy side of the distribution is expected to contain more reactions where the

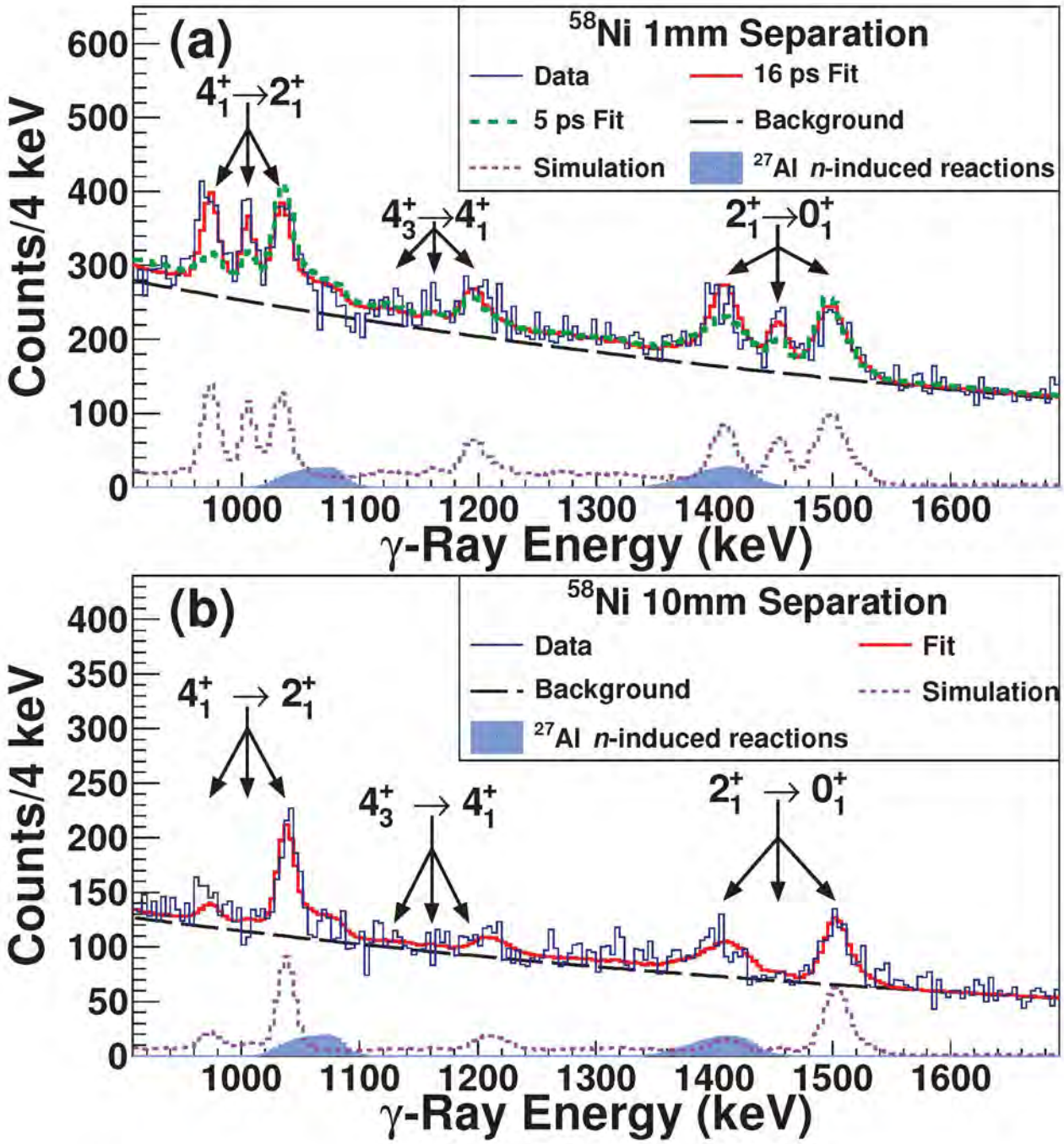

Figure 4.8 Results for the Recoil Distance Method for ^{58}Ni with a 1-mm (top) and 10-mm (bottom) separation between the target and degraders. The data is compared to a spectrum with best fit parameters for state population and ratio of target to degrader reactions. The simulated spectrum is decomposed into the GEANT4 simulation, the background from neutron-induced reactions on ^{27}Al, and the exponential background. Figure is from [91].

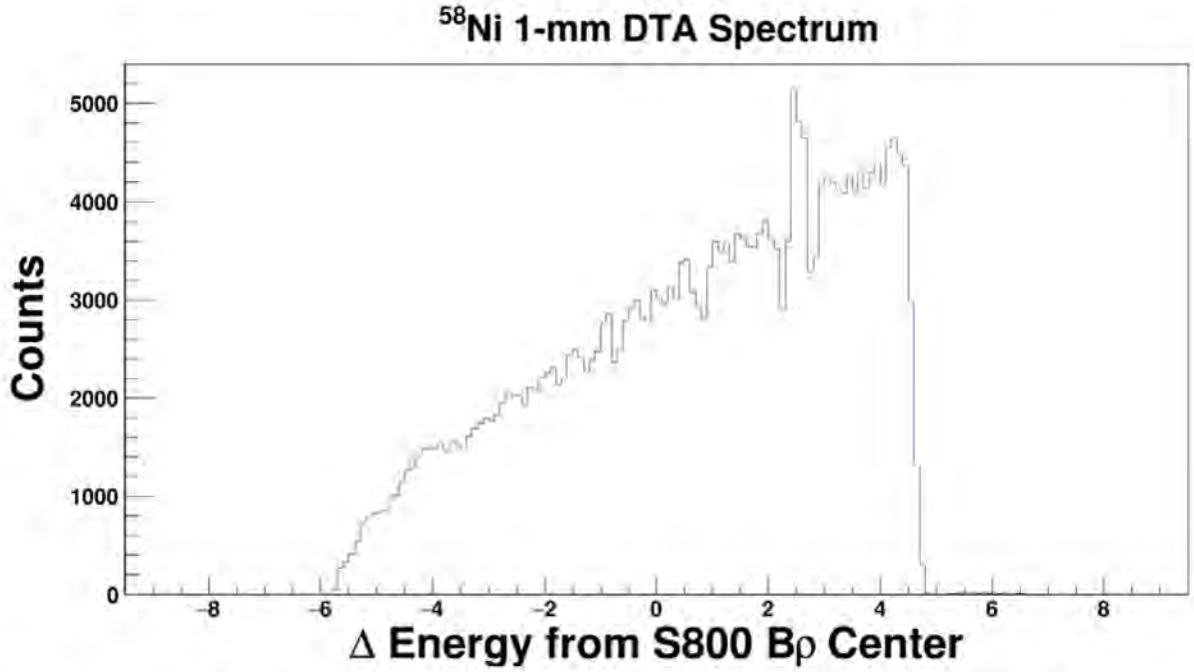

Figure 4.9 The dta spectrum showing the energy distribution for ^{58}Ni fragments observed in the S800 Spectrograph is shown. The x-axis shows the percentage difference from the Bρ central value, 1.9 T-m, which corresponds to an energy of 40 MeV per nucleon. The asymmetric shape demonstrates the enhanced S800 selection for reactions occurring in the degraders.

^{58}Ni was produced in the degraders.

There may be a difference in the energy distributions for ions emitting γ rays in each of the three peaks due to the location of the reaction. A comparison of the dta spectra gated on the fast and slow peaks of the 4_1^+ transition is shown in Figure 4.10. It can be seen that aside from a difference in scale, the distributions are similar and do not indicate a strong correlation to the γ-ray peak. The corresponding distribution gated on the reduced peak was found to also show minimal signs of biasing.

The γ-ray spectrum for the 1-mm separation is presented in Figure 4.8 (a) and compared to the best fit simulation. The simulation is fit over a range from 900 to 1700 keV, which includes three observed transitions. The lifetime of the 2_1^+ state has been measured previously as 0.94 (3) ps, which is too short to be observed with the setup [106][109]. Due to the large feeding contribution of the 4_1^+ state to the 2_1^+, the apparent lifetime of the 2_1^+ state is lengthened by the 4_1^+ lifetime.

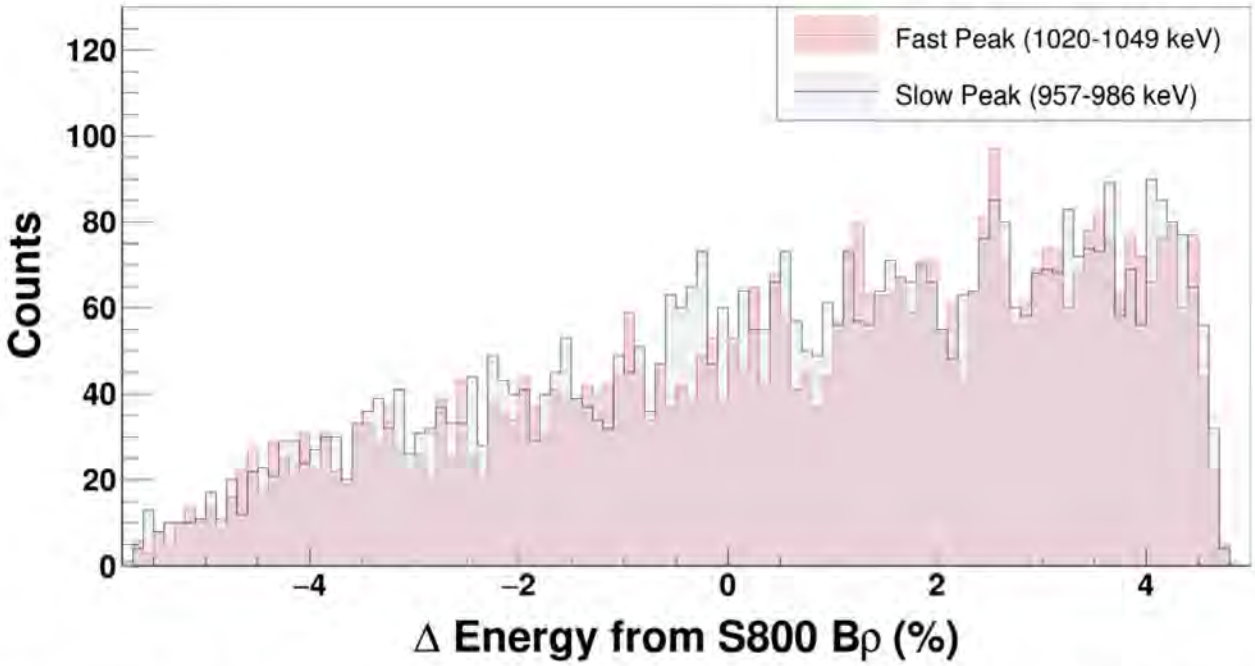

Figure 4.10 The energy distributions for ^{58}Ni fragments in coincidence with the fast and slow components of the 4_1^+ transition energies are shown. The overall dsitribution of the slow component is slightly larger in scale due to the larger yield, but there is no clear difference in the shapes of the distribtuions.

Therefore, the 2_1^+ spectral shape is also sensitive to the lifetime of the 4_1^+ lifetime. The three peak structure for both the 4_1^+ and 2_1^+ states are thus incorporated to measure the lifetime of the 4_1^+ state.

Feeding effects from higher-lying states increase the apparent lifetime of the 4_1^+ state. This is accounted for by assuming that all higher-lying feeding states decay through the observed 4_3^+ state focused on in Figure 4.11. Indeed, the three peak structure in the 4_3^+ state is consistent with a lifetime in the region of 0 to 10 ps, longer than the previously measured lifetime of $0.16^{+0.11}_{-0.07}$ ps [109]. This indicates that indeed there are higher-lying states with finite lifetimes populating the 4_3^+ state. In order to constrain this effective lifetime, the three-peak structure at 1161 keV was analyzed separately between 1080 and 1300 keV. The amplitude of the simulation was taken as a free parameter, while the exponential background was fixed to that of the full 900 to 1700 keV region. The results of a χ^2 minimization for these spectra led to a best fit lifetime of 3^{+5}_{-3} ps. This

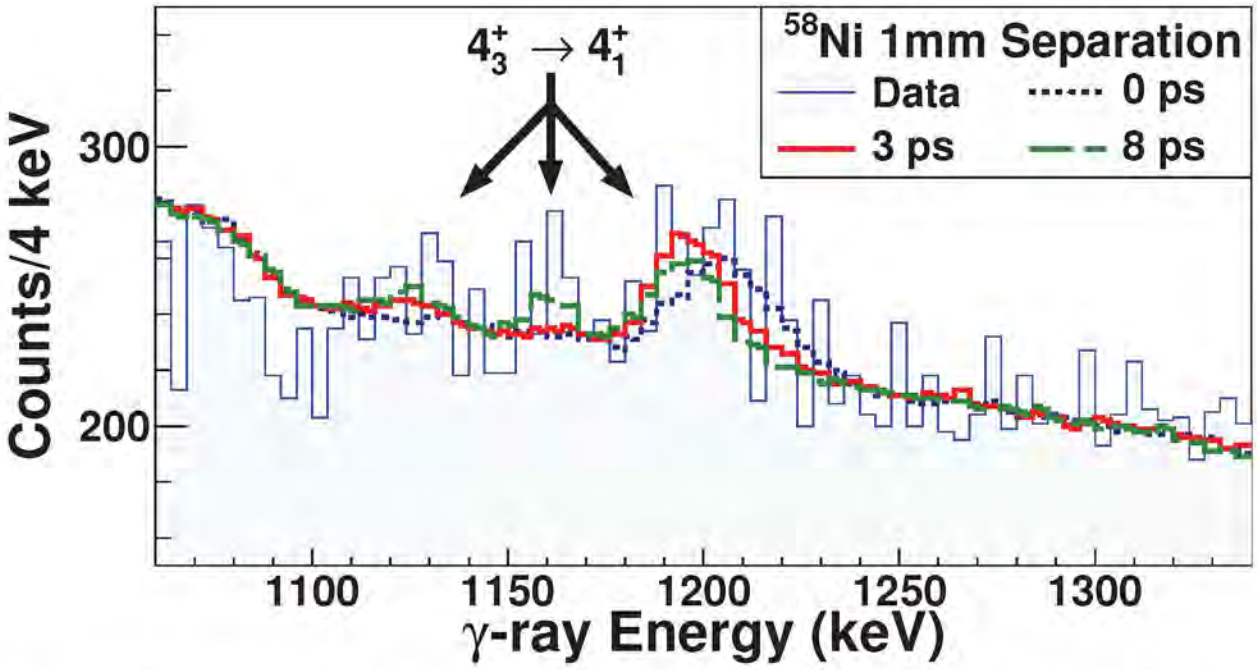

Figure 4.11 A zoomed in γ-ray spectrum for the 1-mm data set focused on the 4_3^+ state is presented. Simulations using a fixed exponential background are compared to the data for the best fit lifetime of 3 ps and for the upper and lower bounds of 8 ps and 0 ps. The figure is from [91].

comparison is shown in Figure 4.11, where the fits for lifetimes of 0 ps, 3 ps, and 8 ps are shown and compared to the 1-mm data. Linear and quadratic backgrounds were also fit to the full 900 to 1700 regions and fixed to account for systematic error from the choice of background shape. The systematic error was found to be marginal.

The best fit lifetime of the 4_1^+ state was found to be 16 ± 1 ps, where the error is statistical. The systematic error in the 4_1^+ lifetime comes from ambiguities in the ratio of reactions in the target to the degrader, and to the feeding contributions from higher-lying states. By analyzing the effects on the 4_1^+ lifetime from varying the reaction ratio and the lifetime of the feeding 4_3^+ state, the systematic errors were quantified. The uncertainty from the reaction ratio was found to be ± 1 ps. The uncertainty due to feeding was constrained with the uncertainty in the apparent lifetime of the 4_3^+ state. This was found to be $^{+1}_{-2.5}$ ps. The systematic error from other sources, including uncertainties in the direct population of states was negligible. The statistical error was ± 1 ps, and by adding the systematic and statistical uncertainties in quadrature, the overall lifetime of the 4_1^+

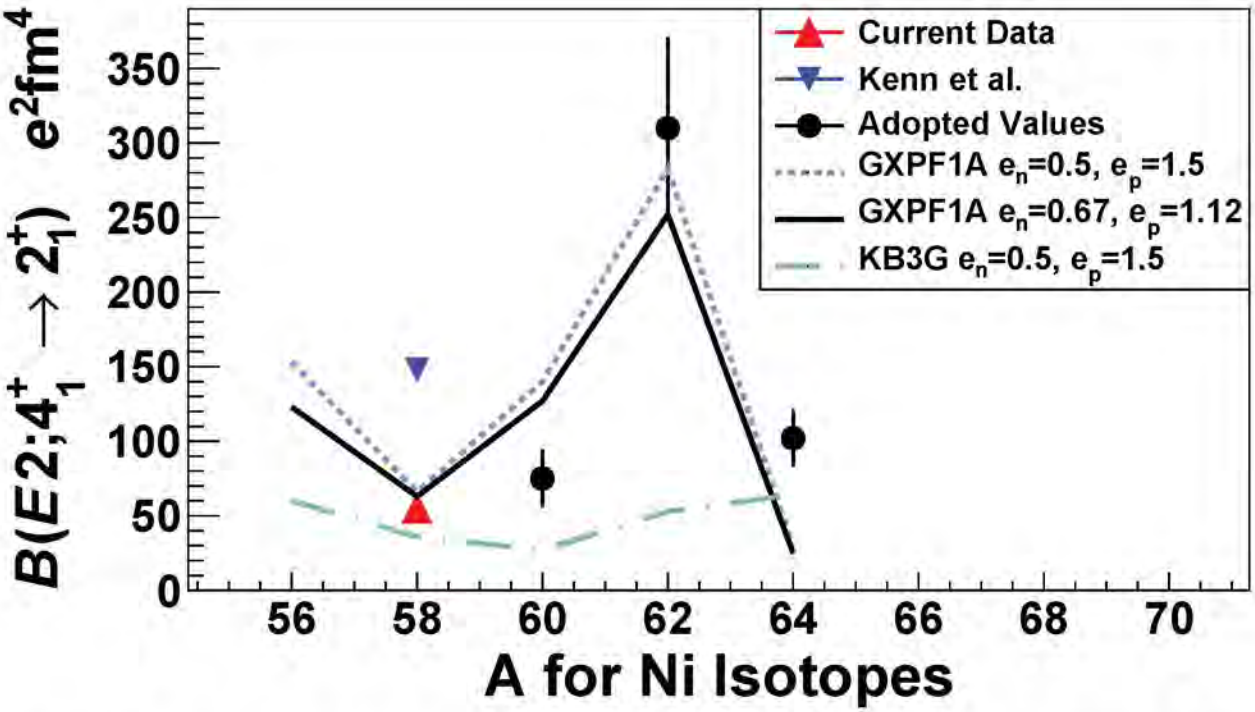

Figure 4.12 The systematics of the $B(E2;4_1^+ \rightarrow 2_1^+)$ values throughout the Nickel isotopic chain. The experimental values are compared with the shell model values from the GXPF1A and KB3G interactions. For the GXPF1A shell model interactions, results for two sets of effective charges are shown. Figure is from [91].

state was found to be 16^{+2}_{-3} ps. The resulting $B(E2;4_1^+ \rightarrow 2_1^+)$ is then $50^{+11}_{-6} e^2\text{fm}^4$.

4.6 Interpretation of ^{58}Ni results

The experimental values of the $B(E2;4_1^+ \rightarrow 2_1^+)$ across the Nickel isotopic chain are presented in Figure 4.12, including both the present measurement of ^{58}Ni and the previous measurement by Kenn et al. [106]. The experimental values for the other isotopes are from the NNDC evaluation [109]. The present result of $50^{+11}_{-6} e^2\text{fm}^4$ can be seen to restore the expected unenhanced $B(E2;4_1^+ \rightarrow 2_1^+)$ in ^{58}Ni relative to ^{60}Ni, consistent with the shell closure at $N = 28$. Indeed, the current result restores the smooth parabolic trend between the shell closures at ^{56,68}Ni, consistent with the systematics of the $B(E2;2_1^+ \rightarrow 0_1^+)$ values presented in Figure 4.2.

To provide a comparison on a quantitative basis, results from the GXPF1A and KB3G shell

model interactions are also presented. The calculations were performed in the full pf shell model space, and a portion of the calculations were performed using the code MSHELL64 [102][103][110]. Two sets of proton and neutron effective charges are used, namely the standard values of e_p=1.5, $e_n = 0.5$ and $e_p = 1.12$, $e_n = 0.67$ which were fit to the mirror $27/2^-$ to $23/2^-$ transitions in ^{51}Fe and ^{51}Mn in [105].

The $B(E2)$ values for the shell model comparisons were determined by calculating the bare E2 matrix elements for protons and neutrons, A_p and A_n, values. These values are presented in Table 4.2. The bare E2 matrix elements, the $B(E2;2_1^+ \rightarrow 0_1^+)$ and the $B(E2;4_1^+ \rightarrow 2_1^+)$ were calculated with the GXPF1A and KB3G interactions with standard and modified effective charges. The calculations were performed in the pf model space and radial integrals were evaluated using harmonic oscillator wave functions, with the harmonic oscillator energy quantum $\hbar\omega = 45A^{-1/3} - 25A^{-2/3}$. The $B(E2)$ is obtained from the bare E2 matrix elements through the relation:

$$B(E2;J_i \rightarrow J_f) = (A_p e_p + A_n e_n)^2/(2J_i+1) \tag{4.1}$$

As can be seen in Figure 4.12, the $B(E2;4_1^+ \rightarrow 2_1^+)$ value of 50^{+11}_{-6} ps from the Recoil Distance Method discussed here agrees more closely with the shell-model calculations than with the DSAM results from [106]. It can also be seen that in the systematics, the result here restores the single enhancement of collectivity at ^{62}Ni, which is also reproduced by the shell-model calculations. This strong peak can be understood to arise from the increased occupation of the neutron $f_{5/2}$ orbital relative to ^{58}Ni, as the neutron $f_{5/2}$ contribution to the $E2$ matrix element adds coherently with those from the neutron $p_{3/2}$ and $p_{1/2}$ orbitals [91].

		GXPF1A				KB3G			
Nucleus	$J_i \to J_f$	$A_p[e\text{fm}^2]$	A_n $[e\text{fm}^2]$	$B(E2)^1$ $[e^2\text{fm}^4]$	$B(E2)^2$ $[e^2\text{fm}^4]$	A_p	A_n	$B(E2)^1$ $[e^2\text{fm}^4]$	$B(E2)^2$ $[e^2\text{fm}^4]$
^{56}Ni	$2_1^+ \to 0_1^+$	14.19	14.19	161	129	13.33	13.33	142	114
^{58}Ni	$2_1^+ \to 0_1^+$	10.11	17.97	117	109	6.13	17.49	64	69
^{60}Ni	$2_1^+ \to 0_1^+$	12.88	22.17	185	171	7.45	22.72	102	111
^{62}Ni	$2_1^+ \to 0_1^+$	15.00	23.38	234	211	7.71	22.58	104	113
^{64}Ni	$2_1^+ \to 0_1^+$	10.50	21.08	138	134	5.16	20.29	64	75
^{56}Ni	$4_1^+ \to 2_1^+$	18.58	18.58	153	123	11.59	11.59	60	48
^{58}Ni	$4_1^+ \to 2_1^+$	9.88	19.01	66	63	6.11	17.81	36	39
^{60}Ni	$4_1^+ \to 2_1^+$	15.40	24.74	140	127	5.63	14.13	27	28
^{62}Ni	$4_1^+ \to 2_1^+$	22.54	33.38	283	252	7.86	19.98	53	55
^{64}Ni	$4_1^+ \to 2_1^+$	7.44	9.87	29	25	1.28	6.04	2.7	3.3

Table 4.2 The values for bare $E2$ matrix elements A_p and A_n are presented. The values were calculated using the GXPF1A and KB3G Hamiltonians. Values are shown for the $2_1^+ \to 0_1^+$ and $4_1^+ \to 2_1^+$ transitions in the Ni isotopes. In addition, $B(E2)$ values are calculated using two sets of effective charges. Calculations with the standard effective charges $e_p = 1.5$, $e_n = 0.5$ are denoted with the superscript 1. Calculations with modified effective charges $e_p = 1.12$, $e_n = 0.67$ are denoted with the superscript 2. Table and caption are from [91].

4.7 Conclusions

The present Recoil Distance Measurement of the 4_1^+ excited state in ^{58}Ni is a model-independent measurement of the lifetime sensitive to the 10 ps region, in contrast to the previous DSAM measurement sensitive to lifetimes on the order of 1 ps or less. The resulting lifetime of 16^{+2}_{-3} ps results in a $B(E2;4_1^+ \rightarrow 2_1^+)$ value of $50^{+11}_{-6}e^2\text{fm}^4$. This value restores the smooth parabolic curve of $B(E2;4_1^+ \rightarrow 2_1^+)$ values for Nickel between the $N = 28$ shell closure and $N = 40$ subshell closure. This indicates that there is no enhancement of collectivity in ^{58}Ni.

Shell model calculations with the KB3G and GXPF1A interactions are consistent with this picture. The predicted values of $36e^2\text{fm}^4$ and $66e^2\text{fm}^4$ calculated respectively with the KB3G and GXPF1A interactions are consistent with the unenhanced collectivity indicated by the present measurement of $50^{+11}_{-6}e^2\text{fm}^4$. Therefore, contributions from ^{40}Ca core breaking or higher-lying *sdg* orbitals may not be needed to interpret the structure of ^{58}Ni within the Nickel isotopic chain.

CHAPTER 5

INVESTIGATION II: ELECTROMAGNETIC TRANSITION STRENGTHS IN ^{27}NE

Electromagnetic transition strengths are useful in studying features of nuclei far from stability. In particular, nuclear states with low orbital angular momentum close to the particle-decay threshold can exhibit extended radial wavefunctions, called halos [26]. The electric dipole operator ($E1$) is proportional to the operator $rY_1(\hat{r})$, and consequently is sensitive to the radial extension of a nucleus. As such, large $E1$ transition strengths are a known feature of halo nuclei [32]. It is also the case that the $E2$ transition strength with the operator r^2Y_2 is anticipated to be sensitive to extended nuclear radii, but this has not yet been observed.

The deformation of nuclei away from spherical shapes is also accessible through electromagnetic transition strengths. The electric quadrupole ($E2$) operator $r^2Y_2(\hat{r})$ is sensitive to the quadrupole deformation or collectivity of nuclei. Furthermore, the magnetic dipole operator ($M1$) is sensitive to the nuclear spin and thus affected by the configuration of the nuclear wavefunction. It has recently been demonstrated that the $M1$ transition strength can be used to identify the dominance of the s-wave component in a valence nucleon, which is the basis of halo formation [111]. For a nucleus with a single particle in a pure s-wave state, the M1 transition cannot occur because there is no spin-flip partner available. Therefore, a hindered M1 transition is expected, as demonstrated in ^{19}C [111]. Deformed nuclei must have contributions from angular momentum states above $l = 0$, breaking the spherical symmetry in its intrinsic wavefunction. Therefore, the $M1$ strength can also be used to probe deformation in nuclei.

The interplay of loosely bound effects and deformation is of particular interest in nuclei far from stability. ^{27}Ne has a low one-neutron separation energy and is one neutron above ^{26}Ne with a large deformation [27][112]. Therefore, ^{27}Ne is a candidate for probing a possible interplay between deformation and loosely bound effects. Furthermore, $E1$, $M1$, and $E2$ transitions among low lying states of ^{27}Ne are all accessible via experiment.

In this work, the transition strengths between bound states of ^{27}Ne have been measured. The $E1$

and $M1$ transition strengths were determined through a lifetime and branching ratio measurement of excited states in ^{27}Ne. The $E2$ transition strength was measured by Coulomb-excitation. In this chapter, the physics motivation for studying ^{27}Ne is expanded upon, and the experimental setup and results are discussed. In addition to the study of ^{27}Ne, a lifetime measurement of nearby ^{28}Ne was performed. Furthermore, a Coulomb-excitation measurement on previously studied ^{30}Mg was undertaken as a reference to validate the present setup. The measurements were all performed in March 2016 during the second GRETINA campaign at the National Superconducting Cyclotron Laboratory.

5.1 Nuclear Structure of ^{27}Ne

^{27}Ne with 10 protons and 17 neutrons has five more neutrons than the most neutron-rich stable isotope ^{22}Ne. ^{27}Ne has a one-neutron separation energy of 1430(110) keV, and therefore serves as a typical example of a loosely bound neutron rich nucleus [27][113]. Furthermore, as an even-odd nucleus, ^{27}Ne is useful for investigating neutron single-particle states at the border between the *sd* and *pf* shells.

^{27}Ne is also near the boundary of the island of inversion centered at ^{31}Mg where the shell closure at N=20 nearly disappears [17]. This causes the ground state configurations of nuclei in the region to occupy the $p_{3/2}$ and $f_{7/2}$ orbitals. This manifests as a change in the spin and parity of the ground states for odd-A nuclei, which are sensitive to single-particle structure. A related tendency for the $N = 17$ isotones is depicted in Figure 1.4. Additionally, the presence of intruder states with negative parity is an indicator of the narrowing shell gap at N=20.

Previous experiments on ^{27}Ne have uncovered many properties of its nuclear structure, including the identification of the energies, spins, and parity for bound and unbound states, as well as the neutron separation energy (S_n). The adopted values are presented in the level scheme in Figure 5.1. The 765 keV first excited state was first observed in ^{27}Ne produced through fragmentation[114]. In that experiment, the 765 keV transition was the only one observed, consistent with there being only

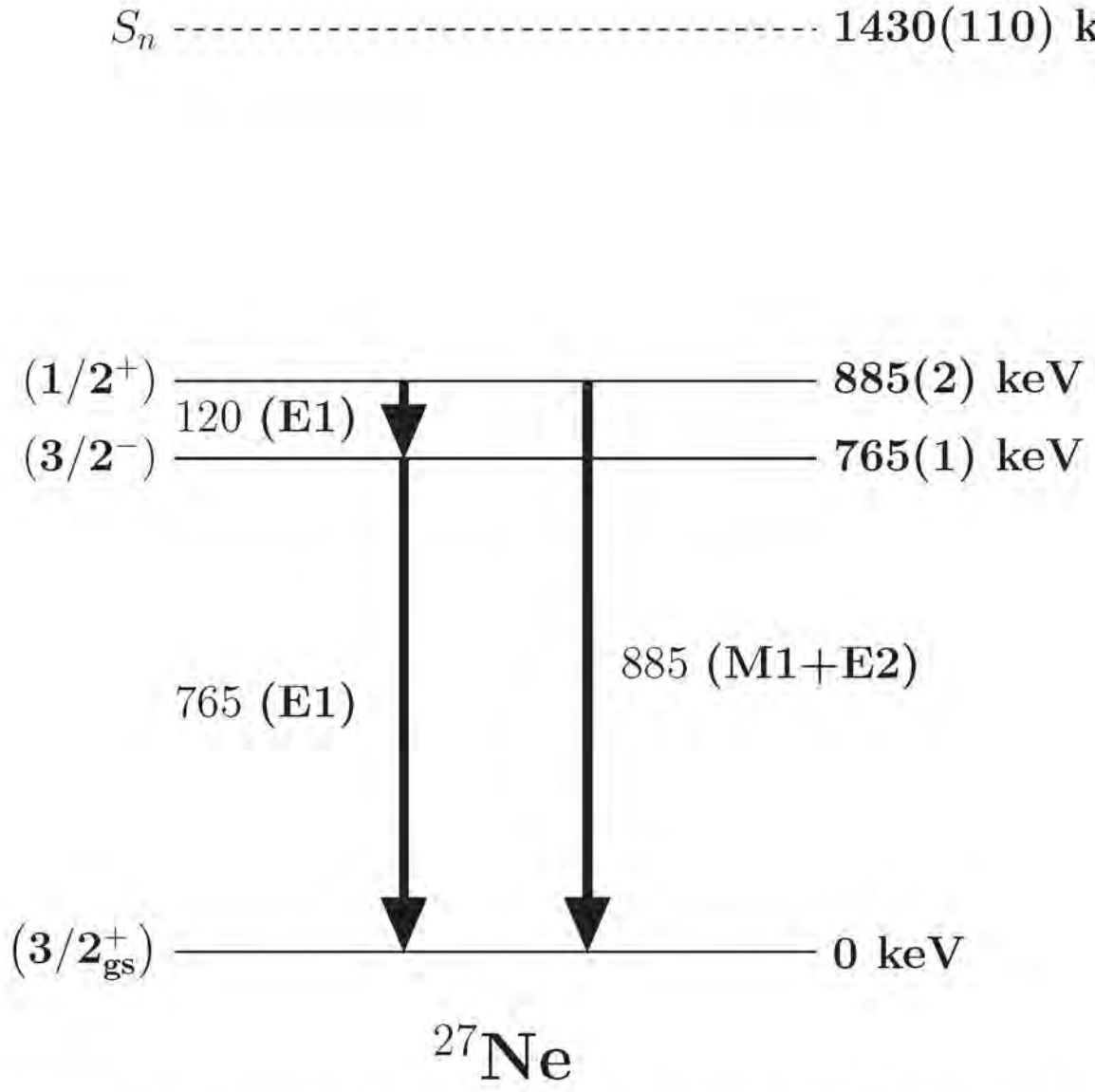

Figure 5.1 The level scheme for ^{27}Ne is presented. The adopted values for state energies and J^π are from [117]. The neutron separation energy is from [27]. γ-ray transitions are shown and are labeled with the transition energy and corresponding multipolarity.

one excited state [114]. Later work using neutron knockout reactions established that an 885 keV state was also present in ^{27}Ne, indicating the potential existence of bound intruder states [115]. In addition, a 119 keV transition was observed between the 885 keV and 765 keV transition, and the level ordering and branching ratio determined [116].

The 765 keV state and 885 keV state were studied to determine their spin and parity, as the pres-

ence of a negative parity first excited state would support the intrusion of single particle structure from the pf-shell, as opposed to the positive parity expected from excitations within the sd-shell. Evidence from a (d,p) transfer reaction on ^{26}Ne supports assigning the 765 keV state with a negative parity [118]. Shell model predictions indicate that if the 765 keV state is negative parity, the 885 keV state should have a J^π of $1/2^+$ [118]. Angular distributions of protons from another (d,p) reaction provide additional evidence that the J^π of the 765 keV state is $3/2^-$ [119]. Additionally, the existence of more than one bound excited state for ^{27}Ne could not be understood without cross-shell effects [118]. These states were compared to Monte Carlo Shell Model calculations which indicate a $3/2^+$ ground state and $3/2^-$ and $1/2^+$ excited states [116]. This evidence supports the lowering of the $N = 20$ shell gap in ^{27}Ne approaching the island of inversion.

In this work, ^{27}Ne is studied to gain insight into loosely-bound effects that may manifest in the lower lying excited states. The 885 keV state with spin $(1/2^+)$ is consistent with a large $l = 0$ contribution. Furthermore the 885 keV state is less than one MeV from the neutron separation energy. This combination of low angular momentum and small binding energy is the prerequisite for halo-formation.

^{27}Ne's excited states can be studied to measure the $E1$, $M1$ and $E2$ transition strengths between them. The 885 keV state decays via an $E1$ transition to the 765 keV state, and in another branch decays via the $M1$ and $E2$ transitions to the ground state. Additionally, the 765 keV state decays via an $E1$ transition to the ground state. The $E1$ transition directly samples over the radial extent of the wavefunction and hence increases with a larger wavefunction. A large $E1$ transition strength is a signature of halo nuclei, and therefore can be measured in ^{27}Ne to test if the 885 keV state is consistent an extended wavefunction.

Besides this, other transitions add further interest in the structure of ^{27}Ne. The $M1$ transition in ^{27}Ne can be used to investigate the dominance of the $l = 0$ contribution in the $1/2^+$ excited state. If the state is primarily $l = 0$, a hindered $M1$ strength is expected. The $E2$ transition strength in nuclei is related to the deformation of the nucleus and can provide information on systematics in the region. An enhanced $E2$ strength may also be an indicator of a radially extended wavefunction.

In this work, the lifetimes of the 885 keV and 765 keV states of ^{27}Ne were constrained using the Recoil Distance Method. The branching ratio from the 885 keV state has been measured previously, and was confirmed in this measurement [116]. The $B(E1;3/2^- \rightarrow 3/2^+_{gs})$ is directly determined by the lifetime of the 765 keV state. However, the lifetime of the 885 keV state is determined by the sum of the decay rates associated with the $B(E1;1/2^+ \rightarrow 3/2^-)$, $B(M1;1/2^+ \rightarrow 3/2^+_{gs})$ and $B(E2;1/2^+ \rightarrow 3/2^+_{gs})$ transition strengths. The $B(E1;1/2^+ \rightarrow 3/2^-)$ is determined from the lifetime of the state and the branching ratio.

The sum of the $M1$ and $E2$ transition strengths is determined by the partial lifetime of the 885 state decaying to the ground state. To separate the $E2$ and $M1$ components, the $B(E2;3/2^+_{gs} \rightarrow 1/2^+)$ was measured using a Coulomb-excitation technique. Thus the M1 transition strength can be found from the other constrained partial lifetimes as:

$$\frac{1}{\tau} = \frac{1}{\tau_{M1}} + \frac{1}{\tau_{E1}} + \frac{1}{\tau_{E2}} \tag{5.1}$$

where τ is the lifetime of the 885 keV state, $\tau_{\pi\lambda}$ is the partial lifetime from the $B(\pi\lambda)$ transition strength. The τ_{E2} is constrained directly from the Coulomb-excitation measurement. The τ_{E1} is found by taking the lifetime of the $1/2^+$ state and dividing by the branching ratio for decays to the $3/2^-$ state. The τ_{M1} is then extracted from the state lifetime and the other two partial lifetimes.

In addition to ^{27}Ne, a lifetime measurement of ^{28}Ne was performed as a reference. The $B(E2;0^+_{gs} \rightarrow 2^+_1)$ has been measured previously through heavy ion inelastic scattering [55][120], and therefore the present method serves as a confirmation with a model-independent measurement. Similarly, ^{30}Mg with a previously measured $B(E2;0^+_{gs} \rightarrow 2^+_1)$ was revisited in the Coulomb-excitation measurement to demonstrate the present Coulomb-excitation setup.

The branching ratio measurement, lifetime measurements, and Coulomb-excitation measurements are described in the next section. First the lifetime and branching ratio measurement setup will be described. The results for ^{28}Ne are shown to validate the present measurement, followed by results for ^{27}Ne. The modified Coulomb-excitation setup is then described. The results for ^{30}Mg are presented and discussed, and is followed by the Coulomb-excitation results for ^{27}Ne. A

discussion of the implications of the measurements in ^{27}Ne is presented last.

5.2 Experimental Setup I: Branching Ratio and Lifetime Measurement

The branching ratio and lifetime of ^{27}Ne were measured at the National Superconducting Cyclotron Laboratory. A γ-ray measurement with only a target was used to constrain the branching ratio. The Recoil Distance Method was employed to measure the lifetimes.

The experiment was performed using the S800 Spectrograph in coincidence with the GRETINA array. A ^{48}Ca primary beam was developed at the coupled-cyclotron facility at 140 MeV per nucleon. This beam was impinged on a ^{9}Be target to make a secondary beam of ^{29}Na which was separated in the A1900. The ^{29}Na secondary beam delivered to the S3 vault had an energy of 90.5 MeV per nucleon with a purity of 48%. Reactions on the target were used to produce fragments of interest, including ^{27}Ne and ^{28}Ne, which were identified in the S800.

The γ rays in this experiment were measured using the GRETINA array [79], using nine detector modules. In this experiment, four detectors were located at forward angles between 20° and 50° while five were placed at angles between 70° and 90°. The forward detectors were used in the lifetime measurement while all detectors were used in the branching ratio and 25-mm separation measurements.

The TRIPLEX Plunger was used to place target and degrader foils into the beamline. The TRIPLEX was placed upstream of GRETINA's center by 13 cm to maximize the geometric efficiency of γ rays emitted at small angles from the beam axis. In the branching ratio measurement only a target foil was used. In the lifetime measurement both a target and degrader foil were used. The target was a 1.0-mm ^{9}Be foil and the degrader was a 0.92 mm-Ta foil. For the lifetime measurement, the target and degrader were positioned near contact to measure the lifetime expected to be near 1 ps. This setting resulted in a separation distance of 50 μm. The experiment was run for three days in this setting.

The excited states in ^{27}Ne and ^{28}Ne can be populated by reactions in the degrader, which must

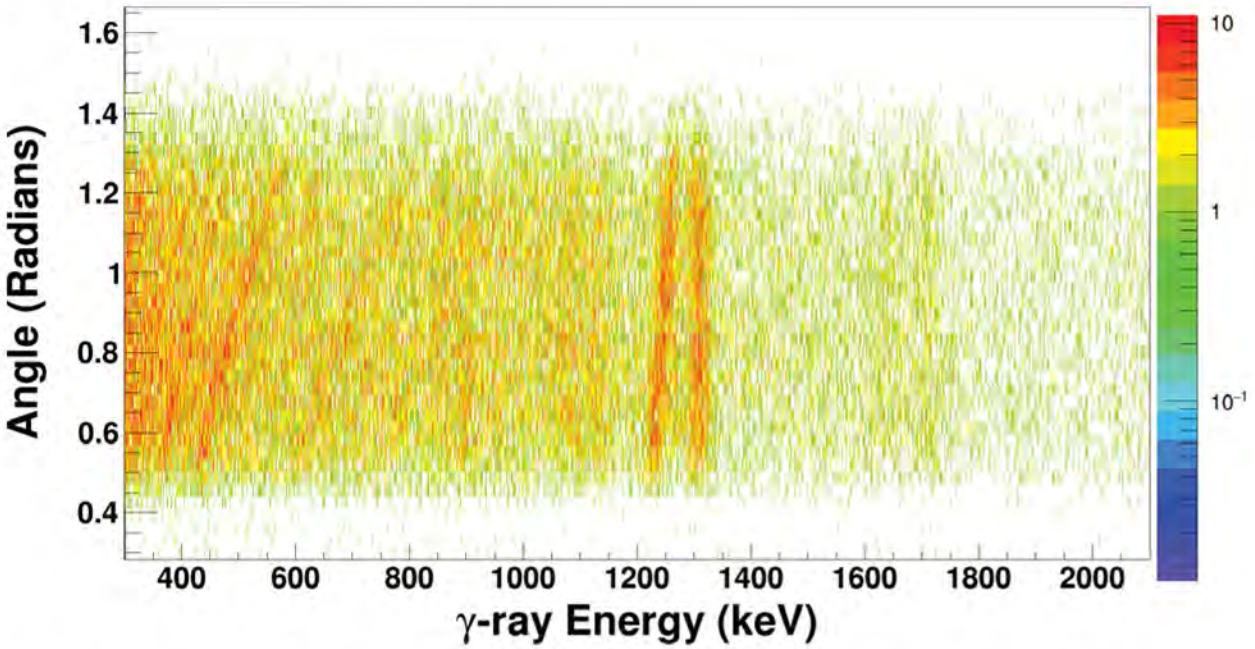

Figure 5.2 A histogram of γ-ray interactions with GRETINA is presented. The Doppler-corrected γ-ray energy is plotted on the x-axis, while the angle from the target to the interaction position is plotted on the y-axis. The two nearly parallel lines near 1305 and 1240 keV are from reactions populating of ^{28}Ne at the target and degrader respectively.

be accounted for in the lifetime measurement. Therefore, a second measurement with a distance between the target and degrader of 25 mm was performed for one day to constrain the population due to reactions in the degrader. The travel time for a nucleus across 25 mm is approximately 250 ps. Since the states of interest have lifetimes expected to be shorter than 10 ps, decays that occur after the degrader must have been populated in the degrader.

In addition, the 25-mm separation measurement results in two distinct peaks for decays occurring before and after the degrader at all angles. Therefore, the entirety of GRETINA can be used to make the measurement. A two-dimensional spectrum showing the separation over all angles is shown in Figure 5.2 for the case of ^{28}Ne. It can be seen that there are two vertical lines corresponding to decays before and after the degrader.

The reaction residues were identified with the S800 Spectrograph. The S800 Spectrograph was used in coincidence with GRETINA to tag γ rays.

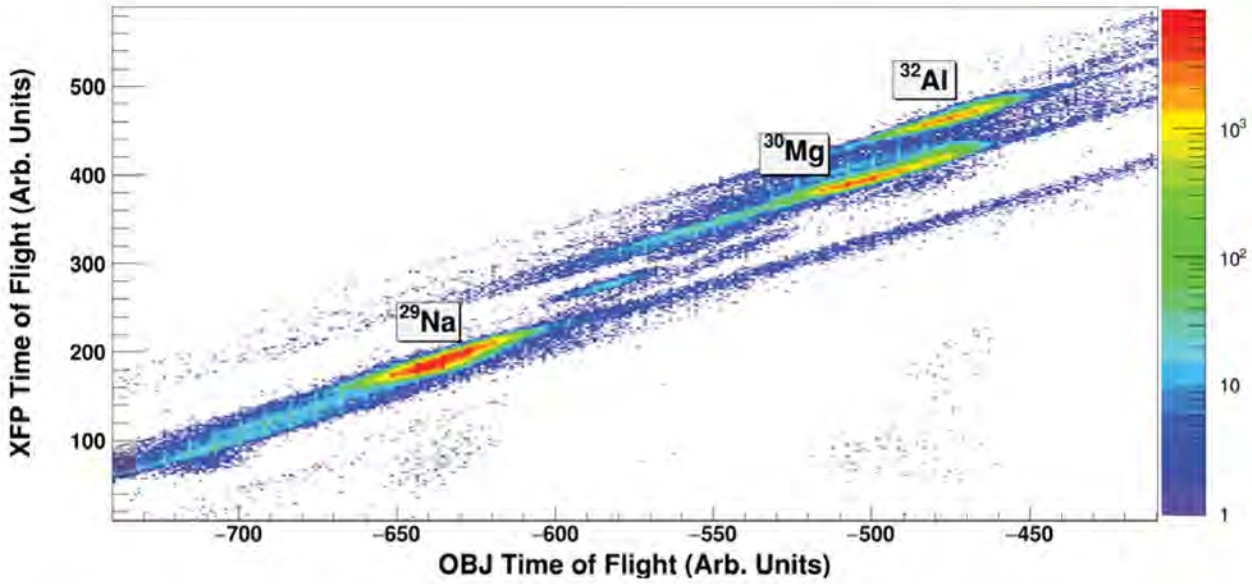

Figure 5.3 A timing signal correlation plot for the incoming ^{29}Na secondary beam is shown. The data is from the target-only measurement. The incoming ^{29}Na beam and contaminants are labeled.

5.2.1 Particle Identification

The secondary beam Particle Identification plot is shown in 5.3. The incoming beam of ^{29}Na was identified using a timing correlation plot between the signals of the S800 OBJ scintillator and the A1900 XFP scintillator.

The residues of interest were found by gating on the incoming spectrum on the ^{29}Na and then looking at the energy deposited in the S800 ion chamber against the corrected time-of-flight for the S800 Object scintillator. This is shown in Figure 5.4 for the target only data, where the ^{29}Na incoming beam and fragmentation products are identified.

5.2.2 Laboratory Frame Background

A number of laboratory frame backgrounds can be observed in the present experiment. As the laboratory frame background can overlap with the peaks of interest, the background was measured for each setting and simulated to determine their Doppler-reconstructed energies. These reconstructed energies were then added to the fit in order to account for these effects. A table of the

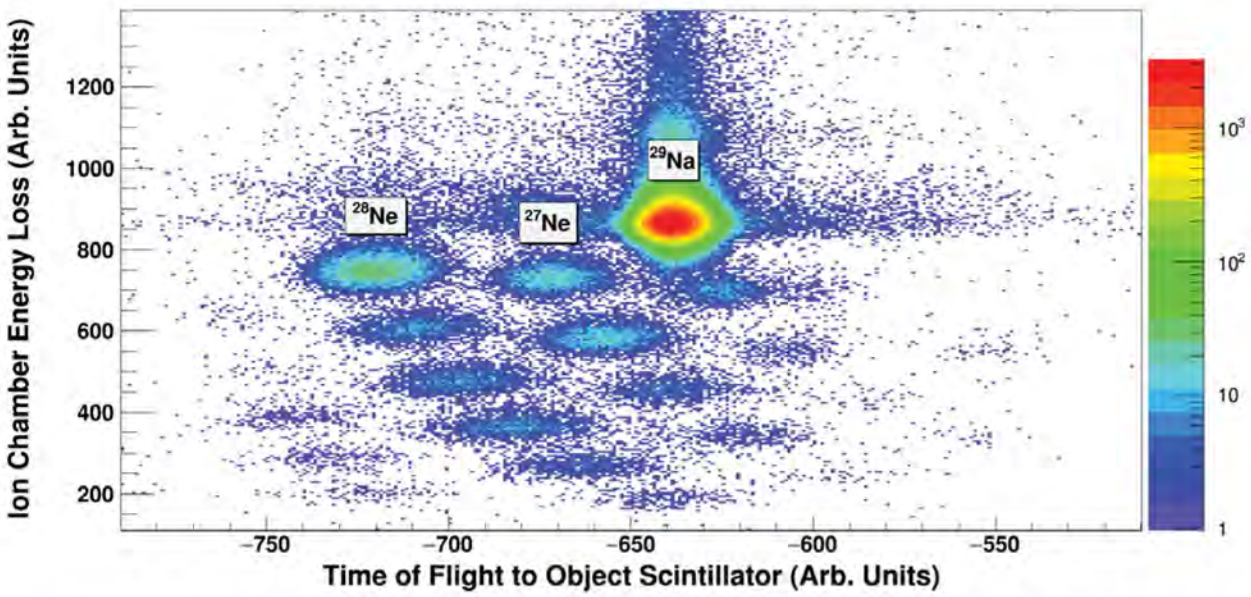

Figure 5.4 The particle identification for reaction products at the S800 is shown. The incoming ^{29}Na beam and the ^{28,27}Ne isotopes generated by the reaction are labeled. Data shown is for the target-only measurement and is gated on the incoming ^{29}Na beam.

γ-ray Energy (keV)	Source	^{27}Ne 25-mm	^{27}Ne 0.05-mm	^{28}Ne 25-mm	^{28}Ne 0.05-mm
511	e^-, e^+	190	260	410	240
596	^{74}Ge (n,n')	470	500	630	310
832	^{72}Ge (n,n')	220	280	180	70
842	^{27}Al (n,n')	180	230	260	140
1014	^{27}Al (n,n')	120	160	170	70
1039	^{70}Ge (n,n')	120	100	150	10

Table 5.1 The number of counts in the peak for each neutron induced background is provided. For each case this is for the cut with a 7.5-cm spherical addback and with the timing cut applied. For the 0.05-mm separation data, the counts are provided for interactions at angles below 40° from the degrader.

background peaks measured for each of the settings is provided in Table 5.1. For the target-only data, the background is minimal and not included.

5.3 ^{28}Ne Measurement

The $B(E2;0^+_{gs} \rightarrow 2^+_1)$ of ^{28}Ne has been measured before through heavy ion inelastic scattering measurements [55][120]. In the measurement reported in [120] the $B(E2;0^+_{gs} \rightarrow 2^+_1)$ was found

to be 269 (136) e^2fm^4. In [55], a more precise value for the $B(E2;0^+_{gs} \rightarrow 2^+_1)$ of 132(23) e^2fm^4 was determined. The lifetime corresponding to the transition strength is 8.2(14) ps. The present measurement of ^{28}Ne serves as a model-independent confirmation of the inelastic scattering measurements. This measurement also demonstrates the sensitivity of the Recoil Distance Method in the current configuration to lifetimes on the order of 1 to 10 ps.

The level scheme for ^{28}Ne is shown in Figure 5.5. The known states include the 2^+ state at 1304 keV, the 4^+ state at 3010 keV, and another 4^+ state at 3904 keV. The 3010 keV state decays via a 1706(5) keV γ ray and the 3904 through a 894(4) keV γ ray [121]. An 1127(4) keV transition has also been previously observed, though it is not known what level it decays from.

5.3.1 Target Only Measurement

The ^{28}Ne γ-ray spectrum from reactions on only the 1.0 mm Be target is shown in Figure 5.6. As there is no low energy γ ray of interest, the 7.5 cm spherical addback is used. Each of the 894, 1127, 1304, and 1710 keV energy γ rays are observed and labeled in the figure.

The population of states was determined by comparison to the GEANT4 based simulation [87]. The cascade of states was simulated, and a direct population to each state determined by varying the relative populations until a best fit was found. This resulted in a population of 14% for the 1127 keV transition state, 57% for the 1304 keV state, 13% for the 3010 keV state and 16% for the 3904 keV state, where the statistical error is 3%.

5.3.2 25-mm Separation

The ^{28}Ne spectrum for the 25-mm separation between the 1.0 mm ^{9}Be target and 0.92 mm Ta degrader is shown in Figure 5.7. Two peak structures for the 894 keV, 1127 keV, 1307 keV and 1710 keV can be observed. GEANT4 simulations incorporating the setup were performed over a range of target-to-degrader ratios, and fit to the data using a scaling factor, an exponential background and the neutron-induced background [46]. As no angle cut is applied, the Doppler-shifted

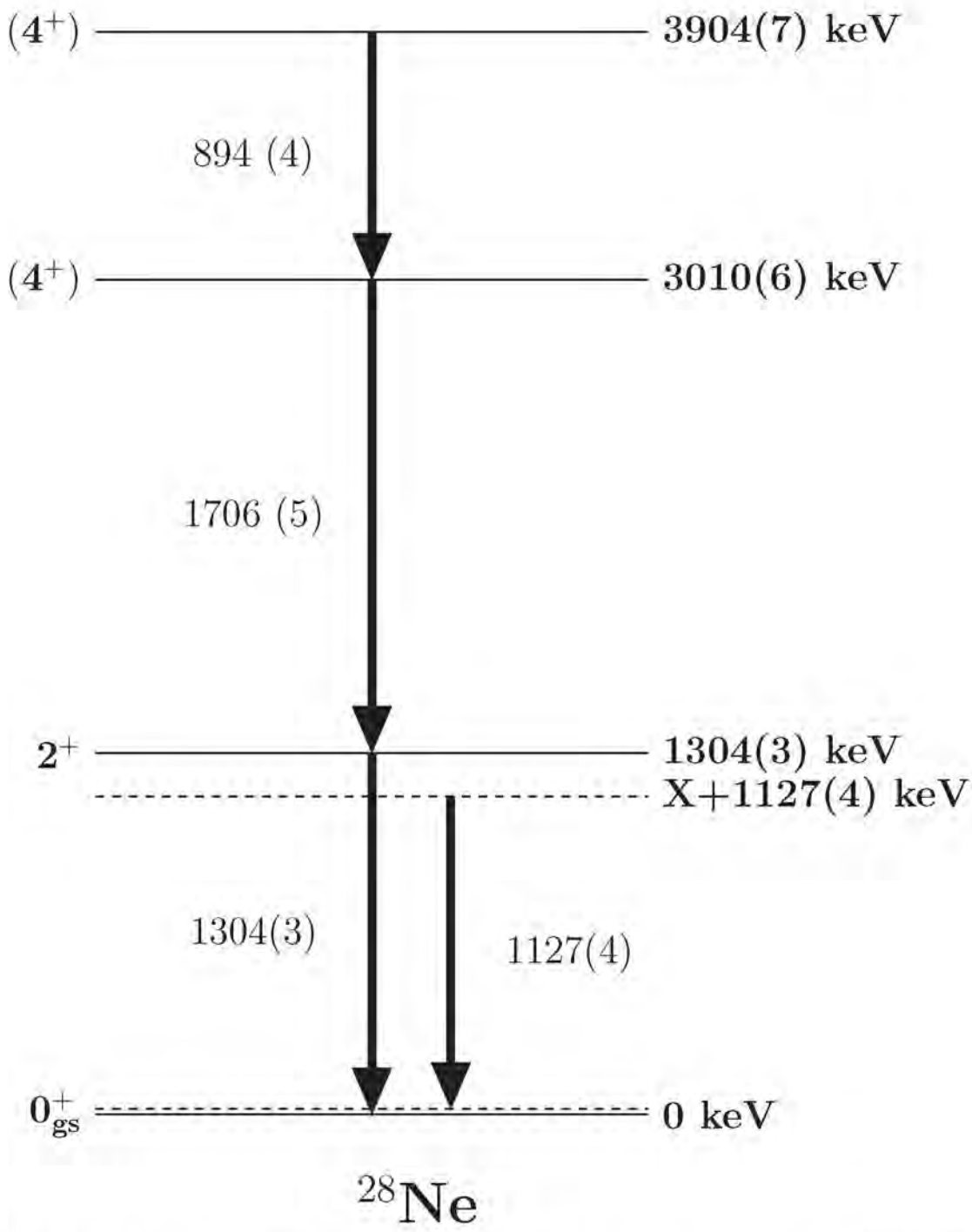

Figure 5.5 The level scheme for ^{28}Ne is shown for known level states and transitions. The 1127 keV transition is a decay between unknown states represented by the dashed lines. The J^{π} assignments and values for state and transition energies are from [121].

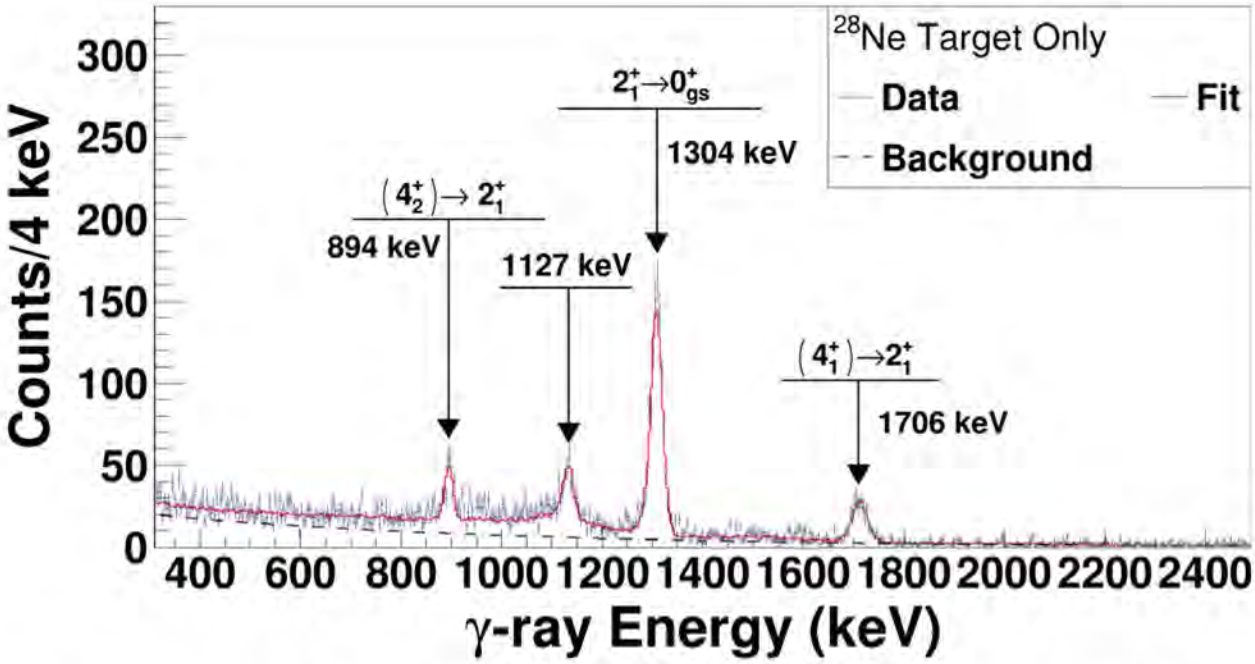

Figure 5.6 The Doppler-corrected γ-ray spectrum for ^{28}Ne with only a 1-mm Be target is presented. The observed transitions are labeled, including the 1127 keV transition decaying from an unknown state. The best fit simulation for the relative population of states is presented in comparison, along with an exponential background.

laboratory frame background is continuous.

The best fit simulation for a target-to-degrader ratio of 2.1 is shown, where the same ratio was used for all transitions. The error in the target-to-degrader ratio is ± 0.1 which is statistical only.

5.3.3 Lifetime Measurement

The γ-ray spectrum for ^{28}Ne with a 50-μm separation between the target and degrader and for GRETINA angles below 40° is shown in Figure 5.8. As in the target only data, the 894 keV, 1127 keV, 1304 keV and 1706 keV transitions are visible. However, the measurement of the lifetime of the excited states of ^{28}Ne in this experiment poses a number of complications that needed to be accounted for, in particular the presence of feeding states and the S800 acceptance.

The presence of feeding states above a state of interest decaying into the state of interest can affect the apparent lifetime. Figure 5.9 shows a comparison of the lifetimes for the 894 keV, 1127

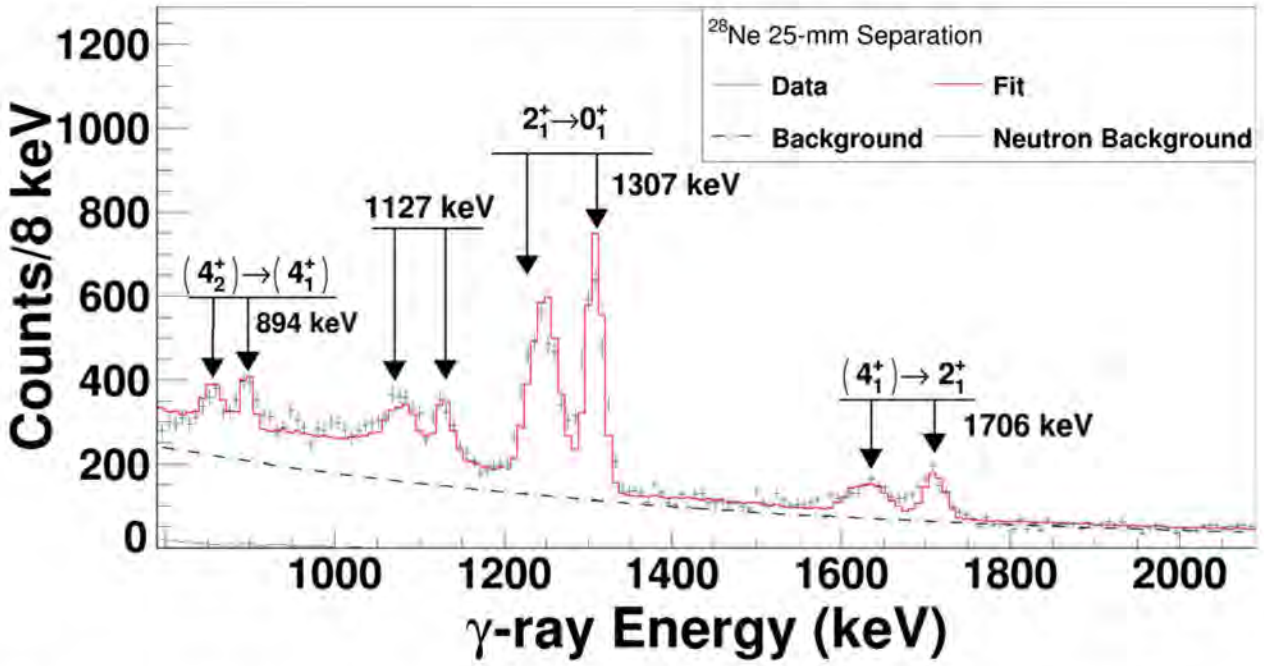

Figure 5.7 The spectrum for the 25-mm separation between target and degrader gated on ^{28}Ne particles is presented. States of interest are labeled and transition energies identified. Two peak structures are apparent for all transitions, and a best fit simulation presented. The best fit simulation is for a ratio of 2.1 reactions on the target for each reaction on the degrader for all states.

keV, and 1706 keV transitions. The feeding lifetimes are listed in Table 5.2, where the error is from statistics only.

As shown in Figure 5.5, the observed 1706 keV transition from the 3010 keV state decays into the 1304 keV state, while the 894 keV transition decays into the 3010 keV state. This means that the lifetimes of these states can change the apparent lifetime of the 1304 keV state through their feeding, and must be taken into account. This was accomplished by incorporating the feeding states into the GEANT4 simulation used to analyze the data, and determining the lifetime for each state according to where it fit in the decay scheme. The simulations are varied over the lifetime of the state and incorporate an exponential background and a scaling parameter as free parameters. The 894 keV transition corresponds to the highest state measured in the cascade and consequently its lifetime was constrained first. Then the lifetime of the 1706 keV transition was measured using the feeding lifetime for the 894 keV transition found previously. As the 1127 keV transition is

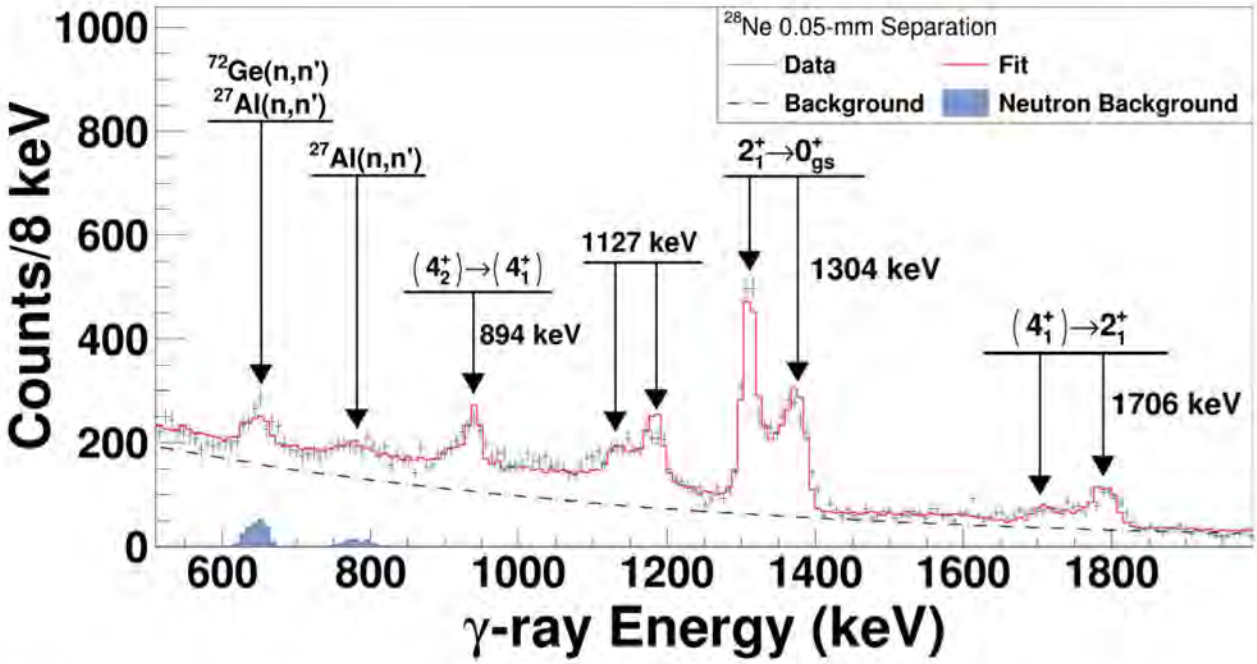

Figure 5.8 The γ-ray spectrum for ^{28}Ne is presented for GRETINA angles below 40° for a 50 μm separation between the target and degrader. The observed transitions are labeled along with the neutron-induced background. A best fit simulation using the best fit lifetimes is overlayed, along with an exponential background. The lifetimes used for the 1304 keV state was 6.25 ps. The lifetimes for higher-lying states are the best fit values in Table 5.2 as discussed in the text.

Transition	Energy (keV)	Lifetime (ps)	Error (ps)
$(4_1^+) \rightarrow 2_1^+$	1711	2.5	0.25
$(4_2^+) \rightarrow (4_1^+)$	894	0	0.5
Unknown	1127	1.5	0.25

Table 5.2 The measured lifetimes for transitions among states lying higher than the 2_1^+ state in ^{28}Ne are presented. Error presented is statistical only.

independent of the other levels, it was measured independently of the cascade. Finally, the full spectrum was fit with the fixed feeding lifetimes and the lifetime of the 1304 keV state was varied.

In order to account for the feeding to the 2_1^+ state, it is assumed that all feeding proceeds via the (4_1^+) and is accounted for by the measured lifetime of 2.5 ± 0.25 ps, where the error is statistical only. It is worth noting that the 2.5 ps lifetime is consistent with the expectation for this 4_1^+ state if the $B(E2)$ is constant for the $4_1^+ \rightarrow 2_1^+$ and $2_1^+ \rightarrow 0_{gs}^+$ transitions. The lifetime of the 4_1^+ state will then be different from the 2_1^+ state by a factor of $\left(\frac{1304}{1706}\right)^5 \approx 0.26$. As the lifetime extracted from

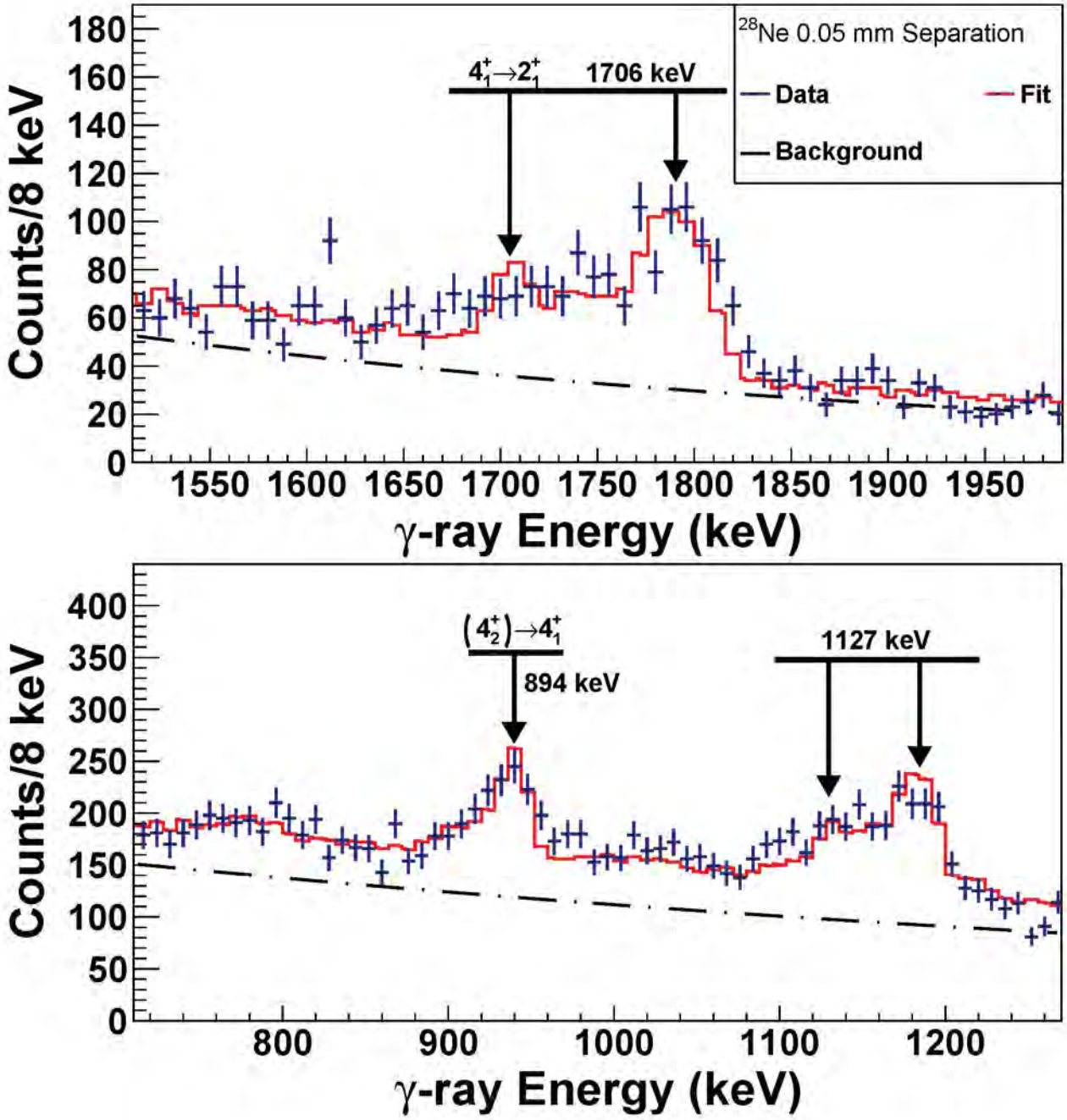

Figure 5.9 ^{28}Ne spectra for the 0.05 mm separation between target and degrader are shown zoomed in to focus on the (Top) 1706 keV and (Bottom) 894 keV and 1127 keV transitions. The data are compared to best fit simulations for each state, which for the 894 keV transition is 0 ps, for the 1127 keV transition is 1.5 ps, and for the 1711 keV transition is 2.5 ps.

the previous inelastic scattering measurement is 8.2 ps, the expected lifetime of the 4_1^+ state would be approximately 2 ps.

To determine the lifetime of the 1304 keV state, the cascade was simulated with the lifetimes extracted above. The 1304 keV state lifetime was then varied in the GEANT4 simulations, which were compared incorporating an exponential background, background from neutron induced γ rays, and a scaling factor. The best fit lifetime was found to be 6.25 ± 0.25 ps. Figure 5.8 shows the best fit simulation compared to the data over all of the measured transitions. The systematic error in the 2_1^+ lifetime came from three sources, namely the uncertainty in the target to degrader population ratio, ambiguity in the feeding lifetime, and effects arising from the momentum distribution.

The systematic error from the uncertainty in the target-to-degrader population ratio was constrained by comparing simulations with the ratio modified to the upper and lower statistical bounds of 2.2 and 2.0 respectively. The lifetime of the 2_1^+ state was varied as above, while feeding lifetimes were kept constant. This resulted in a lower bound of 6 ps and an upper bound of 7 ps. The systematic error arising from uncertainty in the feeding lifetime of the $\left(4_1^+\right)$ state was accounted for by changing the lifetime of the feeding state to the lower and upper limits of 2.25 ps and 2.75 ps in the simulated cascade and again fitting the lifetime of the 1304 keV transition. This error was found to be negligible compared to statistics.

The last source of systematic error in this measurement is due to uncertainty in the energy distribution of the ^{28}Ne reaction products. As the S800 Spectrograph was not optimized to accept ^{28}Ne, only the lower tail of the energy distribution was actually accepted by the spectrograph. The cutoff on the energy distribution corresponds to a cut on the reaction position in the target, because reactions that occur further in the target will have greater energy loss than those occurring earlier due to the higher Z of the ^{29}Na secondary beam compared to the ^{28}Ne reaction product. As the target width of 1.0 mm dominates the region where emissions corresponding to the fast peak in the spectrum occur, this can affect the lifetime. The energy distribution gated on coincidences with GRETINA for ^{28}Ne is shown in Figure 5.10. The lifetime analysis was performed independently

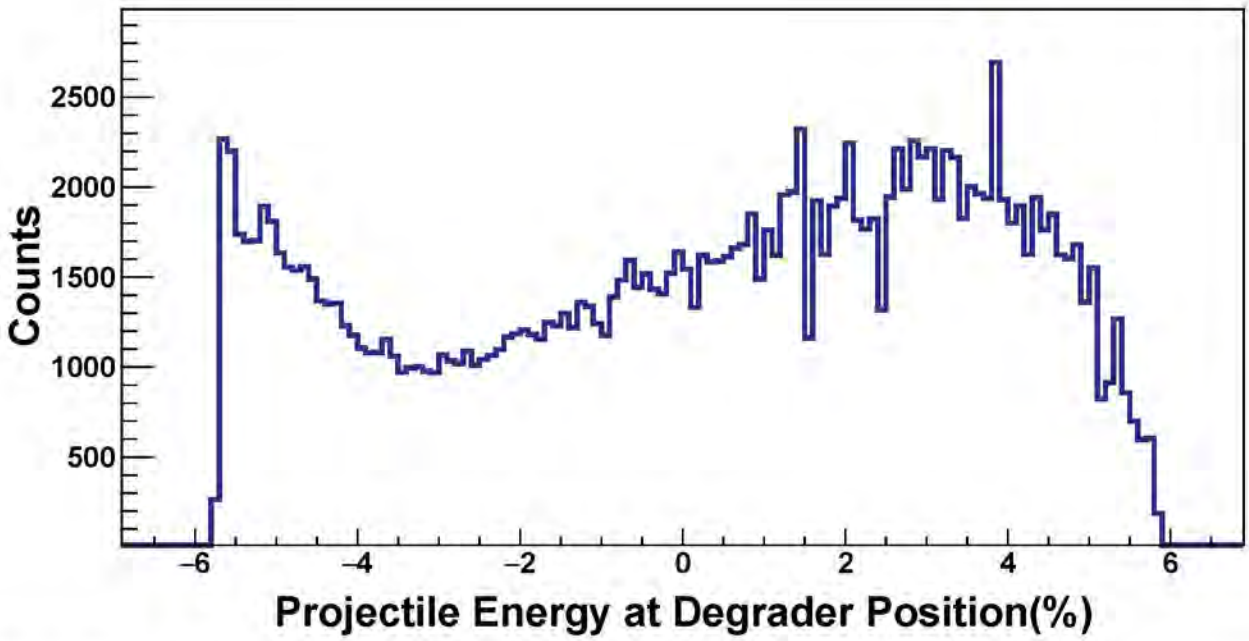

Figure 5.10 The energy distribution for ^{28}Ne reconstructed for after the degrader is presented. The x-axis shows the energy in terms of percentage above or below the $B\rho$ central value, which in this case was 3.02 T-m, which corresponded to an energy of 54.5 MeV per nucleon. The ^{28}Ne makes up the shoulder on the high energy side of the spectrum, while the shoulder on the low energy edge is a secondary beam contaminant in the particle identification. Therefore, only the lower energy tail of the ^{28}Ne distribution is accepted by the S800, and so uncertainty in the lifetime due to uncertainty in the distribution must be constrained.

on the energies above and below the midpoint of the distribution, which was found at 1.0% above the rigidity setting, to evaluate the systemic uncertainty due to the energy distribution. This was done for the 25-mm and 0.05-mm data to determine the target-to-degrader excitation ratios and the lifetimes independently. The ratio for the lower half of the energy distribution was found to be 2.4, while the ratio for the upper half was found to be 0.9. The corresponding lifetime for the upper half of the energy distribution was 6.5 ps, while the lower half of the energy distribution corresponded to 5 ps.

Therefore, the lifetime of the 2_1^+ state was found to be 6.25 ps $\pm$0.25 ps (stat) $^{+0.75}_{-0.25}$ ps (Ratio) $^{+0.25}_{-1.25}$ ps (Energy Distribution), or combining the systematic errors in quadrature, 6.25 ps $\pm$0.25 ps (stat) $^{+0.8}_{-1.3}$ ps (systemic). This corresponds to a $B(E2;0^+_{gs} \rightarrow 2^+_1)$ of $175^{+45}_{-20} e^2\text{fm}^4$. This measurement is consistent with the Coulomb-excitation measurement of 269 (136) $e^2\text{fm}^4$ measured

in [120]. The current result is larger than the previously measured value of 132 (23) e^2fm^4 from heavy ion inelastic scattering in [55], although the two measurements marginally overlap within error.

Indeed, in the previous inelastic scattering experiment, $B(E2)$ values were extracted using ECIS with two optical potentials, determined respectively from ^{20}Ne+^{208}Pb and ^{40}Ar+^{208}Pb interactions [55]. The ^{20}Ne+^{208}Pb optical potential with equal nuclear and Coulomb deformation parameters resulted in a $B(E2)$ of 116 (12) e^2fm^4, while the ^{40}Ar+^{208}Pb optical potential with equal nuclear and Coulomb deformation parameters resulted in a $B(E2)$ of 145 (22) e^2fm^4. The present result indicates that the ^{40}Ar+^{208}Pb optical potential may more accurately model reactions in ^{28}Ne.

5.4 ^{27}Ne Measurement

The lifetimes of the $1/2^+$ and $3/2^-$ states in ^{27}Ne were constrained with the Recoil Distance Method. The target only measurement was used to determine the direct population of states for the measurement. In addition, the target only measurement was used to determine the branching ratio of the $1/2^+$ state which decays by either a 119 keV or an 885 keV γ ray. The branching ratio allows for the extraction of partial lifetimes and is needed in the Coulomb-excitation data where only the yield of the 885 keV γ-ray is measured. In the Recoil Distance Method measurement, the 25-mm separation was used to constrain the population of ^{27}Ne due to reactions in the degrader. The near contact 50-μm separation was used to determine the lifetimes of the excited states.

5.4.1 Target Only Measurement

The branching ratio for ^{27}Ne has previously been measured as $19.3\% \pm 2.5\%$ for the 119 keV transition, and $81.7\% \pm 2.5\%$ for the 885 keV transition [116]. To confirm this measurement, the γ-ray transitions for the reaction on the target with no degrader were measured. As there is only one velocity region in this measurement, the γ rays are measured using all nine GRETINA detectors.

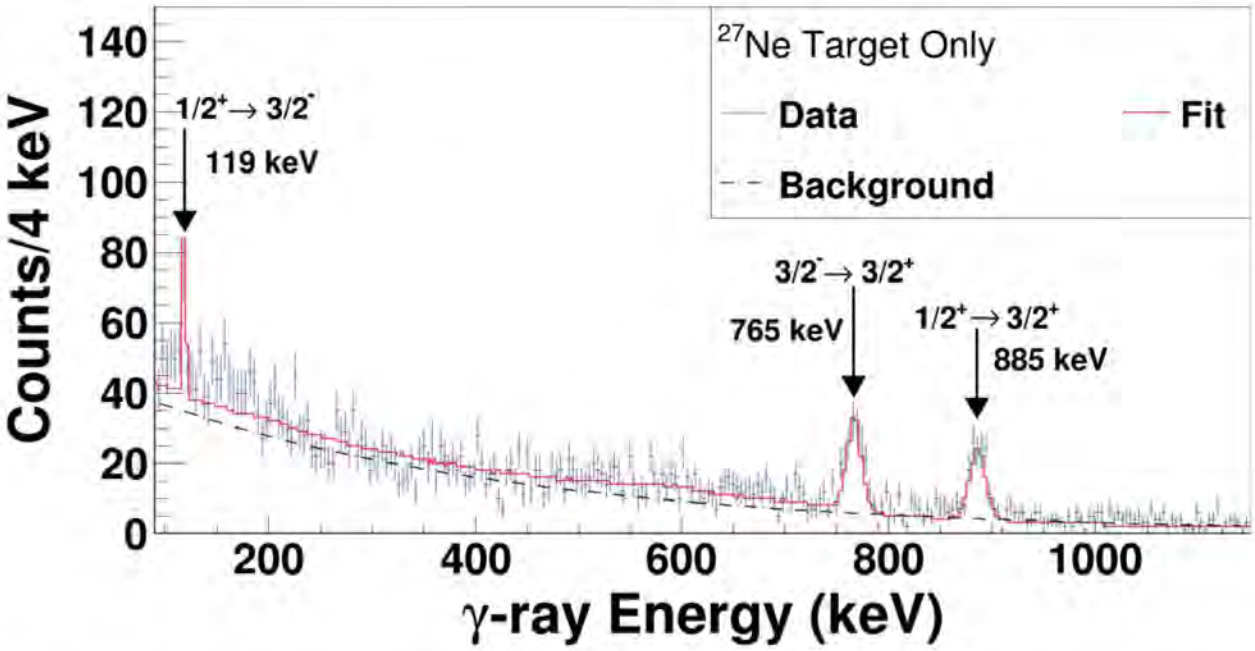

Figure 5.11 The Doppler-corrected spectrum for ^{27}Ne with only a 1 mm thick Be target is shown. The transitions observed are labeled. The data is compared with a best fit simulation to reproduce the branching ratio of the 885 keV state.

As the energy of the 119 keV transition is small and more likely to be dominated by the photopeak, the branching ratio was measured using only the singles data from the GRETINA crystals.

The γ-ray spectrum for the target only data for ^{27}Ne is shown in 5.11. The 119 keV and 885 keV transitions from the $1/2^+$ state are identified along with the 765 keV transition from the $3/2^-$ state.

The branching ratio of the 885 keV state was determined by comparison to a GEANT4 based simulation that incorporates the response function of GRETINA to the Doppler-shifted energies of the emitted γ rays. For simplicity, the γ rays were considered as coming from three states without a cascade and the relative population used to determine the branching ratio. First the 885 keV and 765 keV γ-rays were considered, finding a yield ratio of 52% for the 885 keV transition and 48% for the 765 keV transition. Then this ratio was fixed and the 119 keV transition was considered separately, with the relative yield of the 119 keV state varied. The best fit was found to be for a yield of $17\% \pm 2\%$ for the 119 keV transition, and $83\% \pm 2\%$ for the 885 keV transition, where

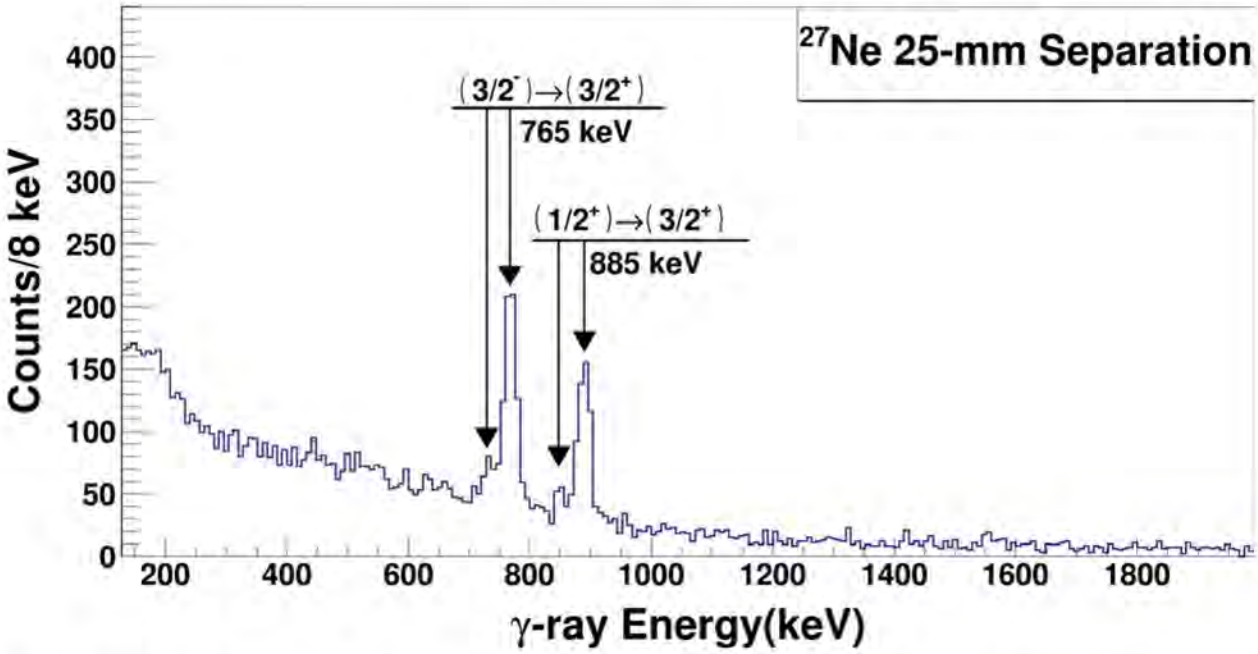

Figure 5.12 The γ-ray spectrum for ^{27}Ne with a 25 mm separation between the target and degrader is presented. Spherical addback with a 7.5-cm radius was employed. Only events in which a single added-back event was measured are included. The observed transitions are identified and labeled.

the error is statistical only. This is consistent with the previous measurement, and is used for the extraction of the partial lifetimes and Coulomb excitation data [116].

5.4.2 25-mm Separation

As in ^{28}Ne, the population ratio due to reactions in the target compared to reactions in the degrader was constrained. This was done by measuring the γ rays with a 25-mm separation between the target and degrader.

The 25-mm spectrum for ^{27}Ne is presented in Figure 5.12, and the observed transitions identified. In this data the 7.5-cm spherical addback was employed. In addition, only events that had a single addback sphere were included, which reduced the background at the 885 and 765 keV reconstructed energies.

The population due to reactions in the degrader was independently measured for the 765 keV and 885 keV states. The spectra focused on the 885 and 765 keV states compared to best fit

simulations for the ratio of population due to reactions in the target to reactions in the degrader are presented in Figure 5.13. It was found there is a significantly larger yield in the 25-mm data for the population of the 765 keV state in the degrader compared to the 885 keV. To individually constrain the population of the 765 and 885 keV states in the degrader, GEANT4 simulations incorporating the current setup were generated varying the ratio. An exponential background was found by fitting it over the spectrum from 500 to 2000 keV. This background was then fixed and the simulations were fit in a limited region for each of the 765 and 885 keV states. The best fit value for the target to degrader population ratio for 885 keV state was 5.2 $\pm$0.6. The best fit value for the 765 keV state was $3.9^{+6.1}_{-0.9}$. The apparent ratio of population in the target to population in the degrader is even larger than the simulated values because the S800 Spectrograph was focused on the fragments produced in the target.

5.4.3 Lifetime Measurement

The γ-ray spectrum for the 0.05-mm separation is presented in Figure 5.14. As before, a cut on the GRETINA angle below 40° is applied. Spherical addback is applied with a 7.5-cm radius. Only events with a single added-back event measured are included to reduce background. The 765 keV and 885 keV levels are identified and labeled, as are the Doppler-shifted laboratory frame backgrounds. In addition neutron induced backgrounds at 1014 and 1040 keV in the Doppler-corrected spectrum overlap with the 765-keV transition energy. However, the overall yield from these background contributions is only 35 counts total, which was found to have a marginal effect on the result as shown in the shaded histogram in Figure 5.14. The 765 keV peak has a significantly larger low-energy tail compared to the 885 keV peak, which indicates that the $3/2^-$ state has a long lifetime compared to the $1/2^+$ state.

The ^{27}Ne spectrum was compared to GEANT4 simulations independently for each of the 765 and 885 keV transitions. Figure 5.15 shows the data along with the best fit simulations and comparisons to a 6 ps and 0 ps lifetime to demonstrate sensitivity. The best fit target-to-degrader population ratios measured previously for the 765 and 885 keV states were used for the corre-

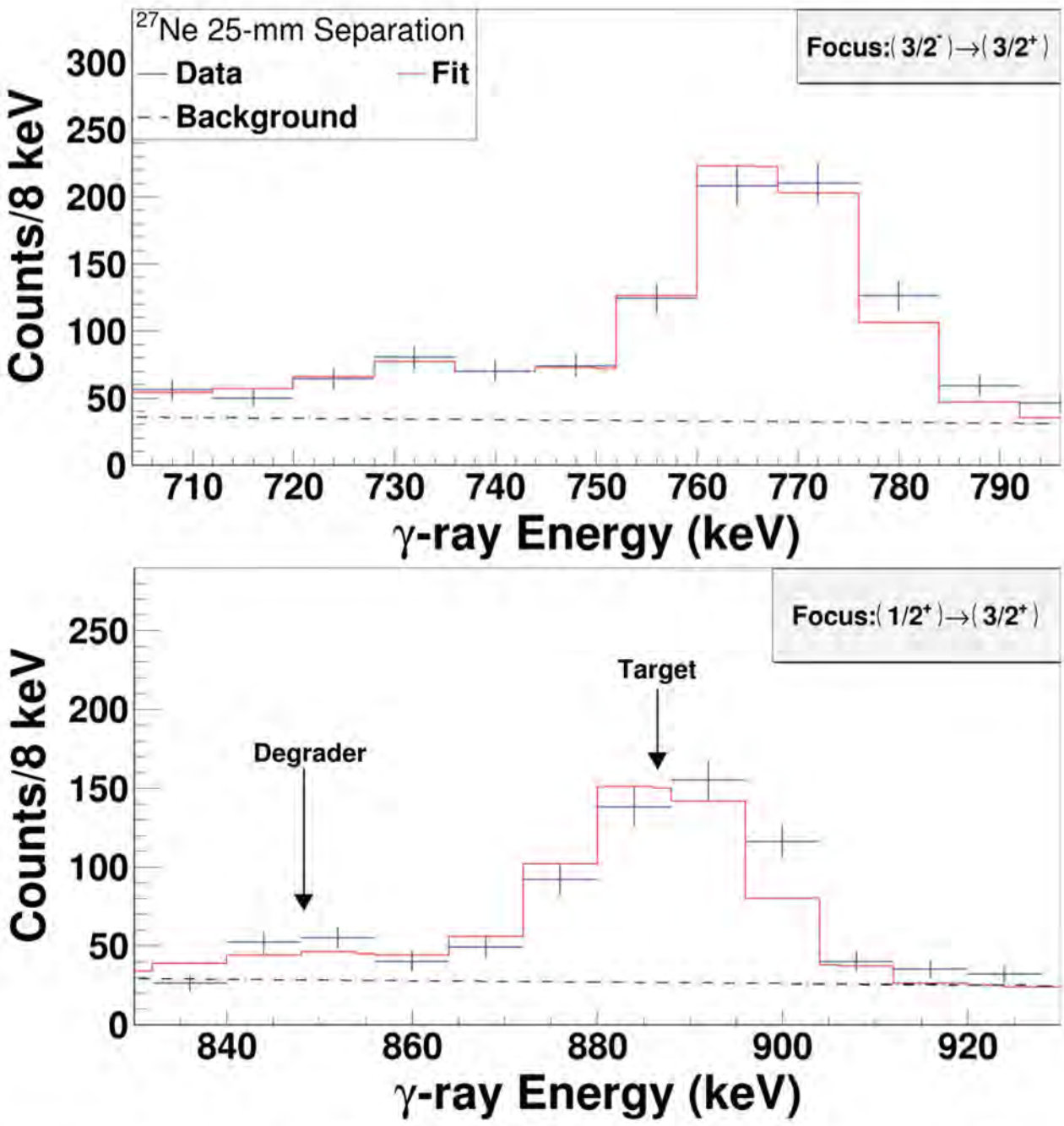

Figure 5.13 γ-ray spectra for ^{27}Ne with a 25-mm separation are presented focused on the 765 keV state (top) and 885 keV state (bottom). Spherical addback with a 7.5-cm radius was employed. Only events with a single added-back event measured in coincidence with the ion are included. Best fit spectra for each of the target-to-degrader excitation ratios are shown along with the fixed exponential background. The ratio for the 765 keV state is 3.9 reactions in the target per reaction in the degrader. The ratio for the 885 keV state is 5.2 reactions in the target per reaction in the degrader.

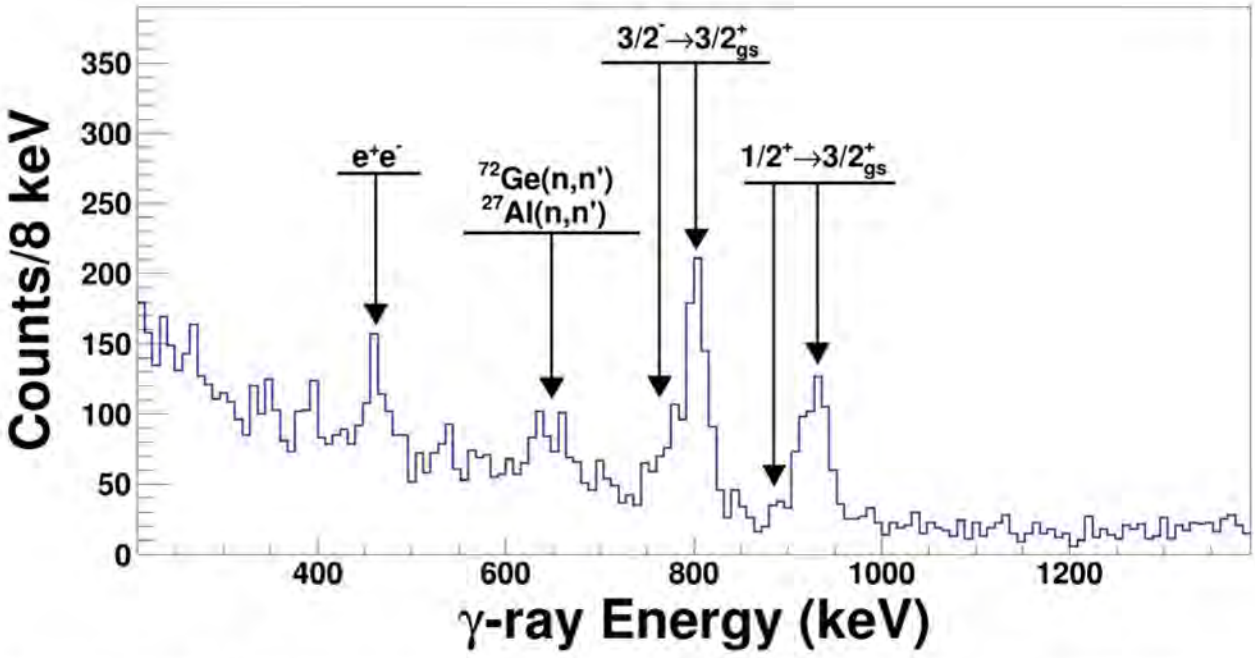

Figure 5.14 The ^{27}Ne γ-ray spectrum for a 0.05-mm separation between the target and degrader is presented for angles below 40°. Spherical addback with a 7.5 cm radius was employed. Only events with a single added-back event measured in coincidence with the ion are included. Peaks from transitions and neutron-induced backgrounds are identified.

sponding lifetime measurement. The χ^2 distributions are presented for each in insets at the top left of each spectrum.

The lifetime of the 885 keV state was determined to have an upper limit of 2.0 ps from the χ^2 distribution in Figure 5.15, where statistical error is included in the determination of the upper bound. Ambiguity in the lifetime due to the ratio of population from reactions in the degrader was found by simulating the spectra using the upper bound of 5.8 and varying the lifetime. This was found to have a negligible effect on the upper bound of 2.0 ps.

The lifetime of the 765 keV state was constrained to be 3.1 ± 0.5 ps, where the error is purely statistical. Systematic error in the measurement came from ambiguity in the ratio of population from reactions on the degrader. The uncertainty was determined by comparison to simulated spectra with an upper bound of 10 and lower bound of 3. The lifetime was varied and the ambiguity was found to be $^{+0.6}_{-0.8}$ ps. The lifetime of the 885 keV state which feeds into the 765 keV state was

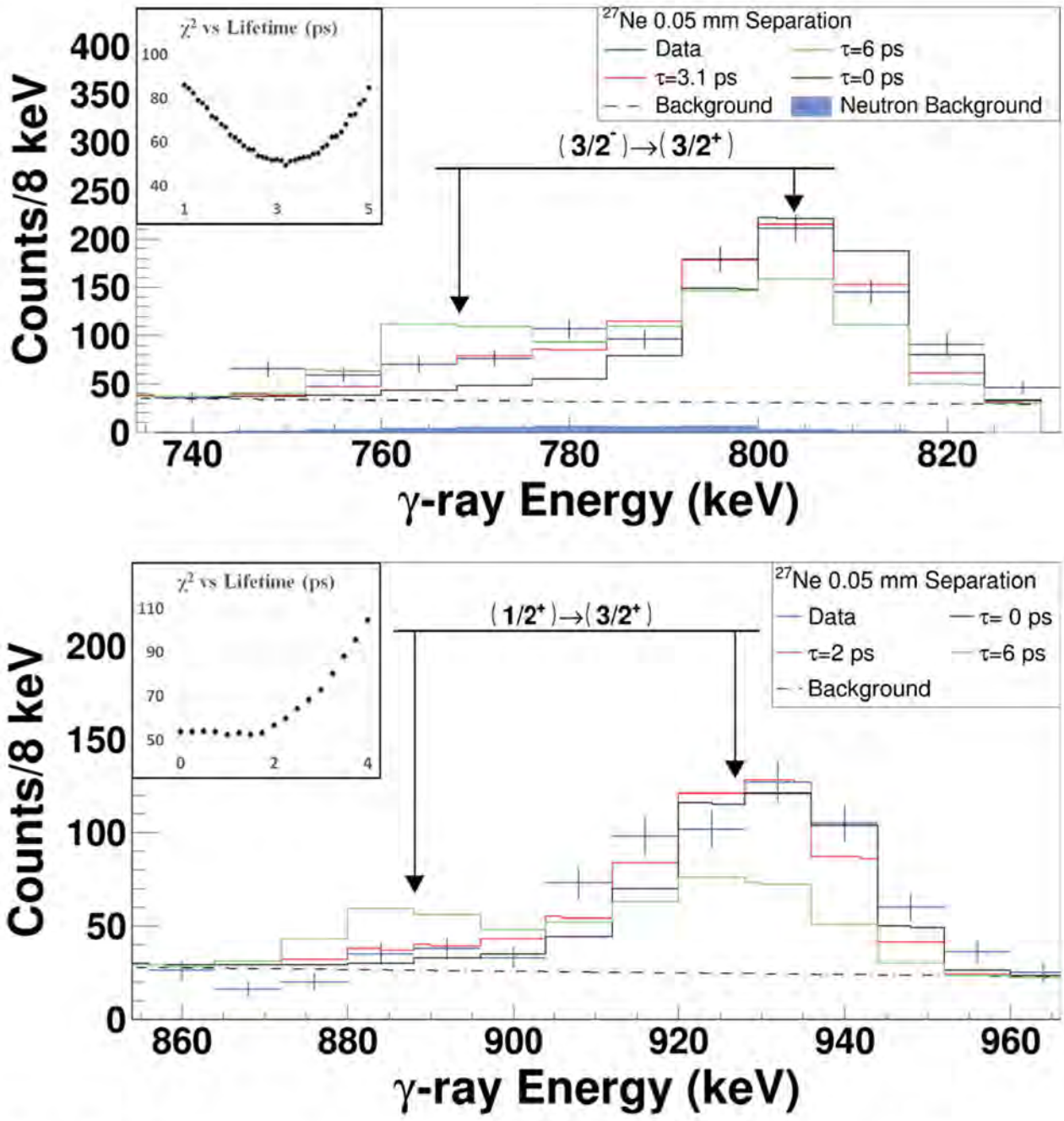

Figure 5.15 The γ-ray spectra for ^{27}Ne with a 0.05-mm separation focused on 765 keV state (top) and 885 keV state (bottom) are shown. The fixed exponential background is presented in both figures, and in (top) the small contribution from neutron-induced background is presented. In both figures a χ^2 plot for the fits is presented, where the number of degrees of freedom is 15 for the 765 keV and 19 for the 885 keV. (top) The best fit simulated spectra with a 765 keV state lifetime of 3.1 ps is compared to simulated spectra with lifetimes 0 ps and 6 ps. (bottom) Simulated spectra with the upper bound 885 keV state lifetimes of 2 ps, is compared to simulated spectra with lifetimes of 0 ps and 6 ps.

assumed to have a 0 ps lifetime in this analysis. The error due to this is considered to be marginal because of the small branching ratio for decays into the 765 keV state, the upper bound lifetime of 2 ps, and the selection of only events with a single coincident added-back γ-ray interaction. The lifetime of the 765 keV state is then $3.1^{+0.6}_{-0.9}$ ps, where the error is the quadratic sum of the statistical and systematic errors.

5.5 Modified Coulomb-excitation measurement

$E2$ transition strengths can be determined from Coulomb-excitation, but at energies above the Coulomb barrier the inelastic scattering can have substantial contributions from nuclear interactions. As such, it is necessary to constrain the impact of nuclear contributions to determine the $E2$ strength. One way in which to do this is to measure inelastic scattering on two targets, one with a low Z, and one with a high Z. The low Z target will have a minimal Coulomb-field and therefore will be sensitive to direct nuclear interactions, while the high Z material will be sensitive to Coulomb-excitation. The downside of measuring the inelastic scattering on both high and low Z materials is that it would require a longer running time, or a reduction in statistics for the two separate materials, which is especially difficult for rare-isotope experiments. However, the method performed in this experiment allows for the simultaneous measurement of reactions on two targets.

In this modified Coulomb-excitation measurement, two foils are mounted in the beamline, separated by a distance determined by the geometry of the detectors. For the present experiment, the distance chosen was 25 mm. Furthermore, the two targets are placed upstream of the γ-ray detectors, in this case by 13 cm. The first target (T_1) is chosen to be the low-Z target, so as to minimize the stopping power. The second target (T_2) is chosen to be the high-Z material, to maximize stopping power. The γ-ray spectra measured in this setup have two distinct peaks for each transition, as in the 25-mm separation measurement of ^{28}Ne as presented in Figure 5.2. The lower energy peak is due to decays that occur after the degrader, while the higher energy peak is due to decays that occur between the target and degrader.

In this experiment, the states of interest are expected to have lifetimes below 10 ps, and the distance corresponds to a flight time of approximately 250 ps. This means that effectively all states that are excited at T_1 decay before T_2 and the two resulting peaks correspond exactly to reactions in T_1 and T_2. As such the relative contribution of Coulomb and nuclear excitations can be found from the peak yields.

The integrated cross section of each reaction can therefore be found as:

$$\sigma_R = \frac{N_\gamma}{N_P \times \sigma_T} = \frac{N_{Coinc}}{\varepsilon_{Coinc}} \frac{1}{N_P \times \sigma_T} = \frac{N_{Coinc}}{\varepsilon_{Coinc}} \frac{1}{N_B \times P_B \times \sigma_T} \tag{5.2}$$

where σ_R is the cross section of the reaction integrated over all angles, N_γ is the number of γ rays emitted, σ_T is the areal number density of the target, N_P is the number of incoming projectiles of interest, N_{Coinc} is the number of counts in the γ-ray peak measured in coincidence with the ion, ε_{Coinc} is the efficiency for measuring a coincidence. This is the combined geometrical and intrinsic efficiency of the γ-ray detector along with the deadtime of the combined spectrograph-detector system. N_B is the number of particles in the beam, P_B is the purity of the beam for the projectile of interest.

Therefore, to determine the cross section and extract the $B(E2)$, it is necessary to determine the total incoming counts from the beam, the purity of the beam, the number of detected gammas in each peak, the areal density of the target, and the efficiency of the detectors.

5.5.1 Coupled Channel Equations

The cross section determined from the measurement can be converted into a $B(E2)$ using a Coupled-Channel calculation code, in this case ECIS97 [57]. The program *Equations Couplées en Itérations Séquentielles* (ECIS) takes as input an optical potential which models the nuclear scattering between the target and projectile nuclei. The Coulomb potential is incorporated using the proton numbers of the target and projectile nuclei. In addition, the energy levels and deformation parameter for the target nucleus are input to calculate the cross section of an excitation into a particular state at a given beam energy. The deformation parameter can be separated into a nuclear compo-

nent ($\beta_{Nuclear}$) and a Coulomb component ($\beta_{Coulomb}$). The optical potential used for both ^{27}Ne and ^{30}Mg was determined from reactions of ^{17}O + ^{208}Pb at 84 MeV per nucleon [58].

To determine the relative importance of nuclear and Coulomb contributions to the reaction cross sections in this experiment, it was assumed that the entire cross section for the ^{9}Be target came from the nuclear contribution. Thus the $\beta_{Coulomb}$ was set to 0 and the $\beta_{Nuclear}$ varied until the calculated cross section matched the experimental values. Then with the $\beta_{Nuclear}$ held at the fixed value, the $\beta_{Coulomb}$ was varied to determine the $B(E2)$ value, which is related to the deformation parameter by:

$$B(E2\uparrow) = \left(\frac{3ZeR^2}{4\pi}\beta_{Coulomb}\right)^2 \tag{5.3}$$

where in this equation, Z is the atomic number of the nucleus, e is the electron charge, and R is the radius of the nucleus, generally calculated as $1.2 \times A^{1/3}$ fm. Error in the $B(E2)$ comes primarily from uncertainty in the measured cross section, with additional error due to uncertainty in the $\beta_{Nuclear}$. Ambiguity in the reaction energy due to loss in the foils was found to have a marginal impact on the results.

5.6 Experimental Setup II: Coulomb Excitation

The lifetime and branching ratio of the ^{27}Ne 885 keV state cannot directly provide information on the $B(M1; 1/2^+ \rightarrow 3/2^+_{gs})$, as there may be a significant component of the lifetime that is from the $E2$ transition strength. The second setup is designed to measure the Coulomb-excitation of ^{27}Ne at energies above the Coulomb barrier to extract the $E2$ directly and therefore constrain the $M1$ strength. The modified Coulomb-excitation setup is used for the first time in this work. Therefore, in addition to the $B(E2; 3/2^+_{gs} \rightarrow 1/2^+)$ of ^{27}Ne, the previously studied $B(E2; 0^+_{gs} \rightarrow 2^+_1)$ of ^{30}Mg was also measured to confirm the method's reliability.

In this experiment, 9 GRETINA detectors were used, four at angles between 20° and 50° and 5 at angles between 70° and 90°. GRETINA was employed in coincidence with the S800, which was used to identify and count the incoming particles. The S800 was operated to record

incoming particles downscaled by a factor of 100 in addition to measuring particles in coincidence with GRETINA. The S800 trigger condition was stored in the data, and therefore the incoming beam could be determined free from the bias from the coincidence condition. Raw scalar numbers of counts at each scintillator were also recorded for the experiment using the S800, from which the total number of beam particles could be extracted. The measurement was performed over the course of two days.

In the experiment, a secondary cocktail beam including ^{27}Ne and ^{30}Mg was produced by impinging a ^{48}Ca beam accelerated to 140 MeV per nucleon at the coupled cyclotrons on a ^{9}Be target. The fragments were selected for at the A1900 and the secondary beam was sent to the S3 vault. The ^{30}Mg secondary beam was at 113 MeV per nucleon, while the ^{27}Ne secondary beam was at 97 MeV per nucleon.

The purity of the beam was measured at the S800 by using the ion-chamber and time signal of the S800 Object scintillator. The trigger condition chosen was for the downscaled singles, with coincidences excluded. The purity of the beam through the S800 was then determined by comparison of the total ions measured in the singles to those identified in the PID as the nucleus of interest. This resulted in a purity of the ^{27}Ne of 28.3 (6)% and ^{30}Mg of 34.7 (7)%. The error in the purity was due to statistical uncertainty and contaminants in the beam gates. The particle identification for the secondary beam at the S800 is presented in Figure 5.16.

The secondary beam was sent through the TRIPLEX plunger which held two foils, a 1.0 mm ^{9}Be target and a 0.92 mm Ta target separated by 25 mm. The ^{9}Be target had an areal density of $1.23 \times 10^{22} \frac{\texttt{atoms}}{cm^2}$. The Ta target had an areal density of $5.08 \times 10^{21} \frac{\texttt{atoms}}{cm^2}$. The TRIPLEX was located 13 cm upstream from the GRETINA center to enable the inelastic-scattering measurement.

5.6.1 GRETINA Efficiency

Because the γ rays emitted in-beam are shifted to forward angles, the combined geometrical and intrinsic efficiencies of GRETINA were determined by comparison to a GEANT4 simulation. GRETINA was calibrated using an ^{152}Eu source located on the tantalum target. The efficiency

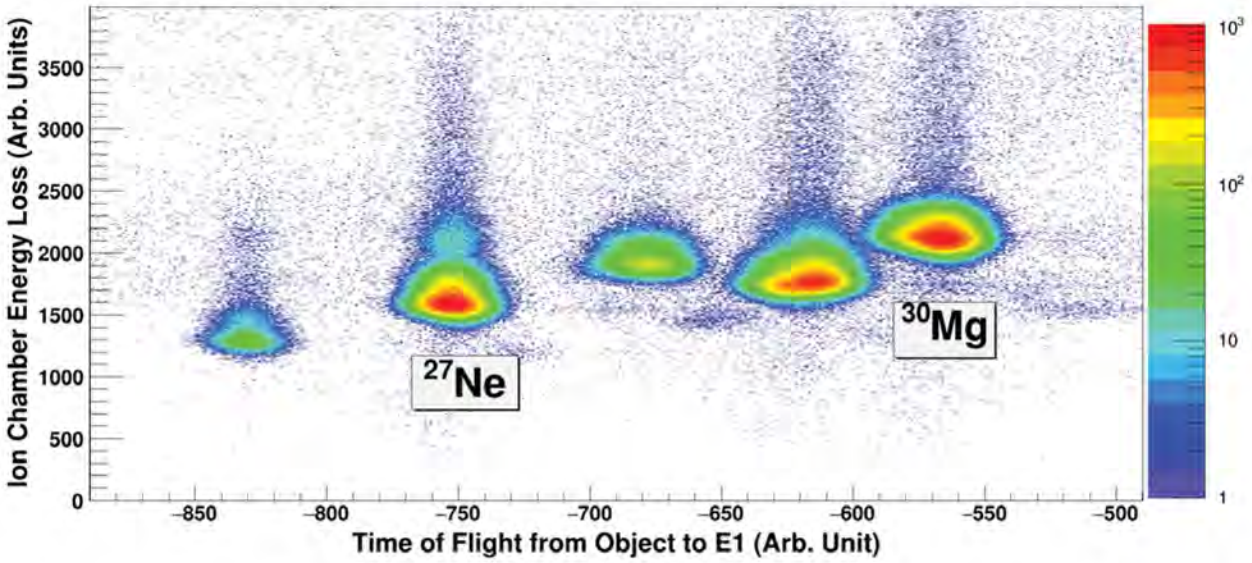

Figure 5.16 The particle identification of the secondary cocktail beam in the S800 focal plane is presented. The ion chamber energy loss is plotted against the time of flight from the S800 Object scintillator to the S800 E1 scintillator. The ^{30}Mg and ^{27}Ne components are labeled.

of a simulated ^{152}Eu source in the same configuration was compared to the measured efficiencies. A scaling factor was then introduced and determined to account for the difference between the simulated and experimental values. A scaling factor of 0.75 ± 0.05 was adopted based on the efficiency of the highest energy γ ray, and where the error is from the uncertainty in the relative efficiencies for each γ-ray energy, the extrapolation to non-measured energies, and comparison with previous work. Values for the simulated and measured efficiencies for selected ^{152}Eu γ-ray energies are shown in Table 3.1.

The efficiency depends on both the decay position and the energy of the γ-ray, meaning that there are different efficiencies for each of the measured γ rays and for each of the two peaks. To determine the efficiency of the γ rays emitted in-flight, decays from the states of interest were simulated at the first and second target positions. The efficiency was determined from this simulation by counting the amount of detected γ-rays in the related peak and comparing against the total number emitted. This number was then scaled by 0.75 to account for differences between the simulation and data. The efficiencies used for each γ-ray from interactions occurring at each position are shown in Table 5.3.

Nucleus	γ-ray Energy (keV)	Target	Efficiency
^{30}Mg	1483	^{9}Be	5.6 (4) %
		Ta	6.2 (4) %
^{27}Ne	885	^{9}Be	7.0 (4)%
		Ta	7.1(4)%

Table 5.3 Scaled simulated efficiencies for the γ ray of interest for ^{30}Mg and ^{27}Ne are presented. Efficiencies for the two targets are different due to the 25 mm separation between the two and the difference in energy from the different β values before and after the projectile travels through the Ta target. Error is from the uncertainties in the efficiency of GRETINA and the scaling factor.

Nucleus	Purity	Total
^{30}Mg	34.7(6) %	$7.6(2) \times 10^{7}$
^{27}Ne	28.3 (7) %	$6.2(1) \times 10^{7}$

Table 5.4 The purity of the beam and total projectile nuclei impinged on the ^{9}Be and Ta targets are listed for ^{30}Mg and ^{27}Ne along with the purity. The error is from statistics and the systematic error in the purity.

In addition, the number of detected γ rays is affected by the dead time of the S800 for coincidence measurements. As the system had a measured dead time of 16.7%, the efficiency of γ-ray collection is decreased by a factor of 0.83, which is corrected for.

5.6.2 Number of Projectile Nuclei

The number of incoming ions incident on the ^{9}Be and Ta targets over the experiment was determined from the S800 singles measured at the E1 scintillator. This was determined to be 2.1×10^{8}. The importance of transmission losses from the targets through the S800 Spectrograph is minimized because the E1 scintillator is used as the trigger, and thus γ rays corresponding to ions not reaching the E1 scintillator will not be included in the measurement. The number of incoming projectile nuclei is therefore the product of the purity and the incoming beams. The total number of incoming nuclei are listed in Table 5.4.

5.6.3 Extraction of γ-ray Counts

Ideally, the γ-ray peaks between the reactions on the target and reactions on the following second target would be clear with no overlap. However, due to the 2% momentum spread in the beam, the difference in beam energies for de-excitations at various depths in the targets and uncertainties in the Doppler-correction, the resulting γ-ray spectra consist of two well defined peaks with an overlap at the energies in between. To account for this overlap, the data was compared to GEANT4 simulations incorporating the beam properties, energy loss in the targets, and the detectors. The ratio of excitations on the first target to excitations on the second target was varied, and the best fit for the two peaks found, with an exponential background and a scaling factor as free parameters in the fit. The simulated spectrum was then decomposed into the components from the first and second targets. A small linear background was subtracted from the simulated peaks to account for Compton-scattering from the two peaks. The counts in the peak with the background subtracted were then scaled by the parameter used in the fit to determine the overall number of counts in the peaks from reactions on each of the targets. This was compared to a method where a linear background was estimated and the integral of the peaks was used to determine the counts due to the first and second targets to determine systematic error in the background subtraction. The ratio of reactions on each target in the simulations was also varied around the best fit to determine the impact of ambiguity in the assignment of γ rays with energies between the two peaks.

5.7 ^{30}Mg Measurement

The $B(E2;0_{gs} \rightarrow 2_1^+)$ for ^{30}Mg has been well studied via Coulomb-excitation, and the present work serves as a benchmark for the modified Coulomb-excitation technique used here [120][122][123]. The $B(E2;0_{gs}^+ \rightarrow 2_1^+)$ values measured in these experiments are presented in Table 5.5, along with the technique used in the measurement. The $B(E2)$ values have been measured using safe and intermediate energy Coulomb-excitation. The intermediate energy Coulomb-excitation was performed in one case using two separate targets to fit the nuclear and Coulomb contributions to

Method	^{30}Mg $B(E2;0^+_{gs} \rightarrow 2^+_1)$ e^2fm^4
Intermediate-energy Coulomb excitation with cut on impact parameter	295 (26) [120]
Intermediate-energy Coulomb excitation with two targets	435 (58) [122]
Safe Coulomb excitation	241(31) [123]

Table 5.5 $B(E2;0^+_{gs} \rightarrow 2^+_1)$ values for ^{30}Mg determined from Coulomb-excitation measurements are presented along with the technique used in the measurement.

coupled channel calculations. In the other intermediate energy Coulomb-excitation measurement, a cut on the ion angle was employed to restrict the impact parameters to those larger than the nuclear radius.

The safe Coulomb-excitation and intermediate-energy Coulomb-excitation using the cut on impact parameters indicate a $B(E2;0^+_{gs} \rightarrow 2^+_1)$ between 200 and 300 e^2fm^4. The previous intermediate-energy Coulomb-excitation measurement using two targets resulted in a significantly larger value of 453 (58) e^2fm^4, and therefore the present measurement validates the modified setup used here and also serves to help resolve this discrepancy among existing data.

The ^{30}Mg spectrum for inelastic-scattering on the ^{9}Be and Ta foils with a 25-mm separation is shown in Figure 5.17 compared to a best fit simulation. Two peaks 1400 and 1485 keV correspond to the de-excitations of the 2^+_1 at the Ta and ^{9}Be targets respectively. Two smaller peaks at 1890 and 1980 keV correspond to de-excitations of the $\left(4^+_2\right) \rightarrow 2^+_1$ transition at the Ta and ^{9}Be targets.

A partial level scheme for ^{30}Mg is presented in Figure 5.18. The presence of the 1978 keV γ-ray transition complicates the results, as it corresponds to a state transition feeding into the 2^+_1. As can be seen in the figure, the 1978 keV transition from the 3461 keV state directly feeds the 2^+_1 state. Furthermore, the other branch from the 3461 keV state populates the $\left(2^+_1\right)$ state via a state at a 2468.4 keV, which in turn decays to the 1482 keV state. As any direct excitation of the higher-lying state will lead to feeding of the 2^+_1 state, this must be accounted for. This is done by finding the cross section of this excitation, and subtracting it directly from the apparent cross section of the 2^+_1. Additionally, the adopted value for the branching ratio of the decay via the 1978 keV transition (0.58 ± 0.15) must be accounted for in determining the cross section. The 978 keV transition is potentially present in the spectrum, but buried in the background from Compton-scattering.

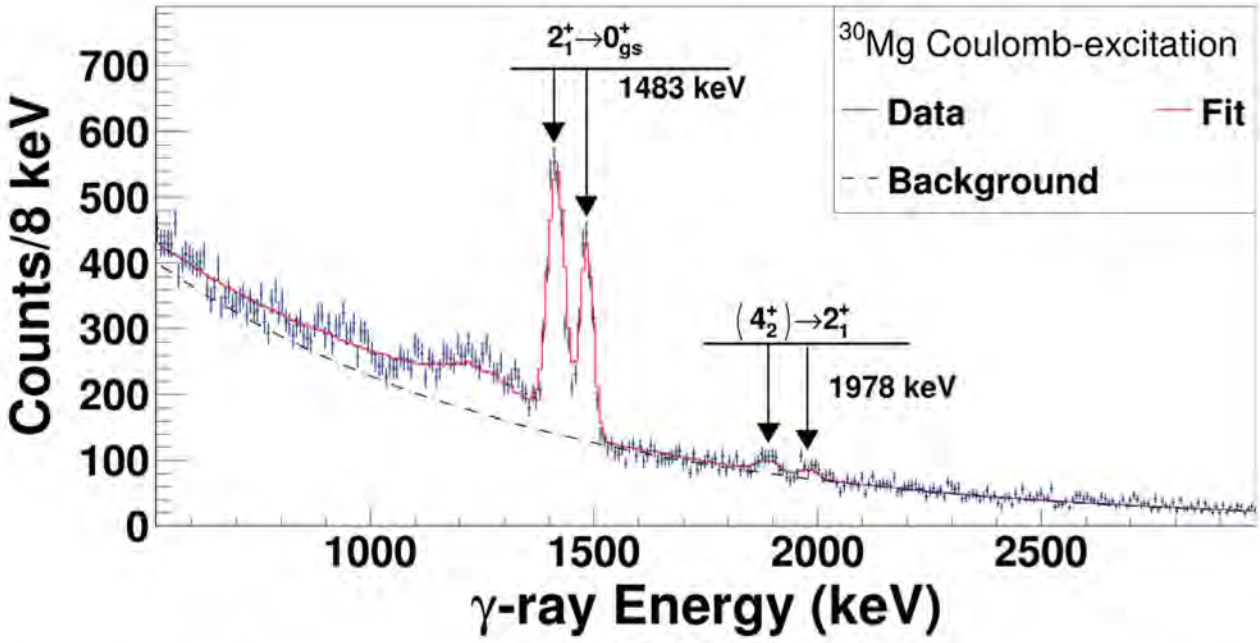

Figure 5.17 The Coulomb-exctiation spectrum for ^{30}Mg using a 1.0 mm ^{9}Be and 0.92 mm Ta target separated by 25 mm is presented. The observed transitions are labeled. The higher (lower) peak components are associated with reactions on the ^{9}Be (Ta) target. A best fit spectrum is presented, with the ratio of reactions on the ^{9}Be target to reactions on the Ta target found to be 0.65. The dashed curve is an exponential background included in the fit.

The measured counts in each of the peaks, the cross section, and the error in the cross section for each of the transitions at each target are provided in Table 5.6. The counts are scaled by the adjusted efficiency determined from simulations and the deadtime of the S800 to determine the total emissions. The total counts impinging on the target are determined from the scalars and purity, and together the cross section is calculated. The systematic error for each comes from error in determining the γ-ray efficiency with GRETINA using the ^{152}Eu source (4%), error in scaling the simulated efficiency to the scaled efficiency (5%), error in background estimation (2%), error in the purity of the ^{30}Mg beam (2%), ambiguity in the assignment of the counts between the two peaks (5%). Additionally, there is an error associated with the branching ratio for the (4_2^+) state (25%). The uncertainty in the cross section of the 2_1^+ state is affected by the uncertainty in the feeding state cross section (5.5%). The systematic errors in Table 5.6 are the quadratic sum of each of the individual systematic errors. The $\beta_{Nuclear}$ for the excitation to the 2_1^+ state was determined

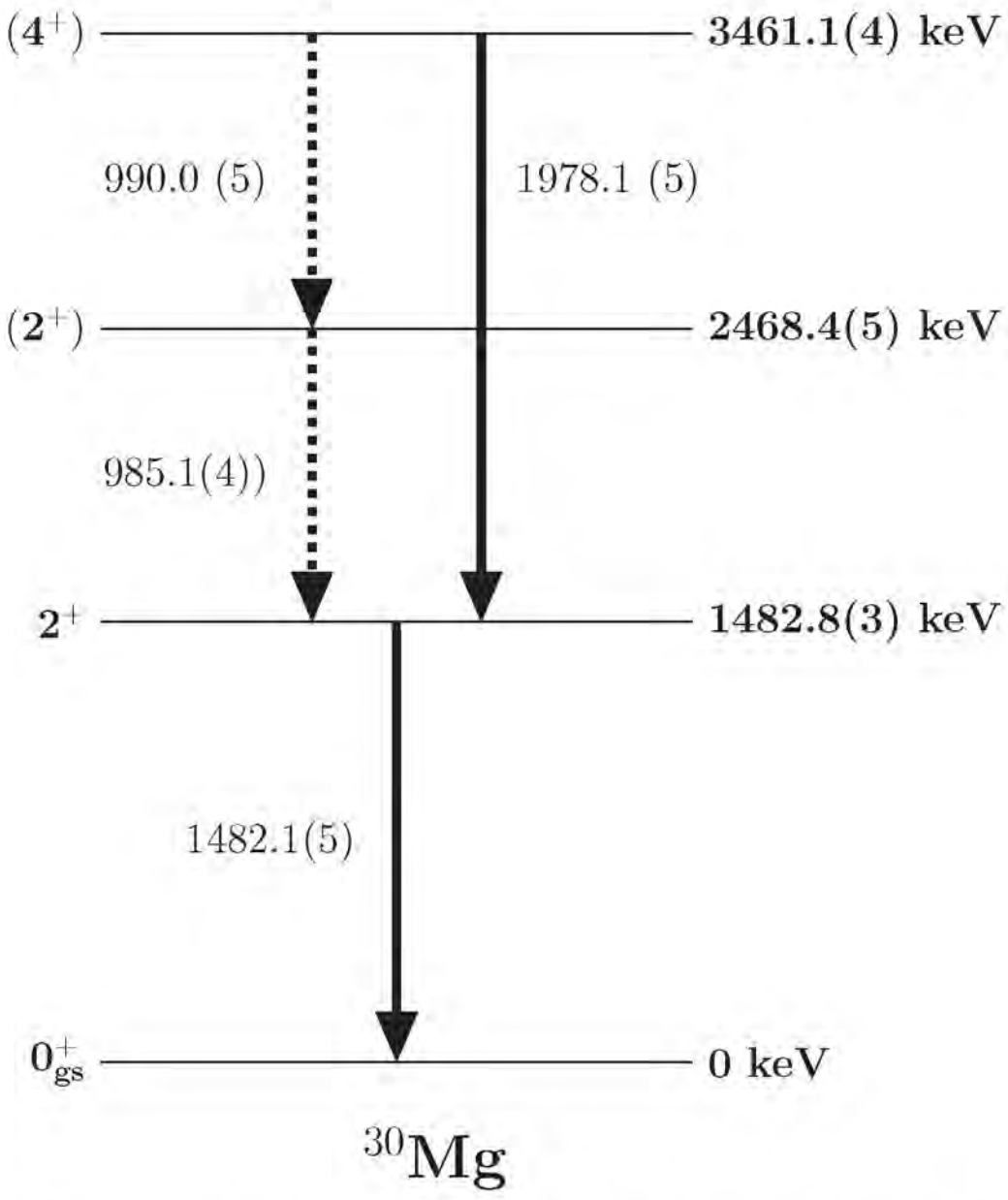

Figure 5.18 The partial level scheme of ^{30}Mg showing states observed in the Coulomb excitation data is presented. The J^{π} assignment and state and transition energies are from [124]. The dashed lines represent transitions not observed in this study because of overlap with Compton events.

State	Transition	Target	γ-ray Counts	σ (mb)	Statistical Error (mb)	Systematic Error (mb)
2_1^+	$2_1^+ \rightarrow 0_{gs}^+$	^{9}Be	1260 (35)	24	1	3
2_1^+	$2_1^+ \rightarrow 0_{gs}^+$	Ta	2100 (45)	88	2	9
(4_2^+)	$(4_1^+) \rightarrow 2_1^+$	^{9}Be	85 (9)	4	0.5	1
(4_2^+)	$(4_1^+) \rightarrow 2_1^+$	Ta	140 (12)	16	1.5	4.5

Table 5.6 The number of γ rays observed and the cross sections for each state in ^{30}Mg are presented for reactions on the ^{9}Be and Ta targets. Statistical and systematic errors are presented for the cross sections, where the systematic error is the quadratic sum of the individual systematic errors discussed in the text. Error for the number of observed γ rays is statistical only. The cross section of the 2_1^+ state corrects for feeding contributions.

by ECIS from the measured cross section of 23 ± 3 mb for the reaction on ^{9}Be. This resulted in a $\beta_{Nuclear}$ value of 0.45^{+2}_{-3}. Using the $\beta_{Nuclear}$ value of 0.45, the ECIS calculations were run to reproduce the excitation cross section on the tantalum, which was 88 ± 9 e^2fm^4. This resulted in a $\beta_{Coulomb}$ of 0.40 ± 0.03(Uncertainty in Cross Section) $\pm$ 0.01 (Uncertainty in $\beta_{Nuclear}$). This corresponds to a $B(E2; 0_{gs}^+ \rightarrow 2_1^+)$ of 254 ± 39 (Uncertainty in Cross Section) ± 13 (Uncertainty in $\beta_{Nuclear}$) e^2fm^4. Thus in total the result was found to be 254 ± 41 e^2fm^4.

This $B(E2; 0_{gs}^+ \rightarrow 2_1^+)$ agrees with the safe Coulomb excitation value of 241 (31) e^2fm^4 [123] and is consistent with the 295(26) e^2fm^4 from the Intermediate-energy Coulomb-excitation with a selection on impact parameter [120]. This agreement indicates that the method of measuring two targets simultaneously successfully allows for the measurement of Coulomb excitation at intermediate energies.

5.8 ^{27}Ne Coulomb Excitation Measurement

The spectrum for the ^{27}Ne Coulomb excitation measurement taken with the 1.0 mm ^{9}Be target and 0.92 mm Ta target separated by 25 mm is presented in Figure 5.19. The 885 keV and 765 keV transitions are identified and labeled along with the best fit simulation using an exponential background and with a population ratio of 0.4 reactions in the ^{9}Be target per reaction in the Ta target.

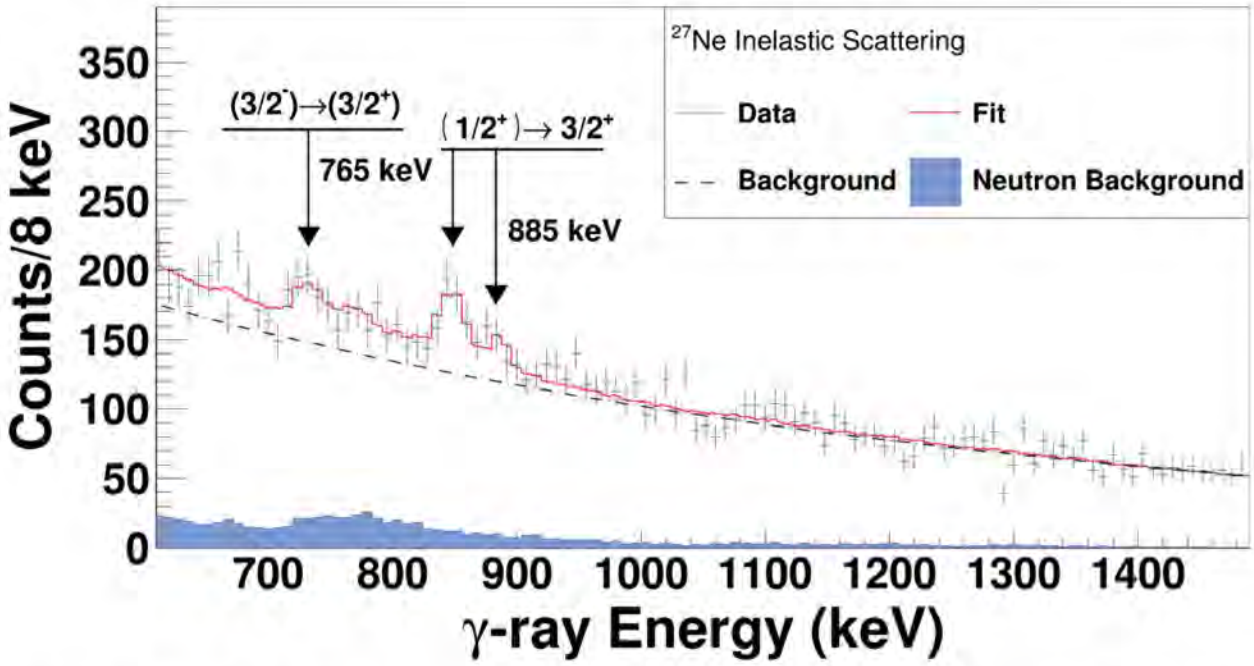

Figure 5.19 The ^{27}Ne Coulomb-excitation spectrum with a ^{9}Be target and Ta target separated by 25 mm is presented. The 885 keV and 765 keV transitions are identified. A best fit simulation with a ratio of 0.4 reactions in the ^{9}Be target per reaction in the Ta target is shown with an exponential background.

The total counts in each peak along with the extracted cross section are presented in Table 5.7. The cross section was extracted from the yield of the 885 keV peak using the simulated GRETINA efficiency of 7%. Additionally, as the 885 keV state has two modes, via the 119 keV transition and the 885 keV transition, the cross section needed to be increased by the inverse of the branching ratio. As measured earlier, this branching ratio is 83(2)%. The statistical error and systematic error are also presented in Table 5.7. Due to the small yield, the statistical error is 8% for the Ta cross section and 13% for the Be cross section. The sources of systematic error include uncertainty in the measured γ-ray efficiency of GRETINA (4%), ambiguity in the scaling of the simulated efficiency (5%), uncertainty in background subtraction (14%), uncertainty in the purity (2%), uncertainty in the assignment of the counts between the two peaks to excitations on the Be or Ta target (6.5% for the Ta, 27% for the Be). In addition, the uncertainty in the branching ratio provides another 2.5% ambiguity in the cross section. The resulting error of 17% for the Ta excitation and 31% for the Be

State	Target	Counts	σ(mb)	Statistical Error (mb)	Systematic error (mb)
$1/2^+$	Be	60(8)	1.7	0.2	0.5
	Ta	155 (12)	10	0.8	1.7

Table 5.7 The γ-ray counts in each peak are presented along with statistical error. The extracted cross sections are presented along with statistical and systematic error, whose sources are discussed in the text.

excitation is determined by adding systematic error in quadrature.

The $B(E2;3/2^+ \rightarrow 1/2^+)$ for ^{27}Ne was determined using ECIS97 [57]. The $\beta_{Nuclear}$ was constrained using the cross section for scattering on the ^{9}Be and found to be 0.12 ± 0.02 where the error is from uncertainty in the cross section. The $\beta_{Coulomb}$ was calculated using ECIS to reproduce the cross section for the Tantalum by setting the $\beta_{Nuclear}$ to 0.12. This resulted in a $\beta_{Coulomb}$ of 0.175 $\pm$0.025 (Uncertainty in Cross Section) $\pm$0.005 (Uncertainty in $\beta_{Nuclear}$). This corresponds to a $B(E2;3/2^+_{gs} \rightarrow 1/2^+)$ of 29^{+9}_{-8} e^2fm^4. This result indicates an $E2$ partial lifetime of 26^{+11}_{-6} ps. As the measured lifetime for the $1/2^+$ state is less than 2.0 ps, the overall $E2$ contribution to the lifetime is small as expected, and the lifetime of the 885 keV state provides information on the $M1$ transition strength.

5.9 Discussion

The results of the lifetime, branching ratio, and Coulomb-excitation measurements were used to extract $B(E1)$, $B(E2)$ and $B(M1)$ transition strengths between bound states in ^{27}Ne. These values for electromagnetic transition strengths and their corresponding partial lifetimes are presented in Table 5.8. The lifetime of the $\left(1/2^+\right)$ state is determined by the sum of the partial lifetimes $E1$, $M1$, and $E2$ as:

$$\frac{1}{\tau} = \frac{1}{\tau_{E2}} + \frac{1}{\tau_{E1}} + \frac{1}{\tau_{M1}} \tag{5.4}$$

where the τ is the total lifetime of the state, and τ_X is the partial lifetime for each of the states.

The lower limits for the $B(E1;1/2^+ \rightarrow 3/2^-)$ and $B(M1;1/2^+ \rightarrow 3/2^+_{gs})$ were determined from the upper limit of the partial lifetime deduced from the experiment. The $B(E2;1/2^+ \rightarrow$

Electromagnetic Transition Strength	Partial Lifetime (ps)	Value	Value (W.u.)
$B(E1;1/2^+ \rightarrow 3/2^-)$	< 13	$> 0.03\ e^2\text{fm}^2$	> 0.05
$B(E2;1/2^+ \rightarrow 3/2^+_{gs})$	26^{+11}_{-6}	$58^{+18}_{-15}\ e^2\ \text{fm}^4$	12(3)
$B(M1;1/2^+ \rightarrow 3/2^+_{gs})$	< 2.6	$> 0.03\mu_N^2$	> 0.02
$B(E1;3/2^- \rightarrow 3/2^+_{gs})$	$3.1^{+0.6}_{-0.9}$	$4.5^{+2}_{-1} \times 10^{-4}\ e^2\text{fm}^2$	$8^{+3}_{-1.5} \times 10^{-4}$

Table 5.8 The electromagnetic transition strengths of ^{27}Ne measured in this work are presented along with the partial lifetime corresponding to that strength. Error presented for lifetimes and transition strengths is from the quadratic sum of systematic and statistical error.

$3/2^+_{gs}$) was determined directly from the Coulomb-excitation data.

The lower limit for the $B(E1;1/2^+ \rightarrow 3/2^-)$ amounts to 0.05 W.u. This value was extracted from the partial lifetime of the 885 keV state decaying to the 765 keV state. The partial lifetime was determined from the lifetime and branching ratio measurement of the $1/2^+$ state of ^{27}Ne.

The lower limit of the $B(M1;1/2^+ \rightarrow 3/2^+)$ is 0.02 W.u. This value was determined from the corresponding partial lifetime. The partial lifetime of the $1/2^+$ state due to the $M1$ transition was determined from the state lifetime and the previously calculated partial lifetimes of the $E1$ and $E2$ transitions.

Figure 5.20 shows the electromagnetic transition strengths measured in ^{27}Ne and those observed in other comparable nuclei. The similarities and discrepancies provide insight into the structure of ^{27}Ne. In particular, the 885 keV state with an expected s-wave contribution and neutron separation energy less than 1 MeV may be expected to manifest halo-like properties. The measured $B(E1;1/2^+ \rightarrow 3/2^+_{gs})$ value with a lower limit of 0.03 e^2fm^2 or 0.05 W.u. can be compared with the enhanced $B(E1)$ transition strengths observed in ^{11,12}Be.

The present $B(E1;1/2^+ \rightarrow 3/2^-)$ of ^{27}Ne with a lower bound of 0.03 e^2fm^2 or 0.05 W.u. can be compared with the $B(E1;1/2^- \rightarrow 1/2^+_{gs})$ of ^{11}Be, with a value of 0.36 (3) W.u. [38][126]. ^{11}Be has a $1/2^+$ ground state, a $1/2^-$ excited state at 320 keV and a neutron separation energy of 501.25 (58) keV [38][125][127]. These features can be understood from the narrowing of the $N = 8$ shell gap in ^{11}Be, in which the $2s_{1/2}$ and $1p_{1/2}$ single particle states become nearly degenerate. ^{11}Be has been well established as a halo nucleus through interaction cross sections and momentum

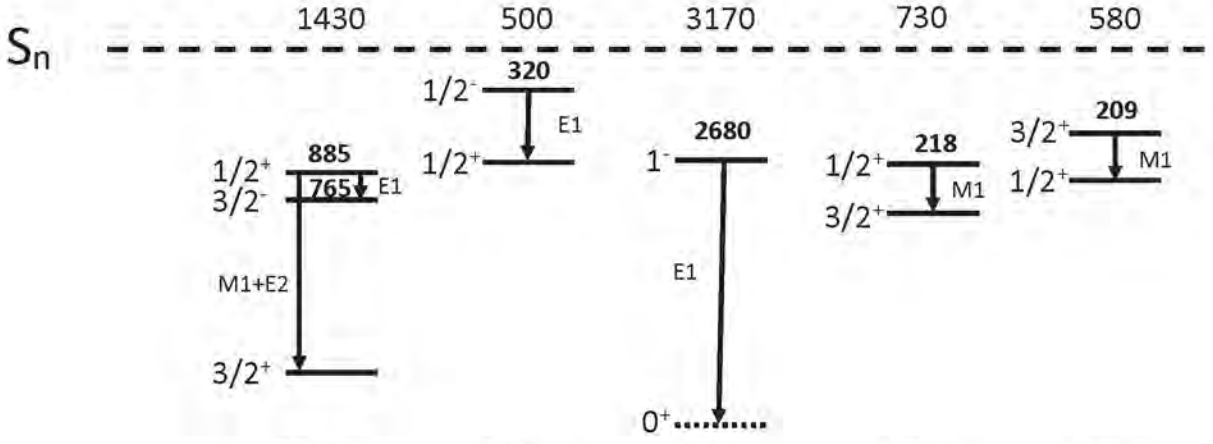

	^{27}Ne	^{11}Be	^{12}Be	^{17}C	^{19}C
B(E1)	>0.05	0.36 (3)	0.05 (2)	X	X
B(M1)	>0.02	X	X	$5.8^{+0.2}_{-0.7} \times 10^{-3}$	$1.79\ (14) \times 10^{-3}$
B(E2)	$4.3^{+1.3}_{-1.1}$	X	X	X	X

Figure 5.20 Level schemes for the bound states of ^{27}Ne, ^{11,12}Be, and ^{17,19}C are presented. Each level scheme is aligned to the neutron separation energy of the nucleus, represented by the dashed line. The neutron separation energy in keV for the ground state of each nucleus is stated above the dashed line. The J^{π} for each level is labeled, and the energies of excited states in keV are shown. The multipolarity of the transitions are also denoted. The energy of the 0^+ state in ^{12}Be is not to scale and is marked with a dotted line. Beneath the level schemes, a table of the downward electromagnetic transition strengths for the transitions shown in each nucleus are presented in Weisskopf units. The data is from the present work and [27][31][38][49][111][113][125].

distribution measurements [128][129][130]. The large $B(E1; 1/2^- \rightarrow 1/2^+_{gs})$ strength in ^{11}Be has been understood as arising from the large radial extent of the halo neutron [38][131].

In a simple picture, the valence neutron of ^{11}Be occupies the $2s_{1/2}$ orbital in the ground state, and occupies the $1p_{1/2}$ orbital in its $1/2^-$ excited state. This is similar to the single particle structure in ^{27}Ne, where the valence neutron occupies the $2p_{3/2}$ orbital in the $3/2^-$ excited state, and where a neutron excitation out of the $2s_{1/2}$ orbital forms the $1/2^+$ state. Therefore from a single particle perspective the $1/2^+ \rightarrow 3/2^-$ state in ^{27}Ne involves transition between s and p orbitals similar to that in the $1/2^- \rightarrow 1/2^+_{gs}$ transition in ^{11}Be. Furthermore, the neutron separation energy in ^{27}Ne is approximately 1.4 MeV from the ground state, but only approximately $500-600$ keV for the $1/2^+, 3/2^-$ excited states, which is comparable to the separation energy in ^{11}Be [27].

Indeed, the phenomenon of certain enhanced $B(E1)$ strengths in nuclei has been previously understood to arise from one or more decoupled loosely-bound halo neutrons [131][132][133][134]. In a simple picture, the decoupled neutrons can oscillate against the core, and this can create a large $E1$ strength among transitions between bound states. In a shell model context, the use of extended single particle wavefunctions can be shown to reproduce an increased $E1$ transition strength for transitions between bound states [131].

For reference, ^{12}Be has the second largest $E1$ strength observed in transitions between bound states in light mass nuclei, with a $B(E1; 0_{gs} \rightarrow 1^-)$ value of 0.051(13) e^2fm^2 or 0.15 (4) W.u. [31]. This $B(E1)$ strength is comparable with the lower limit of 0.05 W.u. for the measured $B(E1; 1/2^+ \rightarrow 3/2^-)$ of ^{27}Ne. Thus, the enhanced $B(E1; 1/2^+ \rightarrow 3/2^-)$ supports the model in which ^{27}Ne is made up of a ^{26}Ne core and a valence neutron with a radially extended wavefunction. This is consistent for a state with a large s-wave contribution and only 500 keV from the neutron separation energy [27]. This is also consistent with the angular momentum components of the $1/2^+$ state being $l = (0, 1)$ as determined from momentum distributions [116].

The $B(E1; 3/2^- \rightarrow 3/2^+_{gs})$ provides additional evidence for the $E1$ enhancement of the $1/2^+$ state. The $3/2^-$ state is common to both the $B(E1; 1/2^+ \rightarrow 3/2^-)$ and $B(E1; 3/2^- \rightarrow 3/2^+_{gs})$. If the valence neutrons in the ground state do not have an extended wavefunction, the $B(E1; 3/2^- \rightarrow$

$3/2^+$) can be taken as a reference strength. Indeed, the $B(E1;3/2^- \rightarrow 3/2^+_{gs})$ with a value of $4.5^{+2}_{-1} \times 10^{-4}$ e^2fm^4 or $8 \pm 3 \times 10^{-4}$ W.u. is smaller than the $B(E1;1/2^+ \rightarrow 3/2^-)$ by a factor of at least 50. This supports the picture of the $1/2^+$ state having a unique nature which can be ascribed to a radially extended wavefunction.

The $M1$ and $E2$ transition strengths can be understood in part through comparison to stable nucleus ^{33}S which is an isotone of ^{27}Ne with 6 more protons. With an even number of protons and a single valence neutron, it can be expected that at low energies ^{33}S still is dominated by the single particle structure of the neutron. The 841 keV state with spin and parity $1/2^+$ has previously been measured to determine the $B(M1;1/2^+ \rightarrow 3/2^+_{gs})$ and $B(E2;1/2^+ \rightarrow 3/2^+_{gs})$ transition strengths of 0.031(4) W.u. and 6(4) W.u. respectively [135][136]. These can be seen to be close to the measured values in ^{27}Ne from decays of the 885 keV state. The $B(M1;1/2^+ \rightarrow 3/2^+_{gs})$ has a lower limit of 0.02 W.u., consistent with the 0.031(4) W.u. in ^{33}S. Furthermore, the $B(E2;1/2^+ \rightarrow 3/2^+_{gs})$ of 12(3) W.u.is consistent within error with the 6(4) W.u. in ^{33}S. The $B(E2)$ strengths in ^{33}S may indicate moderate deformation, or could be due to band mixing [137].

The $B(M1)$ transition strength in loosely-bound nuclei has been investigated previously in ^{19}C [111]. In that work, the $B(M1;3/2^+ \rightarrow 1/2^+_{gs})$ of ^{19}C was found to be $1.79(14) \times 10^{-3}$ W.u, representing one of the smallest observed in the mass region $A < 40$ [111]. Furthermore, the $B(M1;1/2^+ \rightarrow 3/2^+_{gs})$ has been measured in halo nucleus ^{17}C as $5.8^{+0.7}_{-0.2} \times 10^{-3}$ W.u. [49]. The hindered $M1$ transition strengths can be understood in part due to the lack of spin-flip transitions within the *sd*-shell. For that reason, if the valence neutron *s*-wave component were to be entirely dominant in the 885 keV state of ^{27}Ne, the $M1$ transition strength would be expected to be hindered. However, the present data do not support this picture of ^{27}Ne.

The interest in the contribution of the *s*-wave to the $1/2^+$ excited state of ^{27}Ne needs to be discussed in terms of an interaction between loosely-bound effects and deformation because neighboring ^{26,28}Ne are deformed. Indeed, at first glance *s*-wave dominance would be somewhat at odds with the large deformation in neighboring ^{26,28}Ne [55][112]. The deformed ^{26}Ne core would be expected to induce higher angular momentum states in the valence neutron [138]. However, it has

been predicted in theory that for loosely-bound states the norm of the s-wave ($\langle s|s\rangle$) is expected to diverge as $S_n \to 0$. As such, at extreme binding energies the overall contribution of the s-wave will dominate the structure despite the intrinsic deformation [138]. Since the $B(M1)$ would then be dominated by the overlap of the s-wave component, the transition strength would be hindered. However, the present value with a lower bound of 0.02 W.u. is ten times larger than the hindered transition in ^{19}C, suggesting that there is an admixture of $l > 0$ angular momentum states in the 885 keV wavefunction. This indicates that the 885 keV state may have the characteristics of a deformed halo, such as that suggested in ^{31}Ne [139][140] and ^{37}Mg [141].

Comparison of the present data to shell-model calculations may provide an additional indicator of halo formation. The $B(M1; 1/2^+ \to 3/2^+_{gs})$ and $B(E2; 1/2^+ \to 3/2^+_{gs})$ were calculated using the SDPF-M and USD interactions [142]. These calculations predict a $B(M1; 1/2^+ \to 3/2^+_{gs})$ value of 0.033 W.u. and 0.042 W.u. for the SDPF-M and USD interactions respectively. These are consistent with the lower limit of 0.02 W.u. established by the present measurements. The predicted $B(E2; 1/2^+ \to 3/2^+_{gs})$ is between 25 and 35 e^2fm^4, only half that of the measured transition strength. This indicates possible enhancement of collectivity in ^{27}Ne, providing a consistent picture for a deformed halo structure.

5.10 Conclusion

In conclusion, electromagnetic transition strengths between bound states of ^{27}Ne have been measured in this work. The $1/2^+$ state at 885 keV is expected to decay by a combination of $M1$ and $E2$ contributions to the ground state along with $E1$ contributions to the 765 keV state. The $3/2^-$ state at 765 keV is expected to decay via a $E1$ transition to the ground state. The $B(E1; 1/2^+ \to 3/2^-)$ was found to be at least 0.05 W.u., consistent with halo formation. The $B(E1; 3/2^- \to 3/2^+)$ value of $8^{+3}_{-1.5} \times 10^{-4}$ W.u. supports the influence of loosely-bound effects on the 885 keV state as it is 50 times weaker than the $B(E1; 1/2^+ \to 3/2^-)$. The $B(E2; 1/2^+ \to 3/2^+)$ has been measured to decompose the $M1$ strength and indicates the potential interplay of deformation with the loosely-

bound effects in the $1/2^+$ state. The unhindered $B(M1; 1/2^+ \rightarrow 3/2^+)$ transition strength with a lower limit of 0.02 as well as the favored E2 transition are also consistent with a picture of the 885 keV state as a deformed halo.

CHAPTER 6

CONCLUSION

This work investigates the richness of nuclear structure at the floor and edge of the valley of stability through measurements of electromagnetic transition strengths. The electromagnetic transition strengths between bound states of nuclei offer a unique window into the dynamics and internal configuration of the nuclear wavefunction. The nuclear structure accessible to these transition strengths can only be probed through measurements of lifetimes and cross sections. The Recoil Distance Method and modified Coulomb-excitation setup developed and employed in this work have been demonstrated as powerful tools that give us insight into nuclear structure. The continued development of new devices such as GRETINA and the TRIPLEX for precise γ-ray and lifetime measurements is opening up new opportunities for the study of novel features in nuclei.

The lifetime measurement of the 4_1^+ state of ^{58}Ni demonstrates the utility of electromagnetic transition strengths in studying nuclei at the floor of the valley of stability. The measured $B(E2;4_1^+ \rightarrow 2_1^+)$ restores the systematics of the Nickel isotopes to the behavior expected near the shell closure at $N = Z = 28$. The model-independent lifetime measurement enabled by GRETINA and the TRIPLEX plunger could distinguish between an enhanced $B(E2;4_1^+ \rightarrow 2_1^+)$ indicated by a previous measurement and the unenhanced value expected from nuclei near a shell closure.

The lifetime and Coulomb-excitation measurements of the excited states of ^{27}Ne have demonstrated the usefulness of the Recoil Distance Method and inelastic scattering techniques. In this work, the major electromagnetic transition strengths in ^{27}Ne have been constrained, providing direct insight into the nuclear wavefunctions of all the bound states of ^{27}Ne. The enhanced $B(E1;1/2^+ \rightarrow 3/2^-)$ strength relative to the $B(E1;3/2^- \rightarrow 3/2^+_{gs})$ indicates a unique structure in the $1/2^+$ excited state that does not manifest in the $3/2^-$ state. The measured $B(M1;1/2^+ \rightarrow 3/2^+_{gs})$ value is considered to originate from the admixture of non-spherical components to the wavefunction of the valence neutron, indicating that the $1/2^+$ excited state of ^{27}Ne is consistent with a deformed halo. This work has demonstrated that rich variety of physics can be extracted

from the electromagnetic transition strengths of nuclei far from stability.

The present experiments also point to new horizons in studying nuclear structure. On the one hand, the modified Coulomb-excitation setup presented here may be of use in future experiments. On the other hand, the present measurement determined only lower bounds for the $B(E1; 1/2^+ \rightarrow 3/2^-)$ and $B(M1; 1/2^+ \rightarrow 3/2^+_{gs})$ values. A precision measurement of the exact lifetime would be of much interest in determining the scope of the loosely-bound effects in ^{27}Ne. The ^{27}Ne lifetime in the region of less than two picoseconds would be best measured using the Doppler-shift Attenuation Method [41]. However, as ^{27}Ne is a rare isotope, it is difficult to create an appropriate beam at existing facilities. Future developments at the Facility for Rare Isotope Beams may make it possible to develop intense beams of ^{26}Ne [143]. The ReA re-accelerator facility could then be used to produce beams with energies suitable for Doppler-shift Attenuation Method measurements, and allow for a precise determination of the lifetime of the $1/2^+$ state, and hence the electromagnetic transition strengths [60].

In conclusion, the electromagnetic transition strengths of nuclei near and far from stability continue to shed light on the atomic nucleus. The development of new techniques and detectors in combination with the rich array of nuclei to be studied provides fertile ground to find novel features of nuclear structure. The techniques and measurements in this work may point a way for future avenues of study.

BIBLIOGRAPHY

BIBLIOGRAPHY

[1] E. Rutherford, The London, Edinburgh, and Dublin Philosophical Magazine and Journal of Science **21**, 669 (1911).

[2] M. Taketani, S. Nakamura, and M. Sasaki, Progress of Theoretical Physics **6**, 581 (1951).

[3] D. A. Liberman, Phys. Rev. D **16**, 1542 (1977).

[4] R. Casten, *Nuclear Structure from a Simple Perspective*, Oxford Studies in Nuclear Physics (Oxford University Press, 1990).

[5] B. A. Brown, "Lecture notes in nuclear structure physics," (2005), (Unpublished).

[6] W. Heisenberg, Zeitschrift für Physik **77**, 1 (1932).

[7] J. Suhonen, *From Nucleons to Nucleus: Concepts of Microscopic Nuclear Theory*, Theoretical and Mathematical Physics (Springer Berlin Heidelberg, 2007).

[8] "NNDC Chart of Nuclides," `http://www.nndc.bnl.gov/chart/`, accessed: 2017-03-28.

[9] A. Das and T. Ferbel, *Introduction to Nuclear and Particle Physics* (World Scientific, 2003).

[10] N. Bohr and J. A. Wheeler, Phys. Rev. **56**, 426 (1939).

[11] M. G. Mayer, Phys. Rev. **74**, 235 (1948).

[12] M. G. Mayer, Phys. Rev. **75**, 1969 (1949).

[13] O. Haxel, J. H. D. Jensen, and H. E. Suess, Phys. Rev. **75**, 1766 (1949).

[14] S. Raman, C. W. Nestor, and K. H. Bhatt, Phys. Rev. C **37**, 805 (1988).

[15] C. D. Nesaraja and E. A. Mccutchan, Nuclear Data Sheets **133** (2016).

[16] A. Gade and T. Glasmacher, Progress in Particle and Nuclear Physics **60**, 161 (2008).

[17] E. K. Warburton, J. A. Becker, and B. A. Brown, Phys. Rev. C **41**, 1147 (1990).

[18] C. Détraz, M. Langevin, D. Guillemaud, M. Epherre, G. Audi, C. Thibault, and F. Touchard, Nuclear Physics A **394**, 378 (1983).

[19] D. Guillemaud-Mueller, C. Detraz, M. Langevin, F. Naulin, M. de Saint-Simon, C. Thibault, F. Touchard, and M. Epherre, Nuclear Physics A **426**, 37 (1984).

[20] X. Campi, H. Flocard, A. Kerman, and S. Koonin, Nuclear Physics A **251**, 193 (1975).

[21] O. Sorlin and M.-G. Porquet, Progress in Particle and Nuclear Physics **61**, 602 (2008).

[22] B. A. Brown and W. A. Richter, Phys. Rev. C **72**, 057301 (2005).

[23] T. Otsuka, T. Suzuki, R. Fujimoto, H. Grawe, and Y. Akaishi, Phys. Rev. Lett. **95**, 232502 (2005).

[24] A. Navin, D. W. Anthony, T. Aumann, T. Baumann, D. Bazin, Y. Blumenfeld, B. A. Brown, T. Glasmacher, P. G. Hansen, R. W. Ibbotson, P. A. Lofy, V. Maddalena, K. Miller, T. Nakamura, B. V. Pritychenko, B. M. Sherrill, E. Spears, M. Steiner, J. A. Tostevin, J. Yurkon, and A. Wagner, Phys. Rev. Lett. **85**, 266 (2000).

[25] I. Tanihata, Journal of Physics G: Nuclear and Particle Physics **22**, 157 (1996).

[26] I. Tanihata, H. Savajols, and R. Kanungo, Progress in Particle and Nuclear Physics **68**, 215 (2013).

[27] G. Audi, A. Wapstra, and C. Thibault, Nuclear Physics A **729**, 337 (2003).

[28] K. Riisager, A. Jensen, and P. Møller, Nuclear Physics A **548**, 393 (1992).

[29] I. Tanihata, H. Hamagaki, O. Hashimoto, Y. Shida, N. Yoshikawa, K. Sugimoto, O. Yamakawa, T. Kobayashi, and N. Takahashi, Phys. Rev. Lett. **55**, 2676 (1985).

[30] T. Kobayashi, O. Yamakawa, K. Omata, K. Sugimoto, T. Shimoda, N. Takahashi, and I. Tanihata, Phys. Rev. Lett. **60**, 2599 (1988).

[31] H. Iwasaki, T. Motobayashi, H. Akiyoshi, Y. Ando, N. Fukuda, H. Fujiwara, Z. Fülöp, K. Hahn, Y. Higurashi, M. Hirai, I. Hisanaga, N. Iwasa, T. Kijima, A. Mengoni, T. Minemura, T. Nakamura, M. Notani, S. Ozawa, H. Sagawa, H. Sakurai, S. Shimoura, S. Takeuchi, T. Teranishi, Y. Yanagisawa, and M. Ishihara, Physics Letters B **491**, 8 (2000).

[32] N. Fukuda, T. Nakamura, N. Aoi, N. Imai, M. Ishihara, T. Kobayashi, H. Iwasaki, T. Kubo, A. Mengoni, M. Notani, H. Otsu, H. Sakurai, S. Shimoura, T. Teranishi, Y. X. Watanabe, and K. Yoneda, Phys. Rev. C **70**, 054606 (2004).

[33] P. Navrátil, M. Thoresen, and B. R. Barrett, Phys. Rev. C **55**, R573 (1997).

[34] P. Navrátil, J. P. Vary, and B. R. Barrett, Phys. Rev. C **62**, 054311 (2000).

[35] V. F. Weisskopf, Phys. Rev. **83**, 1073 (1951).

[36] V. Zelevinsky, *Quantum Physics: Volume 1: From Basics to Symmetries and Perturbations* (John Wiley & Sons, 2011).

[37] S. Raman, C. N. Jr., and P. Tikkanen, Atomic Data and Nuclear Data Tables **78**, 1 (2001).

[38] D. J. Millener, J. W. Olness, E. K. Warburton, and S. S. Hanna, Phys. Rev. C **28**, 497 (1983).

[39] T. Glasmacher, B. Brown, M. Chromik, P. Cottle, M. Fauerbach, R. Ibbotson, K. Kemper, D. Morrissey, H. Scheit, D. Sklenicka, and M. Steiner, Physics Letters B **395**, 163 (1997).

[40] A. E. Litherland and A. J. Ferguson, Canadian Journal of Physics **39**, 788 (1961).

[41] P. J. Nolan and J. F. Sharpey-Schafer, Reports on Progress in Physics **42**, 1 (1979).

[42] A. Einstein, Annalen der Physik **322**, 891 (1905).

[43] H. Lorentz, in *KNAW Proceedings*, Vol. 6, pp. 1903–1904.

[44] A. Dewald, O. Möller, and P. Petkov, Progress in Particle and Nuclear Physics **67**, 786 (2012).

[45] T. K. Alexander and K. W. Allen, Canadian Journal of Physics **43**, 1563 (1965).

[46] P. Adrich, D. Enderich, D. Miller, V. Moeller, R. Norris, K. Starosta, C. Vaman, P. Voss, and A. Dewald, Nuclear Instruments and Methods in Physics Research Section A: Accelerators, Spectrometers, Detectors and Associated Equipment **598**, 454 (2009).

[47] A. Dewald, S. Harissopulos, and P. von Brentano, Zeitschrift für Physik A Atomic Nuclei **334**, 163 (1989).

[48] H. Iwasaki, A. Dewald, T. Braunroth, C. Fransen, D. Smalley, A. Lemasson, C. Morse, K. Whitmore, and C. Loelius, Nuclear Instruments and Methods in Physics Research Section A: Accelerators, Spectrometers, Detectors and Associated Equipment **806**, 123 (2016).

[49] D. Smalley, H. Iwasaki, P. Navrátil, R. Roth, J. Langhammer, V. M. Bader, D. Bazin, J. S. Berryman, C. M. Campbell, J. Dohet-Eraly, P. Fallon, A. Gade, C. Langer, A. Lemasson, C. Loelius, A. O. Macchiavelli, C. Morse, J. Parker, S. Quaglioni, F. Recchia, S. R. Stroberg, D. Weisshaar, K. Whitmore, and K. Wimmer, Phys. Rev. C **92**, 064314 (2015).

[50] W. Currie, Nuclear Instruments and Methods **73**, 173 (1969).

[51] K. Alder, A. Bohr, T. Huus, B. Mottelson, and A. Winther, Rev. Mod. Phys. **28**, 432 (1956).

[52] T. Glasmacher, Nuclear Physics A **693**, 90 (2001).

[53] A. Winther and K. Alder, Nuclear Physics A **319**, 518 (1979).

[54] T. Motobayashi, Y. Ikeda, K. Ieki, M. Inoue, N. Iwasa, T. Kikuchi, M. Kurokawa, S. Moriya, S. Ogawa, H. Murakami, S. Shimoura, Y. Yanagisawa, T. Nakamura, Y. Watanabe, M. Ishihara, T. Teranishi, H. Okuno, and R. Casten, Physics Letters B **346**, 9 (1995).

[55] H. Iwasaki, T. Motobayashi, H. Sakurai, K. Yoneda, T. Gomi, N. Aoi, N. Fukuda, Z. Fülöp, U. Futakami, Z. Gacsi, Y. Higurashi, N. Imai, N. Iwasa, T. Kubo, M. Kunibu, M. Kurokawa, Z. Liu, T. Minemura, A. Saito, M. Serata, S. Shimoura, S. Takeuchi, Y. Watanabe, K. Yamada, Y. Yanagisawa, and M. Ishihara, Physics Letters B **620**, 118 (2005).

[56] C. Bertulani, Computer Physics Communications **116**, 345 (1999).

[57] J. Raynal, "Notes on ECIS94 (unpublished)," .

[58] J. Barrette, N. Alamanos, F. Auger, B. Fernandez, A. Gillibert, D. Horen, J. Beene, F. Bertrand, R. Auble, B. Burks, J. G. D. Campo, M. Halbert, R. Sayer, W. Mittig, Y. Schutz, B. Haas, and J. Vivien, Physics Letters B **209**, 182 (1988).

[59] D. Morrissey, B. Sherrill, M. Steiner, A. Stolz, and I. Wiedenhoever, Nuclear Instruments and Methods in Physics Research Section B: Beam Interactions with Materials and Atoms **204**, 90 (2003), 14th International Conference on Electromagnetic Isotope Separators and Techniques Related to their Applications.

[60] O. Kester, D. Bazin, C. Benatti, J. Bierwagen, G. Bollen, S. Bricker, S. Chouhan, C. Compton, K. Davidson, J. DeLauter, *et al.*, Proceedings of the SRF2009, Berlin, Germany , 57 (2009).

[61] D. Morrissey, Nuclear Physics A **616**, 45 (1997).

[62] P. Zavodszky, B. Arend, D. Cole, J. DeKamp, G. Machicoane, F. Marti, P. Miller, J. Moskalik, J. Ottarson, J. Vincent, and A. Zeller", "Nuclear Instruments and Methods in Physics Research Section B: Beam Interactions with Materials and Atoms " **"241"**, "959 ("2005"), "The Application of Accelerators in Research and Industry Proceedings of the Eighteenth International Conference on the Application of Accelerators in Research and Industry (CAARI 2004)Eighteenth International Conference on the Application of Accelerators in Research and Industry ".

[63] G. Machicoane, D. Cole, J. Ottarson, J. Stetson, and P. Zavodszky, Review of Scientific Instruments **77**, 03A322 (2006).

[64] D. Leitner and C. Lyneis, "Ecr ion sources," in *The Physics and Technology of Ion Sources* (Wiley-VCH Verlag GmbH & Co. KGaA, 2005) pp. 203–231.

[65] R. Geller, *Electron Cyclotron Resonance Ion Sources and ECR Plasmas* (Taylor & Francis, 1996).

[66] E. O. Lawrence and M. S. Livingston, Phys. Rev. **40**, 19 (1932).

[67] H. Wiedemann, "Circular accelerators," in *Particle Accelerator Physics* (Springer International Publishing, Cham, 2015) pp. 59–80.

[68] H. H. Heckman, D. E. Greiner, P. J. Lindstrom, and F. S. Bieser, Phys. Rev. Lett. **28**, 926 (1972).

[69] C. K. Gelbke, Physica Scripta **1990**, 107 (1990).

[70] J. Dufour, R. D. Moral, H. Emmermann, F. Hubert, D. Jean, C. Poinot, M. Pravikoff, A. Fleury, H. Delagrange, and K.-H. Schmidt, Nuclear Instruments and Methods in Physics Research Section A: Accelerators, Spectrometers, Detectors and Associated Equipment **248**, 267 (1986).

[71] D. Bazin, J. Caggiano, B. Sherrill, J. Yurkon, and A. Zeller, Nuclear Instruments and Methods in Physics Research Section B: Beam Interactions with Materials and Atoms **204**, 629 (2003), 14th International Conference on Electromagnetic Isotope Separators and Techniques Related to their Applications.

[72] M. Berz, K. Joh, J. A. Nolen, B. M. Sherrill, and A. F. Zeller, Phys. Rev. C **47**, 537 (1993).

[73] J. Yurkon, D. Bazin, W. Benenson, D. Morrissey, B. Sherrill, D. Swan, and R. Swanson, Nuclear Instruments and Methods in Physics Research Section A: Accelerators, Spectrometers, Detectors and Associated Equipment **422**, 291 (1999).

[74] G. Knoll, *Radiation Detection and Measurement* (John Wiley & Sons, 2010).

[75] "S800 service level description," `https://wikihost.nscl.msu.edu/S800Doc/doku.php`, accessed: 2017-03-27.

[76] K. Wimmer, D. Barofsky, D. Bazin, L. Fraile, J. Lloyd, J. Tompkins, and S. Williams, Nuclear Instruments and Methods in Physics Research Section A: Accelerators, Spectrometers, Detectors and Associated Equipment **769**, 65 (2015).

[77] K. Meierbachtol, D. Bazin, and D. Morrissey, Nuclear Instruments and Methods in Physics Research Section A: Accelerators, Spectrometers, Detectors and Associated Equipment **652**, 668 (2011), symposium on Radiation Measurements and Applications (SORMA) {XII} 2010.

[78] K. Wimmer and E. Lunderberg, "NSCL S800 ROOT data analysis (unpublished)," .

[79] S. Paschalis, I. Lee, A. Macchiavelli, C. Campbell, M. Cromaz, S. Gros, J. Pavan, J. Qian, R. Clark, H. Crawford, D. Doering, P. Fallon, C. Lionberger, T. Loew, M. Petri, T. Stezelberger, S. Zimmermann, D. Radford, K. Lagergren, D. Weisshaar, R. Winkler, T. Glasmacher, J. Anderson, and C. Beausang, Nuclear Instruments and Methods in Physics Research Section A: Accelerators, Spectrometers, Detectors and Associated Equipment **709**, 44 (2013).

[80] R. Evans, *The Atomic Nucleus* (McGraw-Hill, 1955).

[81] A. Zee, *Quantum Field Theory in a Nutshell: (Second Edition)*, In a Nutshell (Princeton University Press, 2010).

[82] G. A. Ausman Jr and F. B. McLean, Applied Physics Letters **26**, 173 (1975).

[83] B. Phlips, W. Johnson, R. Kroeger, and J. Kurfess, in *Nuclear Science Symposium Conference Record, 2001 IEEE*, Vol. 1 (IEEE, 2001) pp. 207–211.

[84] H. Hubbel and S. Seltzer, "Tables of x-ray mass attenuation coefficients and mass energy-absorption coefficients (2017 mar 2)," (2004).

[85] M. Deleplanque, I. Lee, K. Vetter, G. Schmid, F. Stephens, R. Clark, R. Diamond, P. Fallon, and A. Macchiavelli, Nuclear Instruments and Methods in Physics Research Section A: Accelerators, Spectrometers, Detectors and Associated Equipment **430**, 292 (1999).

[86] K. Vetter, Nuclear Physics A **682**, 286 (2001).

[87] S. Agostinelli, J. Allison, K. Amako, J. Apostolakis, H. Araujo, P. Arce, M. Asai, D. Axen, S. Banerjee, G. Barrand, F. Behner, L. Bellagamba, J. Boudreau, L. Broglia, A. Brunengo,

H. Burkhardt, S. Chauvie, J. Chuma, R. Chytracek, G. Cooperman, G. Cosmo, P. Degtyarenko, A. Dell'Acqua, G. Depaola, D. Dietrich, R. Enami, A. Feliciello, C. Ferguson, H. Fesefeldt, G. Folger, F. Foppiano, A. Forti, S. Garelli, S. Giani, R. Giannitrapani, D. Gibin, J. G. Cadenas, I. González, G. G. Abril, G. Greeniaus, W. Greiner, V. Grichine, A. Grossheim, S. Guatelli, P. Gumplinger, R. Hamatsu, K. Hashimoto, H. Hasui, A. Heikkinen, A. Howard, V. Ivanchenko, A. Johnson, F. Jones, J. Kallenbach, N. Kanaya, M. Kawabata, Y. Kawabata, M. Kawaguti, S. Kelner, P. Kent, A. Kimura, T. Kodama, R. Kokoulin, M. Kossov, H. Kurashige, E. Lamanna, T. Lampén, V. Lara, V. Lefebure, F. Lei, M. Liendl, W. Lockman, F. Longo, S. Magni, M. Maire, E. Medernach, K. Minamimoto, P. M. de Freitas, Y. Morita, K. Murakami, M. Nagamatu, R. Nartallo, P. Nieminen, T. Nishimura, K. Ohtsubo, M. Okamura, S. O'Neale, Y. Oohata, K. Paech, J. Perl, A. Pfeiffer, M. Pia, F. Ranjard, A. Rybin, S. Sadilov, E. D. Salvo, G. Santin, T. Sasaki, N. Savvas, Y. Sawada, S. Scherer, S. Sei, V. Sirotenko, D. Smith, N. Starkov, H. Stoecker, J. Sulkimo, M. Takahata, S. Tanaka, E. Tcherniaev, E. S. Tehrani, M. Tropeano, P. Truscott, H. Uno, L. Urban, P. Urban, M. Verderi, A. Walkden, W. Wander, H. Weber, J. Wellisch, T. Wenaus, D. Williams, D. Wright, T. Yamada, H. Yoshida, and D. Zschiesche, Nuclear Instruments and Methods in Physics Research Section A: Accelerators, Spectrometers, Detectors and Associated Equipment **506**, 250 (2003).

[88] Physik Instrumente, "Piezowalk piezo motors," Accessed 4 March 2017: https://www.physikinstrumente.com/en/technology/piezoelectric-drives/piezowalk-piezo-motors/.

[89] "Tesa technology," http://www.tesatechnology.com/.

[90] A. Zangwill, *Modern Electrodynamics*, Modern Electrodynamics (Cambridge University Press, 2013).

[91] C. Loelius, H. Iwasaki, B. A. Brown, M. Honma, V. M. Bader, T. Baugher, D. Bazin, J. S. Berryman, T. Braunroth, C. M. Campbell, A. Dewald, A. Gade, N. Kobayashi, C. Langer, I. Y. Lee, A. Lemasson, E. Lunderberg, C. Morse, F. Recchia, D. Smalley, S. R. Stroberg, R. Wadsworth, C. Walz, D. Weisshaar, A. Westerberg, K. Whitmore, and K. Wimmer, Phys. Rev. C **94**, 024340 (2016).

[92] B. Blank, M. Chartier, S. Czajkowski, J. Giovinazzo, M. S. Pravikoff, J.-C. Thomas, G. de France, F. de Oliveira Santos, M. Lewitowicz, C. Borcea, R. Grzywacz, Z. Janas, and M. Pfützner, Phys. Rev. Lett. **84**, 1116 (2000).

[93] K. L. Yurkewicz, D. Bazin, B. A. Brown, C. M. Campbell, J. A. Church, D. C. Dinca, A. Gade, T. Glasmacher, M. Honma, T. Mizusaki, W. F. Mueller, H. Olliver, T. Otsuka, L. A. Riley, and J. R. Terry, Phys. Rev. C **70**, 054319 (2004).

[94] Z. Y. Xu, S. Nishimura, G. Lorusso, F. Browne, P. Doornenbal, G. Gey, H.-S. Jung, Z. Li, M. Niikura, P.-A. Söderström, T. Sumikama, J. Taprogge, Z. Vajta, H. Watanabe, J. Wu, A. Yagi, K. Yoshinaga, H. Baba, S. Franchoo, T. Isobe, P. R. John, I. Kojouharov, S. Kubono,

N. Kurz, I. Matea, K. Matsui, D. Mengoni, P. Morfouace, D. R. Napoli, F. Naqvi, H. Nishibata, A. Odahara, E. Şahin, H. Sakurai, H. Schaffner, I. G. Stefan, D. Suzuki, R. Taniuchi, and V. Werner, Phys. Rev. Lett. **113**, 032505 (2014).

[95] P. T. Hosmer, H. Schatz, A. Aprahamian, O. Arndt, R. R. C. Clement, A. Estrade, K.-L. Kratz, S. N. Liddick, P. F. Mantica, W. F. Mueller, F. Montes, A. C. Morton, M. Ouellette, E. Pellegrini, B. Pfeiffer, P. Reeder, P. Santi, M. Steiner, A. Stolz, B. E. Tomlin, W. B. Walters, and A. Wöhr, Phys. Rev. Lett. **94**, 112501 (2005).

[96] O. Sorlin, S. Leenhardt, C. Donzaud, J. Duprat, F. Azaiez, F. Nowacki, H. Grawe, Z. Dombrádi, F. Amorini, A. Astier, D. Baiborodin, M. Belleguic, C. Borcea, C. Bourgeois, D. M. Cullen, Z. Dlouhy, E. Dragulescu, M. Górska, S. Grévy, D. Guillemaud-Mueller, G. Hagemann, B. Herskind, J. Kiener, R. Lemmon, M. Lewitowicz, S. M. Lukyanov, P. Mayet, F. de Oliveira Santos, D. Pantalica, Y.-E. Penionzhkevich, F. Pougheon, A. Poves, N. Redon, M. G. Saint-Laurent, J. A. Scarpaci, G. Sletten, M. Stanoiu, O. Tarasov, and C. Theisen, Phys. Rev. Lett. **88**, 092501 (2002).

[97] T. Marchi, G. de Angelis, J. J. Valiente-Dobón, V. M. Bader, T. Baugher, D. Bazin, J. Berryman, A. Bonaccorso, R. Clark, L. Coraggio, H. L. Crawford, M. Doncel, E. Farnea, A. Gade, A. Gadea, A. Gargano, T. Glasmacher, A. Gottardo, F. Gramegna, N. Itaco, P. R. John, R. Kumar, S. M. Lenzi, S. Lunardi, S. McDaniel, C. Michelagnoli, D. Mengoni, V. Modamio, D. R. Napoli, B. Quintana, A. Ratkiewicz, F. Recchia, E. Sahin, R. Stroberg, D. Weisshaar, K. Wimmer, and R. Winkler, Phys. Rev. Lett. **113**, 182501 (2014).

[98] K. Kolos, D. Miller, R. Grzywacz, H. Iwasaki, M. Al-Shudifat, D. Bazin, C. R. Bingham, T. Braunroth, G. Cerizza, A. Gade, A. Lemasson, S. N. Liddick, M. Madurga, C. Morse, M. Portillo, M. M. Rajabali, F. Recchia, L. L. Riedinger, P. Voss, W. B. Walters, D. Weisshaar, K. Whitmore, K. Wimmer, and J. A. Tostevin, Phys. Rev. Lett. **116**, 122502 (2016).

[99] B. Bastin, S. Grévy, D. Sohler, O. Sorlin, Z. Dombrádi, N. L. Achouri, J. C. Angélique, F. Azaiez, D. Baiborodin, R. Borcea, C. Bourgeois, A. Buta, A. Bürger, R. Chapman, J. C. Dalouzy, Z. Dlouhy, A. Drouard, Z. Elekes, S. Franchoo, S. Iacob, B. Laurent, M. Lazar, X. Liang, E. Liénard, J. Mrazek, L. Nalpas, F. Negoita, N. A. Orr, Y. Penionzhkevich, Z. Podolyák, F. Pougheon, P. Roussel-Chomaz, M. G. Saint-Laurent, M. Stanoiu, I. Stefan, F. Nowacki, and A. Poves, Phys. Rev. Lett. **99**, 022503 (2007).

[100] S. M. Lenzi, F. Nowacki, A. Poves, and K. Sieja, Phys. Rev. C **82**, 054301 (2010).

[101] Y. Tsunoda, T. Otsuka, N. Shimizu, M. Honma, and Y. Utsuno, Phys. Rev. C **89**, 031301 (2014).

[102] M. Honma, T. Otsuka, B. Brown, and T. Mizusaki, The European Physical Journal A - Hadrons and Nuclei **25**, 499 (2005).

[103] A. Poves, J. Sánchez-Solano, E. Caurier, and F. Nowacki, Nuclear Physics A **694**, 157 (2001).

[104] M. Honma, T. Otsuka, B. A. Brown, and T. Mizusaki, Phys. Rev. C **69**, 034335 (2004).

[105] J. M. Allmond, B. A. Brown, A. E. Stuchbery, A. Galindo-Uribarri, E. Padilla-Rodal, D. C. Radford, J. C. Batchelder, M. E. Howard, J. F. Liang, B. Manning, R. L. Varner, and C.-H. Yu, Phys. Rev. C **90**, 034309 (2014).

[106] O. Kenn, K.-H. Speidel, R. Ernst, J. Gerber, P. Maier-Komor, and F. Nowacki, Phys. Rev. C **63**, 064306 (2001).

[107] H. Iwasaki, A. Lemasson, C. Morse, A. Dewald, T. Braunroth, V. M. Bader, T. Baugher, D. Bazin, J. S. Berryman, C. M. Campbell, A. Gade, C. Langer, I. Y. Lee, C. Loelius, E. Lunderberg, F. Recchia, D. Smalley, S. R. Stroberg, R. Wadsworth, C. Walz, D. Weisshaar, A. Westerberg, K. Whitmore, and K. Wimmer, Phys. Rev. Lett. **112**, 142502 (2014).

[108] O. Tarasov and D. Bazin, Nuclear Instruments and Methods in Physics Research Section B: Beam Interactions with Materials and Atoms **266**, 4657 (2008), proceedings of the {XVth} International Conference on Electromagnetic Isotope Separators and Techniques Related to their Applications.

[109] C. D. Nesaraja, S. D. Geraedts, and B. Singh, Nuclear Data Sheets **111**, 897 (2010).

[110] T. Mizusaki, N. Shimizu, Y. Utsuno, and M. Honma, "Code mshell64," Unpublished.

[111] K. Whitmore, D. Smalley, H. Iwasaki, T. Suzuki, V. M. Bader, D. Bazin, J. S. Berryman, B. A. Brown, C. M. Campbell, P. Fallon, A. Gade, C. Langer, A. Lemasson, C. Loelius, A. O. Macchiavelli, C. Morse, T. Otsuka, J. Parker, F. Recchia, S. R. Stroberg, D. Weisshaar, and K. Wimmer, Phys. Rev. C **91**, 041303 (2015).

[112] J. Gibelin, D. Beaumel, T. Motobayashi, N. Aoi, H. Baba, Y. Blumenfeld, Z. Dombrádi, Z. Elekes, S. Fortier, N. Frascaria, N. Fukuda, T. Gomi, K. Ishikawa, Y. Kondo, T. Kubo, V. Lima, T. Nakamura, A. Saito, Y. Satou, E. Takeshita, S. Takeuchi, T. Teranishi, Y. Togano, A. M. Vinodkumar, Y. Yanagisawa, and K. Yoshida, Phys. Rev. C **75**, 057306 (2007).

[113] N. Orr, W. Mittig, L. Fifield, M. Lewitowicz, E. Plagnol, Y. Schutz, Z. W. Long, L. Bianchi, A. Gillibert, A. Belozyorov, S. Lukyanov, Y. Penionzhkevich, A. Villari, A. Cunsolo, A. Foti, G. Audi, C. Stephan, and L. Tassan-Got, Physics Letters B **258**, 29 (1991).

[114] M. Belleguic, F. Azaiez, Z. Dombrádi, D. Sohler, M. J. Lopez-Jimenez, T. Otsuka, M. G. Saint-Laurent, O. Sorlin, M. Stanoiu, Y. Utsuno, Y.-E. Penionzhkevich, N. L. Achouri, J. C. Angelique, C. Borcea, C. Bourgeois, J. M. Daugas, F. D. Oliveira-Santos, Z. Dlouhy, C. Donzaud, J. Duprat, Z. Elekes, S. Grévy, D. Guillemaud-Mueller, S. Leenhardt, M. Lewitowicz, S. M. Lukyanov, W. Mittig, M. G. Porquet, F. Pougheon, P. Roussel-Chomaz, H. Savajols, Y. Sobolev, C. Stodel, and J. Timár, Phys. Rev. C **72**, 054316 (2005).

[115] Z. Dombrádi, Z. Elekes, A. Saito, N. Aoi, H. Baba, K. Demichi, Z. Fülöp, J. Gibelin, T. Gomi, H. Hasegawa, N. Imai, M. Ishihara, H. Iwasaki, S. Kanno, S. Kawai, T. Kishida, T. Kubo, K. Kurita, Y. Matsuyama, S. Michimasa, T. Minemura, T. Motobayashi, M. Notani, T. Ohnishi, H. J. Ong, S. Ota, A. Ozawa, H. K. Sakai, H. Sakurai, S. Shimoura, E. Takeshita, S. Takeuchi, M. Tamaki, Y. Togano, K. Yamada, Y. Yanagisawa, and K. Yoneda, Phys. Rev. Lett. **96**, 182501 (2006).

[116] J. Terry, D. Bazin, B. Brown, C. Campbell, J. Church, J. Cook, A. Davies, D.-C. Dinca, J. Enders, A. Gade, T. Glasmacher, P. Hansen, J. Lecouey, T. Otsuka, B. Pritychenko, B. Sherrill, J. Tostevin, Y. Utsuno, K. Yoneda, and H. Zwahlen, Physics Letters B **640**, 86 (2006).

[117] M. S. Basunia, Nuclear Data Sheets **112**, 1875 (2011).

[118] A. Obertelli, A. Gillibert, N. Alamanos, M. Alvarez, F. Auger, R. Dayras, A. Drouart, G. de France, B. Jurado, N. Keeley, V. Lapoux, W. Mittig, X. Mougeot, L. Nalpas, A. Pakou, N. Patronis, E. Pollacco, F. Rejmund, M. Rejmund, P. Roussel-Chomaz, H. Savajols, F. Skaza, and C. Theisen, Physics Letters B **633**, 33 (2006).

[119] S. M. Brown, W. N. Catford, J. S. Thomas, B. Fernández-Domínguez, N. A. Orr, M. Labiche, M. Rejmund, N. L. Achouri, H. Al Falou, N. I. Ashwood, D. Beaumel, Y. Blumenfeld, B. A. Brown, R. Chapman, M. Chartier, N. Curtis, G. de France, N. de Sereville, F. Delaunay, A. Drouart, C. Force, S. Franchoo, J. Guillot, P. Haigh, F. Hammache, V. Lapoux, R. C. Lemmon, A. Leprince, F. Maréchal, X. Mougeot, B. Mouginot, L. Nalpas, A. Navin, N. P. Patterson, B. Pietras, E. C. Pollacco, A. Ramus, J. A. Scarpaci, I. Stefan, and G. L. Wilson, Phys. Rev. C **85**, 011302 (2012).

[120] B. Pritychenko, T. Glasmacher, P. Cottle, M. Fauerbach, R. Ibbotson, K. Kemper, V. Maddalena, A. Navin, R. Ronningen, A. Sakharuk, H. Scheit, and V. Zelevinsky, Physics Letters B **461**, 322 (1999).

[121] M. S. Basunia, Nuclear Data Sheets **114**, 1189 (2013).

[122] V. Chisté, A. Gillibert, A. Lépine-Szily, N. Alamanos, F. Auger, J. Barrette, F. Braga, M. Cortina-Gil, Z. Dlouhy, V. Lapoux, M. Lewitowicz, R. Lichtenthäler, R. Neto, S. Lukyanov, M. MacCormick, F. Marie, W. Mittig, F. de Oliveira Santos, N. Orr, A. Ostrowski, S. Ottini, A. Pakou, Y. Penionzhkevich, P. Roussel-Chomaz, and J. Sida, Physics Letters B **514**, 233 (2001).

[123] O. Niedermaier, H. Scheit, V. Bildstein, H. Boie, J. Fitting, R. von Hahn, F. Köck, M. Lauer, U. K. Pal, H. Podlech, R. Repnow, D. Schwalm, C. Alvarez, F. Ames, G. Bollen, S. Emhofer, D. Habs, O. Kester, R. Lutter, K. Rudolph, M. Pasini, P. G. Thirolf, B. H. Wolf, J. Eberth, G. Gersch, H. Hess, P. Reiter, O. Thelen, N. Warr, D. Weisshaar, F. Aksouh, P. Van den Bergh, P. Van Duppen, M. Huyse, O. Ivanov, P. Mayet, J. Van de Walle, J. Äystö, P. A. Butler, J. Cederkäll, P. Delahaye, H. O. U. Fynbo, L. M. Fraile, O. Forstner, S. Franchoo, U. Köster, T. Nilsson, M. Oinonen, T. Sieber, F. Wenander, M. Pantea, A. Richter, G. Schrieder, H. Simon, T. Behrens, R. Gernhäuser, T. Kröll, R. Krücken, M. Münch, T. Davinson, J. Gerl, G. Huber, A. Hurst, J. Iwanicki, B. Jonson, P. Lieb, L. Liljeby, A. Schempp, A. Scherillo, P. Schmidt, and G. Walter, Phys. Rev. Lett. **94**, 172501 (2005).

[124] M. S. Basunia, Nuclear Data Sheets **111**, 2331 (2010).

[125] R. Ringle, M. Brodeur, T. Brunner, S. Ettenauer, M. Smith, A. Lapierre, V. Ryjkov, P. Delheij, G. Drake, J. Lassen, D. Lunney, and J. Dilling, Physics Letters B **675**, 170 (2009).

[126] S. S. Hanna, K. Nagatani, W. R. Harris, and J. W. Olness, Phys. Rev. C **3**, 2198 (1971).

[127] Y. Hirayama, T. Shimoda, H. Izumi, A. Hatakeyama, K. Jackson, C. Levy, H. Miyatake, M. Yagi, and H. Yano, Physics Letters B **611**, 239 (2005).

[128] I. Tanihata, T. Kobayashi, O. Yamakawa, S. Shimoura, K. Ekuni, K. Sugimoto, N. Takahashi, T. Shimoda, and H. Sato, Physics Letters B **206**, 592 (1988).

[129] M. Fukuda, T. Ichihara, N. Inabe, T. Kubo, H. Kumagai, T. Nakagawa, Y. Yano, I. Tanihata, M. Adachi, K. Asahi, M. Kouguchi, M. Ishihara, H. Sagawa, and S. Shimoura, Physics Letters B **268**, 339 (1991).

[130] J. H. Kelley, S. M. Austin, R. A. Kryger, D. J. Morrissey, N. A. Orr, B. M. Sherrill, M. Thoennessen, J. S. Winfield, J. A. Winger, and B. M. Young, Phys. Rev. Lett. **74**, 30 (1995).

[131] H. Sagawa, T. Suzuki, H. Iwasaki, and M. Ishihara, Phys. Rev. C **63**, 034310 (2001).

[132] T. Aumann and T. Nakamura, Physica Scripta **2013**, 014012 (2013).

[133] F. Nunes, I. Thompson, and R. Johnson, Nuclear Physics A **596**, 171 (1996).

[134] T. Nakamura, A. M. Vinodkumar, T. Sugimoto, N. Aoi, H. Baba, D. Bazin, N. Fukuda, T. Gomi, H. Hasegawa, N. Imai, M. Ishihara, T. Kobayashi, Y. Kondo, T. Kubo, M. Miura, T. Motobayashi, H. Otsu, A. Saito, H. Sakurai, S. Shimoura, K. Watanabe, Y. X. Watanabe, T. Yakushiji, Y. Yanagisawa, and K. Yoneda, Phys. Rev. Lett. **96**, 252502 (2006).

[135] J. Chen and B. Singh, Nuclear Data Sheets **112**, 1393 (2011).

[136] P. A. Butler, A. J. Brown, P. E. Carr, L. L. Green, A. N. James, C. J. Lister, J. D. MacArthur, P. J. Nolan, and J. F. Sharpey-Schafer, Journal of Physics G: Nuclear Physics **1**, 543 (1975).

[137] P. E. Carr, D. C. Bailey, J. L. Durell, L. L. Green, A. N. James, J. F. Sharpey-Schafer, and D. A. Viggars, Journal of Physics A: Mathematical, Nuclear and General **6**, 685 (1973).

[138] T. Misu, W. Nazarewicz, and S. Åberg, Nuclear Physics A **614**, 44 (1997).

[139] T. Nakamura, N. Kobayashi, Y. Kondo, Y. Satou, N. Aoi, H. Baba, S. Deguchi, N. Fukuda, J. Gibelin, N. Inabe, M. Ishihara, D. Kameda, Y. Kawada, T. Kubo, K. Kusaka, A. Mengoni, T. Motobayashi, T. Ohnishi, M. Ohtake, N. A. Orr, H. Otsu, T. Otsuka, A. Saito, H. Sakurai, S. Shimoura, T. Sumikama, H. Takeda, E. Takeshita, M. Takechi, S. Takeuchi, K. Tanaka, K. N. Tanaka, N. Tanaka, Y. Togano, Y. Utsuno, K. Yoneda, A. Yoshida, and K. Yoshida, Phys. Rev. Lett. **103**, 262501 (2009).

[140] I. Hamamoto, Phys. Rev. C **81**, 021304 (2010).

[141] N. Kobayashi, T. Nakamura, Y. Kondo, J. A. Tostevin, Y. Utsuno, N. Aoi, H. Baba, R. Barthelemy, M. A. Famiano, N. Fukuda, N. Inabe, M. Ishihara, R. Kanungo, S. Kim, T. Kubo, G. S. Lee, H. S. Lee, M. Matsushita, T. Motobayashi, T. Ohnishi, N. A. Orr, H. Otsu, T. Otsuka, T. Sako, H. Sakurai, Y. Satou, T. Sumikama, H. Takeda, S. Takeuchi, R. Tanaka, Y. Togano, and K. Yoneda, Phys. Rev. Lett. **112**, 242501 (2014).

[142] Y. Utsuno and A. Brown, "Private Communication" (2014).

[143] M. Thoennessen, Nuclear Physics A **834**, 688c (2010).